DEVELOPMENT OF NONINVASIVE METHODS FOR MONITORING TISSUE ENGINEERED CONSTRUCTS USING NUCLEAR MAGNETIC RESONANCE

A Dissertation
Presented to
The Academic Faculty

By

Cheryl L Stabler

In Partial Fulfillment
Of the Requirements for the Degree
Doctor of Philosophy in Biomedical Engineering

Georgia Institute of Technology

&

Emory University

May 2004

DEVELOPMENT OF NONINVASIVE METHODS FOR MONITORING TISSUE ENGINEERED CONSTRUCTS USING NUCLEAR MAGNETIC RESONANCE

Approved by:

Dr. Athanassios Sambanis, Advisor

Dr. Ioannis Constantinidis

Dr. Robert C. Long, Jr.

Dr. Elliot Chaikof

Dr. Stephen Hanson

April 2nd, 2004.

ACKNOWLEDGEMENTS

First and foremost, I would like to express my sincere gratitude to my advisor, Dr. Athanassios Sambanis, whose impact on the development of my professional career has been immeasurable. The patience, candor, intelligence, and vision you exhibit everyday as a professor has given me the ideal model to use as I pursue my scientific endeavors. I would also like to thank both Drs Robert Long and Ioannis Constantinidis for their continuous contributions to my development as a scientist and for their personal guidance in the advancement of my career. Furthermore, I would like to extend my appreciation to Drs Elliot Chaikof and Stephen Hanson for their contributions and commitment to this project.

I am also grateful to the universities of Georgia Tech and Emory for allowing me to study in such an amazing academic environment. Specifically, I would like to thank the BME department, GTEC, Dr. Michelle LaPlaca, Dr. Julie Babensee, Donna Brown, Sally Garrish, and Dr. Robert Nerem, for continually providing me with the opportunity to not only conduct and present my scientific work, but to grow professionally in other areas, such as leadership, teaching, and mentoring skills. I would also like to thank all of my lab members, including Shing-Yi Cheng, Tony Tang, Jeff Gross, Neil Mukherjee, Thein Tun, Heather Virginia, Joe Berglund, and Nick Simpson, who have always been so helpful in my research. I am thankful for all the wonderful friends I have made here, who have made this journey so much more enjoyable, especially Cecilia Curry, Jamie Severin, Matt Tate, Ann Ensley, Eric Vanderploeg, Blaise Porter, Shannon Stoot, Ben Keslowsky, Zach Priest, and Ciara Caltagirone.

I would also like to acknowledge my family, both the Stablers and the Andersons, whose love and support have always helped me keep the right perspective. I would especially like to thank my sister Tanya, who shows me by example the researcher I can only strive to be. Finally, I would like to thank my husband Scott, especially for his immense patience during these past five years, support in every aspect of my career, and love, which is beyond what I deserve.

This work was primarily supported by funding from the Georgia Tech/Emory Center (GTEC) for the Engineering of Living Tissues, an ERC Program of the National Science Foundation under Award Number EEC-9731643, as well as from NIH grants DK47858 and DK56890. Upgrade of the NMR instrumentation from the NIH Shared Instrumentation Grant S10-RR13003 is also acknowledged. Partial stipend support was also provided by the NIH training grant (GM08433). This financial support to this interdisciplinary research is greatly appreciated.

TABLE OF CONTENTS

ACKNOWLEDGEMENTS iii

LIST OF TABLES ix

LIST OF FIGURES x

SUMMARY xvii

CHAPTER 1: INTRODUCTION AND RATIONALE 1
1.1. INTRODUCTION 1
1.2. RATIONALE 4

CHAPTER 2: BACKGROUND 10
2.1. CURRENT TREATMENTS FOR INSULIN-DEPENDENT DIABETES 10
2.2. INSULIN-SECRETING CELL TYPE 12
2.3. BIOMATERIALS 13
2.4. CONSTRUCT DESIGNS 16
2.5. NONINVASIVE MONITORING *IN VIVO* 19
2.6. NMR SPECTROSCOPY AND IMAGING 22

CHAPTER 3: THE EFFECTS OF ALGINATE COMPOSITION ON ENCAPSULATED βTC3 CELLS 29
3.1. ABSTRACT 29
3.2. INTRODUCTION 30
3.3. MATERIALS & METHODS 33
3.3.1. Cell culture 33
3.3.2. Alginate 33
3.3.3. Entrapment and culture propagation 34
3.3.4. Analytical techniques 35
3.3.5. Histology 36
3.4. RESULTS 36
3.4.1. Effects of Guluronic Acid Content 36
3.4.2. Effects of Alginate Concentration 41
3.5. DISCUSSION 48

CHAPTER 4: EFFECTS OF ALGINATE COMPOSITION ON THE GROWTH AND OVERALL METABOLIC ACTIVITY OF βTC3 CELLS 54
4.1. ABSTRACT 54
4.2. INTRODUCTION 54
4.3. RESULTS AND DISCUSSION 56

CHAPTER 5: NONINVASIVE MONITORING OF A RETRIEVABLE BIOARTIFICIAL PANCREAS *IN VIVO* 60
5.1. ABSTRACT 60
5.2. INTRODUCTION 61
5.3. MATERIALS AND METHODS 62
5.3.1. Cell Culture and APA Encapsulation 62
5.3.2. NMR Spectroscopy and Imaging 62
5.4. RESULTS AND DISCUSSION 63
5.5. CONCLUSIONS 69

CHAPTER 6: *IN VITRO* CHARACTERIZATION OF βTC3 CELLS IN AGAROSE DISK CONSTRUCTS AS A BIOARTIFICIAL PANCREAS 70
6.1. ABSTRACT 70
6.2. INTRODUCTION 70
6.3. MATERIALS AND METHODS 72
6.3.1. Cell and Cell Culture 72
6.3.2. Construct Fabrication 72
6.3.3. Diffusivity Measurements 74
6.3.4. *In Vitro* Construct Characterization 76
6.3.5. Analytical Techniques 76
6.3.6. Statistical Analysis 77
6.4. RESULTS 78
6.4.1. Effective Diffusivity in Agarose Constructs 78
6.4.2. Diffusion-reaction modeling of construct with cells 80
6.4.3. *In Vitro* Construct Characterization 84
6.5. DISCUSSION 91
6.6. APPENDIX 94
6.6.1. Modeling one-dimensional solute diffusion through slab. 94
6.6.2. Modeling one-dimensional oxygen diffusion and consumption through slab containing βTC3 cells 96

CHAPTER 7: *IN VIVO* CHARACTERIZATION OF βTC3 CELLS IN AGAROSE DISK CONSTRUCTS AS A BIOARTIFICIAL PANCREAS 99
7.1. ABSTRACT 99
7.2. INTRODUCTION 100
7.3. MATERIALS AND METHODS 101
7.3.1. Cell and Cell Culture 101
7.3.2. Construct Fabrication 102
7.3.3. Animal Studies 104
7.3.4. Analytical Techniques 106
7.3.5. Statistical Analysis 106
7.4. RESULTS 106
7.5. DISCUSSION 113

CHAPTER 8: NONINVASIVE MEASUREMENT OF VIABLE CELL NUMBER IN TISSUE ENGINEERED CONSTRUCTS *IN VITRO* USING ^{1}H NMR SPECTROSCOPY 117
8.1. ABSTRACT 117
8.2. INTRODUCTION 118
8.3. MATERIALS AND METHODS 120
8.3.1. Cell Culture 120
8.3.2. Construct Fabrication 120
8.3.3. *In Vitro* Construct Characterization 122
8.3.4. ^{1}H Magnetic Resonance Imaging and Spectroscopy 123
8.3.5. Analytical Techniques 125
8.3.6. Statistical Analysis 125
8.4. RESULTS 125
8.5. DISCUSSION 136

CHAPTER 9: *IN VIVO* NONINVASIVE MONITORING OF VIABLE CELL NUMBER IN TISSUE ENGINEERED CONSTRUCTS USING ^{1}H NMR SPECTROSCOPY 143
9.1. ABSTRACT 143
9.2. INTRODUCTION 144
9.3. MATERIALS AND METHODS 146
9.3.1. Cell Culture 146
9.3.2. Construct Fabrication 147
9.3.3. Animal Studies 148
9.3.4. ^{1}H Magnetic Resonance Imaging and Spectroscopy 149
9.3.5. Analytical Techniques 151
9.3.6. Statistical Analysis 151
9.4. RESULTS 152
9.5. DISCUSSION 160

CHAPTER 10: CONCLUSIONS AND FUTURE WORK 165
10.1. CONCLUSIONS 165
10.2. FUTURE WORK 168

APPENDIX 172
A.1. ^{1}H NMR SPECTROSCOPY OF APA BEADS 172
A.2. IMPLANTATION OF APA BEADS 175
A.3. TESTING OF LOCALIZATION IMPERFECTIONS 178
A.4. TESTING OF AGAROSE/ALGINATE BEAD CONSTRUCTS 181
A.5. EFFECT OF GLUCOSE ON TOTAL-CHOLINE MEASUREMENT 187
A.6. ANESTHESIA EFFECTS ON BLOOD GLUCOSE 191
A.7. TOTAL-CHOLINE CALIBRATION CURVE FOR OTHER BETA CELL LINE 197
A.8. EFFECTS OF MION ON THE METABOLIC AND SECRETORY ACTIVITY OF βTC3 AND βTC-TET CELLS 199
A.9. REFERENCES METHODS 203
A.9.a MTS measurement of viable cell number of alginate beads in agarose . 203

A.9.b Histological processing of Alginate/Poly-L-lysine/Alginate beads..... 203

REFERENCES 205

LIST OF TABLES

Table 1. Table of alginate properties used in this study.. 34

Table 2. Predicted maximum cell densities (or total number) in constructs..... 86

Table A1. Summary of common anesthetic agents for mice. 193

LIST OF FIGURES

Figure 1 . Molecular structure of alginate. 15

Figure 2. Molecular structure of agarose. 16

Figure 3. *In vitro* water-suppressed ^{1}H NMR spectrum of $8x10^{6}$ βTC3 cells 25

Figure 4. Schematic representation of localized NMR spectroscopy. 27

Figure 5. Temporal changes in the rates of (A) glucose consumption (GCR), (B) lactate production (LPR), and (C) insulin secretion (ISR) by βTC3 cells encapsulated in 2% w/v MVG (solid diamonds), LVG (open diamonds), MVM (solid squares), and LVM (open squares) alginates. 38-39

Figure 6. Cross-sections of 2% w/v MVG and LVG APA beads containing βTC3 cells and stained with H/E at the times designated. 40

Figure 7. Cross-sections of 2% MVM and LVM APA beads containing βTC3 cells and stained with H/E at the times designated. 41

Figure 8. Temporal changes in the rates of (A) glucose consumption (GCR), (B) lactate production (LPR), and (C) insulin secretion (ISR) by βTC3 cells encapsulated in 1% w/v MVG (solid diamonds) and LVG (open diamonds) alginates 42-43

Figure 9. Cross-sections of 1% MVG and LVG APA beads containing βTC3 cells and stained with H/E at the times designated. 44

Figure 10. Temporal changes in the rates of (A) glucose consumption (GCR) (B) lactate production (LPR) and (C) insulin secretion (ISR) by βTC3 cells encapsulated in 3% w/v MVM (solid diamonds) and LVM (open diamonds) alginates. 46

Figure 11. Cross-sections of 3% MVM and LVM APA beads containing βTC3 cells and stained with H/E at the times designated. 47

Figure 12. Temporal Changes in the rates of metabolic activity (Glucose Consumption Rate) for βTC3 cells encapsulated in 2% w/v LVG/LVM (solid diamonds), LVG (open diamonds), and 2% LVM (gray diamonds) with representative histological images shown at specified time points 58

Figure 13. Temporal Changes in the rates of Secretion Activity (Insulin Secretion Rate) for βTC3 cells encapsulated in 2% w/v LVG/LVM (solid diamonds), LVG (open diamonds), and 2% LVM (gray diamonds). 59

Figure 14. Schematic representation of construct prototype. APA beads contain entrapped βTC3 cells, while outer region is the silicone ring. 64

Figure 15. Temporal changes in the rates of (A) glucose consumption (GCR) and (B) insulin secretion (ISR) of βTC3 cells encapsulated in APA beads free-floating (solid squares), or confined within 5 mm (solid diamonds), 3 mm (shaded diamonds), or 1.8 mm (open diamonds) thick constructs.. 65

Figure 16. A gradient-echo weighted image of a silicon o-ring with 0.4 mL of APA beads inside (Figure A). The white square is the volume of interest within which the water-suppressed ^{1}H NMR spectrum was acquired (Figure B). 67

Figure 17. A sagittal view through the CJ7/B6 mouse showing the location of the construct (Panel A). A coronal view through the mouse and the o-ring (Panel B). A water suppressed localized ^{1}H NMR spectrum acquired from within the o-ring (Panel C). 68

Figure 18. Schematic representation and dimensions of single agarose disk construct (A) and buffered agarose disk construct (B). The shaded region represents the inner disk containing βTC3 cells entrapped in 2% agarose, while the white region indicates pure 2% agarose. 73

Figure 19. Correlation between viable cell number, assessed by trypan blue, and MTT absorbance for βTC3 cells entrapped in agarose constructs at varying cell loadings. 78

Figure 20. Time course of diffusion of Glucose (A and B) and Insulin (C and D) out of 2% agarose disks without (A and C) and with (B and D) cells. 81-82

Figure 21. Model predicted oxygen profiles for single agarose disk constructs. The model predicted maximum cell density, where the oxygen level at center of construct is set to 7mmHg, is shown for normoxia (A), arterial oxygen (B) and approximated interstitial oxygen (C) conditions..... 85

Figure 22. Model predicted oxygen profiles for buffered agarose disk constructs. The model predicted maximum cell density, where the oxygen level at center of construct is set to 7mmHg, is shown for normoxia (A), arterial oxygen (B) and approximated interstitial oxygen (C) conditions..... 86

Figure 23. Temporal changes in MTT-assessed viable cell number (A) and insulin secretion rates (B) for single agarose disk constructs with initial cell loadings of $14x10^{6}$ cells (diamonds), $10x10^{6}$ cells (squares), and $7x10^{6}$ cells (triangles).. 87

Figure 24. Temporal changes in MTT-assessed viable cell number (A) and insulin secretion rates (B) for buffered agarose disk constructs with initial cell loadings of $7x10^{6}$ cells (diamonds), and $3x10^{6}$ cells (squares). 89

Figure 25. Typical H/E stained histological cross-sections of agarose constructs cultured *in vitro*: (A) single agarose disk on Day 0 containing $10x10^6$ cells; (B) single agarose disk on Day 5 containing $10x10^6$ cells; and (C) buffered agarose disk on Day 5 containing $7x10^6$ cells. 90

Figure 26. Diagram of experimental setup used for diffusivity experiments for single agarose (A) and buffered agarose (B) disk constructs. 94

Figure 27. Schematic representation and dimensions of the single agarose disk construct (A), 16 mm buffered agarose disk construct (B), 13 mm buffered agarose disk construct (C), and agarose beads (D). The shaded regions represent βTC3 cells entrapped in 2% agarose, while the white regions indicates pure 2% agarose..... 103

Figure 28. H/E stained histological cross-sections of explanted constructs after 5 days *in vivo* showing cellular remodeling for a single agarose disk construct (A), a 16 mm buffered agarose disk construct (B), a 13 mm buffered agarose disk construct (C), and agarose beads (D). 107

Figure 29. H/E stained histological cross-sections of a 13 mm buffered agarose disk construct explanted after 5 days *in vivo*. Panels (A-C) represent different regions of the same construct. 109

Figure 30. H/E stained histological cross-sections of explanted constructs after 5 days *in vivo* showing interface between host and implant for (A) cell-free agarose constructs, (B) cell-containing single agarose disk constructs, and (C) cell-containing buffered agarose disk construct..... 109

Figure 31. Percent decrease in blood glucose levels of the diabetic mice following implantation of either a single agarose disk (solid triangles), 16 mm buffered agarose disk (solid diamonds), 13 mm buffered agarose disk (solid squares), or 0.9 mm agarose beads (open diamonds), all with an initial cell loading of $7x10^6$ cells. Implants were compared to controls of cell-free buffered agarose disks (open squares). 111

Figure 32. Percent decrease in blood glucose levels of the diabetic mice following implantation of either a 16 mm buffered agarose disk with an initial cell loading of $7x10^6$ (solid diamonds) or $3x10^6$ (open diamonds) cells.. 112

Figure 33. Percent decrease in blood glucose levels of diabetic mice following implantation of 0.2mL of either agarose or alginate/poly-L-lysine/alginate (APA) beads at a cell density of $3.5x10^7$ cells/mL. 112

Figure 34. Schematic representation of single agarose disk construct (A) and buffered agarose disk construct (B), with overall dimensions shown. Shaded region

represents the entrapped βTC3 cells within 2% agarose, while white region indicates pure 2% agarose. 121

Figure 35. Sagittal (A) and coronal (B) spin-echo ^{1}H NMR images of a buffered agarose disk construct. The white square shown in the coronal image is the VOI used to collect the localized ^{1}H NMR spectrum from the inner cell-containing disk. 126

Figure 36. Water-suppressed, localized ^{1}H NMR spectrum of $14x10^{6}$ βTC3 cells in a buffered agarose disk construct equilibrated in glucose and sera-free DMEM (A), 150mg/dL glucose and sera-free DMEM (B), and 250mg/dL glucose and sera-free DMEM (C). 128

Figure 37. Correlation between viable cell numbers and TCho peak areas for βTC3 cells in agarose constructs. NMR measurements were collected using either the surface coil (filled diamonds) or birdcage coil (open diamonds). 129

Figure 38. Temporal changes in the TCho-assessed viable cell number for single agarose disk constructs with initial cell loadings of $14x10^{6}$ cells (diamonds), $10x10^{6}$ cells (squares), and $7x10^{6}$ cells (triangles). 130

Figure 39. Temporal changes in the TCho-assessed viable cell number for buffered agarose disk constructs with initial cell loadings of $7x10^{6}$ cells (diamonds) and $3x10^{6}$ cells (squares). 131

Figure 40. Temporal profile of TCho, measured from the VOI centered in the cell-containing region of the construct, following hyperthermia-induced cell death for single agarose (filled diamonds) and buffered agarose (filled squares) constructs initially containing $14x10^{6}$ cells. Control is shown by the open diamonds. 132

Figure 41. Correlation between MTT assay absorbance values and TCho peak areas for βTC3 cells in agarose constructs for all time points, construct types, and cell densities tested. 133

Figure 42. Correlation between Insulin Secretion Rates (ISR) and TCho peak areas for βTC3 cells in agarose constructs for the two construct types and three cell loadings tested in the long-term culture experiments. 134

Figure 43. Correlation between choline concentration (mM) and peak area at 3.2 ppm for cell-free agarose constructs equilibrated in varying concentrations of choline buffered in saline 135

Figure 44. TCho measurement of buffered agarose constructs containing either $14x10^{6}$ or $7x10^{6}$ cells, collected in three different glucose concentrations: 450 mg/dL, 250 mg/dL, or 50 mg/dL. Black bars represent the raw TCho peak area under the specified glucose concentration. Striped bars represent the TCho peak area after the glucose contribution is subtracted using the technique presented in the text. White

bars represent the control, i.e. the TCho peak area of the same construct in glucose- and sera-free DMEM. 138

Figure 45. Schematic representation and dimensions of buffered agarose construct used for implantations. The shaded region represents the inner disk containing βTC3 cells entrapped in 2% agarose, while the white region indicates pure 2% agarose. 147

Figure 46. Water-suppressed, localized ^{1}H NMR spectra of implanted 3 mm thick cell-free buffered agarose constructs with radial buffer layers of 0 mm (A), 1 mm (B), and 2.5 mm (C) thickness. 154

Figure 47. Sagittal (A) and coronal (B) spin-echo ^{1}H NMR images of a buffered agarose disk construct. The white square shown in the coronal image is the VOI used to collect the localized ^{1}H NMR spectrum from the inner cell-containing disk. 155

Figure 48. Localized, water-suppressed ^{1}H NMR spectra of an implanted buffered agarose construct containing either no (A, B) or $14x10^{6}$ (C, D) cells. For both constructs, spectra are shown for Day 0 (A, C) and Day 3 (B, D).. 156

Figure 49. Correlation between raw (A) or glucose-corrected (B) *in vivo* TCho peak areas (y-axis) and respective *in vitro* post-explantation (x-axis) TCho peak areas for the same cell-containing construct. 158

Figure 50. Correlation between *in vivo* glucose-corrected TCho peak area and respective *in vitro* MTT assay absorbance for βTC3 cells in agarose constructs.. 159

Figure 51. Time profile of *in vivo* TCho-assessed viable cell numbers for buffered agarose disk constructs with initial loadings of $14x10^{6}$ (solid bars), $8x10^{6}$ (striped bars), and $4x10^{6}$ (white bars) cells, over a period of 14 days. 160

Figure A1. Correlation between TCho and cell density for Alginate/Poly-L-lysine/Alginate beads on Day 0. 173

Figure A2. Correlation between TCho and glucose consumption rate (GCR) for Alginate/Poly-L-lysine/Alginate beads on Day 0 174

Figure A3. Temporal blood glucose levels of STZ-induced diabetic C57-BL/6J mice. A volume of 0.2 mL of APA beads, containing an initial cell density of $3.5x10^{7}$ βTC3 cells/mL alginate, were implanted on Day 0. Day 0 data point was collected prior to implantation. 176

Figure A4. T_2-weighted ^{1}H NMR image of the peritoneal cavity of a live BALB/c mouse three days after the implantation of 0.5 mL of APA beads. 177

Figure A5. Diffusion weighted ^{1}H NMR image of the region shown in Figure A4 by the dashed box. A cluster of implanted APA beads, shown by dark circles in a bright background, is identified by arrows. 177

Figure A6. Gradient-echo ^{1}H NMR image of a silicone/mesh construct containing 0.4 mL of APA beads (Panel A). The white square is the volume of interest where the water-suppressed ^{1}H NMR spectrum was acquired (Panel B). 178

Figure A7. Spin-echo ^{1}H NMR images of a C57BL/6J mouse implanted with a single agarose disk construct (Panels A and C). Respective localized ^{1}H NMR images of the selected VOI (8x8x2mm^{3}), used to isolate the inner region of the implanted construct (Panels B and D). 180

Figure A8. Schematic representation of construct prototype. Alginate beads contain entrapped βTC3 cells, while outer white region is agarose. 181

Figure A9. Sagittal (Panel A) and coronal (Panel B) spin-echo ^{1}H NMR images of an implanted agarose construct containing alginate beads loaded with 7x10^{7} βTC3 cells/mL alginate. The white box shown in Panel B is the VOI selected for the resulting localized, water-suppressed ^{1}H NMR spectra shown in Panel C. 183

Figure A10. Temporal profile of *in vivo* TCho and *in vitro* MTS measurements within agarose constructs containing alginate beads loaded with 7x10^{7} βTC3 cells/mL alginate, over a period of six days. 184

Figure A11. Sagittal spin-echo ^{1}H NMR images of a single implanted agarose construct containing alginate beads loaded with βTC3 cells on Day 1 (Panel A), Day 7 (Panel B), and Day 13 (Panel C). 185

Figure A12. Paraffin embedded histological cross-sections of explanted agarose constructs containing alginate beads loaded with βTC3 cells stained with H/E. Panel A is the histological image of the fibrotic cap surrounding the construct explanted on Day 13 from Figure A11. Panel B represents the typical fibrotic response seen for explanted constructs on Day 13. 186

Figure A13. *In vitro* correlation between glucose concentration and the intensity of the resulting ^{1}H NMR spectroscopy peak at the 3.85 ppm resonance for cell-free agarose constructs bathed in varying concentrations of glucose. 189

Figure A14. *In vitro* correlation between peak intensity at 3.85 ppm and peak area at 3.2 ppm for cell-free agarose constructs bathed in varying levels of glucose. 189

Figure A15. *In vivo* correlation between peak intensity at 3.85 ppm and peak area at 3.2 ppm for cell-free agarose constructs implanted in C57Bl/6J mice. 190

Figure A16. Temporal profile of blood glucose levels for normal C57BL/6J mice collected while either non-anesthetized (open diamonds) or anesthetized (solid diamonds)..... 192

Figure A17. Temporal profile of blood glucose levels for normal C57BL/6J mice collected while either non-anesthetized (open diamonds), anesthetized (solid diamonds), or anesthetized after fasting for 10 hrs (solid triangles)..... 195

Figure A18. Body weight measurements of normal C57BL/6J mice under either non-fasted (open diamonds) or fasted (solid diamond) conditions. 196

Figure A19. Comparison between TCho and viable cell number for βTC3 cells (solid diamonds) and βTC-tet cells (open diamonds). 198

Figure A20. Comparison of glucose consumption rates for βTC3 cells in monolayers. Cells were exposed to varying dilutions (specified by 1:5, etc) of 30mM MION solution and glucose consumption rates were calculated for 4 and 24 hr time periods. 200

Figure A21. Comparison of glucose consumption rates for βTC-tet cells in monolayers. Cells were exposed to varying dilutions (specified by 1:5, etc) of 30mM MION solution and glucose consumption rates were calculated for 4 and 24 hr time periods. 201

Figure A22. Comparison of insulin secretion rates for βTC-tet cells in monolayers. Cells were exposed to varying dilutions (specified by 1:5, etc) of 30mM MION solution and insulin secretion rates were calculated for 4 and 24 hr time periods. 202

SUMMARY

Noninvasive monitoring of tissue engineered constructs would provide insightful information concerning the cell-mediated alterations in structure and metabolism that can dramatically affect the overall efficacy of an implant. Viable cell number is a common parameter used to characterize cellularized tissue engineered constructs. Common methods employed for quantifying viable cell number are destructive, invasive, or indirect. Although these techniques provide some information regarding the overall status of the tissue engineered construct, noninvasive methods that allow for the temporal assessment of viable cell number and construct structural integrity, both *in vitro* and *in vivo*, would provide a valuable tool in the field of tissue engineering.

While recent advancements in imaging modalities and molecular probes have garnered significant attention, the focus of this research was to utilize tools that would allow for assessment without requiring the addition of extrinsic markers or probes. For this study, ^{1}H Nuclear Magnetic Resonance (NMR) imaging and spectroscopy was selected as the methodology of choice, based on its ability to extrude both structural and metabolic information using signals inherent to cells and their surrounding environment. ^{1}H NMR imaging was used to capture general structural features of the tissue engineered substitute, while ^{1}H NMR spectroscopy monitored signals arising from the cells. The ^{1}H NMR spectroscopy signal of total-choline (TCho) was measured and its ability to provide accurate quantitative assessment of viable cell number was investigated. To test the applicability of this method, the bioartificial pancreas was selected as the model tissue engineered construct and βTC3 cells were used as the tested cells.

One of the initial challenges in this study was to establish that accurate TCho signal may be collected from the βTC3 cells under both *in vitro* and *in vivo* conditions. Given the generality of the TCho signal to mammalian cells, localized ^{1}H NMR techniques were utilized to assist in focusing the NMR signal within the βTC3 cells in the construct. Although many construct designs were studied in this research, the most promising design consisted of an agarose planar disk-shaped construct, which retained the βTC3 cells within a definable volume. An outer agarose layer surrounding the disk was added for *in vivo* studies to further isolate the βTC3 cells from surrounding host tissue. Mathematical simulations were employed to characterize diffusive transport of nutrients and metabolites into and out of the construct, while *in vitro* construct studies assessed the secretory function and viable cell number of the entrapped cells over a time period of two weeks. *In vivo* tests were also conducted to examine the effectiveness of the agarose implants in diabetic C57BL/6J mice. While the implants were found to decrease blood glucose levels, their overall effectiveness in restoring normoglycemia was minimal. These results were primarily attributed to low viable cell numbers within the implants, due to either the implementation of the buffer layer or activation of the host response. Overall, however, the architectural features of the construct design were found to permit the collection of TCho signal from the implanted cells without contamination from the surrounding environment *in vitro* and *in vivo*.

While the construct design and NMR acquisition techniques allowed for the collection of a ^{1}H NMR spectrum uncontaminated by surrounding cells, solutes from the surrounding environment could diffuse into the porous agarose construct and some were detectable in the localized spectrum. The diffusion of glucose into the agarose construct,

while desirable in providing nutrients to the entrapped cells, caused errors in TCho measurements at the cell densities and glucose concentrations examined in this study. In order to account for glucose contamination effects, post-acquisition methods were developed to subtract the glucose signal. This approach provided a simple and efficient means to account for glucose contamination effects, which allowed for the precise quantification of TCho in conditions where glucose levels could not be controlled.

After designing and implementing methods to ensure the accurate measurement of TCho from the βTC3 cells, the linear relationship between TCho and viable βTC3 cell number was quantified *in vitro*. TCho measurements from agarose constructs containing βTC3 cells of varying densities were collected at initial time points and over the course of two weeks. TCho data were then compared to the independent cell viability assay MTT, as well as to insulin secretion rates, where strong linear correlations were found. The data collected in this phase of study established TCho, measured by ^{1}H NMR spectroscopy, as an accurate method to noninvasively assess viable βTC3 cell number *in vitro*.

Once the relationship between TCho and viable cell number was established *in vitro*, efforts were focused on translating this technique *in vivo*. ^{1}H NMR spectroscopy and imaging methods were tested using βTC3 cells in buffered agarose disk constructs implanted in C57BL/6J mice. ^{1}H NMR imaging provided high resolution images of the implanted construct, thereby allowing for noninvasive examination of the overall construct structure. *In vivo* measurements of TCho of implanted constructs were found to correlate strongly and linearly to respective *in vitro* TCho and MTT measurements, calculated from explanted constructs. Temporal TCho data from implanted constructs

were also collected noninvasively over two weeks, which allowed for quantitative assessment of the effects of the *in vivo* environment on viable cell number.

The research presented in this thesis demonstrates the potential of applying ^{1}H NMR spectroscopy and imaging for noninvasively ascertaining information, both concerning viable cell number and implant structure, from tissue engineered constructs under dynamic conditions *in vitro* and *in vivo*. Future work in this field could further expand the application of the methods developed here to monitor other cell lines within tissue engineered constructs of appropriate architectural designs.

CHAPTER 1

1. INTRODUCTION AND RATIONALE

1.1. INTRODUCTION

Tissue engineering holds significant promise to provide an alternative or complementary treatment for the millions of people affected annually by organ and tissue loss from accidents, birth defects, and diseases. An example of the potential impact of tissue engineering is for the treatment of insulin-dependent diabetes, of which the common therapy is the bolus subcutaneous or intramuscular injection of insulin. The inability of these injections to avoid either the acute dangers of hypoglycemia or the long-term complications of hyperglycemia, such as diabetic nephropathy, retinopathy, neuropathy, and cardiovascular disease, contributes to its substantial medical cost, which exceeds 92 billion dollars a year [1]. A tissue engineered substitute, consisting of insulin-secreting cells and biocompatible materials, holds significant promise for effectively treating and substantially reducing secondary complications for insulin-dependent diabetics, by providing a highly regulated, insulin-secretion system that responds to environmental glucose levels.

Although the field of tissue engineering is promising, the idea of implanting living cells within a human is significantly complex. While problems such as potential microbiological hazards, continual immune suppression, and cell sourcing are large obstacles that the field must overcome, the characterization and quality control of these implants once they are developed are key issues that must also be addressed. The

capacity of a tissue engineered construct to remodel can result in significant deviations over time, where the cells can alter the overall structure and function of the construct, while also exhibiting dynamic interactions with the host post-implantation. Cell-mediated remodeling can result in the development of regions with high nutrient requirements, degradation of the supporting matrix, accumulation of cell death byproducts, and alterations in cellular phenotype. Therefore, temporal monitoring of the significant structural and functional changes occurring within the construct is of critical importance.

Common methods employed for monitoring tissue engineered constructs are indirect, destructive, or invasive. Monitoring of physiologic end-points, for instance the monitoring of blood glucose levels in a diabetic animal that has received a pancreatic implant, is useful but does not provide direct information on the implant itself. Changes within the implant can also be assessed using destructive and invasive techniques, such as histological cross-sectioning; however, in order to understand dynamic changes *in vivo*, many animal experiments must be conducted in parallel, which introduces substantial variability. Therefore, there is a strong need to develop a reliable methodology that can noninvasively monitor a tissue engineered construct, both in its structural integrity and cellular metabolism.

The endeavor of this thesis was to establish a means to noninvasively monitor a tissue engineered construct *in vitro* and *in vivo*. Specifically, efforts were focused on the use of ^{1}H Nuclear Magnetic Resonance (NMR) imaging and spectroscopy to noninvasively quantify changes in overall structure and viable cell number for tissue engineered constructs. ^{1}H NMR imaging and spectroscopy has three particular advantages over

other modalities: simultaneous collection of spatial and metabolic information; elimination of the need for external molecular probes or enriched media; and the ability to monitor over an unlimited time period. Furthermore, through the application of NMR gradient techniques, it is possible to isolate a volume of interest (VOI) within the domain studied, to obtain structural and metabolic information from that volume alone [2].

The approach of this research was to utilize intrinsic ^{1}H NMR spectroscopic signals in the development of the noninvasive modality, thereby increasing its potential for wide-spread applicability. Total-choline (TCho) is a ^{1}H NMR spectroscopic signal detected in most mammalian cells and is primarily comprised of cell membrane precursors [3]. Published reports suggest this marker may provide a strong indicator of cell number [3-6]. Therefore, the TCho resonance was investigated as a general marker for assessing viable cell number within tissue engineered constructs. The model tissue engineered system employed in this study was the bioartificial pancreas. Construct prototypes were designed and thoroughly investigated *in vitro* and *in vivo*. The ability to collect accurate TCho signal from the cell-containing region of the construct prototype by localized ^{1}H NMR spectroscopy under dynamic environmental conditions was a primary concern. The effects of contaminating solutes on TCho quantification were accurately characterized and methods to account for these effects were developed. *In vivo*, specific architectural features were implemented into the construct design to allow for signal acquisition and avoidance of contamination from the surrounding host tissue. The traditional cell viability assays MTS and MTT were adapted for use as an independent measure of viable cell number within the constructs. Temporal data collected from *in vitro* and *in vivo* experiments were used to identify correlations among NMR

spectroscopic signals and images, insulin secretion rates, and viable cell numbers within the constructs, thereby validating NMR measurements as a means to noninvasively determine the status of a pancreatic substitute both *in vitro* and *in vivo*.

1.2. RATIONALE

This thesis consists of seven distinct topics presented in CHAPTERS 3-9. Most of these chapters represent a modified version of an article published or submitted for publication. The individual chapters contain detailed motivation, research methods, results, and discussion. General background information is presented in CHAPTER 2. Preliminary results, along with verification studies and data too lengthy for publication, are presented in the APPENDIX.

The use of a cell-containing bioartificial pancreas to develop a noninvasive modality required a thorough characterization of the construct. Therefore, our approach was threefold: (1) characterization of the transport of nutrients and metabolites and their respective consumption and production by the cells, based on the biomaterial selected and device shape; (2) *in vitro* characterization of the construct in terms of cell viability and overall secretion dynamics; and (3) *in vivo* evaluation of construct functionality and efficacy. While several different device designs were explored in this research, all constructs utilized the continuous cell line, βTC3, as the delivery vehicle for insulin.

Initial studies used alginate/poly-L-lysine/alginate (APA) beads, which have been studied extensively in our laboratory for earlier NMR bioreactor experiments [7-9]. Extensive mathematical modeling and diffusional studies of APA beads have been published previously [10]; however, CHAPTERS 3 & 4 discuss the *in vitro*

characterization of the long-term effects of the alginate biomaterial on the metabolic and secretory functions of the entrapped cells. These *in vitro* alginate studies provided an understanding of how the cells remodel in the APA constructs over time. Preliminary ^{1}H NMR studies of APA beads *in vitro* were promising, where TCho levels were found to correlate strongly with cell number (R^2=0.96) and their respective glucose consumption rates (R^2=0.91) on Day 0, as illustrated in APPENDIX A1.

APPENDIX A2 presents preliminary *in vivo* testing of the APA beads. While these *in vivo* studies found APA bead implants to effectively restore normoglycemia in diabetic mice (APPENDIX A2), it was identified that the beads would need to be confined within a planar construct for NMR monitoring. This modification was found necessary after significant bead dispersion *in vivo* hindered the ability to noninvasively monitor the implant using localized NMR. Since localized NMR requires the specification of a defined volume of interest, (see CHAPTER 2.6 for more details) the next phase of experiments focused on maintaining the APA beads within a single planar volume.

While the high surface to volume ratio for free-floating APA beads was lost upon confinement of the beads to a single volume, disk-shaped construct designs within a specified range of dimensions were found to result in minimal changes in the functionality of the entrapped cells. CHAPTER 5 details experiments performed using a silicone ring/polypropylene mesh design. While a construct was developed that had metabolic and secretory profiles similar to free-floating APA beads *in vitro*, difficulties arose upon implantation of the construct. The silicone/mesh design was not biocompatible and the host response to the implant was rapid and severe. During these *in vivo* experiments, two major problems in the NMR monitoring of TCho levels of the

implant were identified: (1) imperfections in the localization sequence; and (2) infiltration of significant host tissue into the inter-bead volume of the construct. Therefore, the next phase of experiments focused on characterizing the localization technique and redesigning the construct to increase biocompatibility and prevent host infiltration.

APPENDIX A3 discusses the first stage in the characterization of the localization sequence. Although localized ^{1}H NMR spectroscopy isolates the signal to within the region selected, no NMR localization sequence is perfect and some signal can be collected from outside the VOI specified (see CHAPTER 2 for more detail). Preliminary *in vitro* experiments sought to understand the effects of localization imperfections on accurately quantifying TCho. These *in vitro* experiments found minimal contamination effects when a "buffer" region between the VOI and the contaminating factor was present. These experiments illustrated the need to "buffer" the cell-containing region from the surrounding environment and provided guidelines for their dimensions. *In vivo*, however, imperfections of the localization technique can be further exacerbated due to motion artifacts caused by breathing of the animal. Therefore, more in depth *in vivo* studies were required, once the appropriate prototype construct was developed.

In order to accommodate for the requirement of buffer zones between the cell-containing region of the construct and its surroundings, and to reduce the significant fibrotic response seen in the silicone ring implants, the next construct prototype encased the alginate beads in agarose. This design permitted greater flexibility in varying the thickness of the buffer zones, while preventing the infiltration of host cells within the inter-bead region of the construct. APPENDIX A4 presents preliminary *in vivo* data

collected using this design. The agarose/alginate combination resulted in an excellent contrast between the two biomaterials for the ^{1}H NMR images, which allowed ease in identification of the cell-containing region of the construct and accurate placement of the localized VOI. *In vivo* tests of the implant found the construct to be highly biocompatible in most cases, where a minimal fibrotic response was seen on the outer areas of the construct. Periodic *in vivo* images were found to provide some temporal information regarding the host-cell response in the single case where a significant fibrotic cap developed around the implant. Preliminary *in vivo* results also found TCho measurements from implanted constructs to compare favorably to the *in vitro* cell viability assay MTS, although the significant variability for both measurements were calculated.

After promising results were shown for the alginate/agarose construct design, the cell-containing region was modified from alginate beads to a planar agarose disk, to ease manufacturing and ensure accuracy in cell loading. CHAPTERS 6 and 7 present the results for *in vitro* and *in vivo* characterization of this construct prototype. As discussed previously, the three-fold approach to fully understand the temporal remodeling of this construct was implemented, where diffusional characterization of the biomaterial, mathematical modeling, *in vitro* metabolic and secretory tests, and *in vivo* evaluation of the construct were performed. While it was determined that the addition of the outer agarose buffer layer imparted mass transfer limitations and reduced the overall viable cell number within the construct, it was found that the addition of the outer buffer layer improved the *in vivo* biocompatibility of the construct. Although the effectiveness of the agarose implants in restoring normoglycemia for diabetic mice was minimal, these

studies established that planar agarose disk constructs could be used to stably maintain the cells, both *in vitro* and *in vivo*, over the time frame necessary for our purposes.

Once the specific NMR design requirements were met, the next focus was to extensively characterize the correlation between TCho and viable cell number for the agarose constructs. Although earlier preliminary experiments found a strong correlation between TCho and viable cell number, this study further investigated this relationship under dynamic conditions of cell death and growth over a two week time period. CHAPTER 8 presents the *in vitro* data, where strong linear relationships were found between TCho, the independent cell viability assay MTT, and the secretory activity of the entrapped cells. The RF coil design was also improved from a birdcage coil, the standard coil used for all experiments up to this point, to a more sensitive surface coil, which resulted in an increase in the sensitivity of the TCho measurement of approximately three-fold. Furthermore, the contamination of glucose on the accurate quantification of TCho was identified and methods were developed to subtract for these effects (for more detail see APPENDIX A5). Minimum detection limits of the assay, based on the NMR parameters used, were also quantified. This work laid the foundation for applying these techniques *in vivo*.

When research progressed to the *in vivo* stage, one of the major problems encountered was the significant increase in blood glucose levels when the mouse was placed under anesthesia. APPENDIX A6 illustrates the blood glucose data of these mice in varying experimental conditions. The significant rise in glucose levels while the mice were anesthetized caused detrimental effects on accurately quantifying TCho *in vivo*, given the glucose contamination effects calculated in CHAPTER 8. While it was concluded that

this significant rise in blood glucose levels was due to the use of xylazine, the ketamine/xylazine combination anesthetic was the best choice, given the requirements of the NMR experiments. Therefore, experimental procedures were implemented to combat blood glucose effects, as discussed in APPENDIX A6.

CHAPTER 9 presents the *in vivo* data collected using buffered agarose constructs implanted within C57BL/6J mice. This chapter discusses the preliminary *in vivo* tests used to identify the thickness of the buffer regions required to ensure the accurate collection of ^{1}H NMR spectra from the cell-containing region of the constructs *in vivo*. The accuracy of temporal TCho data collected *in vivo* was verified by comparisons to respective *in vitro* measurements of TCho and MTT from explanted constructs. The results from these experiments illustrated the ability of NMR spectroscopy to accurately and noninvasively measure viable cell number *in vivo*, through the quantification of TCho. These studies also established the range of parameters where the NMR-based methodology is useful, including a sensitivity threshold of 10^6 cells, and provide insight as to how these parameters can be expanded to include other construct designs, cell types, and/or animal models.

The implications of our findings on the use of ^{1}H NMR spectroscopy and imaging for monitoring tissue engineered constructs, specifically the bioartificial pancreas, and the progression of these methods in future research are further discussed in CHAPTER 10.

CHAPTER 2

2. BACKGROUND

2.1. CURRENT TREATMENTS FOR INSULIN-DEPENDENT DIABETES

Diabetes mellitus is a serious pathological condition characterized by hyperglycemia resulting from defects in insulin secretion, insulin action, or both [11]. Diabetes mellitus currently affects an estimated 18 million people in the United States alone, where 5.8 million of them require insulin therapy [1]. While current treatment options for insulin-dependent diabetics, which include periodic blood glucose measurements followed by daily bolus insulin injections or continuous subcutaneous delivery via an insulin pump, are effective, the toll of the disease on its victims is tremendous. The 1993 Diabetes Control and Complications Trial, which found that tight control of glucose levels delays the onset and reduces the intensity of diabetes-related complications, outlined the need for a more physiological control of blood glucose levels beyond what is achieved with bolus insulin injections [12].

The need to dampen the dangerous oscillating pattern of blood glucose levels inherent in bolus injections has motivated research investigating cell-based therapy. By utilizing cells that have the inherent capacity of continually regulated insulin-secretion in response to variable blood glucose levels, tighter regulation and elimination of patient-based delivery is possible. Exciting results have recently been achieved in the area of human islet transplantation [13, 14]. While test subjects are limited to extreme diabetic cases, such as decreased hypoglycemia awareness, labile diabetes, and progressive

complications, the Edmonton group has demonstrated that human clinical islet transplantation with steroid-free immunosuppression can result in long-term insulin independence [13]. With this procedure, patients are injected with human cadaveric islets, isolated from approximately two human pancreata per transplantation, via portal vein injection. Thus far, all patients have required a minimum of two independent transplantation procedures. While these recent clinical trials have been successful, the supply of this cell source, of which significant propagation is unavailable, is insufficient to provide islets for any substantial number of insulin-dependent diabetics. Additionally, the life-long immunosuppression required to sustain treatment is problematic, especially for type 1 diabetics.

Another possible treatment option for insulin-dependent diabetics is the bioartificial pancreas, which utilizes insulin-secreting cells and biocompatible matrices [15-19]. Encapsulation of the implanted cells can partially alleviate the need for immunosuppression, while the flexibility of cell source relaxes the cell availability problem posed by pancreatic islets. For our applications, the resulting bioartificial pancreas must meet four main requirements: (1) retain the viability and functionality of the entrapped cells; (2) be relatively biocompatible; (3) be contained within a single, definable volume so that it may be monitored via NMR; and (4) permit the complete retrieval of the implanted cells, so that the NMR results may be compared with independent assays. In order to fulfill these requirements, great care must be taken in the design. Cell type and loading, polymer selection, and device shape are just a few of the factors that must be considered.

2.2. INSULIN-SECRETING CELL TYPE

In the development of a bioartificial pancreas, cell sourcing is a significant problem. Use of human or porcine primary cells of the pancreas is limited, not only by their low propensity to proliferate *in vitro*, but also their significant loss of desired secretory functions over time in culture [20]. Therefore, many investigators are focused on the development of highly functional and phenotypically stable cell lines that can easily be amplified *in vitro*, particularly to serve as test beds for characterizing cellular phenotype within three-dimensional matrices. Examples of such cell lines include transformed β-cells, engineered somatic cells, and stem cells [21].

The laboratory of Efrat et al has developed a family of continuous β cell lines, the βTC, derived from transgenic animals expressing the SV-40-T-antigen [20, 22-24]. Specifically, the βTC3 cell line has a strong capacity for stable growth in culture, with retention of insulin secretion phenotype for approximately 50 passages [23]. Alleviating the cell availability problem is not the only advantage of utilizing continuous cell lines. Investigators have also found some of these cell lines to possess lower nutrient requirements to maintain normal secretory function, which may be advantageous when entrapped within extravascular constructs. For example, Papas *et al* found βTC3 cells to possess unaltered insulin secretion when maintained at oxygen tensions above 7 mmHg [25], unlike rat islets whose insulin secretion have been found to decrease as much as 50% at oxygen tensions below 30 mmHg [26]. *In vivo*, βTC3 cells within APA beads have been shown to restore normoglycemia in rodents for several weeks (see APPENDIX A2). The major caveats of the βTC3 cell line is their hypersensitivity to glucose and strong propensity for growth. Through further genetic engineering techniques, βTC cell

lines, such as βTC6, βTC7 and βTC-tet, have been developed that exhibit insulin secretion patterns within the physiological range [20]. Furthermore, a greater control over the growth of these cells can be accomplished with the use of the βTC-tet cell line, which utilizes the tetacycline-conditioned gene expression system to control proliferation. βTC-tet cells have demonstrated excellent results in streptozotocin-induced rodents, where studies determined that a graft volume of βTC-tet cells ranging from ~$4x10^6$ to $1x10^7$ cells was able to restore normoglycemia in NOD and NODSCID mice for up to a year (Weber et al, data not published).

2.3. BIOMATERIALS

Although porcine islets and genetically engineered cells lines alleviate the cell sourcing problem, the direct implantation of xenogeneic and/or transformed cells poses significant health hazards and would still force the need for immunosuppression. Therefore, entrapment of cells within permselective biomaterials would provide a barrier between the cells and the host, thereby preventing direct cell-host contact and partially alleviating the need for immunosuppression, while also allowing for ease in locating the implanted cells.

Biomaterials selected for the development of a functional bioartificial pancreas must possess high mass transfer characteristics and mechanical integrity, while maintaining a cell loading adequate to treat the pathological condition. Beta cells typically possess high metabolic needs, which require a steady oxygen and nutrient supply to maintain not only their viability, but their normal secretory capacities [27]. The entrapped cells must also be able to sense changes in their surrounding environment quickly to eradicate

detrimental time lags in glucose stimulated insulin secretion (GSIS). Researchers typically use highly porous but inert biomaterials in the development of the bioartificial pancreas. Natural hydrogels, such as alginate, agarose, and collagen, are the most common choices [17, 28]. These biomaterials are chosen for their high mass transfer characteristics, structural integrity, ease in manufacturing, mild encapsulation conditions, and capacity for modification.

Alginate is a common term for the family of unbranched polymers composed of 1,4-linked β-D-mannuronic and α-L-guluronic acid residues in varying proportions, sequence, and molecular weight (Figure 1). They are abundant in nature and can be found in marine brown algae and capsular polysaccharides in soil bacteria. The gelation of alginate takes place when multivalent cations (usually Ca^{2+}) interact ionically with blocks of guluronic residues between two different chains resulting in a three-dimensional network [29]. The strength of the network depends on the overall fraction of guluronic acid residues and, in particular, the frequency and length of contiguous guluronic acid blocks, the molecular weight of the polymer, and the Ca^{2+} ion concentration at the time of gelation [30]. The physical properties of alginate gels vary widely depending on their chemical composition, i.e., the proportion of guluronic to mannuronic acid residues, the sequential order of these residues, and the overall molecular weight of the polymer. Numerous publications have investigated the effects of chemical composition on the gelation, porosity, biocompatibility, and overall mechanical strength of alginate hydrogels. In summary, alginates possessing a high guluronic acid content develop stiffer, more porous gels, which maintain their integrity for longer periods of time. Therefore, high guluronic alginates have long been advocated for use in

encapsulated cell systems based on their superior mechanical stability, along with their suspected increased biocompatibility [31].

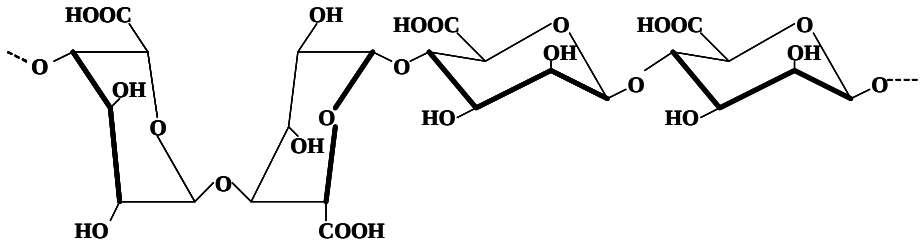

Alginate Fragment:

(--L-GulA-α-1,4-L-GulA-α-1,4-D-ManA-β-1,4-D-ManA-β-1,4- -)

Figure 1 . Molecular structure of alginate.

Agarose is a purified linear galactan hydrocolloid isolated from agar or agar-bearing marine algae. Structurally, it is a linear polymer predominantly composed of repeating units of alternating D-galactopyranosyl and 3,6-anhydro-L-galacto-pyranosyl (Figure 2, I), which are typically considered to be more stable than other naturally occurring polysaccharides [32]. A low level of sulfate is desirable since sulfate can interfere with the homogeneous formation of secondary and tertiary structures during gelation (Figure 2, II) [33]. Agarose exhibits hysteresis in the liquid-to-gel transition, i.e. their gel point is not the same as their melting temperature [34]. Agarose is categorized into several grades on the basis of purity, electroendosmosis, gel strength, gelling temperature, and melting point properties. Low-temperature gelling agarose gels are ideal for entrapping cells, for they remain in solution at 37ºC. High-quality agarose is also commercially available and commonly used for biomedical and pharmaceutical applications [35]. Researchers have found agarose gels to be highly compatible for the entrapment of many

cell lines, including islets, β cell lines, and chondrocytes [36-38], with high biocompatibility and stability *in vivo*.

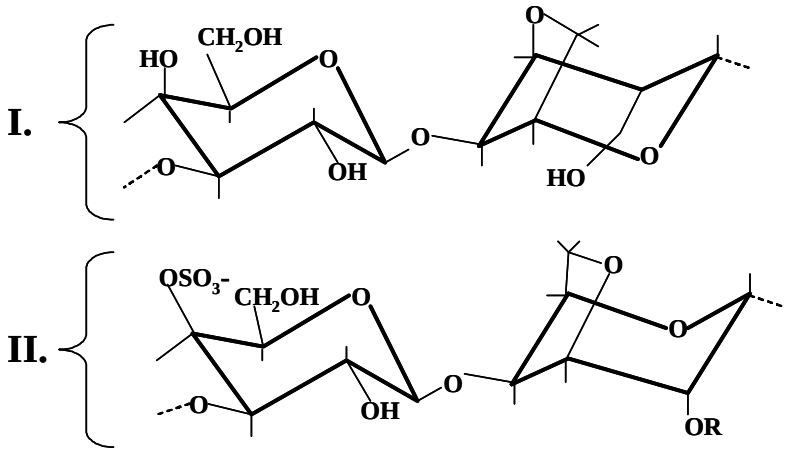

Figure 2. Molecular structure of agarose.

2.4. CONSTRUCT DESIGNS

The development of an appropriate device for the bioartificial pancreas has been a subject of research for over 25 years. Three main designs have been investigated to date: vascular devices [19, 39]; microencapsulation [15, 40]; and macroencapsulation [16, 41-47].

Vascular devices were one of the first prototypes explored for the development of the bioartificial pancreas. Maki *et al* utilized a form of this device using a single-coiled acrylic copolymer tubular membrane contained in a disk-shaped acrylic housing with grafting ends composed of polytetrafluoroethylene (PTFE) was studied [39, 48]. Testing in pancreatectomized dogs found long-term patency of greater than 500 days, with a degree of islet function retained for a period ranging from 1-9 months for allogenic islet

implantations. Blood clotting in response to the vascularized device, however, was a significant problem.

Microencapsulation, used to generate beads in the diameter range from a fraction of a millimeter to millimeter range, has been a promising construct design due to its high surface to volume ratio. Although several different biomaterials have been utilized in microbeads, the most common are alginate and agarose. Lim and Sun developed a method to entrap cells within alginate microbeads by dropping the cell/alginate solution into a bath of calcium chloride using a needle [15]. The size of the cell-filled bead may be controlled through regulated airflow around the tip of the needle [49] or through the newer method using an electrostatic generator [50]. The alginate beads can then coated with a 0.1% poly-L-lysine layer creating a molecular weight cutoff of ~70,000Da, which provides partial immune protection of the entrapped cells. An additional outer coating of alginate is then applied to increase biocompatibility. The alginate/poly-L-lysine/alginate (APA) encapsulated cell system provides both a three-dimensional structure and partial immunoprotection to the entrapped cells, while allowing for the adequate exchange of nutrients. Implantation of islet-containing microcapsules into streptozotocin-induced diabetic and spontaneously diabetic rodent models, along with a few isolated cases of larger animals, have provided long-term correction of hyperglycemia [51-56]. Agarose microbeads have also been utilized for the development of a functional bioartificial pancreas. Agarose beads are typically manufactured through paraffin oil immersion. Kobayashi *et al* found agarose beads containing allogenic islets to be highly effective in restoring normoglycemia in rodent models for periods exceeding 500 days [57]. Allogenic implantation of agarose microbeads containing islets into pancreatectomized

dogs were also moderately successful, where 3 test subjects retained euglycemia for over 30 days [58]. For xenogenic transplantations, the mixing of agarose and polystyrene sulfonic acid (PSS), with coatings of polybrene and carboxy methyl cellulose (CMC), was found necessary to prevent rejection of the implant [59]. Implantations of hamster islets in rodent models using the three-layered agarose constructs have found to increase the efficacy of the implantation from 1 to over 150 days [60].

A major caveat of the *in vivo* applicability of microcapsules is the absence of a reliable mechanism to completely retrieve the implanted microbeads. In order to allow for the retrievability of the implant, researchers have examined the use of macroconstructs such as hollow fibers, rods, and disks. For the purposes of our studies, we limited our macroconstruct design to only planar geometries, for ease in defining the volume of interest (VOI) in localized NMR experiments. Ohgawara and co-workers have developed a planar silicone disk sealed with two semipermeable membranes [61, 62]. Results have found that this planar macroconstruct, loaded with genetically engineered MIN6 cells, can restore normoglycemia in rodents for up to 30 weeks, with a limited fibrotic response [43, 62, 63]. Kuo *et al* used pure alginate to design disk-shaped constructs that were gelled by $CaCO_3$-GDL (D-glucono-δ-lactone), which creates an internal, rather than the typical external, gelation [64]. This technique allows for the design of macroconstructs with a controlled structure, gelation rate, and mechanical properties. Lahooti et al found the use of agarose gel to contain cell-filled APA beads within a disk-shaped macroconstruct design to reduce the significant bead clumping and fibrotic response seen in previous *in vivo* studies of implanted microcapsules [65]. They

have found the implant to improve the ease of retrievability and reduce the fibrotic response, without significantly altering cell viability.

2.5. NONINVASIVE MONITORING *IN VIVO*

Noninvasive modalities applicable to living systems can provide detailed temporal information of *in vivo* experimental treatments, such as genetic engineering, acellular scaffold implants, or tissue engineered substitutes. Currently, the progression of the field of *in vivo* noninvasive monitoring is driven by significant advancements in the areas of molecular and cell biology, electronics and instrumentation. Typically, small-animals models are the first step in characterizing the efficacy of a new treatment. Therefore, monitoring modalities are focused on the development of small-animal instrumentation for relaying both spatial and temporal information for these studies. Approaches to the development of noninvasive techniques for monitoring systems *in vivo* are highly variable. Therefore, a brief overview of some of the emerging technologies is presented.

Imaging of living systems using molecular probes is the most common technique employed. The selection of a particular molecular probe is restricted by the modality chosen to monitor the system and the cell type or function studied. Experimental techniques can choose to monitor cell viability in general, or specific cellular or molecular processes, such as gene expression or protein-protein interactions. Each imaging modality differs in its spatial and temporal resolution, depth penetration, energy expended for image generation, availability of the molecular probe, and the respective sensitivity threshold, specificity, and longevity of the probe [66].

Imaging of radionuclide probes is a common technique, where the image may be collected by either positron emission tomography (PET) or single photon emission computed tomography (SPECT). PET and SPECT provide detailed spatial and temporal images by tracking the emissions from injected radionuclide probes. PET is the most common radionuclide modality chosen for monitoring cells, because of its high sensitivity, which allows a lower dosage of isotopes, and robustness, which permits a greater range of molecular probes. The image resolution of clinical PET scanners is ~6-8 mm^3; however, small animal micro-PET scanners have achieved resolutions on the order of 2 mm^3, with some room for improvement [67]. One of the more recent uses for PET imaging of implanted cells has been the tracking of gene expression by injecting a radiolabeled probe targeted for a specific reporter gene. An example of this was published by Tjuvajer et al, where the growth of transduced herpes simplex virus-1 thymidine kinase (HSK-TK) tumor cells was imaged by PET in rodents after the injection of [^{124}I]FIAU ([^{124}I]2′-fluoro-2′-deoxy-1-β-D-arabinofuransyl-5-iodouracil) [68]. This study has been further expanded to monitor the migration of lymphocytes in SCID mice [69]. PET imaging has also been applied to the study of beta-cells, specifically alterations in beta-cell mass, through the development of beta-cell radioactive labels, such as glibenclamide, tolbutamide, and serotonin, although the imaging resolution for the small percentage of beta cells within the pancreas is a significant limiting factor [70-72]. While nucleotide imaging is promising for tracking cellular function or viability, the research is limited by imaging resolution, probe specificity, transient expression and the need to continually inject radioactive probes. Furthermore, PET is unable to detect

different molecular probes simultaneously, although there is potential for SPECT to develop this capacity by utilizing isotopes of varying energy.

Optical imaging is another modality that has recently garnered attention within the field of *in vivo* noninvasive monitoring. Advancement of charged coupled device (CCD) detectors, which sense the emission of light, have increased the applicability of this modality to living systems, by the reduction of thermal noise and increased sensitivity. Imaging of bioluminescence and fluorescence are the two most common approaches used. Bioluminescence imaging has been used to track the viability of implanted cardiac cells expressing firefly luciferase reporter gene over the course of two weeks [73]. Furthermore, Smith *et al* employed bioluminescent imaging to assess insulin secretion from pancreatic cells in transgenic rodents expressing the firefly luciferase gene, regulated by the rat insulin promoter (RIP), within pancreatic islet cells [74]. The collection of images from cells tagged with fluorescently labeled antibodies or cells expressing the green fluorescent protein (GFP) gene have also been obtained, such as the work by Kaneko et al, which tracked viable cells within the peritoneal cavity of a mouse using variant GFP labeled cells [75]. Another exciting prospect in CCD imaging is the development of nanometer-scale semiconductor crystallites, or Quantum dots, which have the ability to emit monochromatic light of a specific wavelength and color [76, 77]. *In vivo* integration of these stable, water-soluble fluorophores can be monitored, without photobleaching, over time periods extending to four months. While CCD results for monitoring cells *in vivo* are promising, the resulting images are two-dimensional and lack depth information [78-80]. Furthermore, in order to obtain the exact location of the 2-D image in relation to the animal, other imaging techniques, such as photography, PET or

MRI, are typically employed. Finally, surgical techniques may be required to expose internal organs prior to imaging, due to the significant lack of depth penetration for this system (on the order of 1-2 cm) [66].

2.6. NUCLEAR MAGNETIC RESONANCE SPECTROSCOPY AND IMAGING

Nuclear magnetic resonance imaging and spectroscopy is an established noninvasive modality for monitoring living systems. By manipulating magnetic spins, both spatial and metabolic information may be collected from the system studied. Advancements in the field of RF coils and gradients have provided a strong framework for intricate studies using living systems. NMR information from cells may be acquired by cellular tagging using superparamagnetic particles, detected by NMR imaging, or through the monitoring of natural or supplemented nuclei within the cells, such as ^{1}H, ^{19}F, ^{13}C and ^{31}P, which can be detected by NMR imaging and spectroscopy.

The recent development of superparamagnetic particles that have the ability to label specific cells, through phagocytosis or the conjugation of antigen-specific monoclonal antibodies, has advanced the use of NMR imaging for tracking specific cells *in vivo*. The two most common superparamagnetic particles are superparamagnetic iron oxide (SPIRO) and monocrystalline iron oxide nanoparticles (MION). SPIRO integration into cells has been demonstrated for a wide variety of cells types, including the intracytoplasmic tagging of human mesenchymal, rhesus embryonic, and human hematopoietic stem cells, lymphocytes, and HeLa cells [81]. MION, which has a smaller mean core size compared to SPIRO, labeling has also be achieved for several cell types

including T cells, macrophages, HUVEC, and beta cells [82-84] (and see APPENDIX A.8). Published reports on *in vivo* imaging of these contrast agents or visualization of transgene expression are promising [85-87]. Furthermore, studies are expanding the use of SPIRO labeling to assessment of autoimmune diabetes by using CLIO-tat coated SPIRO particles to specifically target lymphocytes and monitor their migration into pancreatic tissue for diabetic rodent models [88]. While this methodology is promising, current problems facing contrast imaging using paramagnetic agents include: low sensitivity, high biolabel load, poor signal-to-noise resolution, long-term stability, toxicity, and specificity.

Monitoring of natural or supplemented nuclei within living systems is possible through NMR imaging and spectroscopy. Images of nuclei may be collected through the use of gradients placed within the bore of the magnet. NMR spectroscopy can be used to noninvasively determine the presence and concentration of compounds, containing the studied nuclei, through the detection and quantification of chemical shifts associated with the specific compounds. A large portion of NMR spectroscopy research on living cells has used perfusion systems, and ^{31}P or ^{13}C enrichment, to study the metabolism of cells. Early studies focused on the development of perfusion systems to maintain cells over extended periods of time, while examining the levels of high and low-energy phosphorous containing compounds of mammalian cells [89-91]. Research within our laboratory has explored the use of NMR spectroscopy to understand genetically engineered insulin-secreting cells entrapped within in APA beads that were perfused in an NMR-compatible bioreactor. The effects of nutrient parameters, such as oxygen and glucose levels, on the ^{31}P NMR spectroscopic signal *in vitro* were examined [8, 9, 92,

93], as well as the relationship between cellular function and energetics [94]. Monitoring systems enriched with NMR sensitive nuclei is another facet of NMR research that can provide detailed information regarding cell fate *in vivo*. Innovative *in vivo* research using ^{19}F has also been conducted by Stegman et al [95]. *In vivo* imaging of cytosine deaminase (CD) transgene expression was possible by tracking the CD-catalyzed conversion of injected 5-fluorcytosine (5-FC) using ^{19}F spectroscopy. Although significant research has been conducted in the characterization of cellular metabolism using ^{31}P, ^{13}C, and ^{19}F, research is typically limited by sensitivity, thereby forcing the enrichment of the system with the NMR sensitive nuclei.

Due to the strong sensitivity and natural abundance of the ^{1}H nuclei, ^{1}H NMR spectroscopy is superior in its capacity to monitor subtle changes in concentrations of studied compounds without the need for additional markers or lengthy techniques. Through the implementation of specifically designed solvent-suppressed adiabatic pulses, the long-term monitoring of detectable metabolites from cells using ^{1}H NMR spectroscopy is feasible. Therefore, by utilizing a similar bioreactor system generated previously in our laboratory for the ^{31}P perfusion studies [8], our group was able to study βTC3 cells within APA beads using ^{1}H NMR spectroscopy [7]. A standard water-suppressed, localized ^{1}H NMR spectrum of βTC3 cells in agarose bathed in glucose- and serum-free DMEM is shown in Figure 3. The two signals of total-choline (TCho), at 3.2 ppm, and extracellular lactate, at 1.3 ppm, are derived from the entrapped cells. For βTC3 cells, the TCho resonance is typically comprised of multiple resonances attributed predominantly to choline-related metabolites, such as phosphocholine (PCho) at ~64%, glycerol-3-phosphocholine (GPC) at ~33%, and choline itself (Cho) at ~3% [7]. These

percentages may vary with culture conditions and other cell types may also contain phosphoethanolamine, inositol and taurine [3]. Previous studies have found strong correlations between TCho and cell number for a variety of cell types *in vitro* and *in vivo* [3-6]. More specifically, ^{1}H NMR spectroscopy studies monitoring TCho of βTC3 cells encapsulated within APA beads found strong correlations between the relative changes in the TCho peak area and the overall metabolic activity of the culture, as measured by glucose and oxygen consumption rates [7]. These findings substantiate the use of ^{1}H NMR spectroscopy to noninvasively monitor implanted βTC3 cells.

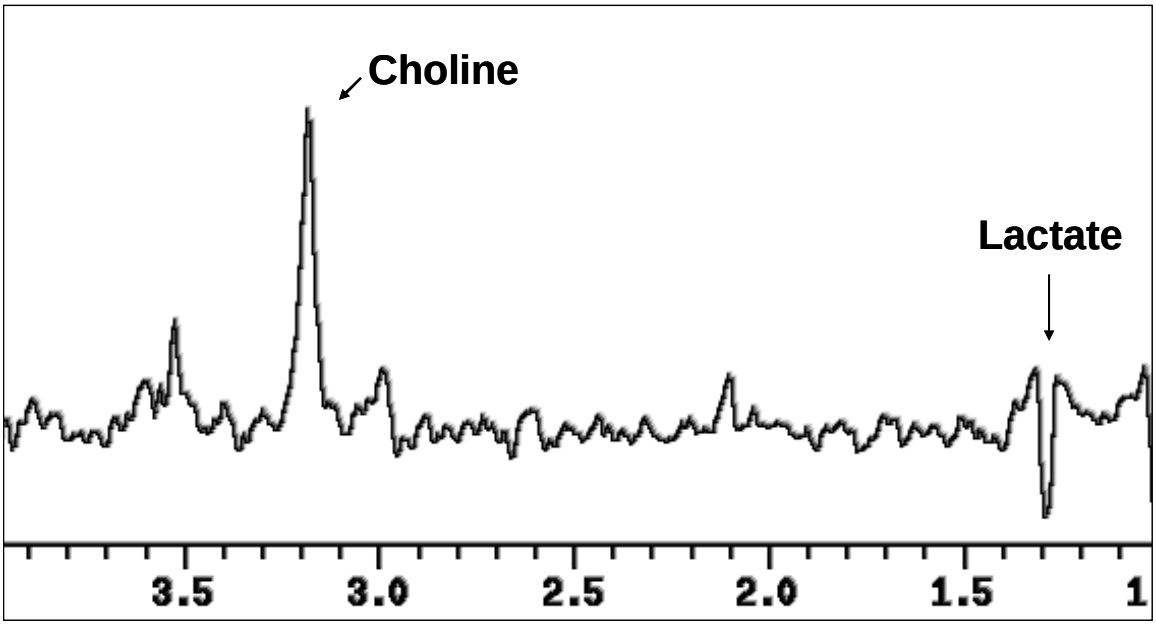

Figure 3. *In vitro* water-suppressed ^{1}H NMR spectrum of $8x10^{6}$ βTC3 cells

In order to accurately assess the functionality of the construct and eliminate the problem of resonances originating from the construct overlapping with signals from the surrounding environment, localized NMR is utilized [96-98]. Through NMR gradient techniques, it is possible to isolate localized regions within the field studied, to extrude structural and metabolic information from that area alone [2]. This is illustrated by the schematic shown in Figure 4, where it shows the localization of the NMR signal to a specific volume of interest (VOI) specified in the acquisition parameters. In Figure 4, the field of view of the RF coil is represented by the outer black square, while the grey region is the collected signal region. A representation of the resulting free induction decay (FID), or measured signal, is illustrated to the right of each figure. Without localization (A), signal is collected from the entire field of view; however, with localization (B), the FID is localized to within the volume of interest (VOI) specified by the acquisition parameters. Note the decrease in signal intensity of the FID upon localization. Therefore, the signal now may be localized to a specific region of interest within the field of view of the RF coil. Localization techniques have been used for the detection of cancerous cells in humans *in vivo,* thereby allowing ^{31}P and ^{1}H NMR spectroscopy to become a feasible technique for use in the clinical setting [99-101]. Furthermore, other groups have used localized NMR to monitor the progression of disease states such as epilepsy, Alzheimer disease, and multiple sclerosis [102-105]. Since no localization sequence is perfect, it is critical to characterize the technique for each specific application.

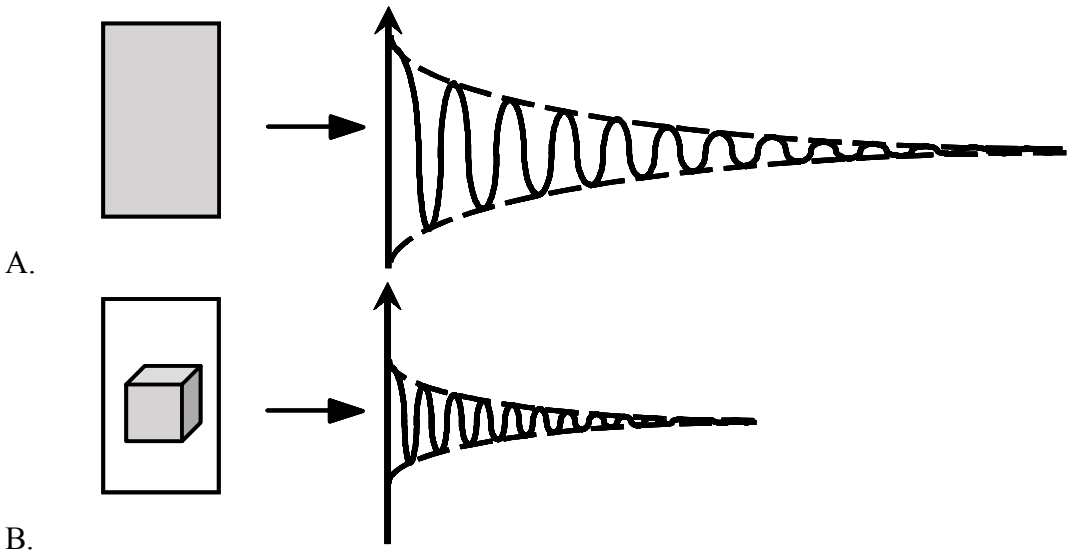

Figure 4. Schematic representation of localized NMR spectroscopy.

NMR imaging is a common technique used in basic studies to noninvasively characterize the structure of human organs, bones, and tissue [106-109]. ^{1}H NMR imaging has also been used to assess disease progression and/or structural damage of cartilage, brain tissue, tumors and atherosclerosis within patients [110-113]. It has even been used to monitor the structural rejection of organ transplants [114]. Due to the dynamic environment of a tissue engineered construct, ^{1}H NMR imaging is a promising tool for monitoring overall structural changes and cellular remodeling of the construct noninvasively over time both *in vivo* and *in vitro*, as well as characterizing the host-implant interface. Our laboratory has investigated using ^{1}H NMR imaging for noninvasively examining structural changes within a tissue engineered construct over time *in vitro*. Through the development of a microcoil with a 40 by 40 μm pixel resolution, cellular remodeling was visualized within an alginate bead over time *in vitro* [115]. Due to the generality of this technique, current studies are examining the use of

this imaging system for other tissue engineered constructs *in vitro*. The use of this specific microcoil system *in vivo*, however, is complicated by the implantation of the coil along with the construct, although published reports have illustrated the effectiveness of implanted surface coils for monitoring structural features, such as spinal cord injury, *in vivo* [116, 117]. Therefore, other systems, such as surface coils and specialized pulse sequences, were substituted to obtain *in vivo* images for our application.

CHAPTER 3

3. THE EFFECTS OF ALGINATE COMPOSITION ON ENCAPSULATED βTC3 CELLS[1]

3.1. ABSTRACT

The effects of alginate composition on the growth of murine insulinoma βTC3 cells encapsulated in alginate/poly-l-lysine/alginate (APA) beads, and on the overall metabolic and secretory characteristics of the encapsulated cell system, were investigated for four different types of alginate. Two of the alginates used had a high guluronic acid content (73% in guluronic acid residues) with varying molecular weight, while the other two had a high mannuronic acid content (68% in mannuronic acid residues) with varying molecular weight. Each composition was tested using two different polymer concentrations. Our data show that βTC3 cells encapsulated in alginates with a high guluronic acid content experienced a transient hindrance in their metabolic and secretory activity because of growth inhibition. Conversely, βTC3 cells encapsulated in alginates with a high mannuronic acid content experienced a rapid increase in metabolic and secretory activity as a result of rapid cell growth. Our data also demonstrated that an increase in either molecular weight or concentration of high mannuronic acid alginates did not alter the behavior of encapsulated βTC3. Conversely, an increase in molecular weight and concentration of high guluronic acid alginates prolonged the hindrance of

[1] Modification of paper published in **Biomaterials**, 22: 1301-1310 (2001).

glucose metabolism, insulin secretion and cell growth. These observations can be best interpreted by changes in the microstructure of the alginate matrix i.e. interaction between the contiguous guluronic acid residues and the Ca^{+2} ions, as a result of the different compositions.

3.2. INTRODUCTION

The encapsulation of cells within semipermeable membranes for the purpose of immunoisolation from the host has many potential applications in tissue engineering, ranging from the treatment of Parkinson's disease to chronic pain. A major field of study within encapsulated cell systems has been the encapsulation of insulin-secreting cells for the long-term treatment of diabetes. Studies on the encapsulation of islets, as well as transformed β-cells, have yielded promising results [19, 118].

Alginate is the biomaterial commonly used in the entrapment of cells. Additional layers of poly-L-lysine and alginate are typically added to coat the central alginate matrix to improve the stability of the gel [119] as well as to create an immunoisolation barrier [120]. This method of encapsulation has many advantages. Alginate/poly-L-lysine/alginate (APA) beads provide structural integrity and immunoprotection to the entrapped cells, they are easy to manufacture, the molecular weight cutoff of the membranes can be manipulated, encapsulation takes place under mild conditions, and all solutions used are aqueous.

Alginate is a common term for a family of unbranched polymers composed of 1,4-linked β-D-mannuronic and α-L-guluronic acid residues in varying proportions, sequence, and molecular weight. They are abundant in nature and they can be found as

structural components of marine brown algae and as capsular polysaccharides in soil bacteria. Alginate gelation takes place when divalent or multivalent cations (usually Ca^{+2}) interact ionically with blocks of guluronic residues between two different chains resulting in a three-dimensional network. The model that best describes this interaction is the "egg-box model" [29]. The strength of this network depends on the overall fraction of guluronic acid residues and in particular the frequency and length of contiguous guluronic acid blocks, the molecular weight of the polymer, and the Ca^{+2} ion concentration at the time of gellation [30].

The physical properties of alginate gels vary widely depending on their chemical composition, i.e., the proportion of guluronic to mannuronic acid residues, the sequential order of these residues, and the overall molecular weight of the polymer. Numerous publications have investigated the effects of chemical composition on the gellation, porosity, biocompatibility, and overall mechanical strength of alginate hydrogels [121-126]. In summary, alginates possessing a high guluronic acid content develop stiffer, more porous gels, which maintain their integrity for longer periods of time. Furthermore, during Ca^{+2} crosslinking, they do not undergo excessive swelling and subsequent shrinking, thus, they can better maintain their form [127]. Conversely, alginates rich in mannuronic acid residues develop softer, less porous beads, which tend to disintegrate easier with the passage of time. Alginates with a high mannuronic acid content are also plagued by a high degree of swelling and shrinking during Ca^{+2} cross-linking [127].

The effect of guluronic acid content on alginate biocompatibility is a subject of debate. Some investigators have advocated the use of a highly purified alginate rich in guluronic acid residues [56, 128], while others have disregarded the effects of chemical

composition and stress the importance of high purity [129]. Although these studies have increased awareness concerning the importance of using a highly purified and well-characterized alginate, the effects of alginate properties on the growth and metabolic activity of the entrapped cells have yet to be fully quantified. An initial investigation of these effects was recently published by our laboratory [130]. This study concluded that alginates with a high guluronic acid content inhibited cellular growth, and thus the overall metabolic activity of the culture was diminished, for a period of 20 days before allowing the cells to proliferate and recover. Conversely, alginates with a high mannuronic acid content provided an environment supportive of cell growth although their strength and stability characteristics were not desirable. In that initial report, two different alginates were employed, one with a high guluronic acid content and another with a high mannuronic acid content. These alginates were characterized only in terms of their guluronic acid content. Their molecular weights were not known and the alginate concentration used to generate the two types of beads was not the same (1.5% for the high guluronic acid alginate and 2% for the high mannuronic acid alginate). The information provided by that study highlighted the effects of alginate composition to encapsulating cells and the stressed need for a thorough evaluation of these effects. The current study investigates these effects in a thorough manner by delineating the effects of guluronic/mannuronic ratio, molecular weight and density of the polymer. In addition, the property of alginate gel responsible for the behavior of encapsulated cells is postulated, while the significance of our results on tissue engineering and particularly on the development of a bioartificial pancreas is discussed.

3.3. MATERIALS & METHODS

3.3.1. Cell culture

βTC3 cells were obtained from the laboratory of Shimon Efrat, Albert Einstein College of Medicine, Bronx, NY. Cells were cultured as monolayers in T-flasks and fed fresh medium consisting of Dulbecco's Modified Eagle's Medium (DMEM) with 25mM glucose and supplemented with 15% horse serum, 2.5% bovine serum, 1% penicillin-streptomycin, and L-glutamine to a final concentration of 6 mM (SIGMA, St. Louis, MO) every 2-3 days.

3.3.2. Alginate

Four types of alginate were used in this study: a high molecular weight, high guluronic acid content alginate (MVG); a low molecular weight, high guluronic acid content alginate (LVG); a high molecular weight, high mannuronic acid content alginate (MVM); and a low molecular weight, high mannuronic acid content alginate (LVM) (all four types of alginate were provided by Pronova Biomedical, Norway). Some key properties of these alginates are listed in Table 1, including guluronic acid and guluronic acid block (GG) content, shown as a percentage of total alginate, average molecular weight, and viscosity, for a 1% w/v solution. Each type of alginate was tested at two concentrations. MVG and LVG alginates were examined at 2% and 1% w/v, while MVM and LVM alginates were examined at 2% and 3% w/v. All alginate solutions were prepared by dissolving alginate in physiological saline (0.95% NaCl). The presence of non-crosslinking Na^+ ions is desired to generate a more homogeneous gel bead [122].

Table 1. Table of alginate properties used in this study.

	MVG	LVG	MVM	LVM
Guluronic acid (%)	73	73	38	38
GG content (%)	60	56	20	18
Molecular Weight	231,000	189,000	226,000	209,000
Viscosity (mPas)	322	156	234	193

3.3.3. Entrapment and culture propagation

βTC3 cells were entrapped in alginate gel beads based on the protocol developed by Sun [15, 131]. Cells were harvested from monolayer cultures using trypsin-EDTA (Sigma, St. Louis, MO) and suspended in sodium alginate at a density of 3.5 x 10^7cells/mL alginate. Viable cell counts were performed using the trypan blue (Sigma, St. Louis, MO) exclusion method. Droplets of the alginate/cell suspension were added in a 1.1% $CaCl_2$ solution for gellation. Two methods were used to generate the droplets. In the first, the suspension was extruded via a 20-gauge needle into a 1.1% $CaCl_2$ solution; the droplet size was controlled by parallel airflow. In the second, suspension droplets were created with an electrostatic bead generator (Pronova Biomedical, Norway). The droplet size was regulated by one or more of the following parameters: the electrostatic potential, the distance between the needle and the $CaCl_2$ solution, and the diameter of the needle. Both methods yielded bead sizes of 0.9-1 mm.

Alginate beads containing cells were placed in a spinner flask, fed with 50 mL of fully supplemented DMEM, positioned within a 37 °C humidified incubator, and allowed

to recover for a period of 24 hours. Following this recovery period the beads were treated with $CaCl_2$, CHES, PLL (Sigma, MW:19,200), and 0.2% alginate (of the same type as that used for the core material) to create the final APA beads as previously described [8, 94]. Three encapsulations were performed for each combination of alginate composition and concentration examined. Aliquots of the beads (ranging from 1.5-2mL) from each entrapment were transferred into separate T-75 flasks with 50 mL of culture medium and placed on an orbital shaker within a humidified 37˚C, 5% CO_2/95% air incubator. For all entrapments, one of the T75 flasks was used to withdraw samples of beads for histology examination while the others were used to quantify the rates of glucose consumption, lactate production and insulin secretion. This practice minimized errors in the quantification of these rates. Both sets of flasks were compared by histology when the experiment was terminated in order to verify that they resulted in identical cultures. All flasks (n=7 per alginate type/concentration) were fed every 2-3 days by complete replacement of the culture medium.

3.3.4. Analytical techniques

Glucose and lactate concentrations in medium samples were determined using an EKTACHEM DT60 bioanalyzer (Eastman Kodak, Rochester, NY). Insulin was assayed by liquid-phase radioimmunoassay (Linco Research, St. Charles, MO). The kit utilized an antibody made specifically against rat insulin, and had an 100% reactivity against both human and rat insulin and a sensitivity of 0.1 ng/ml. Calculation of the rates of consumption or production were based on the change in the amount of glucose, lactate, or insulin (amount = volume x concentration) between feedings, divided by the

corresponding time period. These rates were normalized to a unit of 10^5 cells added initially to the culture.

3.3.5. Histology

Histology samples for each alginate type were taken approximately every seven days. A sample of beads was removed from the histology designated flask, washed with 1.1% $CaCl_2$, and fixed in 3% glutaraldehyde. After sectioning, the slides were stained with hematoxylin/eosin (H/E).

3.4. RESULTS

3.4.1. Effects of Guluronic Acid Content

Figure 5 illustrates the temporal changes in the rates of glucose consumption (GCR), lactate production (LPR), and insulin secretion (ISR) by βTC3 cells encapsulated in 2% w/v MVG (solid diamonds), 2% w/v LVG alginates (open diamonds), 2% w/v MVM (solid squares) and 2% w/v LVM alginates (open squares). Each point on the graphs represents the average metabolic and secretory rate from the three independent encapsulations, while the values determined for each encapsulation represent the average rate exhibited by the culture over a period of two to three days depending on the feeding cycle. The error bars represent the standard deviation from the mean. The graphs indicate that βTC3 cells encapsulated in either of the two high guluronic acid content alginates (MVG or LVG) displayed an initial decrease in the metabolic and secretory activity of the culture. The metabolic rates, GCR and LPR, recovered sooner and at a faster rate with the lower molecular weight polymer (LVG) than with the higher

molecular weight polymer (MVG). Both alginate cultures eventually surpassed their initial GCR and LPR values, however, ISR did not recover beyond its initial value for either alginate. Conversely, βTC3 cells encapsulated in either of the two high mannuronic acid content alginates (MVM or LVM) displayed a continuous increase in both metabolic and secretory rates. Since beads made from alginates that are rich in mannuronic acid residues are softer and tend to deteriorate faster [132], MVM and LVM beads began to break within 2-3 weeks from encapsulation. As a result the measurement of the metabolic and secretory rates became erratic and the cultures were terminated. Our data show no significant differences between MVM and LVM cultures.

At regular time intervals, samples of beads from these cultures were fixed, cross-sectioned and stained with H/E to examine the growth pattern of encapsulated βTC3. Figure 6 shows representative histology cross-sections of MVG (Days 1, 14, 35, and 50) and LVG beads (Days 1, 14, and 35) stained with H/E. For the first few days after entrapment, βTC3 cells were >90% viable and uniformly distributed throughout the beads as previously reported [130]. Subsequently, the cell viability decreased and overall growth was hindered, leaving only a few randomly dispersed pockets of viable cells remaining within the beads. This decline in viability persisted for 2-5 weeks depending on the molecular weight of the alginate. Viable βTC3 cells encapsulated in LVG alginate beads that persisted during the initial period of hindered growth began to proliferate approximately 20 days after entrapment by growing into ever increasing clusters. These clusters were randomly dispersed throughout the APA beads. A similar pattern of growth was also observed for MVG encapsulated cells. However, the development of the

clusters was delayed until approximately 30 days after encapsulation, and the average number of clusters observed per bead was smaller. These data support the metabolic and secretory changes displayed in Figure 5 for the two high guluronic acid content alginates.

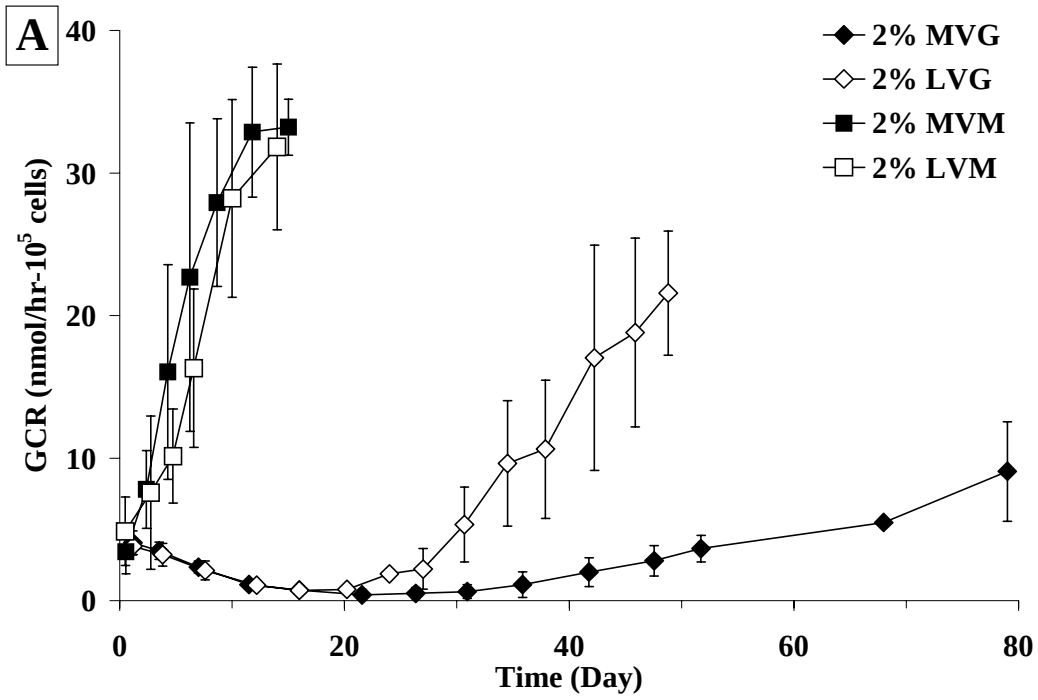

Figure 5. Temporal changes in the rates of (A) glucose consumption (GCR), (B) lactate production (LPR), and (C) insulin secretion (ISR) by βTC3 cells encapsulated in 2% w/v MVG (solid diamonds), LVG (open diamonds), MVM (solid squares), and LVM (open squares) alginates.

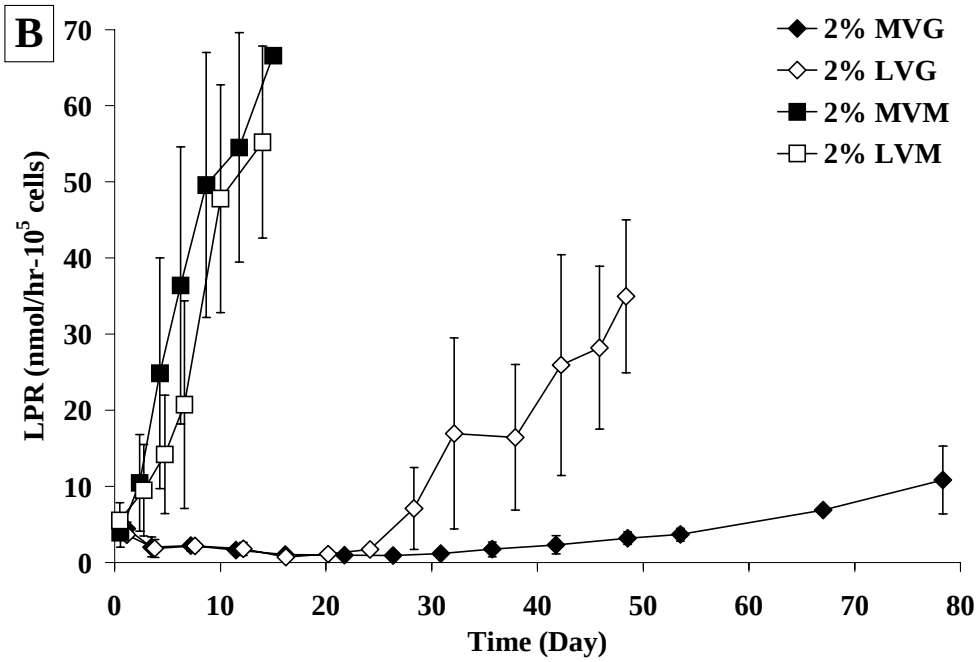

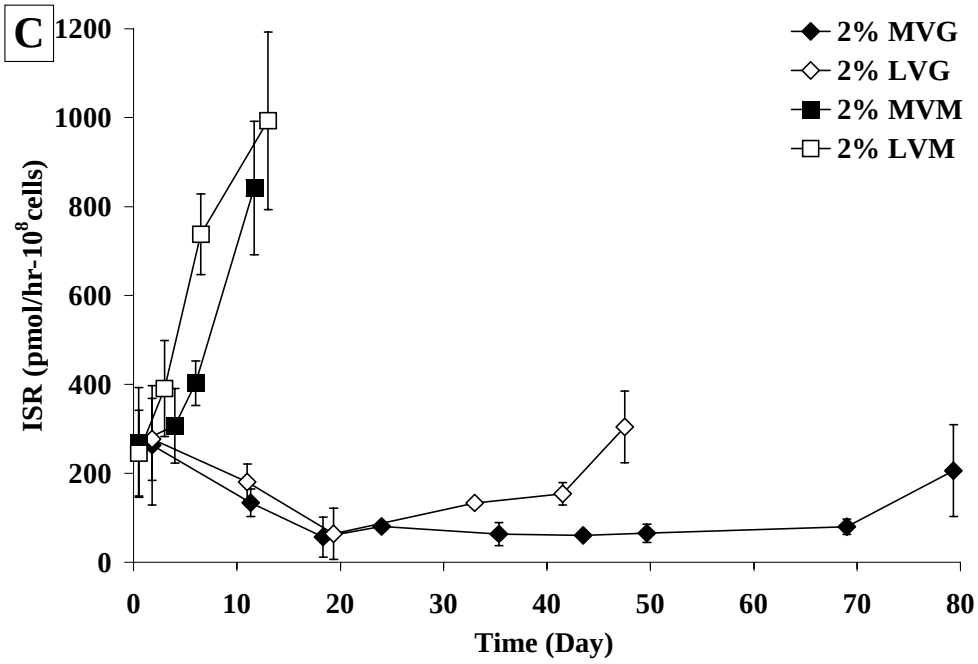

Figure 5. (continued) Temporal changes in the rates of (A) glucose consumption (GCR), (B) lactate production (LPR), and (C) insulin secretion (ISR) by βTC3 cells encapsulated in 2% w/v MVG (solid diamonds), LVG (open diamonds), MVM (solid squares), and LVM (open squares) alginates.

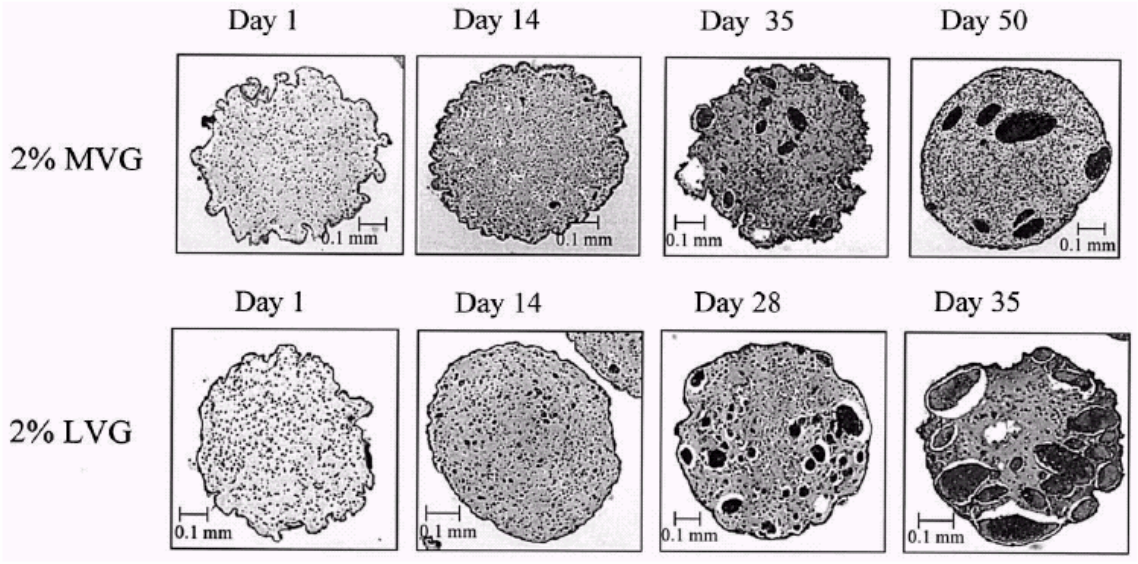

Figure 6. Cross-sections of 2% w/v MVG and LVG APA beads containing βTC3 cells and stained with H/E at the times designated.

Figure 7 shows representative cross-sections of 2% w/v MVM and 2% w/v LVM beads (Day 1, 7, 16 and 29) stained with H/E. Encapsulated βTC3 cells began to proliferate immediately after encapsulation and by day 16 had increased substantially with preferential growth at the periphery of the bead. At this point bead breakage was observed. However, a few beads were maintained for an additional 10-14 days. The beads that maintained their integrity during this extended culture period displayed a cell layer ~0.2 mm thick at the periphery, whereas cells in the center of the bead were dead. This "o-ring" like growth pattern has been reported in the literature for encapsulations of βTC3 cells in alginates that did not have a precisely defined composition [9, 119, 130].

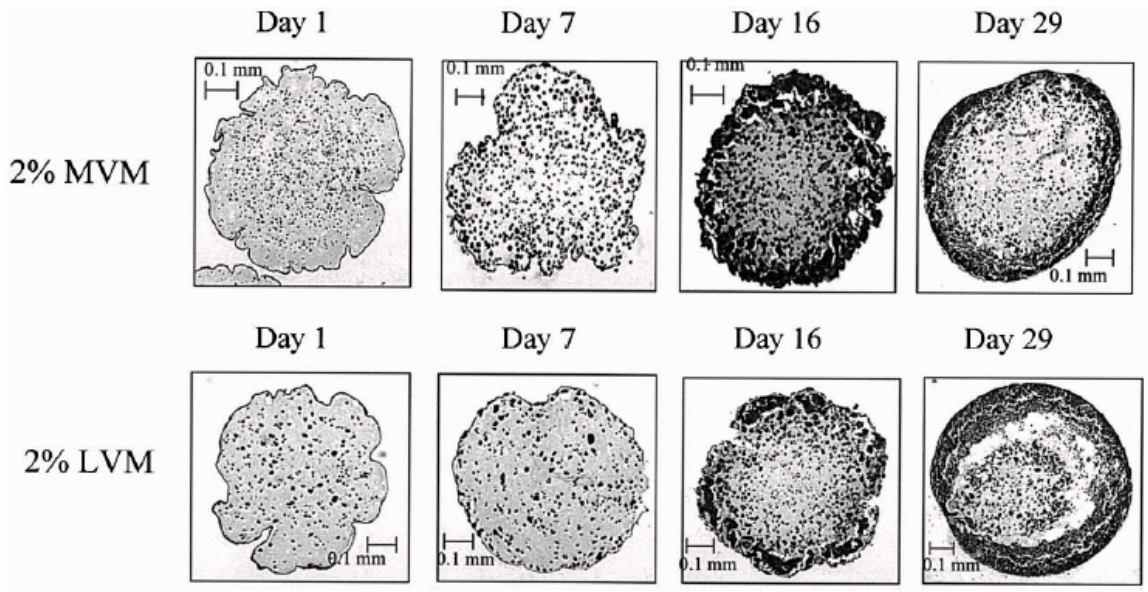

Figure 7. Cross-sections of 2% MVM and LVM APA beads containing βTC3 cells and stained with H/E at the times designated.

3.4.2. Effects of Alginate Concentration

3.4.2.a. MVG and LVG

The effects of alginate concentration on the metabolic and secretory profiles as well as the growth characteristics of βTC3 cells encapsulated in high guluronic acid content alginates were examined by decreasing the concentration of MVG and LVG alginates to 1% w/v before cross-linking with 0.1 M $CaCl_2$. Figure 8 shows the temporal changes in GCR, LPR and ISR for βTC3 cells encapsulated in 1% w/v MVG (solid diamonds) and 1% w/v LVG breads (open diamonds). Comparing these metabolic and secretory profiles with those shown in Figure 5 (2% w/v MVG and LVG) and traced in this figure for easy visual comparisons, a couple of differences become apparent. First, cells encapsulated in both MVG and LVG at 1% w/v do not display a decline in either metabolic or secretory rates, but rather a lag period of approximately 10 days followed by an increase in

metabolic and secretory rates. Second, the significant differences displayed in GCR, and LPR profiles at 2% w/v alginate (Figure 5) are diminished at 1% w/v alginates, although a pattern of higher values for the 1% w/v LVG encapsulation is seen. For ISR, however, a difference between the profiles of 1% w/v MVG and 1% w/v LVG is detected as the values of ISR begin to increase following the lag period. LVG encapsulated cultures displayed a faster recovery than the corresponding MVG cultures.

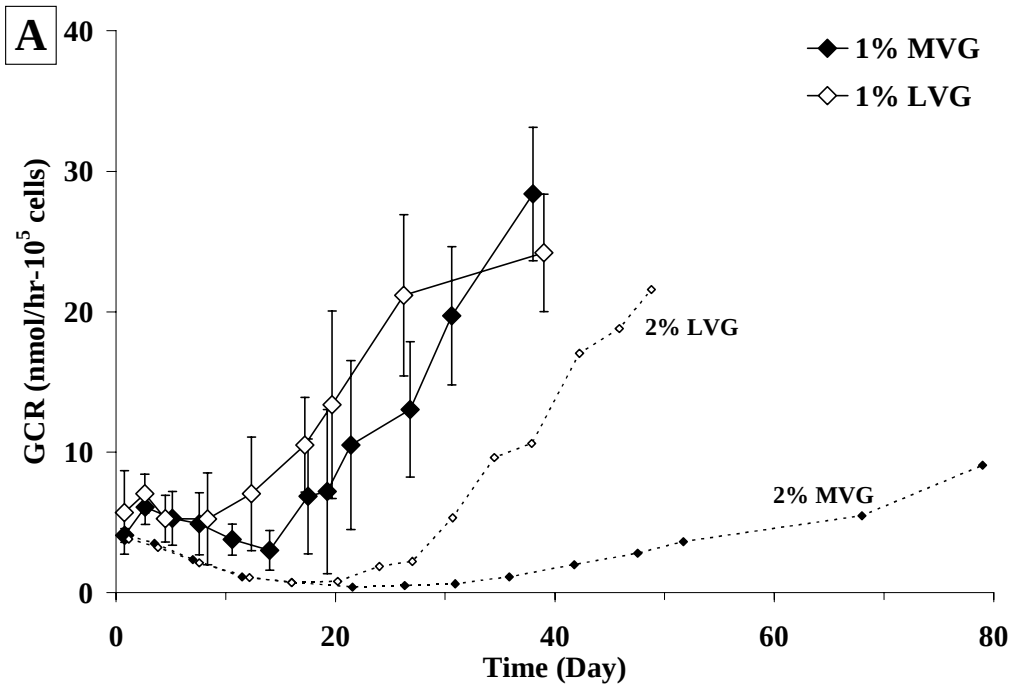

Figure 8. Temporal changes in the rates of (A) glucose consumption (GCR), (B) lactate production (LPR), and (C) insulin secretion (ISR) by βTC3 cells encapsulated in 1% w/v MVG (solid diamonds) and LVG (open diamonds) alginates.

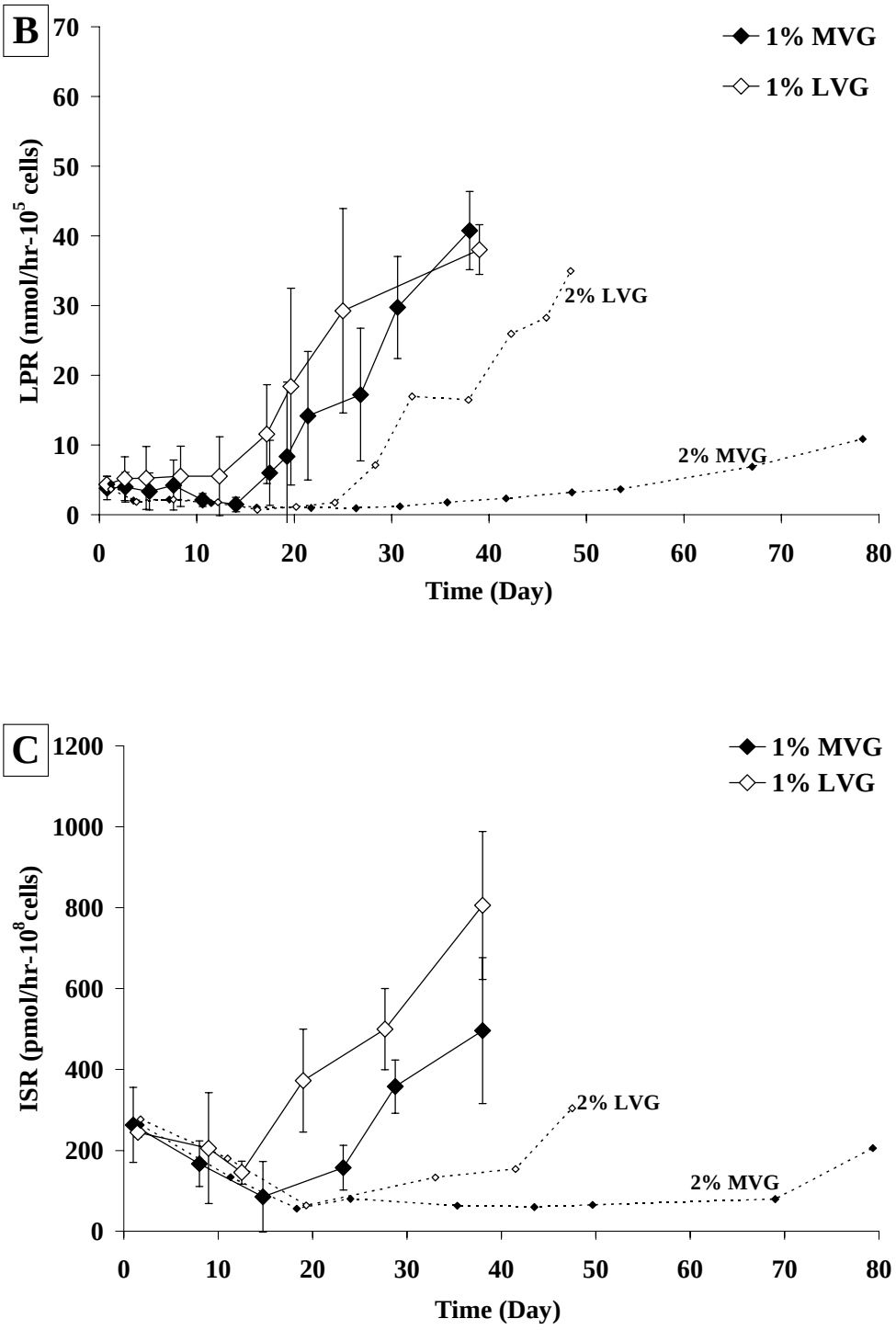

Figure 8. (continued) Temporal changes in the rates of (A) glucose consumption (GCR), (B) lactate production (LPR), and (C) insulin secretion (ISR) by βTC3 cells encapsulated in 1% w/v MVG (solid diamonds) and LVG (open diamonds) alginates.

Figure 9 shows representative cross-sections of 1% w/v MVG and LVG beads at Days 1, 6, and 23 stained with H/E. Unlike the 2% w/v alginates, βTC3 cells encapsulated in 1% w/v MVG or LVG display a steady increase in viable cells. Furthermore, the growth pattern found within the 1% w/v alginates, appears to be less random than that observed in 2% w/v encapsulations. A great portion of cell clusters were gathered on the periphery of the bead. By Day 25, cell clusters dominated the periphery of the beads, and consequently the beads began to rupture.

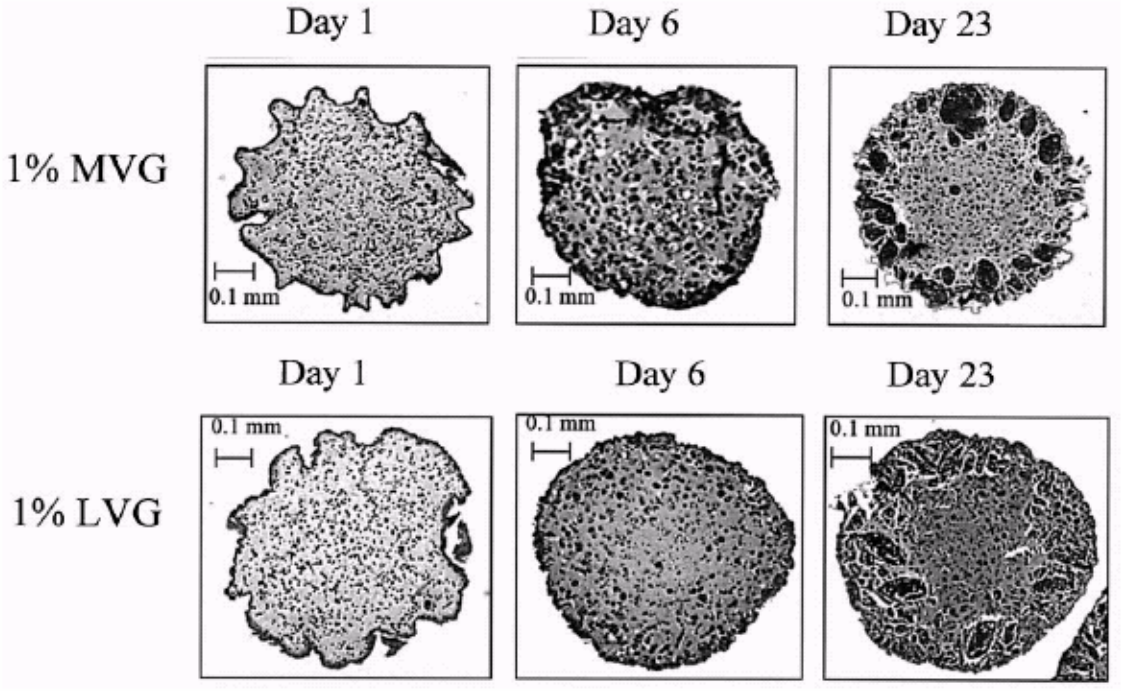

Figure 9. Cross-sections of 1% MVG and LVG APA beads containing βTC3 cells and stained with H/E at the times designated.

3.4.2.b. MVM and LVM

Figure 10 illustrates the temporal changes in GCR, LPR, and ISR by βTC3 cells encapsulated in 3% w/v MVM (solid diamonds) and in 3% w/v LVM (open diamonds) alginates. Cell encapsulated in either 3% w/v MVM or 3 w/v LVM demonstrated a steep increase in both metabolic and secretory rates post-entrapment that continues until bead breakage. There are no significant differences between these profiles. Comparing these profiles to those shown in Figure 5 for 2% w/v MVM and 2% w/v LVM cultures (these profiles are also traced in this figure for easy visual comparison) lead us to conclude that an increase in the concentration of high mannuronic acid content alginates does not affect the overall metabolic and secretory rates of the encapsulated cells.

Figure 11 shows representative cross-sections at Days 1, 14, and 26 from βTC3 cells encapsulated in 3% w/v MVM and 3% w/v LVM alginates. Similar to what is shown in Figure 7, encapsulated βTC3 cells began to proliferate immediately after encapsulation with preferential growth at the periphery of the bead. This histology examination did not display observable differences between the two high mannuronic alginates at 3% w/v alginate concentration or between the 2% w/v and 3% w/v encapsulations.

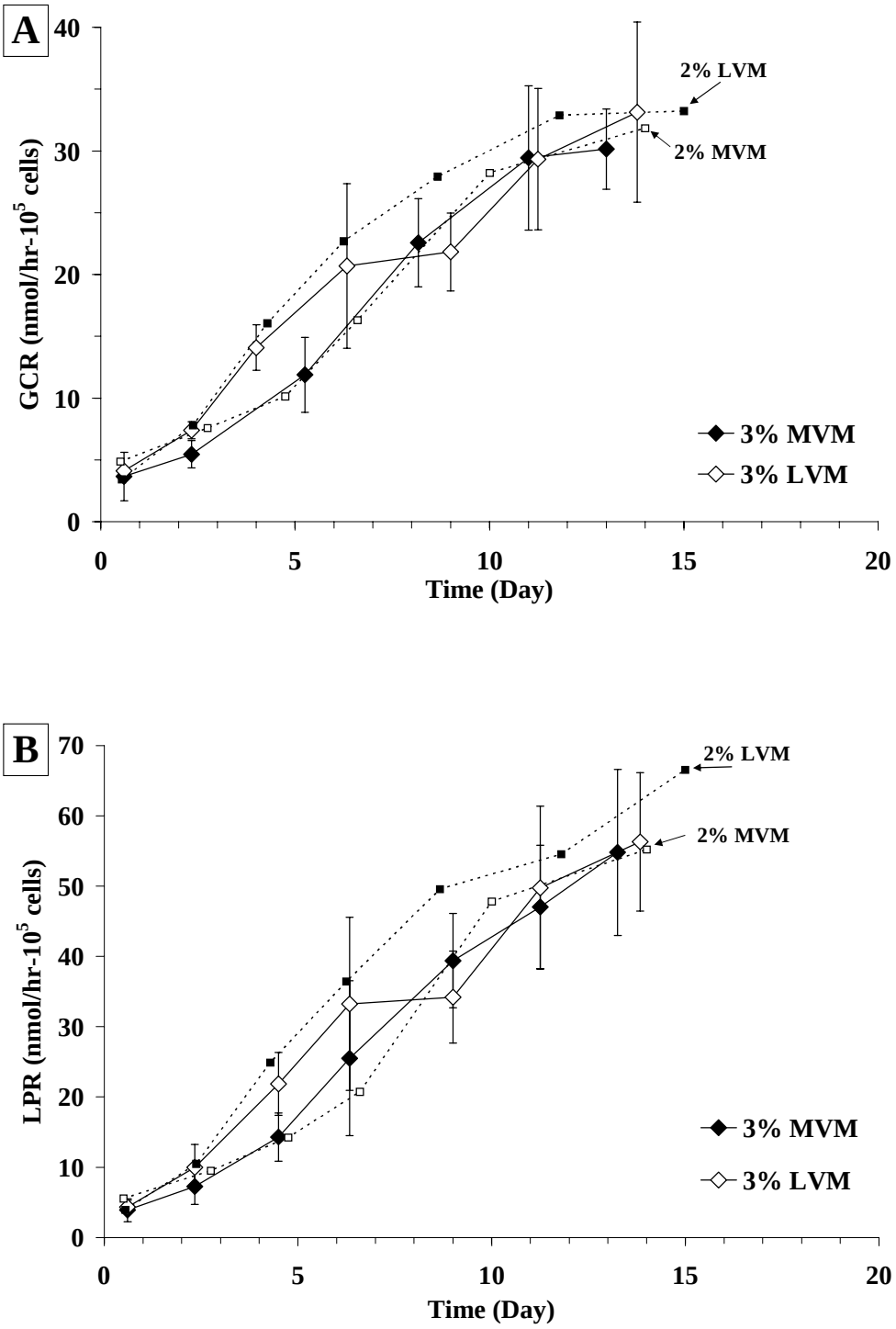

Figure 10. Temporal changes in the rates of (A) glucose consumption (GCR) (B) lactate production (LPR) and (C) insulin secretion (ISR) by βTC3 cells encapsulated in 3% w/v MVM (solid diamonds) and LVM (open diamonds) alginates.

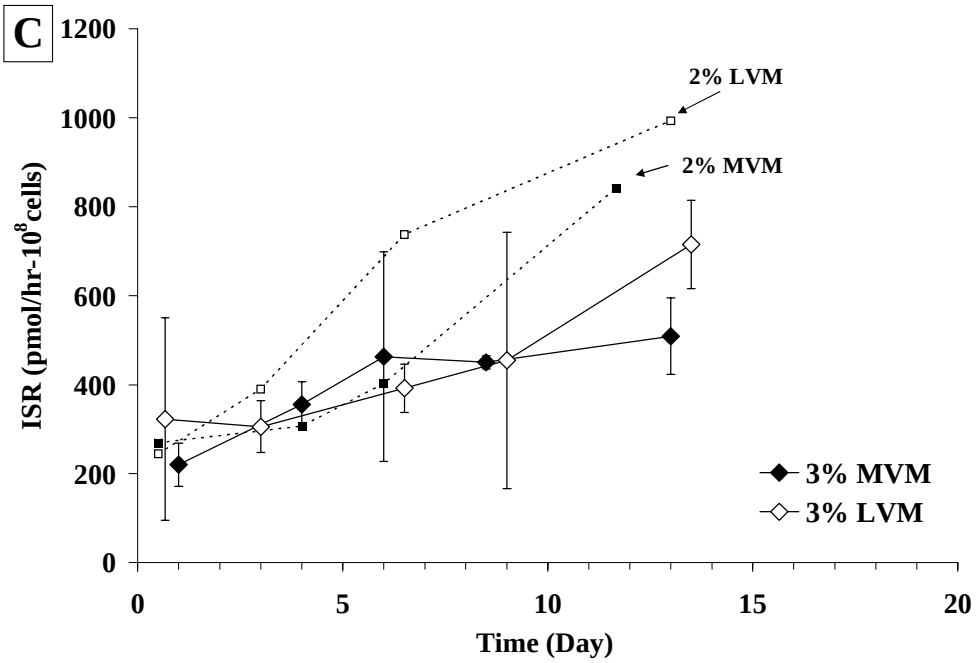

Figure 10 (continued). Temporal changes in the rates of (A) glucose consumption (GCR) (B) lactate production (LPR) and (C) insulin secretion (ISR) by βTC3 cells encapsulated in 3% w/v MVM (solid diamonds) and LVM (open diamonds) alginates.

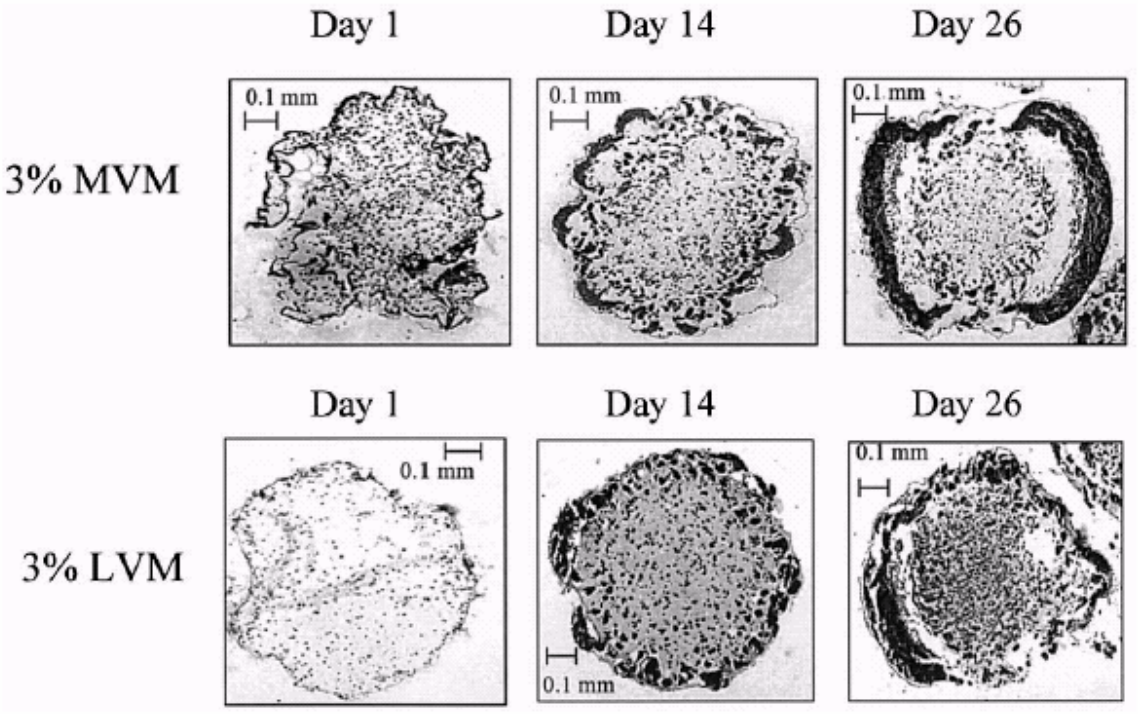

Figure 11. Cross-sections of 3% MVM and LVM APA beads containing βTC3 cells and stained with H/E at the times designated.

3.5. DISCUSSION

Extracellular matrices are known to influence the behavior of encapsulated cells [133]. Therefore, it is not surprising that βTC3 cells encapsulated in alginate gels of varying composition exhibited differences in their growth dynamics, which correlated with the overall metabolic and secretory activities of the cultures. These changes were a function of chemical composition, molecular weight, and concentration of alginate; however, the exact cause responsible for these effects is unclear. A property of alginate gels that can best interpret our data is the strength of the gel network. It is documented in the literature that alginates with a high guluronic acid content form a more structured crosslinking network due to the formation of junction zones between Ca^{2+} ions and contiguous guluronic acid residues (a.k.a. guluronic blocks) from different alginate chains. The model that describes this interaction is the "egg-box model" [29]. In the event that gellation takes place in the presence of high $CaCl_2$ concentration such as the 0.1 M solution used in the present experiments, multiple layers of junction zones are formed strengthening the resultant network. This network is postulated to behave similar to a rigid cylinder [134]. Thus, the stronger the network the more difficult it is to displace it. Consequently, cell growth might be inhibited within a strong cohesive gel network.

Comparing data acquired from 2% w/v MVG versus MVM alginates or LVG versus LVM alginates reveals that an increase in guluronic acid content hinders the growth of encapsulated cells. This is attributed to the strong gel network formed by the MVG and LVG alginates due to their high content of guluronic blocks (60% and 56% for MVG and LVG respectively versus 20% for MVM and 18% for LVM). The delayed cell growth

observed in the MVG and LVG alginates especially at the 2% w/v alginate concentration is attributed to a progressive weakening of this network over time. Since culture media have significantly lower $CaCl_2$ concentration than the 0.1 M $CaCl_2$ solution used for gellation, repetitive feedings during a prolonged culture period will result into a leaking of the Ca^{2+} ions, thereby weakening the gel network. The random location of viable cells that survived and proliferated during the initial inhibitory period in the 2% w/v MVG or LVG alginates is attributed to areas where the alginate network is not as tightly knit. The presence of these randomly placed clusters was previously attributed to the inhomogeneous gellation of high guluronic acid alginates [130]; however, this interpretation is unlikely given the radial distribution of gel inhomogeneity [122] and the present data. Alternatively, in alginates with a high mannuronic acid content (MVM and LVM), the cell growth and the overall metabolic and secretory activities were not inhibited because of the weaker gel network formed by such alginates. Therefore, the pattern of cell growth at the periphery of the beads that was observed in all MVM and LVM cultures is dictated by oxygen availability, as previously described [8, 130].

Molecular weight is known to influence the strength of the gel network in a biphasic manner [30]. A correlation between gel strength and molecular weight exists only for molecular weights up to approximately 250 kDaltons. This correlation ceases for higher molecular weight polymers. It is important to note that the effects of molecular weight on gel strength are not as strong as those imposed by an increasing guluronic content [30]. The effects of alginate molecular weight on encapsulated βTC3 cells are demonstrated by comparing data acquired from MVG versus LVG alginates and from MVM versus LVM alginates. Our data show that cells encapsulated in 2% w/v LVG

alginate (189 kDaltons) displayed the same initial inhibitory effects as the higher molecular weight MVG alginate (231 kDaltons), however the LVG-encapsulated cells started recovering earlier and proliferated faster than cells encapsulated in MVG alginate. This distinction in molecular weight was not observed in alginates with weaker gelling networks such as the mannuronic-rich alginates (MVM and LVM). With the 1% w/v MVG and LVG cultures, the differences between molecular weight were not significant but there was a prevailing pattern that the lower molecular weight afforded a higher metabolic activity to the encapsulated cells. The secretory activity between LVG and MVG at 1% w/v alginate gels was significantly different supporting the pattern observed in the metabolic rates.

The effects of alginate concentration on the encapsulated cells were assessed by performing two sets of experiments. In the first set, the concentration of MVG and LVG alginates was reduced from 2% w/v to 1% w/v in an attempt to weaken the rigidity of the APA beads and mimic the environment of a high mannuronic acid alginate. Conversely, in the second experiment, the concentration of MVM and LVM alginates was elevated from 2% w/v to 3% w/v in an attempt to strengthen the APA beads and mimic the environment of a high guluronic acid alginate. Reduction of the MVG and LVG concentration had the predicted effect. The temporal profiles of the metabolic and secretory rates as well as the growth pattern and dynamics of encapsulated cells displayed growth hindrance but not cell death during in the first 2-3 weeks after encapsulation. Alternatively, increasing the concentration of MVM and LVM did not follow the predicted pattern. There was no difference in either the metabolic and secretory rates or

the growth dynamics and pattern of βTC3 cells encapsulated in 2% and 3% w/v alginate concentration.

From a mechanistic point of view, our data show that it is not simply the overall rigidity of the matrix that is responsible for the behavior of the encapsulated cells, but rather the strength of the alginate gel network at the microstructure level. This conclusion is deduced from the following three comparisons. A) βTC3 cells encapsulated in 1% w/v MVG or LVG alginates displayed slower growth and metabolic and secretory rates than cells encapsulated in 3% w/v MVM or LVM alginates. A 3% w/v MVM or LVM matrix, albeit high in mannuronic acid residues, generates a significantly denser gel than the 1% w/v MVG or LVG matrix and thus tolerates a higher load before breakage [30]. Yet, the 3% w/v MVM and LVM matrices provide a more favorable environment for encapsulated cell growth. B) βTC3 cells encapsulated in 2% w/v MVM or LVM alginates displayed the same metabolic activity with similar cultures encapsulated in 3% w/v MVM or LVM alginates. Independent mechanical measurements have shown that the 3% w/v alginate bead is significantly more rigid than a 2% w/v alginate bead [30]. Yet, the metabolic activity and growth characteristics of encapsulated βTC3 cells were independent of alginate concentration for these alginates. C) Comparing our previously published data from βTC3 cells encapsulated in 1.5% w/v MVG beads with a liquefied core [130] versus current data from βTC3 cells encapsulated in 1% w/v MVG with a gelled core, we observe no difference between the two cultures. Beads with gelled cores are significantly more rigid than beads with liquefied cores, yet they behave similarly. Therefore, our data cannot be interpreted simply in terms of the overall rigidity or density of the matrix, the way Helmlinger et al. have interpreted the

inhibition of spheroid growth within agarose beads [135], since stresses at the microscale within the alginate matrix may vary significantly and not be directly correlated with macroscopic parameters. It is our postulate that it is the strength of the alginate gel network at the microstructure level, resulting from the "egg-box" configuration of guluronic residues and calcium [29, 30, 134], that can best interpret the majority of our results and thus is responsible for the behavior of encapsulated cells.

Our data illustrate that the appropriate selection of an extracellular matrix can provide, at least partial, control of cell growth. This is of great importance to tissue engineering, since cell growth is a generic issue that transcends across many types of transformed cell-based tissue-engineered constructs. As indicated by the case of a bioartificial pancreas, alginates with a high guluronic acid content and at high concentration, which are traditionally favored for the encapsulation of mammalian islets, might not be appropriate for the encapsulation of proliferating cells. Similarly, APA beads with a gelled alginate core have superior mechanical properties over similar beads with a liquid core, but the restrictive environment of the gel and/or its chemical composition might be detrimental to the proliferation of the encapsulated cells. It should also be noted that the prolonged decline and subsequent recovery of cells encapsulated in 2% w/v MVG and LVG alginates might result in a change of cell phenotype. This is potentially a problem or a blessing for tissue engineering applications depending on whether the altered phenotype provides the function sought by the tissue engineered construct. A better understanding of the effects of alginate composition on cell phenotype is currently underway in our laboratory.

In summary, our data demonstrate that alginate composition has a significant effect on the viability and growth of encapsulated βTC3 cells and consequently on the overall metabolic and secretory activities of the cultures. For the encapsulation of βTC3 cells and possibly other transformed cells with similar growth characteristics, our data indicate that a 1%–1.5% w/v LVG alginate provides a favorable environment, while maintaining a sufficient mechanical stability, thereby providing an excellent vehicle for *in vitro* and possibly *in vivo* experimentation.

CHAPTER 4

4. EFFECTS OF ALGINATE COMPOSITION ON THE GROWTH AND OVERALL METABOLIC ACTIVITY OF βTC3 CELLS[2]

4.1. ABSTRACT

The effects of alginate composition on the metabolic and secretory activity of βTC3 cells were explored *in vitro*. Earlier studies found that alginates high in guluronic acid content transiently impart detrimental effects on the entrapped βTC3 cells, while alginates high in mannuronic acid content result in bead rupture after fourteen days. This study explored the use of an intermediate alginate containing a 55% guluronic acid content and 45% mannuronic acid content. *In vitro* monitoring of the metabolic and secretory activity of the entrapped βTC3 cells, along with histological examinations, found this alginate to stabilize the cultures to a statistical plateau over a period of approximately two weeks. After this period, the cultures exhibited metabolic and secretory behaviors similar to a high mannuronic alginate. The applicability of this alginate to provide a combination of mechanical strength and stable growth is discussed.

4.2. INTRODUCTION

The encapsulation of cells within semipermeable membranes for the purpose of immunoisolation from the host has many potential applications in tissue engineering,

[2] Modification of paper published in Ann NY Acad Sci, 961: 130-133 (2002).

ranging from the treatment of Parkinson's disease to the encapsulation of insulin-secreting cells for the long-term treatment of diabetes [19, 118]. Alginate is the biomaterial commonly used in the entrapment of cells. Additional layers of poly-L-lysine and alginate are typically added to coat the central alginate matrix to improve the stability of the gel [119] as well as to create an immunoisolation membrane [15]. The advantages of alginate/poly-L-lysine/alginate (APA) beads include structural integrity and at least partial immunoprotection to the entrapped cells, ease in manufacture, and manipulation of the molecular weight cutoff of the membranes.

Alginate is a common term for a family of unbranched polymers composed of 1,4-linked β-D-mannuronic and α-L-guluronic acid residues in varying proportions, sequence, and molecular weight. The gelation of alginate takes place when multivalent cations (usually Ca^{2+}) interact with blocks of guluronic residues between two different chains resulting in a three-dimensional network [29]. The strength of the network depends on the overall fraction of guluronic acid residues the molecular weight of the polymer, and the Ca^{2+} ion concentration at the time of gelation [30]. The physical properties of alginate gels vary widely depending on their chemical composition. In summary, alginates possessing a high guluronic acid content develop stiffer, more porous gels, which maintain their integrity for longer periods of time whereas alginates rich in mannuronic acid have reciprocal properties. Therefore, high guluronic alginates have long been advocated for use in encapsulated cell systems [31].

Given the variety of physical properties associated with alginate composition, it is reasonable to hypothesize that encapsulated cells might be affected differently by changes in the alginate composition. In CHAPTER 3, we have explored these effects by

entrapping βTC3 cells within alginates of varying molecular weight, structure, and concentration. Through these studies, we were able to determine that a high guluronic alginate at a 2% w/v concentration, although advocated for use by other research groups due to its strength and stability, has detrimental effects on βTC3 cells by inhibiting their normal growth and overall metabolic activity for almost 60 days. A high mannuronic alginate at 2% and 3% w/v concentrations permitted βTC3 cell growth at an exponential rate, until the microbeads broke due to the high cell density. Furthermore, the growth patterns of the βTC3 within the high guluronic alginates and the high mannuronic alginates, in general, differ significantly from an o-ring to a clustering pattern.

4.3. RESULTS AND DISCUSSION

In continuation of these studies, an encapsulation system that provided some control over excessive cell growth while maintaining structural integrity for *in vivo* implantation would prove to be advantageous. In an attempt to strike a balance between the strength of the high guluronic alginate and the cell-favorable environment of the high mannuronic alginate, a composite alginate was created using a 2% w/v concentration of a high guluronic alginate (LVG) and a 2% w/v concentration of a high mannuronic alginate (LVM) in a 50/50 ratio. The resulting alginate had 55% guluronic acid content and 45% mannuronic acid content. Figures 12 and 13 illustrate the temporal changes in the rates of glucose consumption (GCR) and insulin secretion (ISR) by βTC3 cells encapsulated in 2% w/v LVG/LVM (solid diamonds), compared with 2% w/v LVG alginates (open diamonds) and 2% w/v LVM (gray diamonds). Each point on the graphs represent the average overall metabolic and secretory rate from the three independent encapsulations,

while the values determined for each encapsulation are the average rate exhibited by the culture over a period of two to three days depending on the feeding cycle. The error bars represent the standard deviation from the mean. The graphs illustrate that βTC3 cells encapsulated the 50/50 mixture of LVG/LVM maintain a statistical plateau in their overall metabolic and secretory activity for approximately two weeks. This is compared to the 2% LVG alginate, which display a decrease in the overall metabolic and secretory activity over the course of almost one month, and the 2% LVM alginate, which show an exponential increase in the overall metabolic and secretory rates following entrapment. H/E stained histology images also demonstrate the growth of the cells within the APA beads, where the βTC3 cells within the 2% LVG/LVM mixture exhibit a semi-clustering growth pattern of cells throughout the bead. Therefore, through these experiments, an alginate was created that controls the proliferation rate of the βTC3 cells and retains the mechanical properties necessary for safe implantation for two weeks. Our data demonstrate that the appropriate selection of an extracellular matrix can provide, at least partial, control of cell growth.

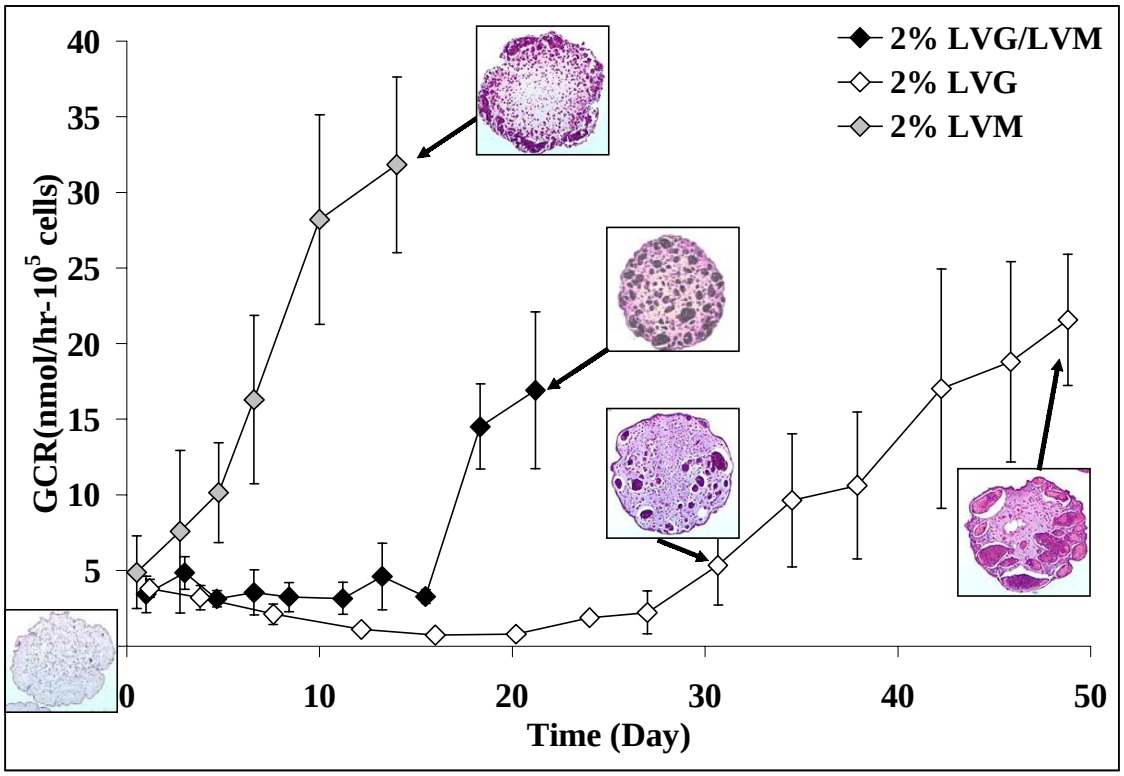

Figure 12. Temporal Changes in the rates of metabolic activity (Glucose Consumption Rate) for βTC3 cells encapsulated in 2% w/v LVG/LVM (solid diamonds), LVG (open diamonds), and 2% LVM (gray diamonds) with representative histological images shown a specified time points.

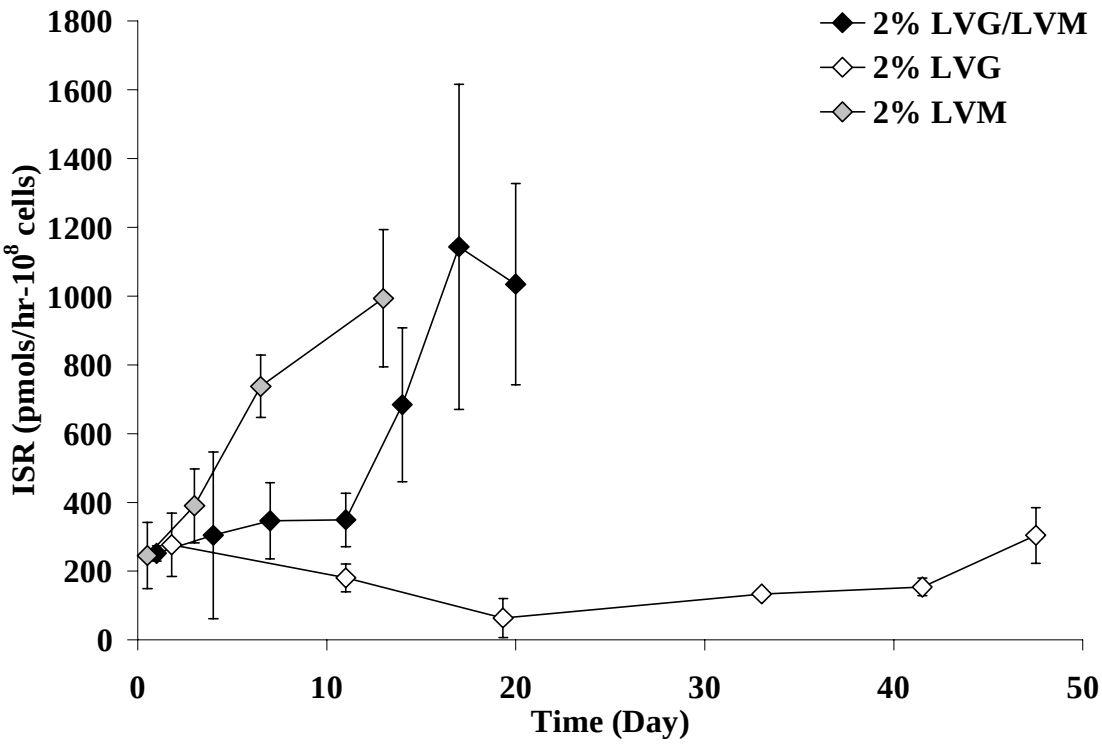

Figure 13. Temporal Changes in the rates of Secretion Activity (Insulin Secretion Rate) for βTC3 cells encapsulated in 2% w/v LVG/LVM (solid diamonds), LVG (open diamonds), and 2% LVM (gray diamonds).

CHAPTER 5

5. NONINVASIVE MONITORING OF A RETRIEVABLE BIOARTIFICIAL PANCREAS *IN VIVO*[3]

5.1. ABSTRACT

This study explores the ability of ^{1}H Nuclear Magnetic Resonance (NMR) imaging and spectroscopy to collect spatial and metabolic information from an implanted bioartificial pancreas. The implant consisted of alginate/poly-L-lysine/alginate (APA) beads confined within a planar construct, fabricated from a silicone o-ring and sealed with a polypropylene mesh of pore size 500 μm. *In vitro* metabolic and secretory assessment of the device found levels comparable to free floating APA beads when the device thickness was approximately 1.8 mm. Localized, water-suppressed ^{1}H NMR spectra were collected from the device *in vitro*. *In vivo* localized, water-suppressed ^{1}H NMR spectra, comparable to *in vitro* results, were obtained from implanted 5 mm thick constructs on Day 0, by localizing the collected signal to a volume inside of the implant. ^{1}H NMR images allowed for accurate positioning of the localized volume of interest (VOI). The implications of this research on monitoring implanted tissue engineered constructs using ^{1}H NMR imaging and spectroscopy are discussed.

---

[3] Modification of paper published in **Ann NY Acad Sci,** 961: 298-301, (2002)

5.2. INTRODUCTION

The bioartificial pancreas is a potentially efficacious treatment for diabetes, which could provide physiologic blood-glucose regulation without immunosuppressive medication, administered with relative ease, and be readily available [15, 19]. Although various designs have been considered, the design most commonly used to generate these tissue engineered constructs is based on the microencapsulation of insulin-secreting cells in a biocompatible matrix that provides mechanical support and, at least, partial immunoprotection [15]. A variety of cells have been used in these constructs including mammalian islets and transformed β-cell lines [43, 136], and the matrix most frequently utilized is the alginate/poly-L-lysine/alginate (APA) bead. At present, our only means of assessing the efficacy for an implanted bioartificial pancreas is to measure the blood glucose concentration of the host. Developing a noninvasive imaging technique that can monitor the viability and function of encapsulated cells as well as the integrity of the matrix is of critical importance. Nuclear Magnetic Resonance (NMR) has the ability to provide both biochemical and structural information, under either *in vivo* or *in vitro* conditions.

Retrieval of all APA beads following IP implantation is difficult due to the dispersal of the beads throughout the peritoneal cavity. A possible solution to this problem is to contain the beads within a device that can be easily retrieved. This device, however, can impose additional diffusion barriers and thus be detrimental to the metabolic and secretory activity of the encapsulated cells. A benefit of such containment is the ability to acquire NMR spectra localized from within the device. This study shows our efforts in

developing a NMR based methodology to monitor a retrievable bioartificial pancreatic construct *in vivo*.

5.3. MATERIALS AND METHODS

5.3.1. Cell Culture and APA Encapsulation

βTC3 cells were obtained from the laboratory of Dr. Shimon Efrat (Albert Einstein College of Medicine, New York, N.Y.) and cultured as previous described in CHAPTER 3. Encapsulation of βTC3 cells in APA beads was based on the initial protocol by Sun [15] and modified to suit our need. The alginate solution employed in these studies had a 2%w/v density and a 45%/55% mannuronic/guluronic content. The final APA beads measured ≈800 μm in diameter and contained initially $5x10^7$ βTC3 cells/ml alginate.

5.3.2. NMR Spectroscopy and Imaging

NMR imaging and spectroscopy examinations were performed using a Varian/Inova 4.7T horizontal bore magnet operating at 200.56 MHz (Varian, Inc., Palo Alto, CA). The magnet was equipped with an 11.7 cm inner diameter self-shielded gradient system with a maximum gradient strength of 25 gauss/cm. NMR signal was transmitted and received using a 16-element quadrature birdcage coil of 3.6 cm inner diameter and a 7 cm length. For *in vitro* experiments, constructs were placed within a sterile centrifuge tube filled with saline, and the tube was centered in the coil. For *in vivo* scans, anesthetized animals were centered and secured inside the coil. Subsequently, the RF coil was positioned in the isocenter of the magnet.

Scout ^{1}H NMR gradient-echo images (TR = 200 ms, TE = 3.5 ms, acquisition time of 51 sec) were acquired to determine the position of the construct. Once the center of the construct was identified, localized ^{1}H NMR spectra were acquired from a 3 mm thick volume of interest (VOI), centered within the cell-containing region of the construct. Shimming of the water signal was performed on the selected VOI using a localized non-water suppressed Point RESolved Spectroscopy (PRESS) sequence [137]. Water-suppressed spectrum on the same VOI was acquired using three CHemical Shift Selective (CHESS) pulses prior to executing the PRESS localization sequence. The PRESS pulse parameters used for all of the experiments were TR equal to 3 sec and a total TE, defined as $2t_1 + 2t_2$ (t_1 = 12.5 ms, t_2 = 33 ms), of 91 ms. All localized, water-suppressed ^{1}H NMR spectra were the average of 256 acquisitions, collected at a constant receiver gain using real-time digital signal processing. The total time required to collect each water-suppressed spectrum was 12 min 56 sec. Spectral data were processed using the frequency domain analysis package supplied in VNMR from Varian. Time domain data were apodized with an exponential line broadening of 3 Hz, Fourier transformed, with the residual water signal removed by digital filtering, and the baseline corrected where necessary. A Lorentzian function was fitted to the resulting TCho peak at 3.2 ppm using manufacturer-provided software to determine the area under the peak.

5.4. RESULTS AND DISCUSSION

A prototype model that consisted of a 13 mm diameter silicone ring with a polypropylene mesh of pore size 500 μm covering the top and bottom of the ring was considered for the containment of the APA beads (Figure 14). The thickness of the

construct was varied from 1.8 mm to 5 mm, where approximately 0.25 to 0.65 ml of APA beads could be injected into the ring and packed tightly within the construct. Figure 15 illustrates temporal profiles of the *in vitro* metabolic and secretory activities of the encapsulated βTC3 cells contained within three construct prototypes, compared to free-floating APA beads. As can be seen from the figure, while the glucose consumption rates of the constructs were not compromised by containment within the ring, the insulin secretion rates were significantly decreased when confined within the 3 mm or 5 mm thick constructs. From this data, it can be concluded that the 1.8 mm silicone construct was the most promising design for containment of APA beads, without compromising function.

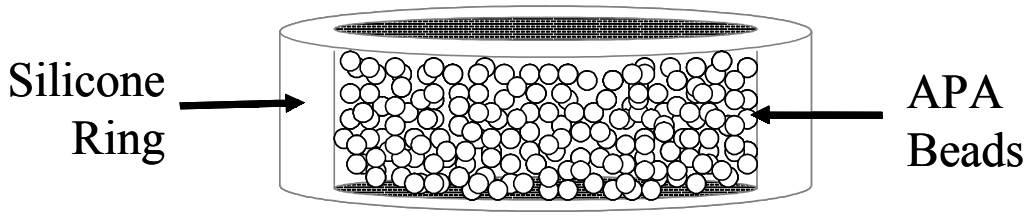

Figure 14. Schematic representation of construct prototype. APA beads contain entrapped βTC3 cells, while outer region is the silicone ring.

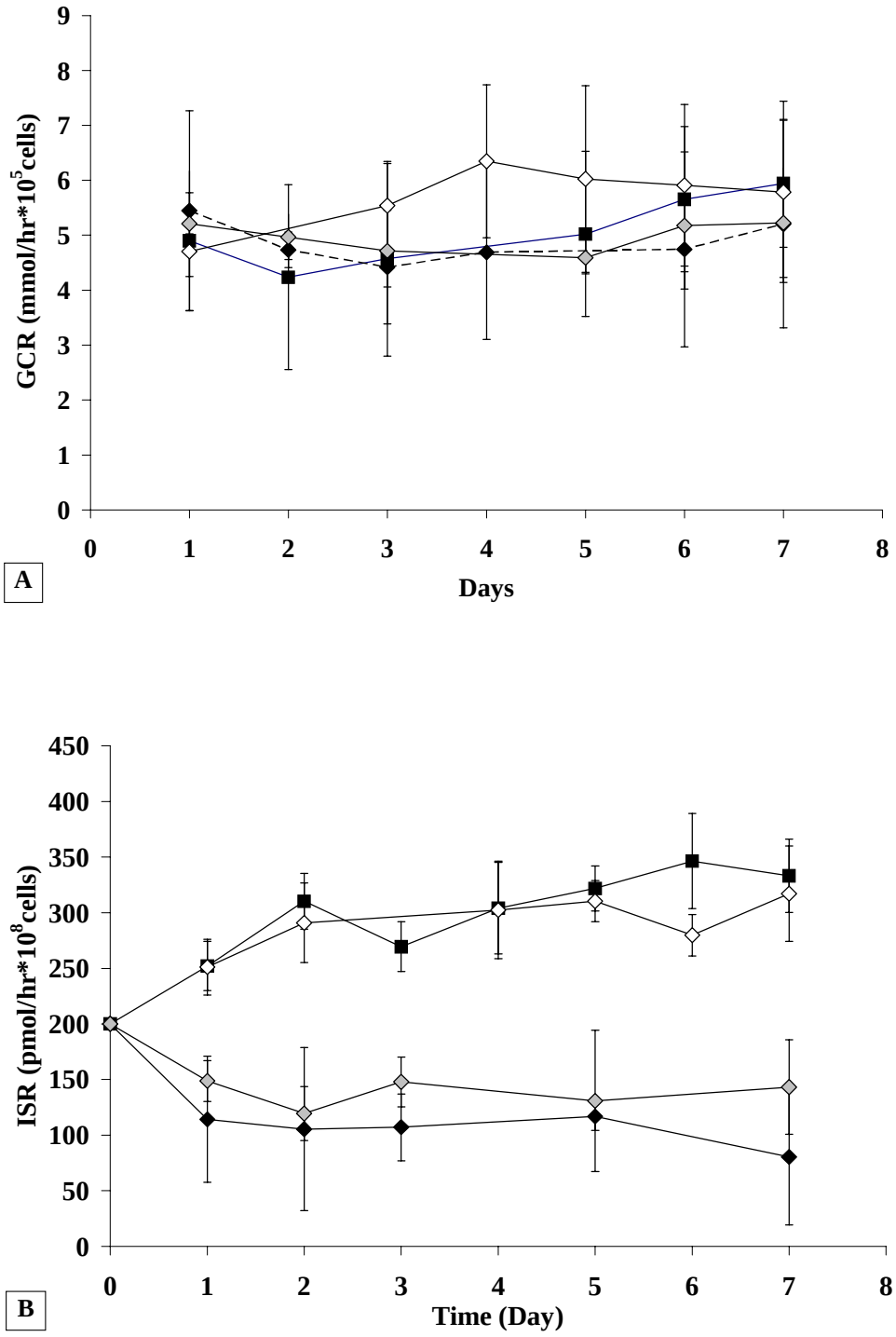

Figure 15. Temporal changes in the rates of (A) glucose consumption (GCR) and (B) insulin secretion (ISR) of βTC3 cells encapsulated in APA beads free-floating (solid squares), or confined within 5 mm (solid diamonds), 3 mm (shaded diamonds), or 1.8 mm (open diamonds) thick constructs.

In vitro experiments were performed to optimize the NMR acquisition parameters. Figure 16 shows a gradient-echo image of a 3 mm construct, loaded with APA beads that contained βTC3 cells, showing the silicon ring (dark circle) and individual APA beads distributed uniformly inside the ring. The white square represents the volume of interest (VOI) within which the water suppressed ^{1}H NMR spectrum was acquired. The resulting spectrum shows a strong total-choline or TCho peak.

Preliminary *in vivo* experiments were initiated using normal C57BL/6J mice. A construct of 5 mm thickness was surgically implanted in the peritoneal cavity using a midline celiotomy. Immediately following implantation, the anesthetized animal was placed within the coil and positioned in the magnet. Figure 17 (Panels A and B) shows two orthogonal gradient-echo images of the mouse, delineating the location of the construct. Figure 17C shows a typical water-suppressed ^{1}H NMR spectrum, which was localized to the region within the construct. It should be note that the acquisition parameters and volume of interest for the *in vivo* spectrum were identical to the ones used during the *in vitro* experiment. The resulting *in vivo* spectrum was acquired in approximately 13 min. We have previously demonstrated that the 3.2 ppm resonance detected by ^{1}H NMR, commonly called total-choline or TCho, is a sensitive marker of cell proliferation and oxygen consumption by APA encapsulated βTC3 cells [7]. Therefore, the ability to detect total-choline from encapsulated cells noninvasively *in vivo* could permit us to monitor the proliferation and oxygenation of these cells. Such information is critical in assessing the functionality and possibly the longevity of an implanted construct.

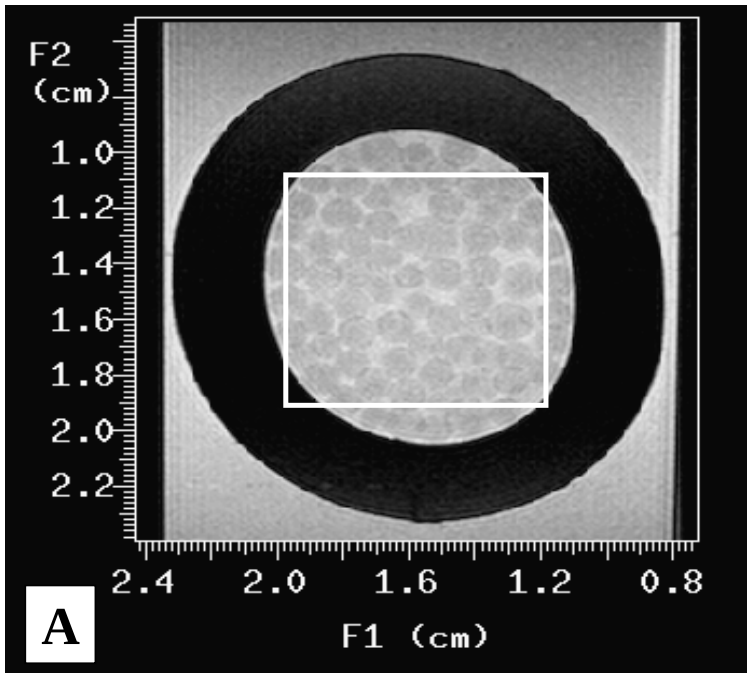

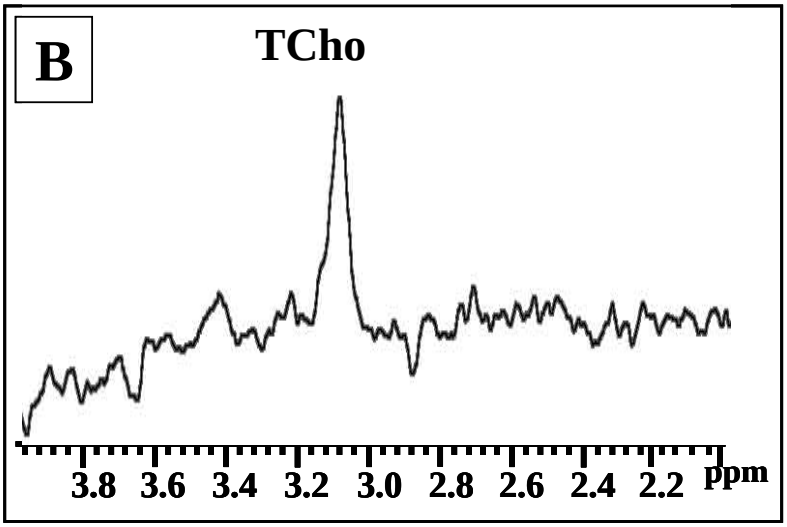

Figure 16. A gradient-echo image of a silicon o-ring with 0.4 mL of APA beads inside (Figure A). The white square is the volume of interest within which the water-suppressed ^{1}H NMR spectrum was acquired (Figure B).

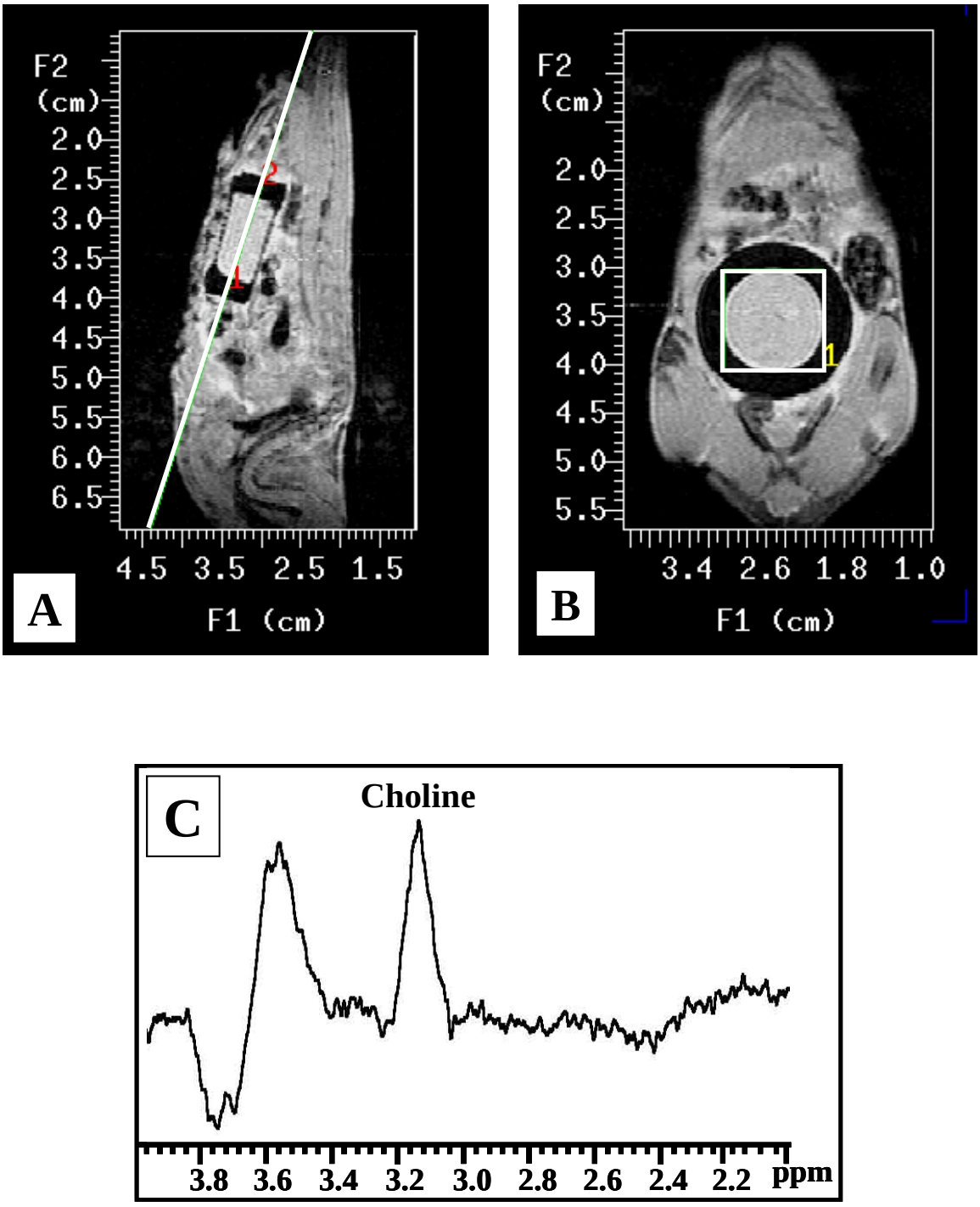

Figure 17. A sagittal view through the C57BL/6J mouse showing the location of the construct (Panel A). A coronal view through the mouse and the o-ring (Panel B). A water suppressed localized ^{1}H NMR spectrum acquired from within the o-ring (Panel C).

5.5. CONCLUSIONS

Overall, we have demonstrated that APA beads containing βTC3 cells can be restrained within the confines of a construct without significantly affecting the metabolic and secretory activity of the cells when the thickness is approximately 1.8 mm. In addition, localized ^{1}H NMR spectra can be collected from an implanted construct *in vivo*, setting the foundations to monitor a tissue-engineered construct *in vivo*.

CHAPTER 6

6. *IN VITRO* CHARACTERIZATION OF βTC3 CELLS IN AGAROSE DISK CONSTRUCTS AS A BIOARTIFICIAL PANCREAS

6.1. ABSTRACT

This study investigated the use of agarose macroconstructs for the development of a bioartificial pancreas. Two disk-shaped macroconstruct prototypes were examined: (i) a single disk construct comprised of agarose and βTC3 cells; and (ii) a buffered disk construct consisting of agarose and βTC3 cells, coated with an additional layer of pure agarose. Diffusional studies of glucose and insulin were performed to characterize the transport properties of the material. Diffusion-reaction models were used to generate oxygen profiles for the two construct prototypes, and these models were compared to experimental *in vitro* results of cell viability and secretory activity. The applicability of this research in the development of agarose-based constructs for use as a bioartificial pancreas is discussed.

6.2. INTRODUCTION

Diabetes mellitus is a serious pathological condition characterized by impaired insulin production and oscillation of glucose levels. While the generally accepted current treatment for insulin-dependent diabetes involves blood glucose monitoring and multiple daily insulin injections, a treatment that can provide a more physiological control of blood glucose levels could significantly decrease diabetic secondary complications, such

as retinopathy, neuropathy, nephropathy [12]. A tissue engineered pancreatic substitute, consisting of insulin-secreting cells and biocompatible materials, holds significant promise for treating insulin-dependent diabetics through continual regulation of insulin secretion in response to glucose. Use of transformed β cells, such as the continuous β cell lines developed by Efrat et al [23, 138], relaxes the cell availability problem posed by pancreatic islets, while also utilizing cells that have lower oxygenation requirements for insulin secretion [25]. Encapsulation of the implanted cells can partially alleviate the need for immunosuppression.

Development of a pancreatic substitute based on encapsulated insulin-secreting cells requires (i) a thorough construct design accounting for the transport of nutrients and metabolites and their respective consumption and production by the cells; (ii) *in vitro* characterization of the construct in terms of cell viability and the overall secretion dynamics; and (iii) *in vivo* evaluation of the construct functionality and efficacy. In this paper, we focus on the first two stages of development described above: the design, fabrication and *in vitro* characterization of a pancreatic substitute.

The construct selected for study consists of mouse insulinoma cells encapsulated in agarose in a disk-shaped construct. The ability of purified agarose, a common hydrogel used for cell encapsulation [27, 47, 57, 65, 139, 140], to maintain entrapped βTC3 cells was explored. In this study, two macroconstruct designs were examined, and the constructs were experimentally evaluated *in vitro*. Advantages and shortfalls of the implemented design approach, and possible compromises in construct functionality imparted by the foregoing architectural features, are discussed.

6.3. MATERIALS AND METHODS

6.3.1. Cell and Cell Culture

βTC3 cells were obtained from the laboratory of Shimon Efrat, Albert Einstein College of Medicine, Bronx, NY. Cells were cultured as monolayers in T-flasks and fed every 2-3 days with fresh medium consisting of Dulbecco's Modified Eagle's Medium (DMEM) with 25 mM glucose and supplemented with 15% horse serum, 2.5% bovine serum, 1% penicillin-streptomycin, and L-glutamine to a final concentration of 6 mM (Sigma, St. Louis, MO). Upon confluency, βTC3 cells were trypsinized using 0.25% Trypsin with EDTA (Sigma, St. Louis, MO) and either split for propagation or used in construct fabrication (passage numbers 33-48).

6.3.2. Construct Fabrication

Two types of agarose constructs were used in this study (Figure 18). One was a single 2% agarose disk with entrapped βTC3 cells and final dimensions of 1.8 mm height and 11 mm diameter (Figure 18A). The other was a buffered agarose disk, consisting of the single cell-containing agarose disk coated with an additional layer of pure 2% agarose, to final dimensions of 3 mm height and 16 mm diameter (Figure 18B). The presence of this buffer layer was found necessary to minimize the contribution of fat deposits on the NMR spectrum acquired from implanted constructs. These *in vivo* studies are reported in CHAPTER 9.

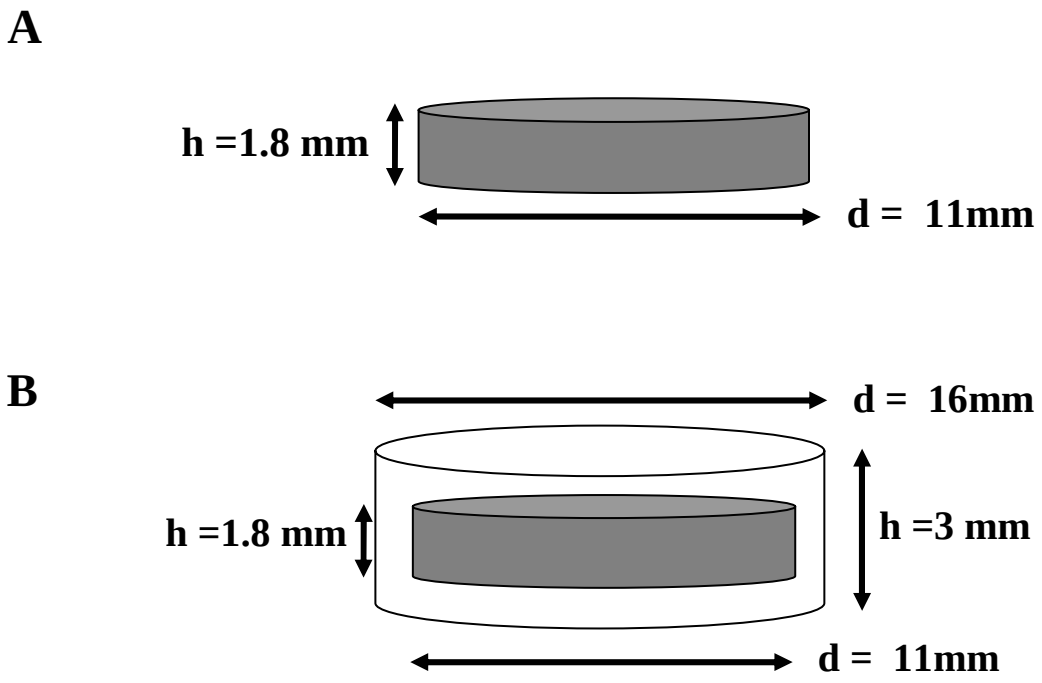

Figure 18. Schematic representation and dimensions of single agarose disk construct (A) and buffered agarose disk construct (B). The shaded region represents the inner disk containing βTC3 cells entrapped in 2% agarose, while the white region indicates pure 2% agarose.

Agarose (SeaPlaque, low gelling, 1250g/cm^2 gel strength) was obtained from Cambrex, NJ. The agarose powder was dissolved in PBS at 2%(w/v) according to the supplier's instructions, and the solution was sterile-filtered through a 0.2-μm filter (Pall, East Hills, NY) while still warm (>40ºC). Viable cell counts were performed on the freshly trypsinized βTC3 cell suspension using the trypan blue (Sigma, St. Louis, MO) exclusion method prior to centrifugation. The cell pellet was then suspended in the agarose solution at 37ºC at the cell loading specified for each experiment and evenly mixed using a syringe with a 20G needle. Pre-sterilized 1.8 mm thick Lexan sheets (McMaster-Carr, Atlanta, GA) with 11 mm diameter holes were fastened to pre-sterilized

Lexan bases by H-clamps and used as molds. The molds were filled to capacity with the agarose/cell mixture (0.2 mL in volume) and allowed to cool at room temperature until gelled (~ 3 mins). For single agarose constructs (Figure 18A), the disks were removed from the molds and placed in fully supplemented DMEM. For buffered agarose constructs (Figure 18B), the cell-containing disks were removed from their molds and placed into larger Lexan molds of 3 mm height and 16 mm diameter, fabricated from 3 mm thick Lexan sheets. These larger molds were partially filled with 2%(w/v) agarose solution prior to placement of the cell-containing disks and then filled to capacity after the inner disk was centrally aligned. Constructs were allowed to solidify at room temperature for 5 min before being placed in fully supplemented DMEM.

6.3.3. Diffusivity Measurements

Glucose and insulin diffusivities through agarose were measured by mixing glucose or porcine insulin (both from Sigma) with 2% (w/v) agarose and casting 1.5 mm slabs into wells of a six well plate. The concentrations of glucose and insulin in the slabs were 18 mg/mL and 0.1 mg/mL, respectively. These initial concentrations were selected to allow for accurate measurement of solutes during the initial stages and were based on the sensitivity of their respective assays. The agarose/solute solutions were allowed to gel for approximately 5 min at room temperature before 3 mL of PBS solution were added to each well, marking time zero of the experiment. Plates were placed on an orbital shaker for mixing and tests were performed at room temperature. For glucose, 5μL samples were collected from each well at intervals of 1 min during 0-20 min, 2 min during 20-30 min, 5 min during 30-60 min, and 15 min during 60-120 min. For insulin, 150 μL

samples were collected, while 150 μL of pure PBS was added, in order to maintain a constant volume, from each well at intervals of 1 min during 0-10min, 2 min during 10-20 min, 5 min during 20-60 min, and 15 min during 60-240 min. Finally, for each run, a sample was collected after 24 hours and compared to the previously collected sample to verify equilibrium.

To assess the effect of cells on effective diffusivities, glutaraldehyde-deactivated cells were incorporated into the agarose constructs. Glutaraldehyde deactivation prevented consumption or production of glucose or insulin by the cells, while retaining the basic elements of cell structure. Cells were deactivated through incubation with 1% glutaraldehyde for 1 minute, the glutaraldehyde was removed through a series of four washes with PBS, and the dead cells were suspended at a density of $5x10^7$ cell/mL with agarose/glucose or agarose/insulin solutions prepared as described above. The mixture was then cast into 6 well plates and tested using the same method described for the pure agarose experiments.

To assess the effects of an agarose/agarose interface on the effective diffusivity, a buffered slab was created by first casting 0.9 mm thick slabs in 6 well plates using 2% agarose and 25.2 mg/mL glucose or 0.14 mg/mL porcine insulin solution. The slabs were allowed to gel for 5 mins, and then coated with an additional 0.6 mm layer of pure 2% agarose. Testing of the composite slab was then delayed 30 min for the glucose and for 100 min for the insulin tests to allow for equilibration of the solute concentration within the entire construct volume. At time 0, 3mL of PBS was added to each cast and samples were collected in a manner identical to that described above.

For each experimental type, a minimum of three independent experiments were conducted, and data were fitted to the appropriate one-dimensional diffusion equation to estimate the effective diffusivity.

6.3.4. *In Vitro* Construct Characterization

For *in vitro* studies, both constructs types containing different initial cell numbers were examined. For single agarose constructs, initial cell loadings were $14x10^6$, $10x10^6$, and $7x10^6$ cells, while buffered agarose constructs initially contained $7x10^6$ and $3x10^6$ cells. For each experiment, twelve identical constructs were fabricated and split into two groups of 6 constructs each. Each group was placed in a 125 mL spinner flask (Wheaton, Millville, NJ) containing 35 mL of fully supplemented DMEM. The spinner flasks were placed on a spinner plate in a humidified 37°C, 5% CO_2 / 95% air incubator and were agitated at 30 rpm. The time duration of each experiment was 13 days. Complete media changes were performed every other day. Samples for insulin analysis were collected every 24 hrs. Two constructs from one spinner flask were removed on Days 0, 1, 3, 5, 7, and 13 for MTT and histology testing.

6.3.5. Analytical Techniques

Glucose concentrations in samples were measured using a calibrated Elite Glucometer (Bayer, PA). Insulin concentrations in samples from the diffusion experiments, where insulin was the only protein in solution, were measured with a Coomassie blue-based total protein assay (Pierce, IL). A calibration curve was generated for each assay run using the stock insulin solution diluted to the appropriate range.

Insulin from *in vitro* incubation experiments was measured with an ultra-sensitive mouse insulin EIA kit (ALPCO, NH) following the manufacturer's protocol.

To measure the viable cell number in a construct using the CellTiter 96 MTT (3-(4,5-dimethylthiazol-2-yl)-2,5-diphenyl-tetrazolium bromide) assay (Promega, Madison, WI), the construct was cut into four equal segments. Three of the segments were incubated in separate wells of a 12-well plate (Corning, Acton, MA), each containing 3 mL of fully supplemented DMEM and 450 μL of MTT, for 4 hrs at 37˚C, 5% CO2 / 95% air. Following incubation, each construct segment was placed in a mortar, ground using a pestle, and returned to its original well. Two milliliters of Solubilization/Stop solution was added to each well and the plate was sealed and placed within a humidified 37˚C, 5% CO2/95% air incubator for 24 hrs to fully dissolve the formazan crystals. A volume of 120 μL of the final solution in each well was then transferred to a 96 well plate, and the absorbance was read at 595 nm. Absorbance values read from the three segments were then numerically averaged. A viable cell number calibration curve for the MTT assay was generated by varying the initial cell loading of βTC3 cells within agarose constructs over the appropriate experimental range, Figure 19.

Samples designated for histology were fixed in 3% glutaraldehyde for 48 hrs and then prepared for paraffin embedding and sectioning. After sectioning into 5μm samples, the slides were stained with hematoxylin/eosin (H/E).

6.3.6. Statistical Analysis

All measurements are presented as the mean ± SD. All statistical analyses were performed using a two-sample t-test. Results were considered significantly different when *p*-values were less than 0.05.

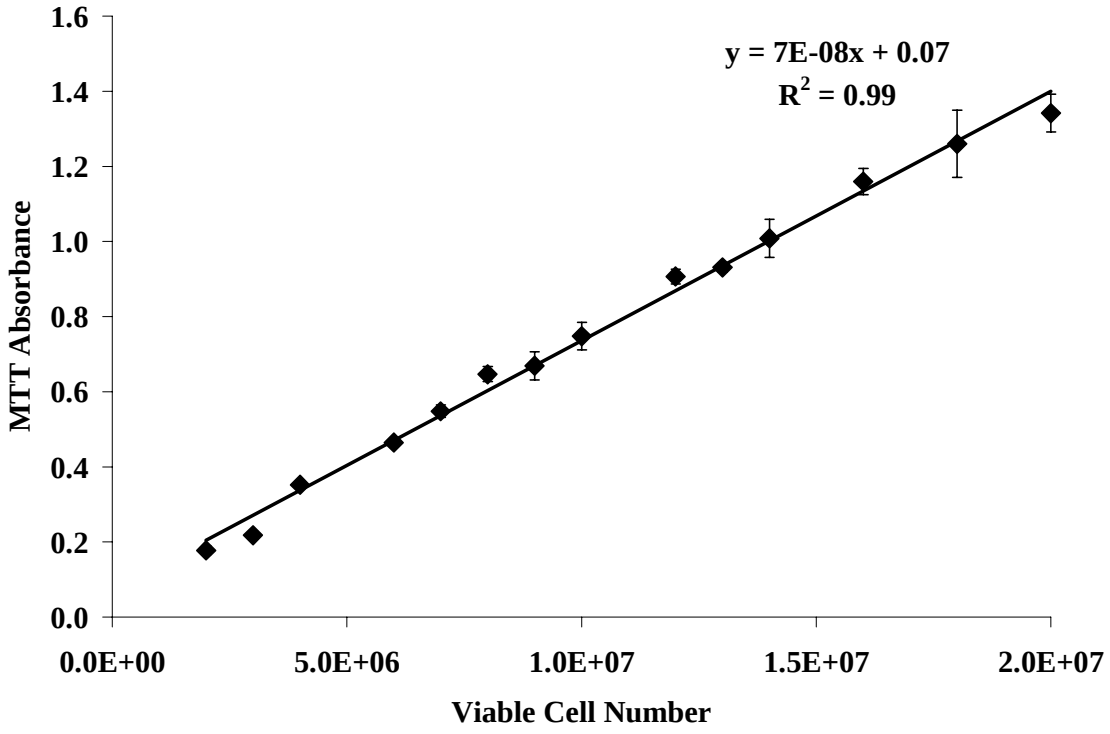

Figure 19. Correlation between viable cell number, assessed by trypan blue, and MTT absorbance for βTC3 cells entrapped in agarose constructs at varying cell loadings.

6.4. RESULTS

6.4.1. Effective Diffusivity in Agarose Constructs

Equation (1) describes the diffusion of solutes out of the agarose and into the solution for the experimental conditions outlined in the Methods section, assuming one-dimensional diffusion, uniform concentration of the solute in solution, adequate mixing of the bathing solution, constant effective diffusivity, and a partition coefficient of 1 (see section 6.6 for more details) [141, 142].

$$\frac{C_b}{C_o} = \frac{1}{1+\alpha}\left[1 - \sum_{n=1}^{\infty} \frac{2\alpha(1+\alpha)}{1+\alpha+\alpha^2 q_n^2} \exp\left(-\frac{Dq_n^2 t}{L^2}\right)\right] \quad (1)$$

where the parameters are defined as: D effective diffusivity of solute out of the agarose slab; L slab thickness; C_o initial concentration of solute in agarose; C_b concentration of solute in the bulk solution; α ratio of the bulk liquid volume to agarose slab volume; and q_n the nth root of the equation $\tan q_n = \frac{3q_n}{3 + q_n\alpha}$. To simulate experimental results, only three terms of the series in equation (1) were required, based on the magnitude of the term $\exp\left(-\frac{Dq_n^2 t}{L^2}\right)$.

Expressing equation (1) in the form of the total amount of solute M_t in solution at time t as a fraction of M_{inf}, the corresponding quantity after infinite time, one obtains:

$$\frac{M_t}{M_{\inf}} = \left[1 - \sum_{n=1}^{\infty} \frac{2\alpha(1+\alpha)}{1+\alpha+\alpha^2 q_n^2} \exp\left(-\frac{Dq_n^2 t}{L^2}\right)\right] \qquad (2)$$

where the parameters are defined as: $M_t = V_b C_b$; $M_{\inf} = \frac{V_s C_o}{(1+1/\alpha)}$; V_b volume of the bulk solution; and V_s volume of the agarose slab. For glucose measurements, a total of only 5.8% of the solution was removed during sampling, therefore volume changes were not taken into account. While the volume of the bathing solution remained constant during the insulin experiments, the insulin concentration in the bathing solution was altered by the removal of sampled fluid and the addition of insulin-free fluid. Therefore, insulin concentrations were corrected at each experimental and theoretical data point during the analysis to account for these effects. The effective diffusivity D for each solute was determined by fitting equation (2) to experimental data, with D as the only adjustable parameter.

Figures 20A and B show experimental and theoretical results for the diffusion of glucose out of single cell-free agarose constructs (Figure 20A) and cell-containing single agarose constructs (Figure 20B). Effective diffusivities were measured to be 4.26×10^{-4} cm^2/min and 3.22×10^{-4} cm^2/min for the cell-free and cell-containing constructs, respectively, or 103% and 78% of glucose diffusivity in water at 25ºC [143]. Results for insulin diffusivity through single agarose constructs are shown in Figures 20C and D. Insulin effective diffusivities for the cell-free and cell-containing constructs were measured to be 1.15×10^{-4} cm^2/min and 9.19×10^{-5} cm^2/min, respectively, or 96% and 77% of the diffusivity in water at 25ºC [144]. In all cases, results from the buffered agarose/agarose constructs were statistically identical to those from the corresponding single layer constructs.

6.4.2. Diffusion-reaction modeling of construct with cells

To evaluate the viable cell number that can be supported in the agarose constructs, diffusion/reaction models were developed to simulate the axial concentration profile of dissolved oxygen, since dissolved oxygen is typically the limiting nutrient for extravascular constructs [145-148]. To simulate the oxygen profile within the construct, the following assumptions were made: (i) mass transport primarily in axial dimension; (ii) cellular oxygen consumption following Monod's model; and (iii) homogeneous distribution of cells in the agarose matrix.

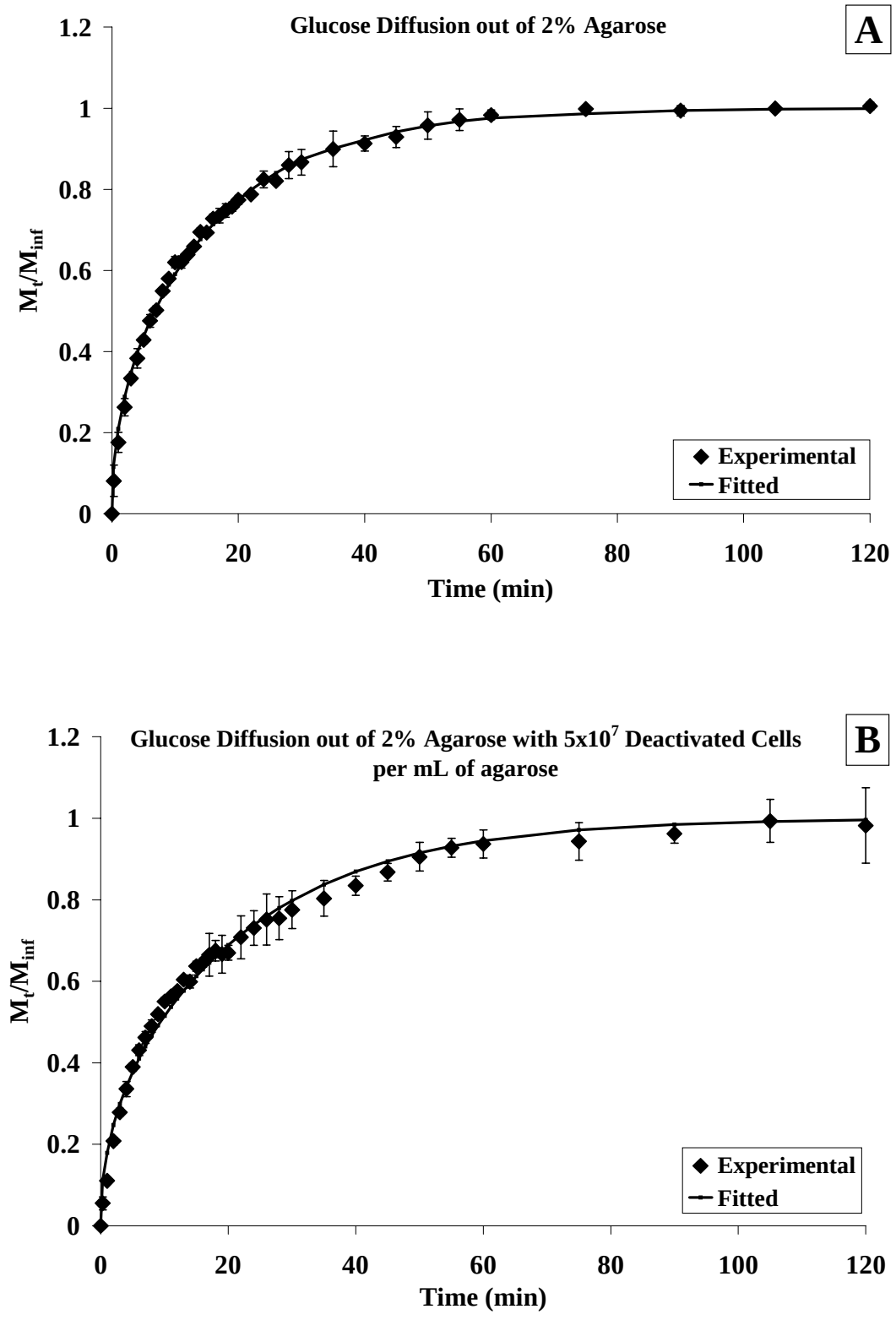

Figure 20. Time course of diffusion of Glucose (A and B) and Insulin (C and D) out of 2% agarose disks without (A and C) and with (B and D) cells.

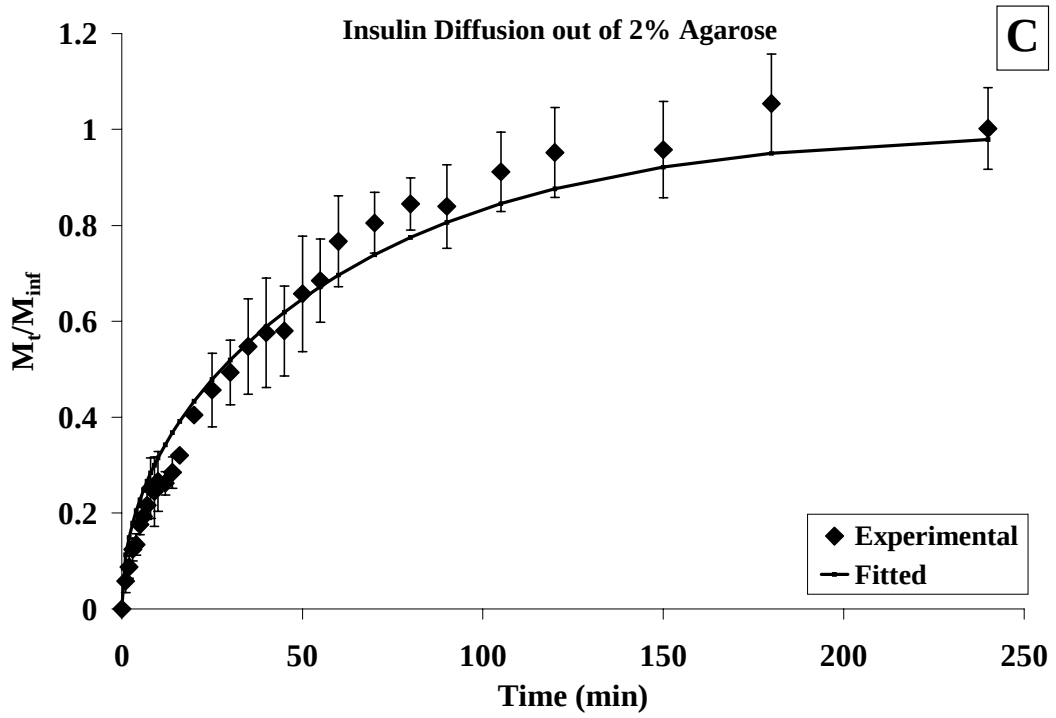

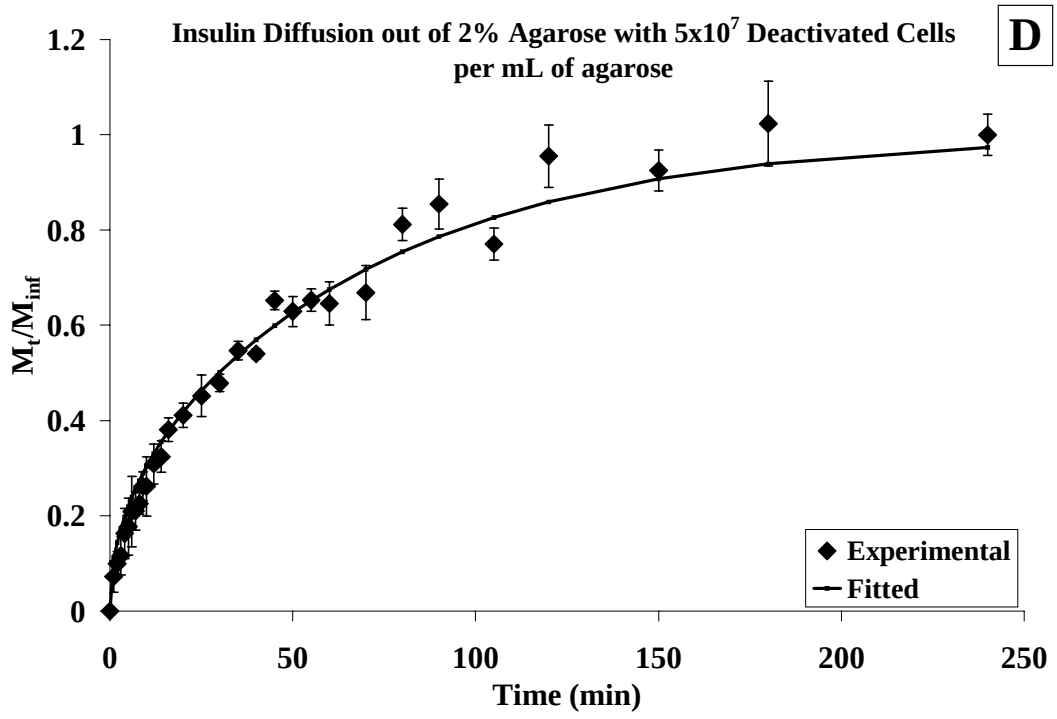

Figure 20 (continued). Time course of diffusion of Glucose (A and B) and Insulin (C and D) out of 2% agarose disks without (A and C) and with (B and D) cells.

Based on these assumptions, the resulting steady-state equation for oxygen concentration is:

$$\frac{\partial^2 C_A}{dz^2} = \frac{B}{D_{eff}} \frac{v_{\max} C_A}{K_M + C_A} \tag{3}$$

with boundary conditions of:

$$\frac{\partial C}{\partial x}(x = 0) = 0 \qquad C(x = 0) = C_s = 7 mmHg$$

The oxygen tension at the center is set at 7 mm Hg based on earlier experimental data (see next paragraph for more details). In the above equation, the parameters are defined as: C_A the concentration of oxygen; B the viable cell density within the construct; D_{eff} the oxygen effective diffusivity; v_{max} the maximal rate of oxygen consumption by the βTC3 cells; and K_M the Michaelis kinetic constant for oxygen consumption by the cells.

For βTC3 cells, earlier experiments concluded that oxygen tensions above 7 mmHg were required for the cells to retain their secretory capacity [25, 92, 149], thereby this tension was set as the minimum threshold (C_{ox} = 9.5x10^{-3} mM). Parameters v_{max} and K_M, which are inherent to the cell type, were estimated at 2 μmol/(10^{9}cells•min) and 0.01 mM, respectively, based on earlier published work [10, 149, 150]. The oxygen diffusivity in the agarose constructs was not measured in the earlier section; however, studies have found that the ratio of effective diffusivity in a matrix to the molecular diffusivity in water is not dependent on molecular size [151]. Therefore, the oxygen effective diffusivity could be estimated based on the percentages calculated in the glucose and insulin diffusivity experiments, which is approximately 100% for pure agarose and 75% for cell-containing agarose. The oxygen diffusivity in water at 37ºC has been estimated previously, using the Wilke-Change equation, to be 1.8x10^{-3} cm^2/min [149].

Thus, the oxygen effective diffusivities for the cell-free agarose and cell-containing agarose regions were assumed to be 100% ($1.8x10^{-3}$ cm^2/min) and 75% ($1.35x10^{-3}$ cm^2/min) of the oxygen diffusivity in water at 37ºC, respectively.

Axial profiles of dissolved oxygen concentration for three bulk oxygen concentrations, at three different cell densities, are shown in Figure 21 for single agarose constructs and Figure 22 for buffered agarose constructs. The bulk oxygen concentrations used in the calculations correspond to normoxia (Cox = 0.2 mM), arterial oxygen (Cox= 0.1 mM) and interstitial oxygen concentrations (Cox = ~ 0.05 mM). These simulations determined the maximum cell loading in each construct at the three bulk oxygen tensions, where all the cells are at or above the 7 mmHg oxygen threshold. These results are summarized in Table 2 where the cell density is converted to total cell number within the construct, using the volume of the experimental constructs (0.2mL).

6.4.3. *In Vitro* Construct Characterization

The experimental *in vitro* temporal profiles of viable cell number, measured by MTT, and insulin secretion rate (ISR) for single agarose constructs are shown in Figures 23 A and B. Three initial cell loadings were selected for study to correspond to approximately that supported by a normoxic environment ($1.0x10^6$ cells/mL), followed by one lower ($7.0x10^6$ cells/mL) and one higher ($1.4x10^7$ cells/mL) than modeling predictions (initial cell loadings are based on measurements made using fabrication using the trypan blue exclusion method). MTT results (Figure 23A) show an increase in viable cell number for all of the constructs during the first 24 hrs, with a decline in viable cell number over the subsequent days towards an equilibrium value of approximately $7.5x10^6$ cells by Day 5.

After initial fluctuations, the ISRs of all constructs also stabilized to the same statistical plateau after approximately 5 days in culture.

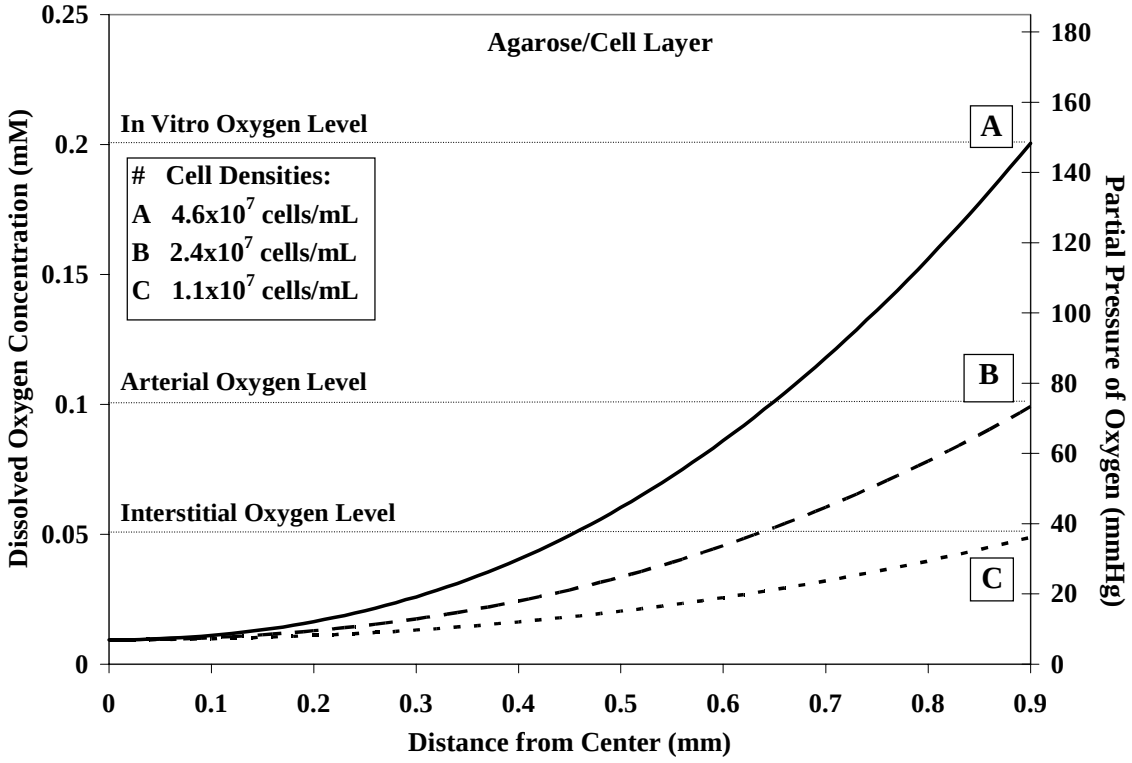

Figure 21. Model predicted oxygen profiles for single agarose disk constructs. The model predicted maximum cell density, where the oxygen level at center of construct is set to 7mmHg, is shown for normoxia (A), arterial oxygen (B) and approximated interstitial oxygen (C) conditions.

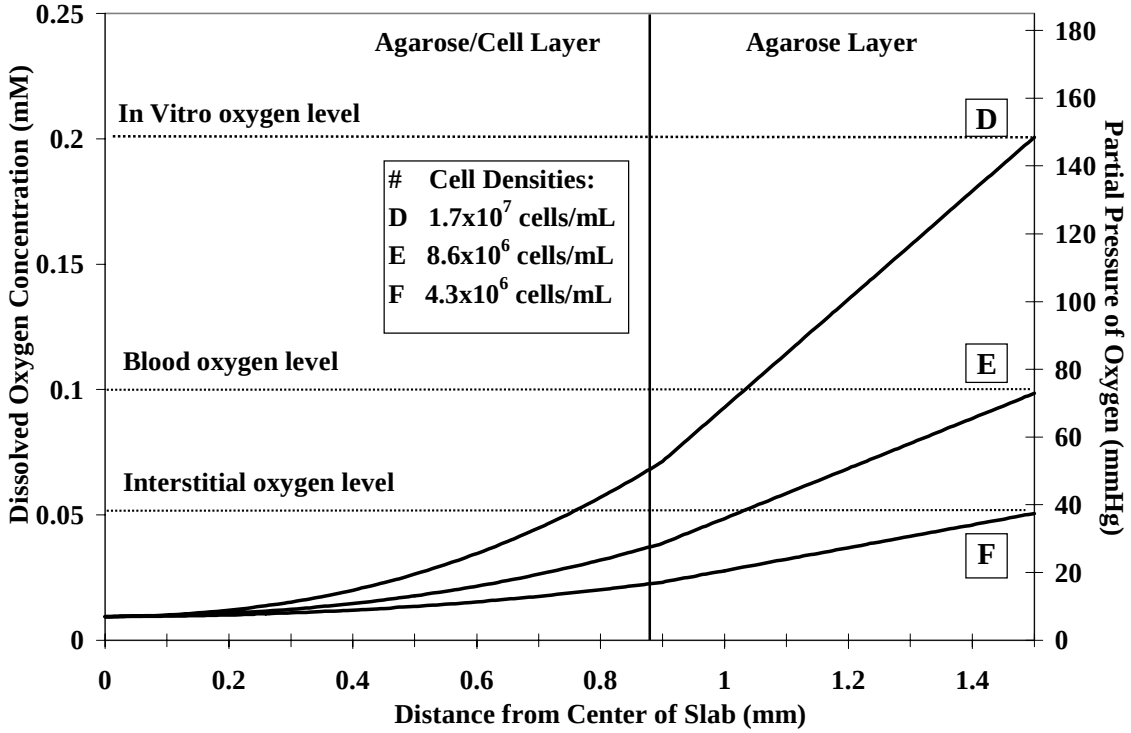

Figure 22. Model predicted oxygen profiles for buffered agarose disk constructs. The model predicted maximum cell density, where the oxygen level at center of construct is set to 7mmHg, is shown for normoxia (D), arterial oxygen (E) and approximated interstitial oxygen (F) conditions.

Table 2. Predicted maximum cell densities (or total number) in constructs

Construct Type	Normoxia (0.2 mM)	Arterial oxygen (0.1 mM)	Interstitial oxygen (0.05 mM)
Single	4.6×10^7 cell/mL agar or 9.2×10^6 cells	2.4×10^7 cell/mL agar or 4.8×10^6 cells	1.1×10^7 cell/mL agar or 2.2×10^6 cells
Buffered	1.7×10^7 cell/mL agar or 3.4×10^6 cells	8.6×10^6 cell/mL agar or 1.7×10^6 cells	4.3×10^6 cell/mL agar or 1.3×10^6 cells

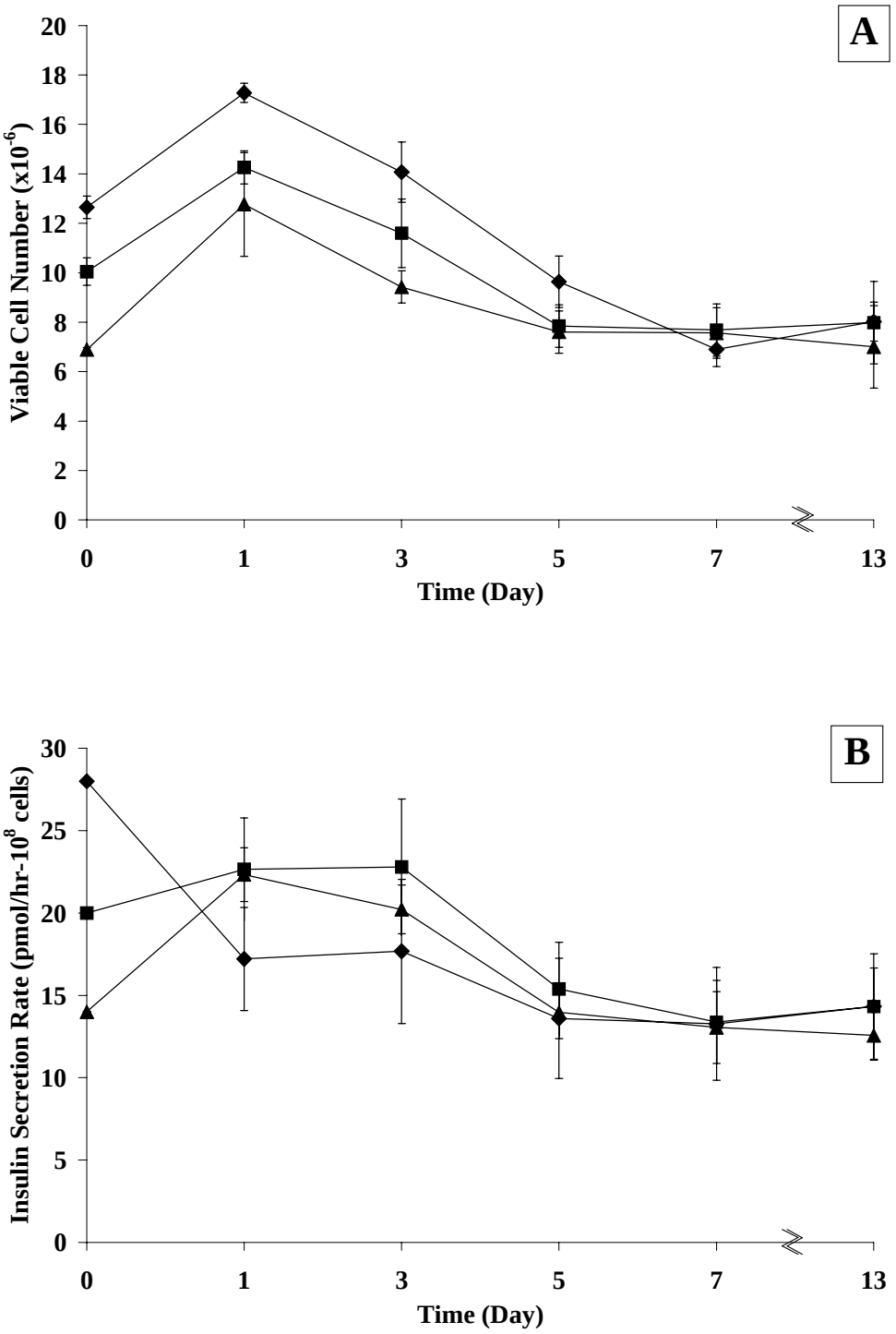

Figure 23. Temporal changes in MTT-assessed viable cell number (A) and insulin secretion rates (B) for single agarose disk constructs with initial cell loadings of $14x10^6$ cells (diamonds), $10x10^6$ cells (squares), and $7x10^6$ cells (triangles).

Comparable experiments using buffered agarose constructs involved two different initial cell loadings, one approximately equal to that calculated by the model to be supported by normoxia ($3x10^6$cells) and a higher one ($7x10^6$ cells) (initial cell loadings are based on measurements made during fabrication using the trypan blue exclusion method). For the latter, the model predicts that only 40% of cells are exposed to oxygen levels at or above 7 mmHg. Results of MTT-assessed viable cell numbers and ISRs are shown in Figures 24 A and B, respectively. Constructs initially loaded with $7x10^6$ cells exhibited a decline in viable cell number, which stabilized to ~$1.6x10^6$ cells at the end of the experiment. In constructs loaded with $3x10^6$ cells, the viable cell number slowly declined over the first 7 days before plateauing at ~$1.6x10^6$ cells. The ISR for constructs initially seeded with $7x10^6$ cells exhibited a steady decline over the first 5 days before stabilizing at ~30% of its initial levels. The ISR profile for constructs initially seeded with $3x10^6$ cells exhibited an increase from Day 0 to 2, followed by a decrease from Day 3 to 5, before remaining stable thereafter at ~80% of its initial value.

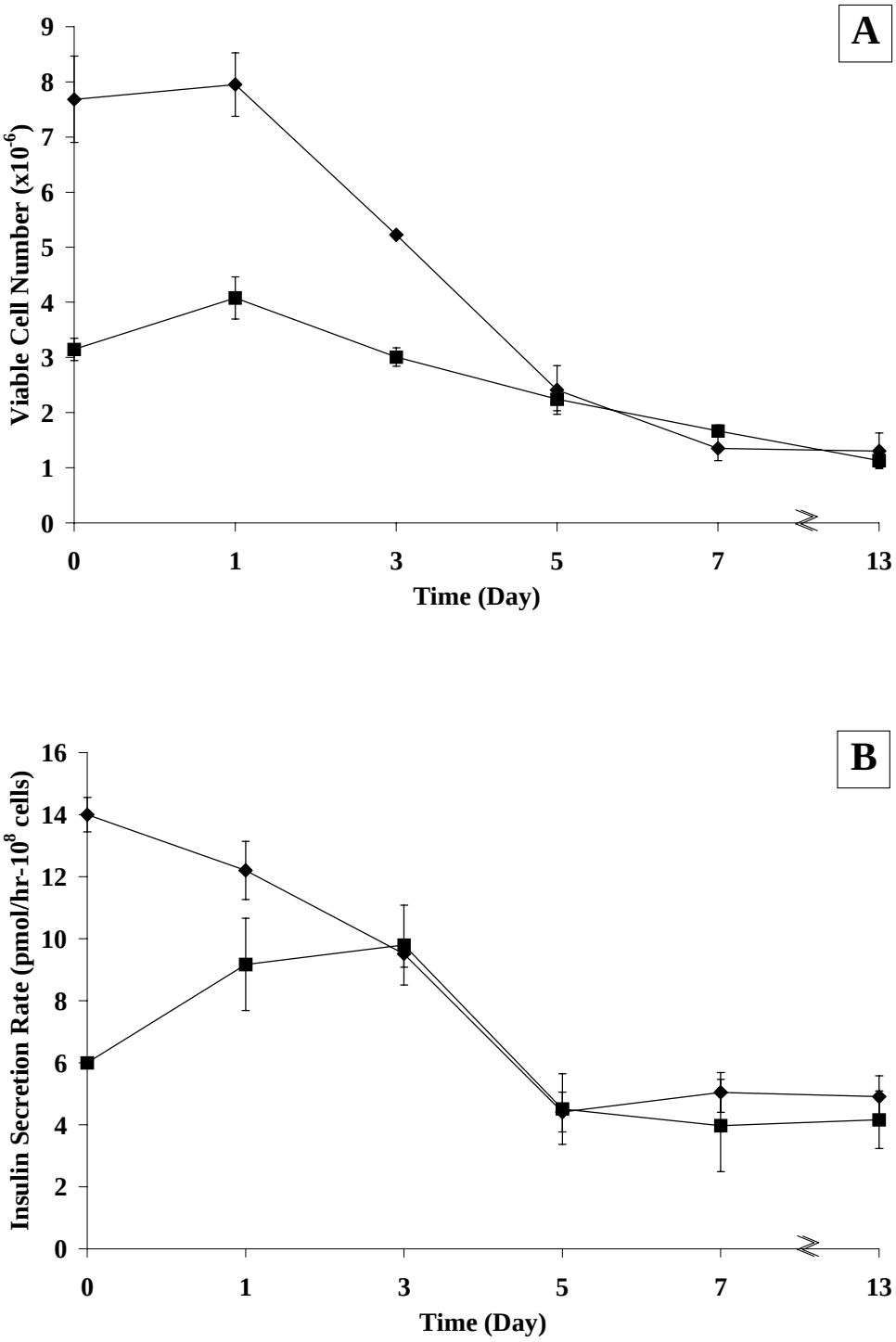

Figure 24. Temporal changes in MTT-assessed viable cell number (A) and insulin secretion rates (B) for buffered agarose disk constructs with initial cell loadings of $7x10^6$ cells (diamonds), and $3x10^6$ cells (squares).

H/E stained histological cross-sections of agarose constructs cultured *in vitro* are shown in Figure 25. Figure 25A shows a typical Day 0 construct with a homogeneous distribution of viable single cells throughout the cell-containing domains. By day 5, all of the constructs exhibited some remodeling, with the majority of the live cells found in clusters at the periphery of the cell-containing domains of the construct. Figure 25, B and C are typical examples of this remodeling for both the single and buffered constructs. For all buffered agarose constructs, no cell migration was observed into the pure agarose buffer domains (Figure 25 C).

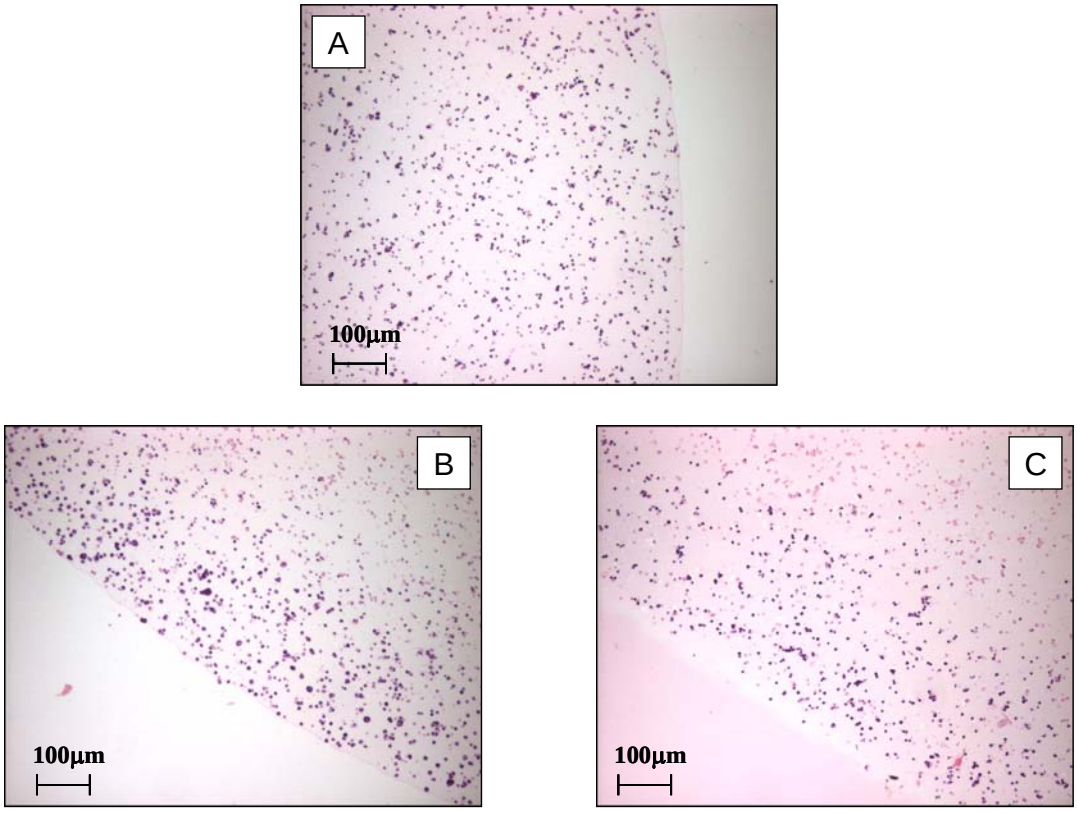

Figure 25. Typical H/E stained histological cross-sections of agarose constructs cultured *in vitro*: (A) single agarose disk on Day 0 containing $10x10^6$ cells; (B) single agarose disk on Day 5 containing $10x10^6$ cells; and (C) buffered agarose disk on Day 5 containing $7x10^6$ cells.

6.5. DISCUSSION

This study focused on the design, development and *in vitro* characterization of agarose macroconstructs containing βTC3 cells as a pancreatic substitute. Initial studies examined the diffusion of critical solutes, in particular glucose and insulin, and determined effective diffusivities in pure 2% agarose to be 103% and 96% of the diffusivities of glucose and insulin, respectively, in water at 25^{o}C. These measurements are within the range of previously published values for pure hydrogels of similar concentrations [152-154]. While the insulin diffusivity is somewhat higher than published work on other hydrogels, such as alginate, this could be due to variations in the quaternary structure of the insulin protein used in the experiment [155, 156]. For agarose constructs containing deactivated cells, a decrease of ~25% was calculated for both solutes, which is within the literature range for hydrogels containing cells deactivated through similar methods [47, 152, 157, 158]. Since glutaraldehyde deactivation renders the dead cells impermeable, it is possible that constructs containing live cells have somewhat higher diffusivities. Finally, experiments using buffered agarose constructs found the presence of the agarose interface to have an undetectable effect on the diffusion of glucose or insulin.

Using mathematical models to develop oxygen profiles provided an estimation of the cellular environment within the agarose constructs. *In vitro* monitoring of the insulin secretion and total cell viability profiles tested the applicability of the modeling results. For the single agarose constructs, after an initial transient period, the ISR and MTT values plateaued to statistically similar levels, regardless of the initial cell loading. The plateau values for the single agarose disk constructs are only slightly lower than the

modeling predictions, indicating oxygen as the dominating parameter for establishing cell functionality and viability for this construct type. Similar results were also obtained for the buffered agarose constructs, in the fact that both the ISR and MTT values plateaued to the same level regardless of the initial cell loading. The mathematical model of the buffered agarose constructs predicted that all of the cells should be above the 7 mm Hg threshold at a cell loading of $3.4x10^6$ cells or lower. An unexpected decline in both the ISR and MTT profiles of the $3x10^6$ cell loading, however, was seen between Day 3 and 5 that was below Day 0 levels. Therefore, the addition of the outer agarose layer imparts a negative effect on the entrapped cells after three days in culture, by a mechanism not accounted for in the oxygen model.

Cellular remodeling observed for all the constructs after 3-4 days in culture might provide an explanation for the disparity between model and experimental results in the buffered agarose constructs. While the presence of a peripheral band of cell clusters at the inner cell/agarose disk was expected, given earlier results showing this pattern for βTC3 cells entrapped in other permissive matrices, e.g., high mannuronic alginate, it is plausible that the addition of the outer agarose layer imparts additional mechanical stress to the cell clusters at the periphery of the inner disk, thereby reducing their proliferative capacity and resulting in the decrease in insulin secretion and viable cell number observed on Day 5 *in vitro*. Indeed, the detrimental effects of mechanical stress on the growth of cell clusters when entrapped in agarose concentrations greater than 0.9% has been documented in the literature, where spheroid growth was significantly inhibited once a threshold level of solid stress was attained [135].

Overall, the mathematical model developed in this study provided a useful initial estimation for oxygen profile of the cells within the construct, based on its architecture and scaffold material. While the *in vitro* buffered agarose disk results were not compatible with model predictions after 3 days in culture, comparisons between model and experimental results highlighted the detrimental effects of the outer agarose layer addition, which were not revealed in the diffusional studies. Similar models have been utilized to predict environmental conditions and identify critical parameters for cells within other tissue engineered devices. Tziampazis and Sambanis used diffusion/reaction models to characterize the cellular environment within alginate/poly-l-lysine/alginate microbeads and predict appropriate bead size ranges [149]. Dulong *et al* used finite element techniques to develop oxygen, glucose, and insulin transport models, which identified oxygen transport and cell density as the most significant parameters affecting overall cell viability and function for islets entrapped in hollow-fiber constructs [148, 159]. Overall, published reports identified construct architecture and oxygen levels as dominating parameters in establishing the functionality and viable cell number within extravascular, highly porous constructs, which correlate well with the results presented in this study.

Future work is focused on characterizing the efficacy of these agarose disk-shaped implants for restoring normoglycemia in diabetic rodent models. The data collected in this study will provide guidelines for the implantation study, such as appropriate cell loadings, construct architecture and expected secretion levels.

6.6. APPENDIX

6.6.1. Modeling one-dimensional solute diffusion through slab.

Figure 26 illustrates the experimental set up used to measure effective diffusivities.

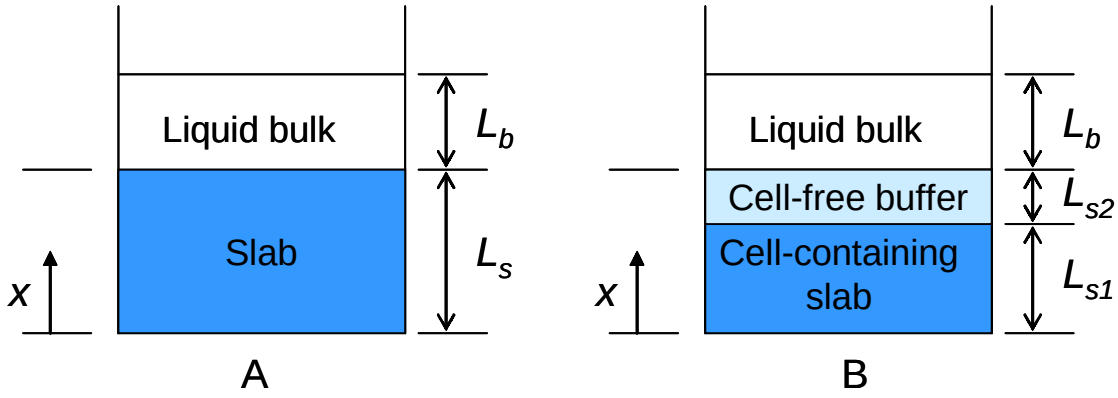

Figure 26. Diagram of experimental setup used for diffusivity experiments for single agarose (A) and buffered agarose (B) disk constructs.

Assuming constant physical properties, transport in the slab by diffusion alone in the axial direction *x*, and an initially homogeneous solute distribution in the slab, the equation describing the system is [142]:

$$\frac{\partial C}{\partial t} = D\frac{\partial^2 C}{\partial x^2} \tag{4}$$

with initial condition: $C(0 \le x \le L, t = 0) = C_o$ (5)

and boundary conditions: $C(x = L_s, t) = C_s(t)$ (6)

and $\frac{\partial C}{\partial x}(x = 0, t) = 0$ (7)

where, *C(x,t)* solute concentration in the agarose slab at axial position x and time t; *D* effective diffusivity of solute through agarose slab; L_s thickness of slab, which is equal to

L_{s1} + L_{s2} for the buffered agarose experiments; C_o initial concentration of solute in agarose slab; C_s concentration of solute at the surface of the slab.

If the slab is exposed to a well-mixed bath, and assuming no boundary effects at the interface, the concentration of solute in the slab at the surface (C_s) is related to the bulk concentration (C_b) as follows: $C_s = KC_b$ (8)

where K is the partition coefficient between the bulk solution and the slab. Since the agarose slab is mostly water, K was assumed equal to 1 (also verified in experimental methods).

Invoking the mass balance equation between the slab and the solution, one obtains:

$$V_b \frac{\partial C_b}{\partial t} = AD \frac{\partial C}{\partial x}\bigg|_{x=Ls} \tag{9}$$

where V_b is the volume of bulk solution and A the cross-sectional area of both the solution and the slab. Thus:

$$V_b = L_b A$$

where L_b is the height of the bulk solution. Equation (9) then becomes:

$$L_b \frac{\partial C_b}{\partial t} = D \frac{\partial C}{\partial x}\bigg|_{x=L_s} \tag{10}$$

In the experiments of this study, the solution was initially free of solute, thus the initial condition is:

$$C_b(t=0) = 0 \tag{11}$$

Equations (4) and (10) with their respective initial and boundary conditions can be solved to calculate the concentration, $C_b(t)$, in solution. The analytical solution for diffusion of solute out of the slab and into the bulk, which is initially free of solute, is [141, 142]:

$$\frac{C_b}{C_o} = \frac{1}{1+\alpha}\left[1 - \sum_{n=1}^{\infty} \frac{2\alpha(1+\alpha)}{1+\alpha+\alpha^2 q_n^2} \exp\left(-\frac{Dq_n^2 t}{L_s^2}\right)\right] \tag{12}$$

where α is the ratio of bulk liquid to slab volume, i.e.

$$\alpha = \frac{L_b A}{L_s A} = \frac{L_b}{L_s} \tag{13}$$

and q_n is the nth root of the equation

$$\tan q_n = \frac{3q_n}{3+\alpha q_n} \tag{14}$$

In all simulations reported in this study, only three terms in the series of equation (12) were needed to accurately solve the equation based on the magnitude of the term Dt/L_s^2. Expressing equation (12) in the form of the concentration of solute C_t in the bulk solution at time t as a fraction of C_∞, the corresponding quantity after infinite time, one obtains:

$$\frac{C_t}{C_\infty} = \left[1 - \sum_{n=1}^{\infty} \frac{2\alpha(1+\alpha)}{1+\alpha+\alpha^2 q_n^2} \exp\left(-\frac{Dq_n^2 t}{L_s^2}\right)\right] \tag{15}$$

where $$C_\infty = \frac{C_o}{(1+\alpha)}$$

6.6.2. Modeling one-dimensional oxygen diffusion and consumption through slab containing βTC3 cells.

Monod kinetics were assumed for the specific rate ν of oxygen and glucose consumption by βTC3 cells [149]:

$$\nu = \frac{\nu_{\max} C}{K_M + C} \tag{16}$$

where C is the solute concentration, v_{max} the maximum specific rate of consumption, and K_M the Michaelis constant in the Monod expression. The equation describing one-dimensional diffusion and consumption is

$$\frac{\partial C}{\partial t} = D_{eff}(\frac{\partial^2 C}{\partial x^2}) + R_A \tag{17}$$

where R_A is the consumption rate per unit volume of construct, or

$$R_A = -N\frac{v_{\max} C}{K_M + C} \tag{18}$$

In the above equation, N (cells/mL) is the density of cells in agarose. The initial and boundary conditions are:

$$C(0 \le x \le L_s, t = 0) = C_o \quad ; \qquad C(x = L_s, t) = C_s(t) \quad ;$$

$$\frac{\partial C}{\partial x}(x = 0, t) = 0$$

At steady state:

$$\frac{\partial^2 C}{\partial x^2} = \frac{N}{D_{eff}}\frac{v_{\max} C}{K_M + C} \tag{19}$$

Modeling simulations were used to identify construct design parameters that resulted in the cells at the center being exposed to oxygen tensions no less than 7 mmHg, or 9.46×10^{-3} mM . Equation (19) was integrated using finite differences as follows.

$$\frac{d^2 C}{dx^2} = \frac{C_{i+1} - 2C_i + C_{i-1}}{\Delta x^2}$$
$$\frac{dC}{dx} = \frac{C_{i+1} - C_{i-1}}{2\Delta x}$$

Applying to equation (19):

$$\frac{(C_{i+1} - 2C_i + C_{i-1})}{\Delta x^2} = \frac{N}{D_{eff}}\frac{v_{\max} C_i}{K_M + C_i}$$

or

$$C_{i+1} = 2C_i - C_{i-1} + \frac{\Delta x^2}{D_{eff}}\left(\frac{Nv_{\max}C_i}{K_M + C_i}\right) \qquad (20)$$

for i = 0,1,….M. At x=0:

$$C_0 = 9.46\text{x}10^{-3}\,\text{mM} \qquad \text{and} \qquad \frac{C_1 - C_{-1}}{2\Delta x} = 0, \text{ or } C_1 = C_{-1}$$

Substituting in (20)

$$C_1 = C_0 + \frac{\Delta x^2}{2D_{eff}}\left(\frac{Nv_{\max}C_0}{K_M + C_0}\right)$$

With C_o known, C_1 could thus be calculated, and equation (20) could then be used to advance the integration towards the surface of the construct.

For buffered agarose constructs, integration from the center to the surface of the inner slab, corresponding to $x=L_{s1}$, was carried out as above. For diffusion in the cell-free buffer zone, equation (19) becomes:

$$\frac{\partial^2 C}{\partial x^2} = 0 \qquad \text{or} \qquad C=A_1 x+A_2$$

where A_1 and A_2 are constants. These constants were calculated from the boundary conditions at the interface:

$$C(x = L_{s1}-) = C(x = L_{s1}+)$$
$$D_{eff}\frac{\partial C}{\partial x}(x = L_{s1}-) = D_{agarose}\frac{\partial C}{\partial x}(x = L_{s1}+)$$

where D_{eff} is the effective oxygen diffusivity through agarose with cells and $D_{agarose}$ is the effective oxygen diffusivity through the pure agarose buffer zones.

CHAPTER 7

7. *IN VIVO* CHARACTERIZATION OF βTC3 CELLS IN AGAROSE DISK CONSTRUCTS AS A BIOARTIFICIAL PANCREAS

7.1. ABSTRACT

This study characterized the *in vivo* efficacy of agarose disk constructs for use as a bioartificial pancreas. Four construct prototypes were examined: (i) an 11 mm in diameter single disk construct comprised of agarose and βTC3 cells; (ii) a 16 mm in diameter buffered disk construct consisting of agarose and βTC3 cells, coated with an additional layer of pure agarose; (iii) a 13 mm in diameter buffered disk construct consisting of agarose and βTC3 cells, coated with an additional layer of pure agarose; and (iv) 0.9 mm in diameter beads comprised of agarose and βTC3 cells. *In vivo* experiments examined construct stability and efficacy in restoring normoglycemia for STZ-induced diabetic mice and were compared against implants of agarose beads. Implantation of agarose constructs resulted in up to 50% reduction in blood glucose levels. Histological studies found the addition of the outer agarose coating to reduce host-mediated cell death; however, mass transport limitations imposed by the addition of the outer coating appeared to be detrimental. The applicability of this research in the development of agarose-based constructs for use as a bioartificial pancreas is discussed.

7.2. INTRODUCTION

Diabetes mellitus is a serious pathological condition involving damaged pancreatic islets, impaired insulin production, and poor glycemic control. Typically, treatment for insulin-dependent diabetics includes blood glucose monitoring and multiple daily insulin injections. The 1993 Diabetes Control and Complications Trial, which found that tight control of glucose levels delays the onset and reduces the intensity of diabetes-related complications, outlined the need for a more physiological control of blood glucose levels beyond what is achieved with bolus insulin injections [12]. While the implantation of human islets has been successful in recent clinical trials [13, 14], the supply of this cell source, of which significant propagation is unavailable, is insufficient to provide islets for any substantial number of insulin-dependent diabetics. Additionally, the life-long immunosuppression required to sustain treatment is problematic, especially for type 1 diabetics.

A tissue engineered pancreatic substitute, consisting of insulin-secreting cells and biocompatible materials, holds significant promise for treating insulin-dependent diabetes through continual regulation of insulin secretion in response to glucose. Use of transformed β cells, such as the continuous β cell lines developed by Efrat et al [23, 138], relaxes the cell availability problem posed by pancreatic islets, while also utilizing cells that have lower oxygenation requirements for insulin secretion [25]. Encapsulation of the implanted cells can partially alleviate the need for immunosuppression.

Development of a pancreatic substitute based on encapsulated insulin-secreting cells requires (i) a thorough construct design accounting for the transport of nutrients and metabolites and their respective consumption and production by the cells; (ii) *in vitro*

characterization of the construct in terms of cell viability and the overall secretion dynamics; and (iii) *in vivo* evaluation of the construct functionality and efficacy. With regard to (iii) in particular, it is useful to be able to monitor the construct noninvasively, by a method such as Nuclear Magnetic Resonance (NMR) spectroscopy or imaging, as this would establish an important link between implantation and end-point physiologic effects in animal experiments [115, 160].

In this paper, we describe the *in vivo* characterization of a pancreatic substitute consisting of mouse insulinoma cells encapsulated in pure agarose. CHAPTER 6 demonstrated that agarose is an appropriate hydrogel for maintaining βTC3 cells over reasonable time periods. Furthermore, the disk-shaped design is advantageous *in vivo*, since it affords ease in implantation and complete retrievability. The *in vivo* efficacy of the construct designs were examined by implantation within diabetic mice. Advantages and shortfalls of the disk-shaped agarose implants, and comparisons to agarose bead implants, are presented.

7.3. MATERIALS AND METHODS

7.3.1. Cell and Cell Culture

βTC3 cells were obtained from the laboratory of Shimon Efrat, Albert Einstein College of Medicine, Bronx, NY. Cells were cultured as monolayers in T-flasks and fed every 2-3 days with fresh medium consisting of Dulbecco's Modified Eagle's Medium (DMEM) with 25 mM glucose and supplemented with 15% horse serum, 2.5% bovine serum, 1% penicillin-streptomycin, and L-glutamine to a final concentration of 6 mM (Sigma, St. Louis, MO). Upon confluency, βTC3 cells were trypsinized using 0.25%

Trypsin with EDTA (Sigma, St. Louis, MO) and either split for propagation or used in construct fabrication (passage numbers 33-48).

7.3.2. Construct Fabrication

Four agarose construct designs were used in this study (Figure 27). One was a single 2% agarose disk with entrapped βTC3 cells and final dimensions of 1.8 mm height and 11 mm diameter (Figure 27A). The second was a buffered agarose disk, consisting of the single cell-containing agarose disk coated with an additional layer of pure 2% agarose, to final dimensions of 3 mm height and 16 mm diameter (Figure 27B). These two constructs were characterized *in vitro* in CHAPTER 6. The third construct consisted of the single cell-containing agarose disk coated with an additional layer of pure 2% agarose, to final dimensions of 3 mm height and 13 mm diameter (Figure 27C). Finally, the fourth construct consisted of agarose beads 0.9 mm in diameter. (Figure 27D).

Agarose (SeaPlaque, low gelling, 1250g/cm2 gel strength) was obtained from Cambrex, NJ. The agarose powder was dissolved in PBS at 2%(w/v) according to the supplier's instructions, and the solution was sterile-filtered through a 0.2-μm filter (Pall, East Hills, NY) while still warm (>40ºC). In the fabrication of each construct type, viable cell counts were performed on the freshly trypsinized βTC3 cell suspension using the trypan blue (Sigma, St. Louis, MO) exclusion method prior to centrifugation. The cell pellet was then suspended in the agarose solution at 37ºC at the cell loading specified for each experiment and evenly mixed using a syringe with a 20G needle.

Disk-shaped constructs were fabricated using methods described extensively in CHAPTER 6. The 13 mm buffered agarose disk constructs were fabricated by identical

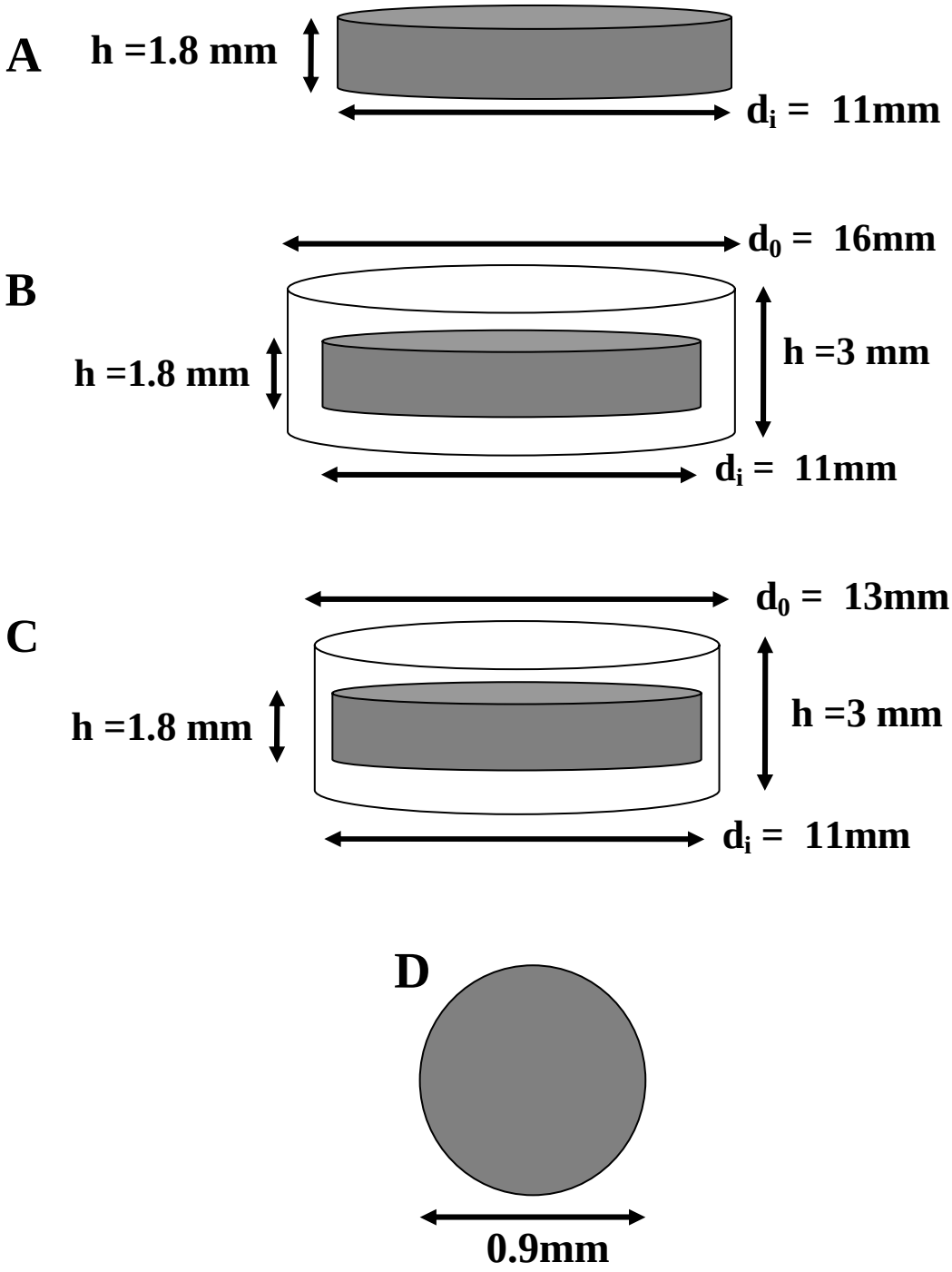

Figure 27. Schematic representation and dimensions of the single agarose disk construct (A), 16 mm buffered agarose disk construct (B), 13 mm buffered agarose disk construct (C), and agarose beads (D). The shaded regions represent βTC3 cells entrapped in 2% agarose, while the white regions indicates pure 2% agarose.

methods as those described in CHAPTER 6, with the exception that the final mold size was 13 mm in diameter and 3 mm in height. Furthermore, agarose beads were also fabricated for use as controls. Freshly trypsinized βTC3 cells at a density of $3.5x10^7$ cells/mL were evenly suspended in sterile-filtered 2% SeaPlaque agarose within a sterile round bottom glass tube and maintained at 37ºC. Sterilized paraffin oil (Sigma) at 37ºC was then gently poured onto the cell agarose solution and the tube was capped. The liquids were emulsified by manual shaking to form the desired size of agarose solution droplets and then immersed in an ice bath for 5 min with gentle agitation to induce gelation of the agarose beads. After the addition of 30 mL of cold Hanks Buffered Saline Solution (HBSS) to the tube, the mixture was centrifuged at 500 rpm for 5 mins. The oil phase was removed by suction and this process was repeated 3 times to thoroughly remove residual oil. A sample of the beads was taken to quantify the bead diameter, which was found to be 0.9 ± 0.23 mm.

After fabrication, each construct type was separately transferred to individual 125 mL spinner flasks containing 35 mL of HBSS. The spinner flasks were then placed on a spinner plate in a humidified 37˚C, 5% CO_2 / 95% air incubator and agitated at 30 rpm awaiting transplantation.

7.3.3. Animal Studies

All animal experiments were approved by the Institutional Animal Care and Use Committee (IACUC) at Emory University. Male C57BL/6J mice of at least 20 grams were obtained from Jackson Laboratories (Bar Harbor, Maine) and used for surgical implantations. Mice were made diabetic through a single IP injection of streptozotocin

(STZ; 200mg/kg body weight). Blood glucose levels were monitored daily via tail clipping and measured using an Elite Glucometer (Bayer, PA). Mice that maintained a blood glucose level above 350 mg/dL for three consecutive days were used for diabetic implantation studies. Control mice (not STZ injected, nondiabetic) were used for biomaterial implantation studies.

For implantation, mice were sedated using an IP injection of ketamine/xylazine (150/15 mg/kg body weight) and one agarose construct was implanted within the peritoneal cavity via a 2 cm midline celiotomy. For biomaterial implantation studies, cell-free buffered disk constructs were implanted into normal C57BL/6J mice to assess the host response and mechanical stability. Explantation of the constructs was performed on Days 2, 5, 8, 15, and 30. For studies using STZ-injected diabetic mice, all four construct forms were tested: (i) single agarose disks, (ii) 16 mm buffered agarose disks, (iii) 13 mm buffered agarose disks, and (iv) agarose microbeads. Single agarose disks were tested using an initial cell loading of $7x10^6$ (n=20). Buffered agarose disks of 16 mm in diameter were tested at initial cell loadings of $7x10^6$ (n=20) and $3x10^6$ (n=3) cells, while 13 mm buffered agarose disks were tested using an initial cell loading of $7x10^6$ cells (n=9). For agarose microbeads, 0.2 mL of beads at a cell density of $3.5x10^7$ cell/mL were loaded into the peritoneal cavity, resulting in a total of $7x10^6$ cells implanted (n=3). Mice were euthanized using CO_2 asphyxiation either on Day 5 or 6. Agarose disk constructs were explanted using forceps, while agarose beads were retrieved using a series of saline lavages. All explants were set aside for histological examination.

7.3.4. Analytical Techniques

Blood glucose samples were collected via tail clipping and measured using a calibrated Elite Glucometer (Bayer, PA). Samples designated for histology were fixed in 3% glutaraldehyde for 48 hrs and then prepared for paraffin embedding and sectioning. After sectioning into 5μm samples, the slides were stained with hematoxylin/eosin (H/E).

7.3.5. Statistical Analysis

All measurements are presented as the mean ± SD. All statistical analyses were performed using a two-sample t-test. Results were considered significantly different when *p*-values were less than 0.05.

7.4. RESULTS

All agarose implants were easily explanted from the peritoneal cavity and found to maintain their structural integrity at all time points examined. Representative histological images of constructs upon explantation after 5 days *in vivo* are shown in Figure 28. Histological images of single agarose disk constructs (Fig 28A) showed significant βTC3 cell death near the outer edges of the construct. Examining histological cross-sections, the thickness of this region was found to be 0.77 mm ± 0.41 mm, although histological processing may have altered the actual size of these regions. This pattern of cell death at the periphery was not observed for single agarose disks maintained *in vitro*. Figure 28B illustrates a typical histological cross-section of a 16 mm buffered agarose disk construct. As was seen *in vitro*, the implanted cells retained a high viability primarily at the periphery of the cell-containing region, with the majority of cell death located at the inner

regions of the construct. For the 13 mm buffered agarose disk construct (Figure 28C), a majority of the viable cells were located at the periphery of the construct, thereby exhibiting a similar H/E staining pattern as that seen for the 16 mm buffered agarose disk constructs. The H/E images of the agarose beads (Figure 28D), however, showed significant cell death, where only a small fraction of the cells within the beads are viable.

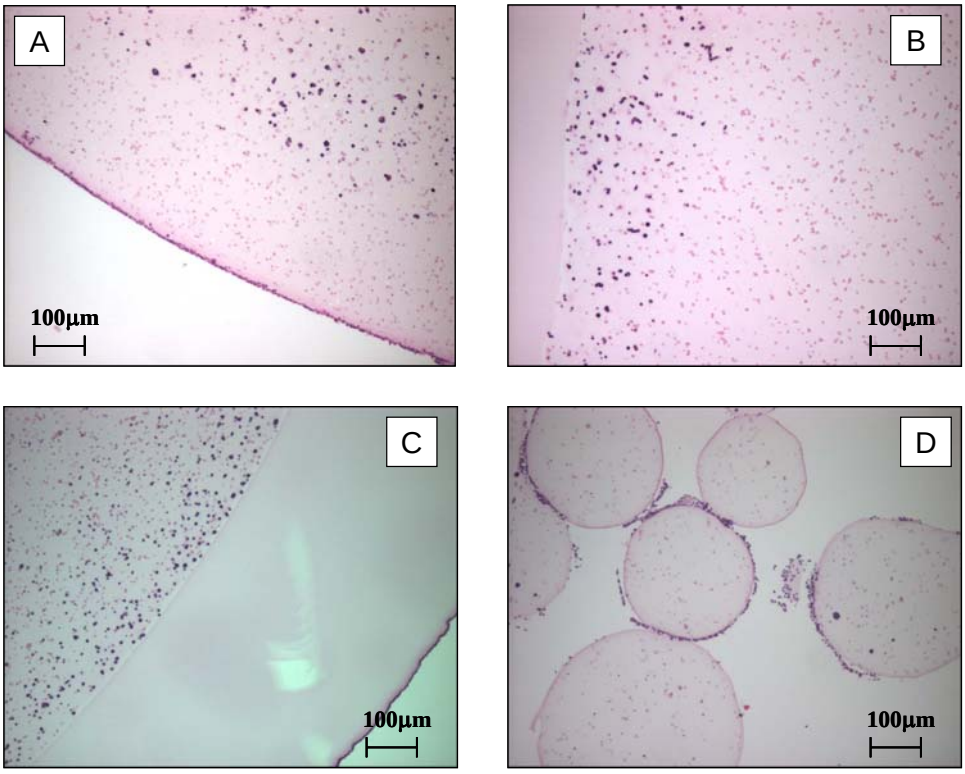

Figure 28. H/E stained histological cross-sections of explanted constructs after 5 days *in vivo* showing cellular remodeling for a single agarose disk construct (A), a 16 mm buffered agarose disk construct (B), a 13 mm buffered agarose disk construct (C), and agarose beads (D).

For some portions of the 13 mm buffered agarose disk constructs, cell death was observed at the outer periphery of the cell-containing region of the construct. Figure 29 shows histological images collected from the same 13 mm buffered agarose construct,

where some portions exhibited peripheral cell death. The region of cell death seen at the outer edges of the cell-containing regions of the 13 mm buffered agarose constructs was much smaller than that found for the single agarose disk constructs.

Representative histological images of the host response to the implants are shown in Figure 30 (A, B and C). The host response to cell-free constructs was moderate, with a maximum thickness of approximately 2-3 cells. In some rare cases, a stronger inflammatory response was visualized, but this aberration appeared sporadically and was unrelated to the implantation time period. The host's response to agarose implants containing βTC3 cells are shown in Figures 30 B and C. For the agarose constructs, the host response was similar to that seen in the cell-free implants, for the implantation times examined in this study (6 days). In all cases, the host cells were relegated to the periphery of the agarose material and did not penetrate into the gel.

The efficacy of the agarose implants containing $7x10^6$ cells in restoring normoglycemia for STZ-induced diabetic C57BL/6J mice is shown in Figure 31. Since the blood glucose levels of the diabetic mice prior to implantation was highly variable, data is represented as the percent decrease in blood glucose level following implantation to allow for the averaging of the data among mice that received identical implants. Percent decrease was calculated by $\frac{BG_t - BG_0}{BG_0} \times 100$ where BG_0 is the blood glucose value at Day 0 and BG_t is the blood glucose at time, t. Figure 31 shows the percent decrease in blood glucose levels of the diabetic mice following implantation of either a single agarose disk (solid triangles), 16 mm buffered agarose disk (solid diamonds), 13 mm buffered agarose disk (solid squares), or 0.9 mm agarose beads (open diamonds), all with an initial cell loading of $7x10^6$ cells. Temporal changes were compared to controls

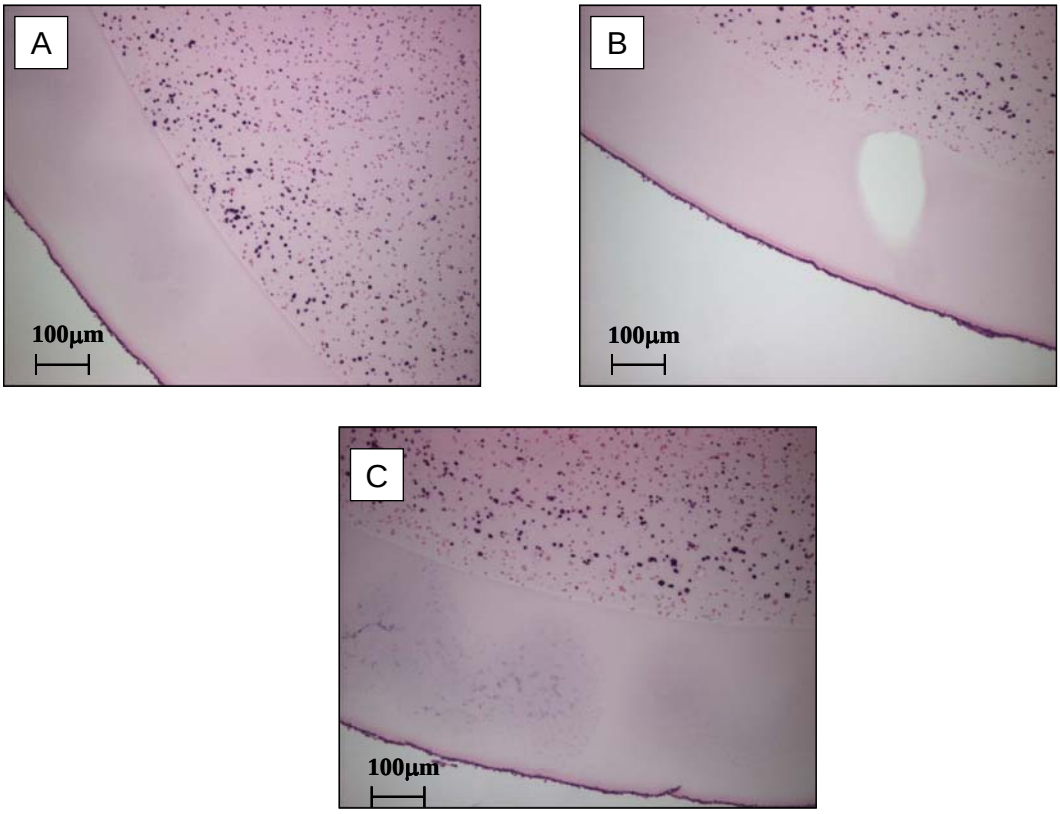

Figure 29. H/E stained histological cross-sections of a 13 mm buffered agarose disk construct explanted after 5 days *in vivo*. Panels (A-C) represent different regions of the same construct.

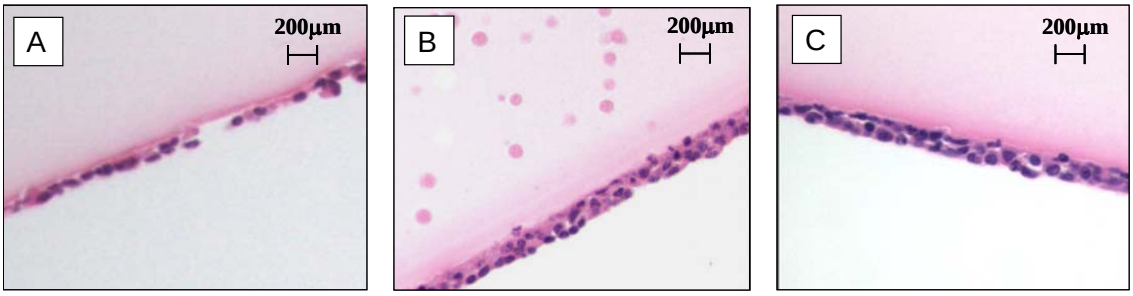

Figure 30. H/E stained histological cross-sections of explanted constructs after 5 days *in vivo* showing interface between host and implant for (A) cell-free agarose constructs, (B) cell-containing single agarose disk constructs, and (C) cell-containing buffered agarose disk construct.

of cell-free buffered agarose disk implants (open squares). Compared to cell-free controls, statistically significant improvement in blood glucose levels was seen for all time points in the 16 mm buffered agarose disk implants, and up to day 3 for the single agarose disk, 13 mm buffered agarose disk, and agarose bead implants. While the data exhibit a general trend that 16 mm buffered agarose implants resulted in lower blood glucose levels than the single agarose and 13 mm agarose disk implants, only the 16 mm buffered and single agarose disk implants were statistically different on Day 1. While the implants were effective in reducing blood glucose levels, normoglycemia (70-150 mg/dL blood glucose) was only transiently attained for approximately 3 days in 10% of the mice studied (n=55). In a similar experiment reported in Figure 32, buffered agarose disk implants of 16 mm in diameter initially loaded with $3x10^6$ cells were found to result in only moderate decreases in blood glucose levels during the entire implantation time period. Figure 33 compares the percent change in blood glucose for STZ-induced diabetic C57BL/6J mice receiving either agarose or alginate/poly-L-lysine/alginate (APA) beads of identical cell loading (see APPENDIX A2), where the % blood glucose change achieved by APA beads was significantly higher than the agarose beads for all time points.

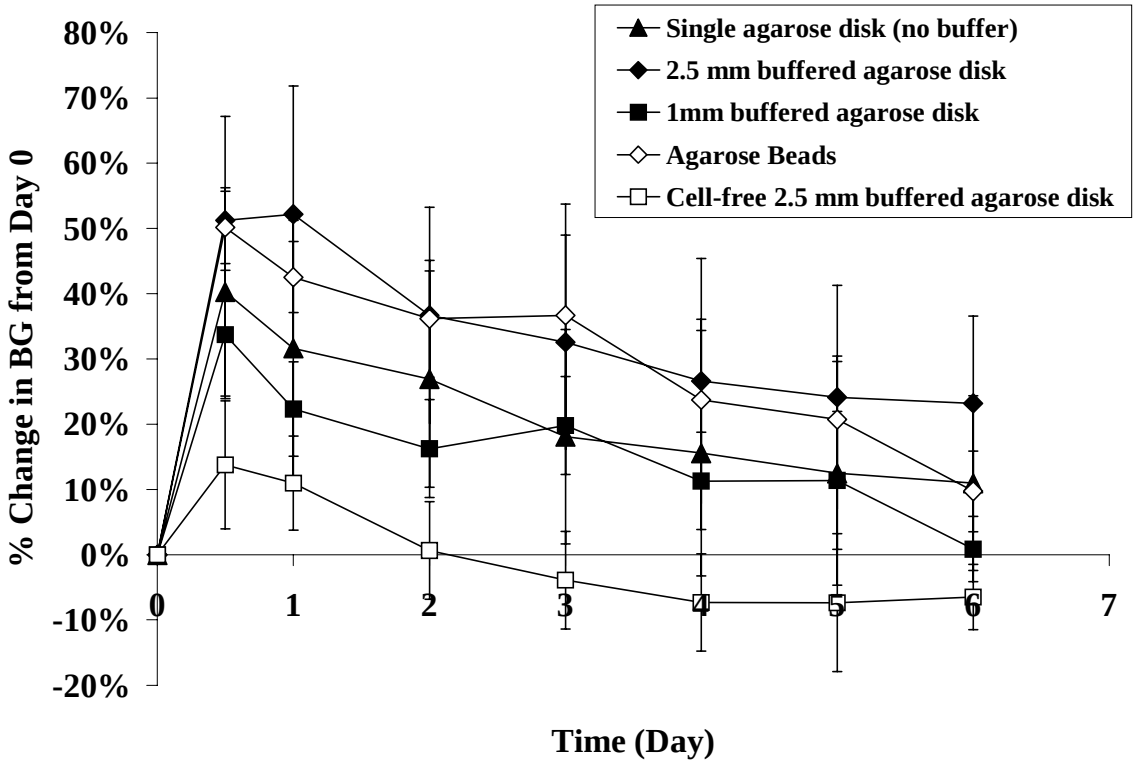

Figure 31. Percent decrease in blood glucose levels of the diabetic mice following implantation of either a single agarose disk (solid triangles), 16 mm buffered agarose disk (solid diamonds), 13 mm buffered agarose disk (solid squares), or 0.9 mm agarose beads (open diamonds), all with an initial cell loading of $7x10^6$ cells. Implants were compared to controls of cell-free buffered agarose disks (open squares).

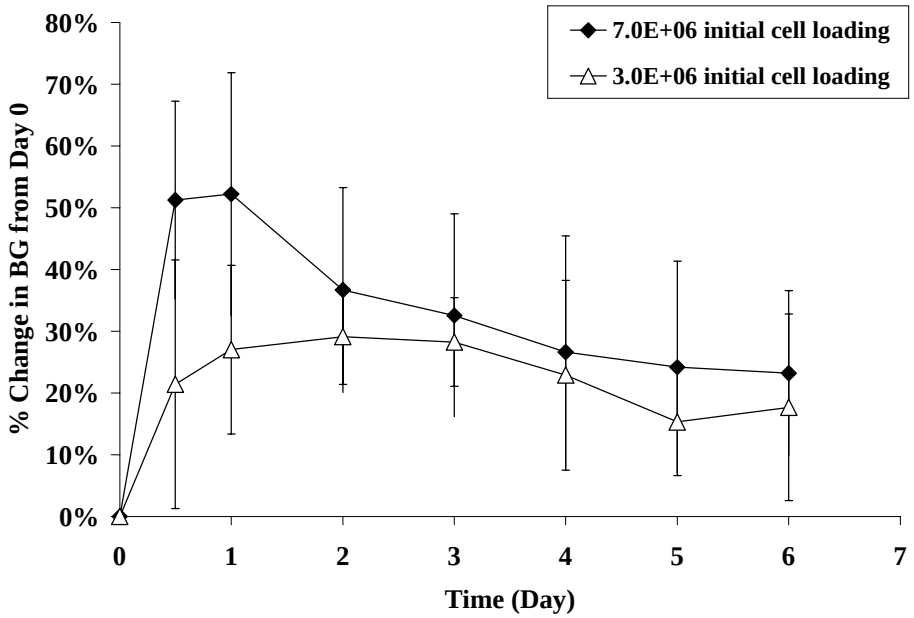

Figure 32. Percent decrease in blood glucose levels of the diabetic mice following implantation of either a 16 mm buffered agarose disk with an initial cell loading of $7x10^6$ (solid diamonds) or $3x10^6$ (open diamonds) cells.

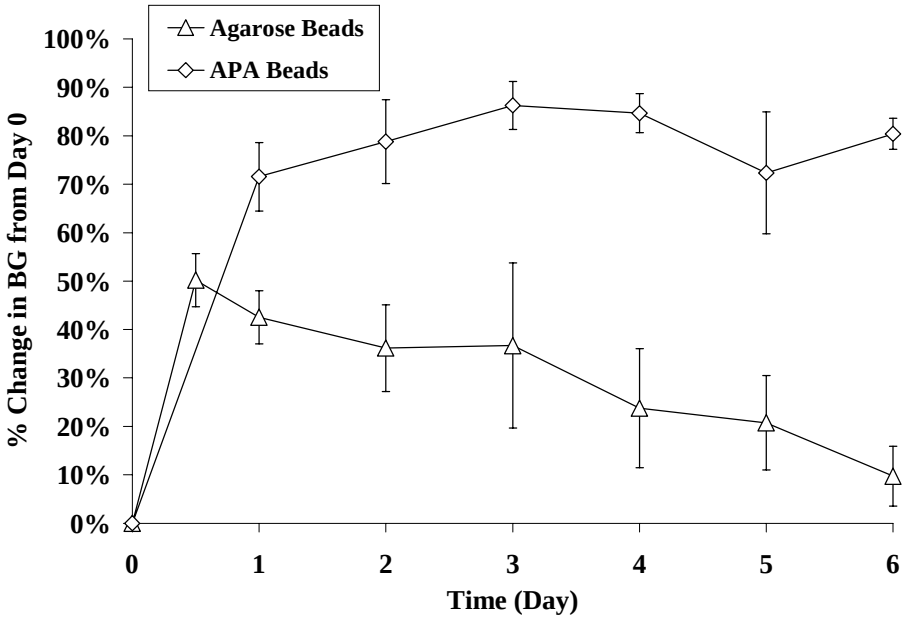

Figure 33. Percent decrease in blood glucose levels of diabetic mice following implantation of 0.2mL of either agarose or alginate/poly-L-lysine/alginate (APA) beads at a cell density of $3.5x10^7$ cells/mL.

7.5. DISCUSSION

This study focused on the *in vivo* characterization of agarose constructs containing βTC3 cells as a pancreatic substitute. *In vivo* experiments of cell-free agarose constructs found the constructs to be well tolerated by the host and elicit minimal fibrotic responses, while maintaining their structural integrity for one month *in vivo*. Observed histological results found a comparable fibrotic response in both the cell-containing and cell-free implants, over the one-week time period studied. The effect of implantation on cell viability for the single agarose disks and the agarose beads, however, was unexpected. While *in vitro* studies found the single agarose disks to exhibit high levels of viable cells at the periphery of the construct (see CHAPTER 6), *in vivo* studies revealed significant cell death at the periphery of the agarose implant. While a similar host response was found on all implants, this pattern of cell death was not observed for the 16 mm buffered agarose disk implants. Furthermore, only a small region of cell death at the periphery in the 13 mm buffered agarose constructs was observed at a sporadic portions of some constructs. Therefore, it is postulated that addition of the outer agarose layer reduces host-mediated cell death at the periphery by: (i) preventing direct cell-host contact, which could activate the direct antigen presentation pathway, thereby resulting in peripheral cell death; and/or (ii) creating a transport distance between the implanted cells and the host cells large enough to prohibit the toxic accumulation of soluble host factors, such as cytokines, superoxide radicals, or hydrolytic enzymes, into the cell-containing region of the construct and/or reduce the shedding of graft protein or peptide antigens, which would activate the host immune system via the indirect antigen presentation pathway.

Literature supports both theories. For (i), it is widely documented that inadequate encapsulation of cells within biomaterials leads to activation of the host immune response, which can lead to cell death within the implant. Direct interactions between the graft and host cells activate host $CD8^+$ T cells via the direct antigen presentation pathway, leading to damage of the graft cells [161]. De Vos *et al* have linked the failure of APA bead implants to restore normoglycemia in diabetic rodents to inadequate encapsulation of the islets [127, 162], while Iwata *et al* have also obtained similar results using agarose beads and allogeneic islets [57, 163]. Therefore, direct cell to cell contact between the host and the βTC3 cells could be the instigating factor that results in the significant cell death observed for both the single agarose disk and agarose bead constructs.

Regarding theory (ii), published reports have also documented that increasing the distance between the implanted cell and the host increases implant efficacy and cell viability, when the support matrix is pure agarose or alginate, a biomaterial with similar mass transport properties [149]. For example, Lanza *et al* documented significant improvement in efficacy and cell viability using pure alginate and xenogeneic islets by simply increasing the bead diameter from 1600 μm to greater than 3700 μm [164], while Jain *et al* achieved long-term efficacy for xenogeneic islets using pure agarose macrobeads 6000-8000 μm in diameter [139, 165]. Since islet loading within the implants was unaltered in these studies, increases in bead diameter resulted in an increase in the distance between the implanted cell and the host. Therefore, these reports support our data, which show that the incorporation of a buffer region between the host and the implanted cells reduces host-mediated cell death.

Published studies further suggest that this buffer region may not be necessary when either the host's immune system is suppressed or immunoprotective barriers are incorporated into the implant. Examples of this include the addition of immunosuppressant agents, such as cyclosporine or 15-deoxyspergualin, [164, 166-168], or the incorporation of immunoprotective materials such as poly(styrene sulfonic acid) into agarose and the addition of outer coatings of polybrene and carboxy methyl cellulose [47, 59, 60], of which both methods were found to increase the efficacy of discordant islets in agarose implants for STZ diabetic rodent models. Published reports using transformed cell lines in pure agarose are limited; however, long-term efficacy has been documented for an allogeneic transformed beta cell line in diabetic rodents after their incorporation between 0.1μm nucleopore membranes and silicon [61]. Studies in our laboratory and by Weber *et al* (unpublished data) have also found success using βTC3 cells when alginate was coated with poly-L-lysine (APA beads), where normoglycemia was attained in STZ-diabetic mice for time periods from two to ten weeks. These reports suggest that the incorporation of an immunoprotective barrier increases the long-term efficacy of implants using xenogeneic or transformed cell lines.

The transient effectiveness of the buffered agarose disk implants, however, is attributed to significant cell death in the inner regions of the construct over time, due to mass transport limitations. As the mathematic models illustrated in CHAPTER 6, the incorporation of the 2.5 mm outer buffer layer imparts mass transfer limitations and is predicted to result in functional cell numbers lower than 1.3×10^6 cells. Separate *in vivo* studies in our laboratory with buffered agarose constructs found significant declines in viable cell number over the first 48 hrs, with a final plateau of approximately 2×10^6 cells

attained by Day 5 (see CHAPTER 10). Results from constructs at cell loadings of $3x10^6$ cells suggest that this number of βTC cells is inadequate to restore normoglycemia.

Future work is focused on characterizing the mechanism of the host-mediated cell death seen in the single agarose disks by eliminating or reducing the immunological response of the host through the use of immunosuppressive agents or immunocompromised mouse models.

CHAPTER 8

8. NONINVASIVE MEASUREMENT OF VIABLE CELL NUMBER IN TISSUE ENGINEERED CONSTRUCTS *IN VITRO* USING ^{1}H NMR SPECTROSCOPY[4]

8.1. ABSTRACT

Noninvasive monitoring of tissue engineered constructs is of critical importance for accurate characterization of constructs and their remodeling *in vitro* and *in vivo*. This study investigated the utility of ^{1}H NMR spectroscopy to noninvasively quantify viable cell number in tissue engineered substitutes *in vitro*. Agarose disk-shaped constructs containing βTC3 cells were employed as the model tissue engineered system. Two construct prototypes containing different initial cell numbers were monitored using localized, water-suppressed ^{1}H NMR spectroscopy over the course of 13 days. ^{1}H NMR measurements of the total-choline resonance at 3.2 ppm were compared with results from the traditional cell viability assay MTT and with insulin secretion rates. Results show a strong linear correlation between total-choline and MTT (R^2 = 0.86), and between total-choline and insulin secretion rate (R^2 = 0.90). Overall, this study found noninvasive measurement of total-choline to be an accurate and nondestructive assay for monitoring viable βTC3 cell numbers in tissue engineered constructs. The applicability of this method to *in vivo* monitoring is also discussed.

---

[4] Modification of paper submitted for peer review, 2004.

8.2. INTRODUCTION

Tissue engineering holds significant promise to provide an alternative or complementary treatment for the millions of people affected annually by tissue and organ loss from accidents, birth defects, and diseases [28]. Tissue engineered substitutes constitute highly dynamic systems, where cells significantly alter the structure, metabolic activity and overall function of the construct over time, while also exhibiting a dynamic interface with the host post-implantation. For the accurate characterization of these constructs, noninvasive monitoring of viable cell number and the dynamics of cellular turnover would be highly useful, particularly for construct development studies, long-term construct growth in bioreactors, and in vivo monitoring applications.

Current methods for assessing viable cell number are typically based on metabolic activity or labeling techniques. Common assays include: (i) mitrochondrial enzyme reduction of a tetrazolium compound, such as MTT [169] and MTS [170] into its respective formazan byproduct; (ii) cellular redox indicators such as Alamar Blue [171]; (iii) ATP quantification through bioluminescence [172]; (iv) S-phase incorporation of BrDU [173]; and (v) co-staining with fluorescent DNA-specific dye for live cells, such as SYTO [174]. Excluding MTS and Alamar blue, use of these assays requires disruption of the construct integrity, and damage to the cells and surrounding matrix. Furthermore, none are directly applicable to *in vivo* monitoring.

This paper explores the use of Nuclear Magnetic Resonance (NMR) spectroscopy to develop an accurate assay for noninvasive quantification of viable cell number in a tissue engineered construct, which would be applicable both *in vitro* and *in vivo*. NMR

spectroscopy noninvasively determines the presence and concentration of specific compounds through their characteristic chemical shift and signal amplitude. Although several nuclei, such as ^{13}C and ^{31}P, can be detected by NMR spectroscopy, the strong sensitivity of the ^{1}H nucleus makes ^{1}H NMR spectroscopy superior in its capacity to monitor subtle changes in the concentrations of highly-mobile, proton-containing compounds, such as phospholipid metabolites [3]. The focus of this study is the resonance at 3.2 ppm. The observed peak is comprised of multiple resonances attributed predominantly to choline-related metabolites such as phosphocholine (PCho), glycerol-3-phosphocholine (GPC), and choline itself (Cho), as well as contributions by phosphoethanolamine, inositol and taurine [3]. This resonance at 3.2 ppm is commonly referred to as "total-choline" (TCho), and this term is used henceforth in this study. Published reports have correlated the area of the TCho peak to cell number, for several cell types [3 , 6]. More specifically, ^{1}H NMR spectroscopy studies monitoring TCho of βTC3 cells encapsulated within alginate/poly-l-lysine/alginate (APA) beads found strong correlations between the relative changes in the TCho peak area and the overall metabolic activity of the culture, as measured by glucose and oxygen consumption rates [7].

This study aims to verify the direct relationship between viable cell number and total choline peak area, while exploring ^{1}H NMR spectroscopy as a means to noninvasively monitor tissue engineered constructs. The system employed consisted of mouse insulinoma βTC3 cells entrapped within a disk-shaped agarose construct, which is used in our laboratory as a model pancreatic tissue substitute. Measurements of the TCho peak area were correlated to results from the established MTT assay, as well as overall

insulin secretion rates. Minimum detection limits of the TCho-based assay and the effects of interfering solutes were also quantified.

8.3. MATERIALS AND METHODS

8.3.1. Cell Culture

βTC3 cells were obtained from the laboratory of Shimon Efrat, Albert Einstein College of Medicine, Bronx, NY. Cells were cultured as monolayers in T-flasks and fed every 2-3 days with fresh medium consisting of Dulbecco's Modified Eagle's Medium (DMEM) with 25 mM glucose and supplemented with 15% horse serum, 2.5% bovine serum, 1% penicillin-streptomycin, and L-glutamine to a final concentration of 6 mM (Sigma, St. Louis, MO). Upon confluency, βTC3 cells were trypsinized using 0.25% Trypsin with EDTA (Sigma, St. Louis, MO) and either split for propagation or used in construct fabrication (passage numbers 33-48).

8.3.2. Construct Fabrication

Two types of agarose constructs were used in this study (Figure 34). One was a single 2% agarose disk with entrapped βTC3 cells and final dimensions of 1.8 mm height and 11 mm diameter (Figure 34A). The other was a buffered agarose disk, consisting of the single cell-containing agarose disk coated with an additional layer of pure 2% agarose, to final dimensions of 3 mm height and 16 mm diameter (Figure 34B). The presence of this buffer layer was found necessary to minimize the contribution of fat deposits on the NMR spectrum acquired from implanted constructs. These *in vivo* studies are reported in CHAPTER 9.

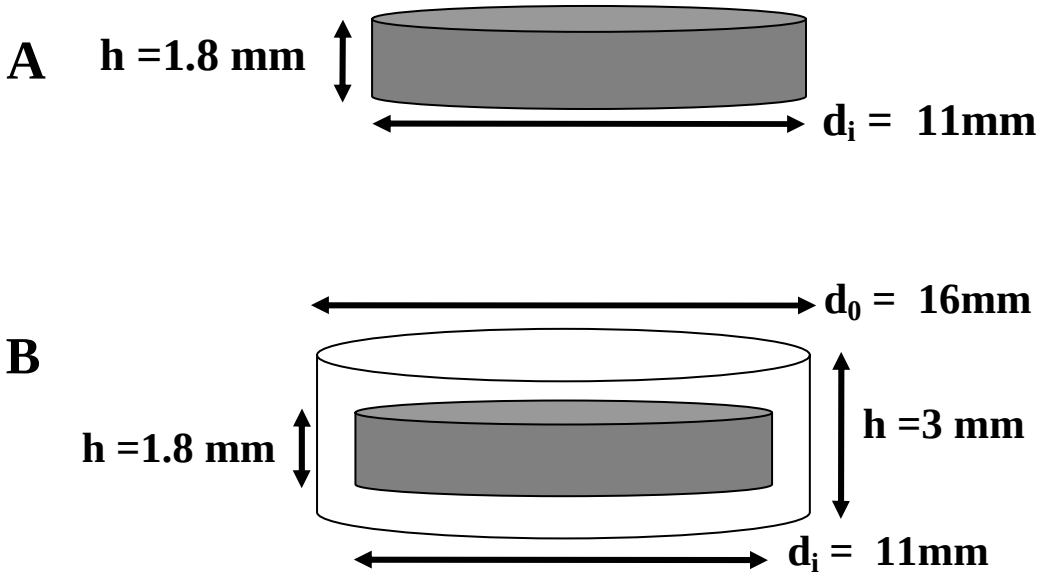

Figure 34. Schematic representation of single agarose disk construct (A) and buffered agarose disk construct (B), with overall dimensions shown. Shaded region represents the entrapped βTC3 cells within 2% agarose, while white region indicates pure 2% agarose.

Agarose (SeaPlaque, low gelling, 1250g/cm2 gel strength) was obtained from Cambrex, NJ. The agarose powder was dissolved in PBS at 2%(w/v) according to the supplier's instructions, and the solution was sterile-filtered through a 0.2-μm filter (Pall, East Hills, NY) while still warm (>40ºC). Viable cell counts were performed on the freshly trypsinized βTC3 cell suspension using the trypan blue (Sigma, St. Louis, MO) exclusion method prior to centrifugation. The cell pellet was then suspended in the agarose solution at 37ºC at the cell loading specified for each experiment and evenly mixed using a syringe with a 20G needle. Pre-sterilized 1.8 mm thick Lexan sheets (McMaster-Carr, Atlanta, GA) with 11 mm diameter holes were fastened to pre-sterilized Lexan bases by H-clamps and used as molds. The molds were filled to capacity with the agarose/cell mixture (0.2 mL in volume) and allowed to cool at room temperature until gelled (~ 3 mins). For single agarose constructs (Figure 34A), the disks were removed

from the molds and placed in fully supplemented DMEM. For buffered agarose constructs (Figure 34B), the cell-containing disks were removed from their molds and placed into larger Lexan molds of 3 mm height and 16 mm diameter, fabricated from 3 mm thick Lexan sheets. These larger molds were partially filled with 2%(w/v) agarose solution prior to placement of the cell-containing disks and then filled to capacity after the inner disk was centrally aligned. Constructs were allowed to solidify at room temperature for 5 min before being placed in fully supplemented DMEM.

8.3.3. *In Vitro* Construct Characterization

For Day 0 calibration studies, constructs of both types were fabricated with varying cell loadings from $20x10^6$ to $1x10^6$ cells. NMR and MTT experiments were performed within 4 hrs post-entrapment on three constructs for each cell loading. For long-term *in vitro* studies, both constructs types containing different initial cell numbers were examined. For single agarose constructs, initial cell loadings were $14x10^6$, $10x10^6$, and $7x10^6$ cells, while buffered agarose constructs were $7x10^6$ and $3x10^6$ cells. For each experiment, twelve identical agarose constructs were fabricated and split into two groups of 6 constructs each. Each group was placed in a 125 mL spinner flask (Wheaton, Millville, NJ) containing 35 mL of fully supplemented DMEM. The spinner flasks were placed on a spinner plate in a humidified 37˚C, 5% CO2 / 95% air incubator and were agitated at 30 rpm. The time duration of each experiment was 13 days. Complete media changes were performed every other day. Samples for insulin assays were collected every 24 hours. NMR and MTT analyses were performed on Days 0, 1, 3, 5, 7, and 13,

where three different constructs were tested by NMR and two constructs by MTT at each time point.

For cell death experiments, both single and buffered agarose disk constructs containing a high cell loading of $14x10^6$ cells were scanned using NMR and then exposed to a 55ºC bath of phosphate buffered saline for 2 min to induce cell death. Following heat exposure, constructs were incubated in glucose- and sera-free DMEM, and NMR spectra from the constructs were collected over the course of 12 hrs.

8.3.4. ^{1}H Magnetic Resonance Imaging and Spectroscopy

NMR imaging and spectroscopy examinations were performed using a Varian/Inova 4.7T horizontal bore magnet operating at 200.56 MHz (Varian, Inc., Palo Alto, CA). The magnet was equipped with an 11.7 cm inner diameter self-shielded gradient system with a maximum gradient strength of 25 gauss/cm. NMR signal was transmitted and received using either a birdcage or a home-built surface coil. The 16-element quadrature birdcage coil had a 3.6 cm inner diameter and a 7 cm length, while the customized surface coil measured 35 mm in length and 24 mm in width and was attached to the outside of a 32 mm diameter polycarbonate tube. For each experiment, the construct was washed three times in the specified bathing medium, placed in a sterile 50 mL centrifuge tube containing 50 mL of the same medium, centered within the coil, and positioned at the magnet's isocenter.

Standard ^{1}H NMR gradient-echo images (TR = 200 ms, TE = 3.5 ms, acquisition time of 51 sec) were acquired to determine the position of the construct, and a single high

resolution spin-echo image (TR = 2 sec, TE = 40 ms, acquisition time of 17 min and 10 sec) was collected to provide a more detailed image of the construct structure.

Localized ^{1}H NMR spectra were acquired from a 2 mm thick volume of interest (VOI), centered within the cell-containing region of the construct. Shimming of the water signal was performed on the selected VOI using a localized non-water suppressed PRESS sequence [137]. Water-suppressed spectrum on the same VOI was acquired using three CHESS pulses prior to executing the PRESS localization sequence. The PRESS pulse parameters used for all of the experiments were TR equal to 3 sec and a total TE, defined as $2t_1 + 2t_2$ (t_1 = 12.5 ms, t_2 = 33 ms), of 91 ms. At the TR time selected, the magnetization was completely relaxed. The TE time, selected to reduce the glucose signal intensity, was found to result in minimal (~5%) changes in TCho, when compared to the shortest echo time allowable by the sequence. All localized, water-suppressed ^{1}H NMR spectra were the average of 256 acquisitions, collected at a constant receiver gain using real-time digital signal processing. The total time required to collect each water-suppressed spectrum was 12 min 56 sec. Spectral data were processed using the frequency domain analysis package supplied in VNMR from Varian. Time domain data were apodized with an exponential line broadening of 3 Hz, Fourier transformed, with the residual water signal removed by digital filtering, and the baseline corrected where necessary. A Lorentzian function was fitted to the resulting TCho peak at 3.2 ppm using manufacturer-provided software to determine the area under the peak.

8.3.5. Analytical Techniques

To measure the viable cell number in a construct using the CellTiter 96 MTT (3-(4,5-dimethylthiazol-2-yl)-2,5-diphenyl-tetrazolium bromide) assay (Promega, Madison, WI), the construct was cut into four equal segments. Three of the segments were incubated in separate wells of a 12-well plate (Corning, Acton, MA), each containing 3 mL of fully supplemented DMEM and 450 μL of MTT, for 4 hrs at 37°C, 5% CO_2/95% air. Following incubation, each construct segment was placed in a mortar, ground using a pestle, and returned to its original well. Two milliliters of Solubilization/Stop solution was added to each well and the plate was sealed and placed within a humidified 37°C, 5% CO_2/95% air incubator for 24 hrs to fully dissolve the formazan crystals. A volume of 120 μL of the final solution in each well was then transferred to a 96 well plate, and the absorbance was read at 595 nm. Absorbance values read from the three segments were then numerically averaged. Insulin samples were analyzed using an ultra-sensitive mouse insulin EIA kit (ALPCO, Windham, NH) following the manufacturer's protocol.

8.3.6. Statistical Analysis

All measurements are presented as the mean ± SD. All statistical analyses were performed using a two-sample t-test. Results were considered significantly different when p-values were less than 0.05.

8.4. RESULTS

Typical ^{1}H NMR images of a buffered agarose construct containing βTC3 cells, obtained using the RF surface coil, are shown in Figure 35. Figure 35A shows a spin-

echo image of a sagittal (parallel to the axis of the magnet bore) view of the construct. The construct is positioned at the center of the excitation field of the coil. Figure 35B is a spin-echo image of a coronal view through the planar center of the same agarose construct. The boundary between the inner cell-containing agarose disk and the outer agarose layer is easily discernable, allowing for accurate central placement of the VOI in the cell-containing agarose disk, as indicated by the white square.

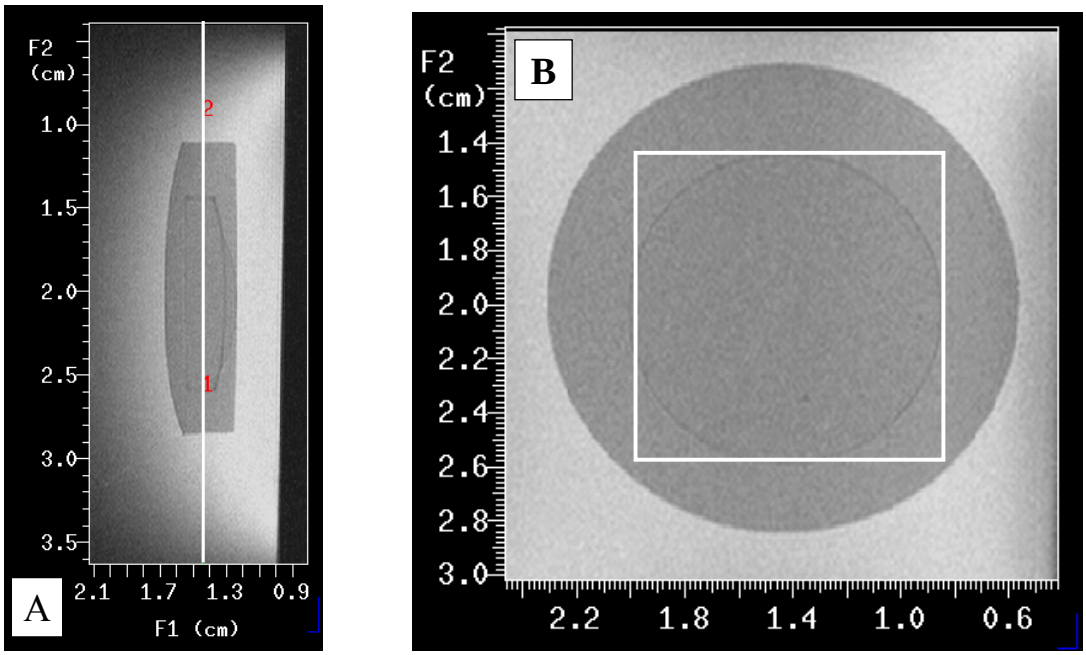

Figure 35. Sagittal (A) and coronal (B) spin-echo ^{1}H NMR images of a buffered agarose disk construct. The white square shown in the coronal image is the VOI used to collect the localized ^{1}H NMR spectrum from the inner cell-containing disk.

Figure 36 shows localized, water-suppressed ^{1}H NMR spectra of a buffered agarose disk construct containing $14x10^{6}$ βTC3 cells, equilibrated in media containing varying levels of glucose. All spectra were acquired using a home-built surface coil and are displayed at the same vertical scale. Each spectrum represents the average of 256

acquisitions with an exponential line broadening of 3 Hz. The assignments of ^{1}H NMR resonances are indicated accordingly. Figure 36A is the spectrum for the construct in sera- and glucose-free DMEM. The dominant resonance at 3.2 ppm is assigned to TCho. Figures 36B and 36C are spectra derived from the same construct, but bathed in sera-free DMEM containing 150 mg/dL and 250 mg/dL glucose, respectively. The collection of resonances downfield of the TCho resonance, ranging from 3.85 to 3.22 ppm, is attributed to glucose. Note the increase in the intensity and linewidth of the TCho peak with increasing concentrations of glucose in the bathing medium. The interference of glucose in accurately quantifying the TCho area was alleviated by using one of the following two approaches: (i) removing glucose by rinsing and incubating the construct in glucose and sera-free medium immediately prior to and during spectrum acquisition; or (ii) correcting for the glucose interference post-acquisition. To establish the feasibility of using TCho to measure viable cell number in the constructs, the first option was implemented. A method to correct for the contribution of glucose to the TCho area was also developed and is described later in this article. Unless explicitly stated otherwise, ^{1}H NMR spectra were acquired from constructs in glucose- and sera-free media, and thus no glucose correction was implemented.

Figure 37 illustrates the correlation between TCho, measured by ^{1}H NMR spectroscopy shortly after construct preparation, and viable cell number, measured by Trypan Blue in the cell suspension prior to entrapment. Data were collected using both types of constructs and grouped by the RF coil used to collect the NMR signal. The data show that the TCho peak area is directly proportional to the number of viable βTC3 cells within the VOI of the agarose constructs for either RF coil design. In comparison with

the birdcage coil, the surface coil increased the sensitivity of the TCho measurement three-fold, with a minimum quantifiable TCho signal at $1x10^6$ cells. Thus, the surface coil was used to collect all ^1H NMR spectra for the subsequent experiments, and the standard curve shown for the surface coil in Figure 37 was used to interpolate the measured TCho peak area to viable cell number.

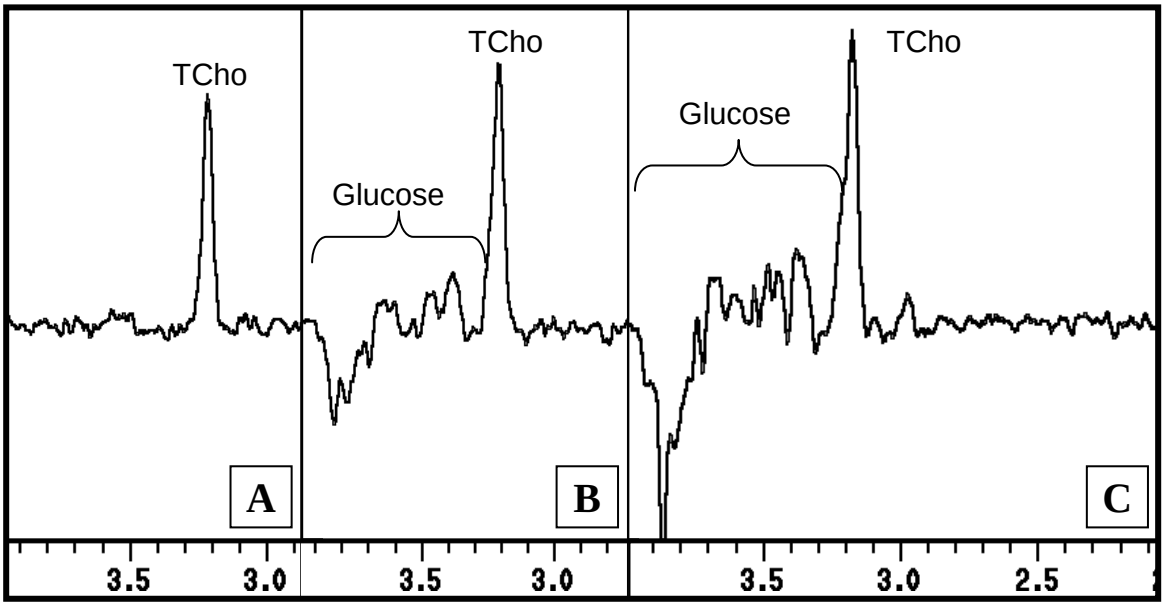

Figure 36. Water-suppressed, localized ^1H NMR spectrum of $14x10^6$ βTC3 cells in a buffered agarose disk construct equilibrated in glucose and sera-free DMEM (A), 150mg/dL glucose and sera-free DMEM (B), and 250mg/dL glucose and sera-free DMEM (C).

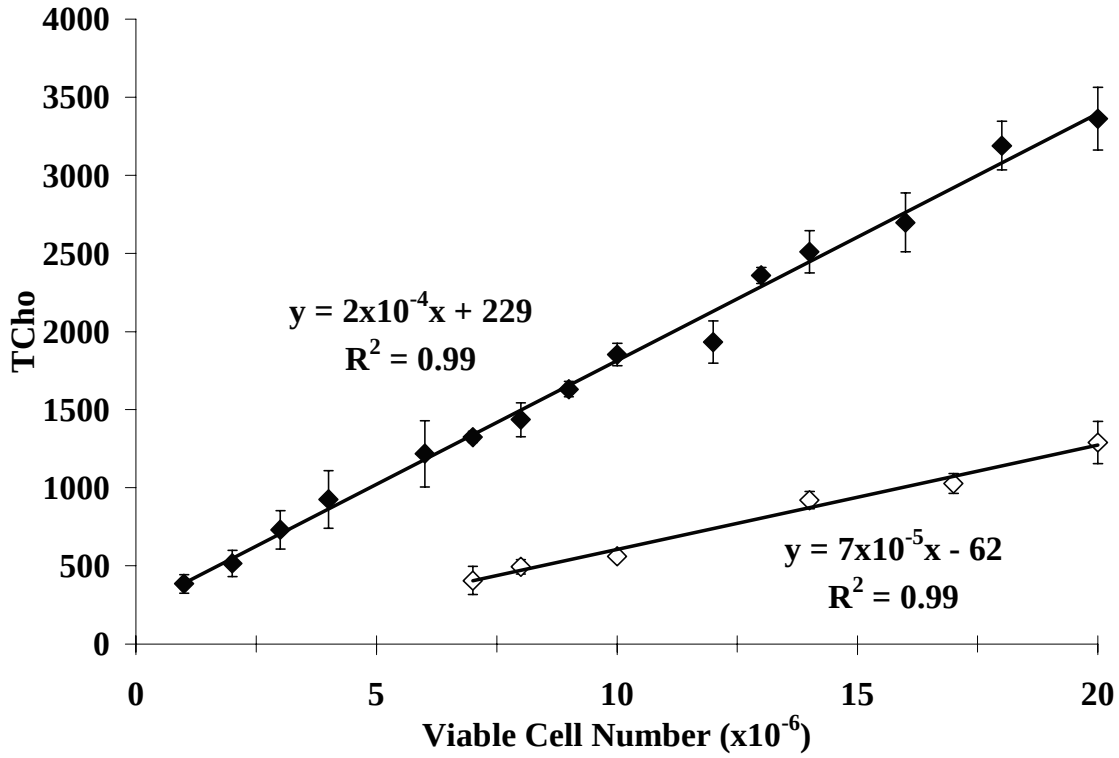

Figure 37. Correlation between viable cell numbers and TCho peak areas for βTC3 cells in agarose constructs. NMR measurements were collected using either the surface coil (filled diamonds) or birdcage coil (open diamonds).

In vitro experiments monitored the temporal changes in TCho along with MTT absorbance and insulin secretion rate. These experiments were conducted with both types of constructs loaded with different cell numbers. Earlier studies established the range of cell loadings for each construct type that are predicted to result in an increase, decrease, or stabilization of viable cell number (see CHAPTER 6). For the single agarose disk constructs, three different cell loadings were used, where a net decrease ($14x10^6$ cells), no net change ($10x10^6$ cells), and a net increase ($7x10^6$ cells) in viable cell number would be expected over time. For the buffered agarose constructs, two different cell loadings were prepared, where a net decrease ($7x10^6$ cells) and increase ($3x10^6$ cells) in

viable cell number was anticipated. Figure 38 shows the temporal profiles of the TCho–assessed viable cell number for single agarose disk constructs with varying initial cell numbers. Although the three cell loadings are statistically different on Day 0, the viable cell number for all of the constructs stabilizes to the same statistical plateau after approximately 3 days in culture. For the buffered agarose disk constructs, Figure 39 shows the temporal changes in TCho-assessed viable cell number for the two different initial cell loadings. Viable cell numbers in constructs from both initial conditions follow similar patterns and were statistically different only on Days 0 and 5.

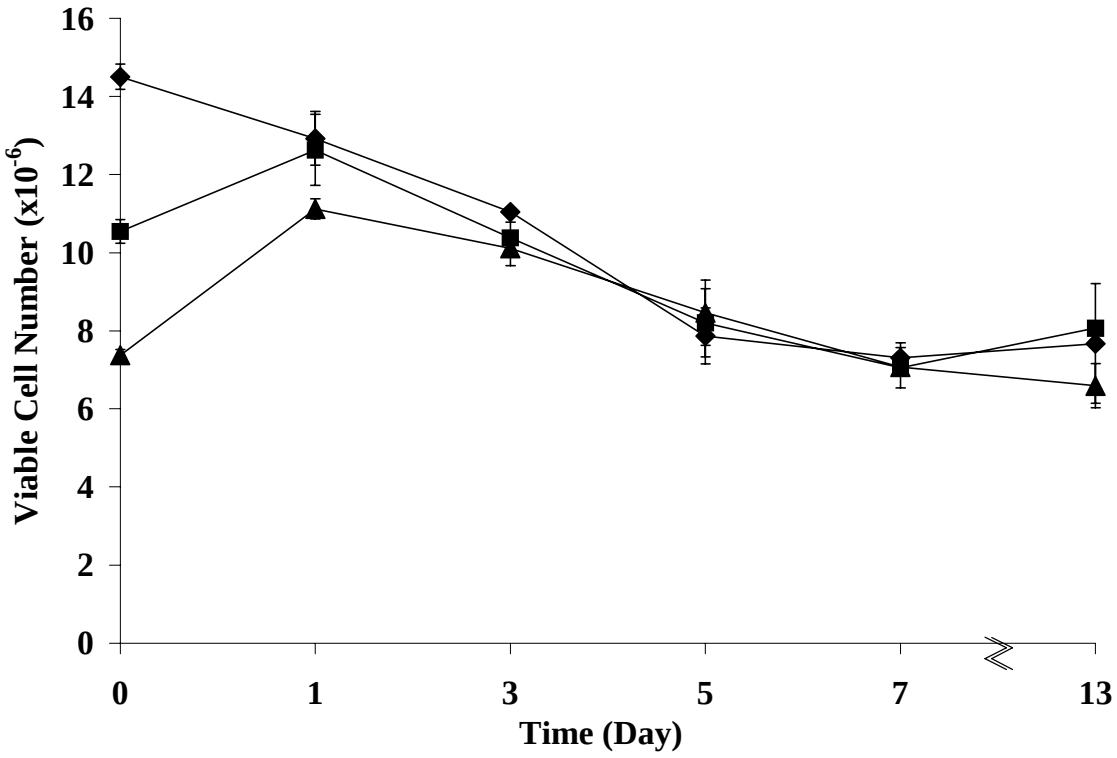

Figure 38. Temporal changes in the TCho-assessed viable cell number for single agarose disk constructs with initial cell loadings of $14x10^6$ cells (diamonds), $10x10^6$ cells (squares), and $7x10^6$ cells (triangles).

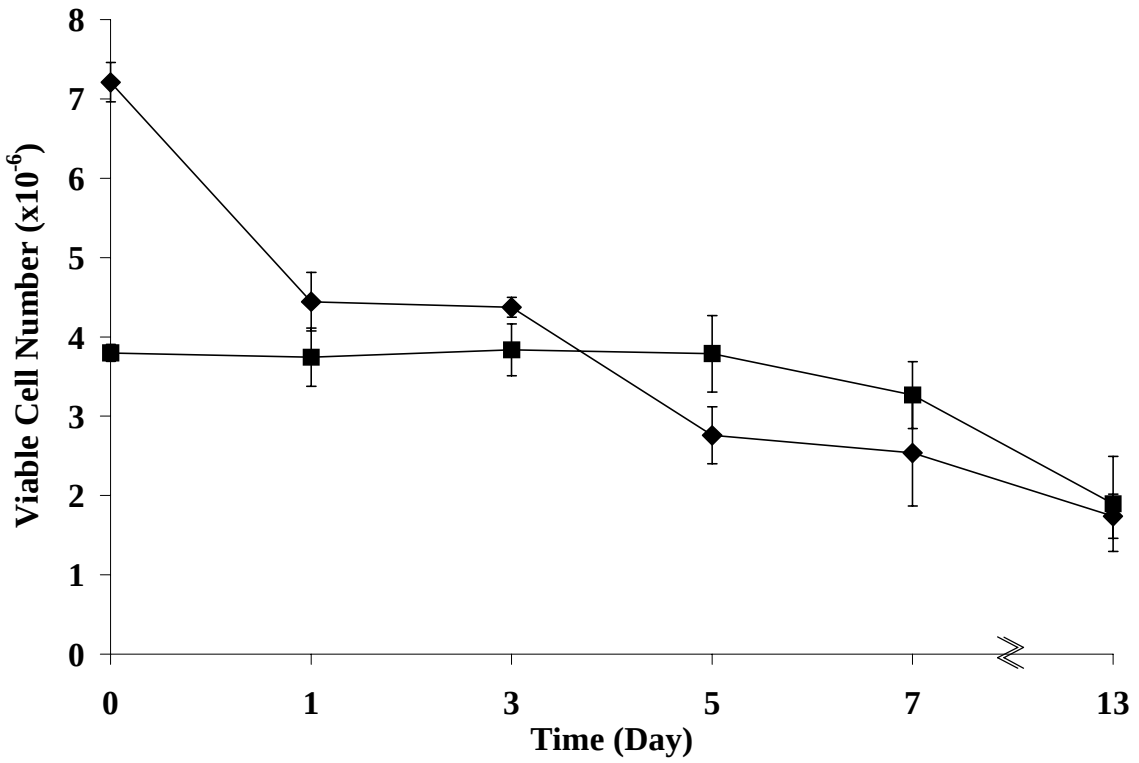

Figure 39. Temporal changes in the TCho-assessed viable cell number for buffered agarose disk constructs with initial cell loadings of $7x10^6$ cells (diamonds) and $3x10^6$ cells (squares).

In order to test if dead cells contribute significantly to the TCho resonance, experiments inducing cell death in both construct types by excessive hyperthermia (55ºC for 2 min) were performed. TCho was monitored in constructs prior to and following lethal hyperthermic treatment of the entrapped cells was monitored over time. Data is shown in Figure 40, where time zero data points were collected prior to hyperthermic episode. For single agarose disk constructs (filled diamonds), TCho dropped by approximately 50% after 30 mins with complete depletion within 5 hrs, while for buffered agarose constructs (filled squares), TCho decreased by roughly 50% after 1 hr and were completely depleted after 10 hrs. Control experiments were also performed

under identical experimental conditions, excluding the hyperthermia episode (open diamonds). A decline of approximately 15% TCho was recorded for all constructs over the course of 12 hrs.

Figure 41 illustrates the strong linear correlation ($R^2 = 0.86$) between the TCho peak area and MTT absorbance. All time points, construct types, and cell loadings tested are included as data points in this figure.

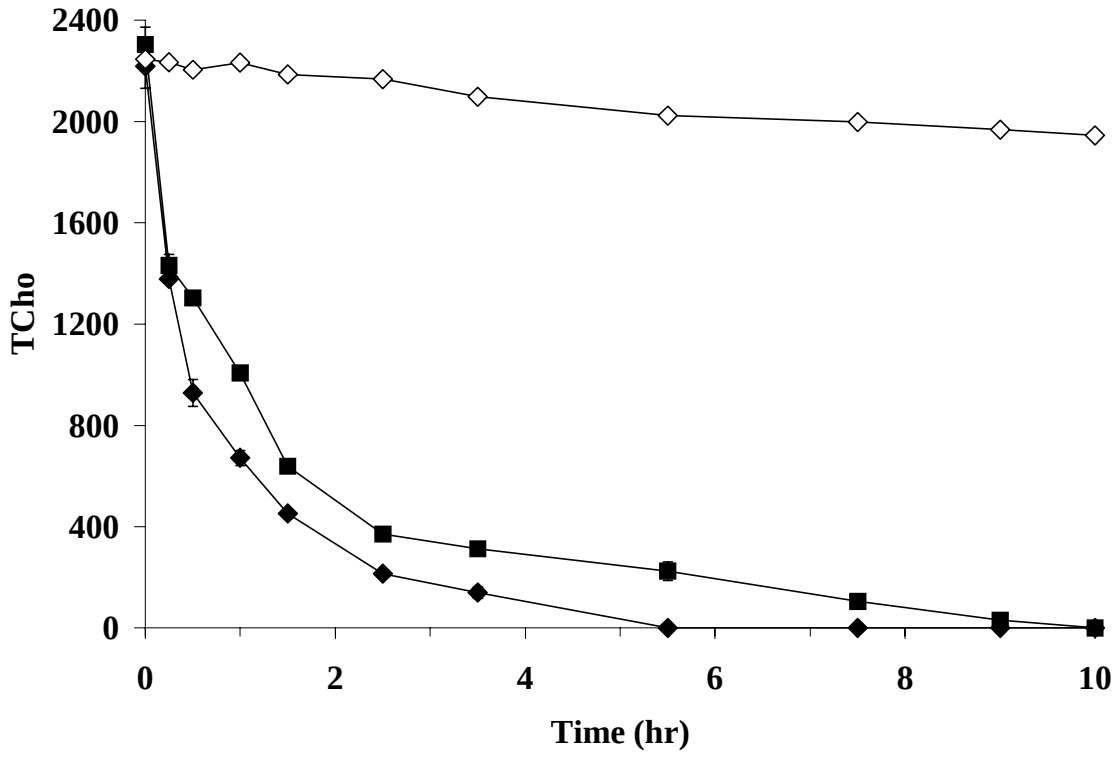

Figure 40. Temporal profile of TCho, measured from the VOI centered in the cell-containing region of the construct, following hyperthermia-induced cell death for single agarose (filled diamonds) and buffered agarose (filled squares) constructs initially containing $14x10^6$ cells. Control is shown by the open diamonds.

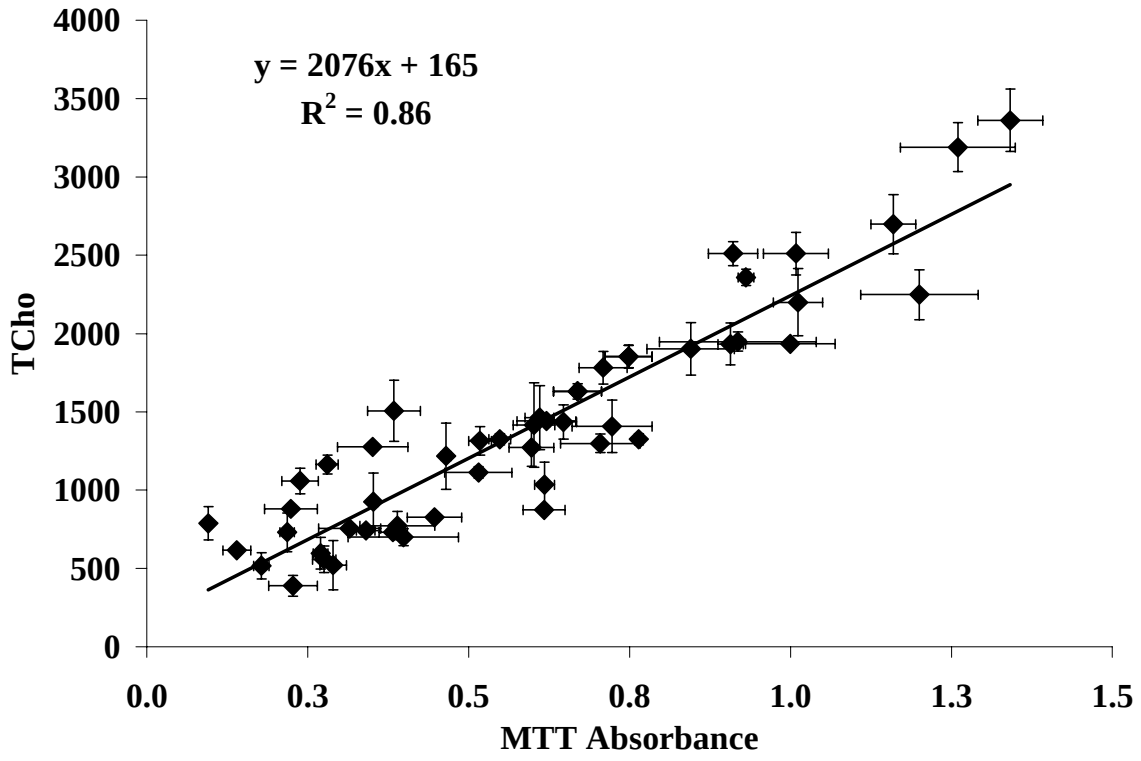

Figure 41. Correlation between MTT assay absorbance values and TCho peak areas for βTC3 cells in agarose constructs for all time points, construct types, and cell densities tested.

Figure 42 shows the correlation between TCho peak areas and their respective insulin secretion rates for the two construct types and five initial cell loadings tested in the in vitro time experiments. The data show a strong linear relationship with a correlation coefficient of 0.90.

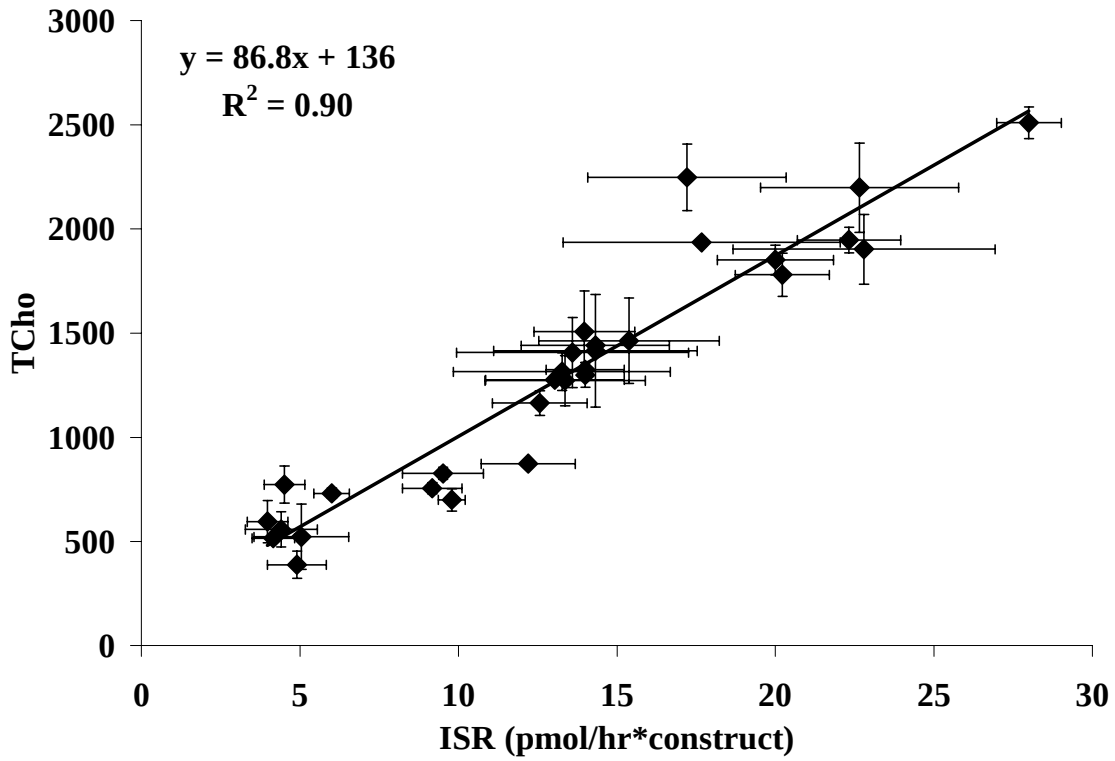

Figure 42. Correlation between Insulin Secretion Rates (ISR) and TCho peak areas for βTC3 cells in agarose constructs for the two construct types and three cell loadings tested in the long-term culture experiments.

To gain a perspective of the levels of TCho present within the βTC3 cells, ^{1}H NMR spectroscopy experiments were performed using cell-free buffered agarose constructs bathed in varying concentrations of choline buffered in saline. Spectra were acquired using the surface coil under the same NMR acquisition parameters employed for the cell-containing construct experiments. Using this method, commonly called a phantom replacement reference [175], the VOI location, coil loading, and surrounding environment within the surface coil is similar to that used to collect the cell-containing construct measurements. Choline concentrations tested were 1.44, 1.0, 0.75, 0.5, and 0.25 mM. The resulting calibration curve is shown in Figure 43. Based on this data,

there is approximately 0.1 mmol of choline per 10^{10} cells, assuming that T_2 and T_1 differences between choline in solution and TCho within cells are negligible.

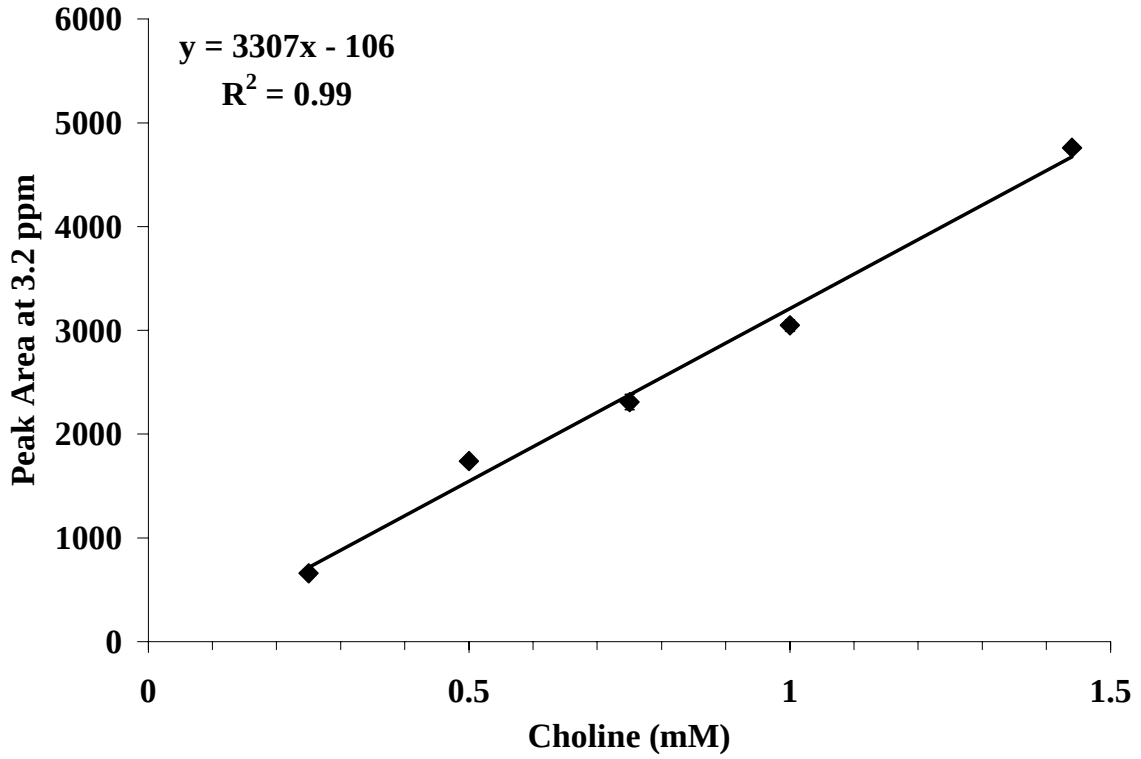

Figure 43. Correlation between choline concentration (mM) and peak area at 3.2 ppm for cell-free agarose constructs equilibrated in varying concentrations of choline buffered in saline.

As illustrated in Figure 36, one of the glucose peaks interferes with TCho at 3.2 ppm, thus resulting in an overestimation of the TCho peak area. For cases where the complete removal of glucose from the VOI is not feasible or desirable, the negative peak of glucose at 3.85 ppm can be used to indirectly determine the glucose contribution to the 3.22 ppm resonance. The strict ratio of the glucose peaks at 3.85 ppm and 3.22 ppm was quantified

by collecting ^{1}H NMR spectra from cell-free agarose constructs equilibrated in DMEM with various concentrations of glucose (for more detail, see APPENDIX A5). Once this ratio was determined, accurate estimation of the 3.22 ppm glucose peak area could be made through the quantification of the 3.85 ppm glucose peak. Therefore, in constructs with cells, the contribution of glucose to the 3.2 ppm peak area can be indirectly quantified and subtracted, allowing for the accurate measurement of TCho. Figure 44 illustrates the use of this technique using buffered agarose constructs containing cell loadings of either $14x10^{6}$ or $7x10^{6}$ cells. Constructs were first placed in medium containing the level of glucose specified and the TCho peak area was quantified and reported before (Figure 44, black bars) and after correcting for the glucose contribution (Figure 44, striped bars). The same constructs were then washed free of glucose, placed in sera- and glucose-free DMEM, and the TCho signal was measured to serve as the control (Figure 44, white bars). While the uncorrected TCho data from constructs containing glucose showed artificially high results, the glucose-corrected TCho values were in agreement with the TCho measurements in the glucose-free environment.

8.5. DISCUSSION

This study establishes the use of ^{1}H NMR-measured TCho as an accurate index for the noninvasive quantification of viable cell number in a model tissue engineered substitute. TCho peak areas strongly correlated with viable βTC3 cell numbers in the VOI of agarose constructs over a wide range, from $1x10^{6}$ to more than $20x10^{6}$ viable

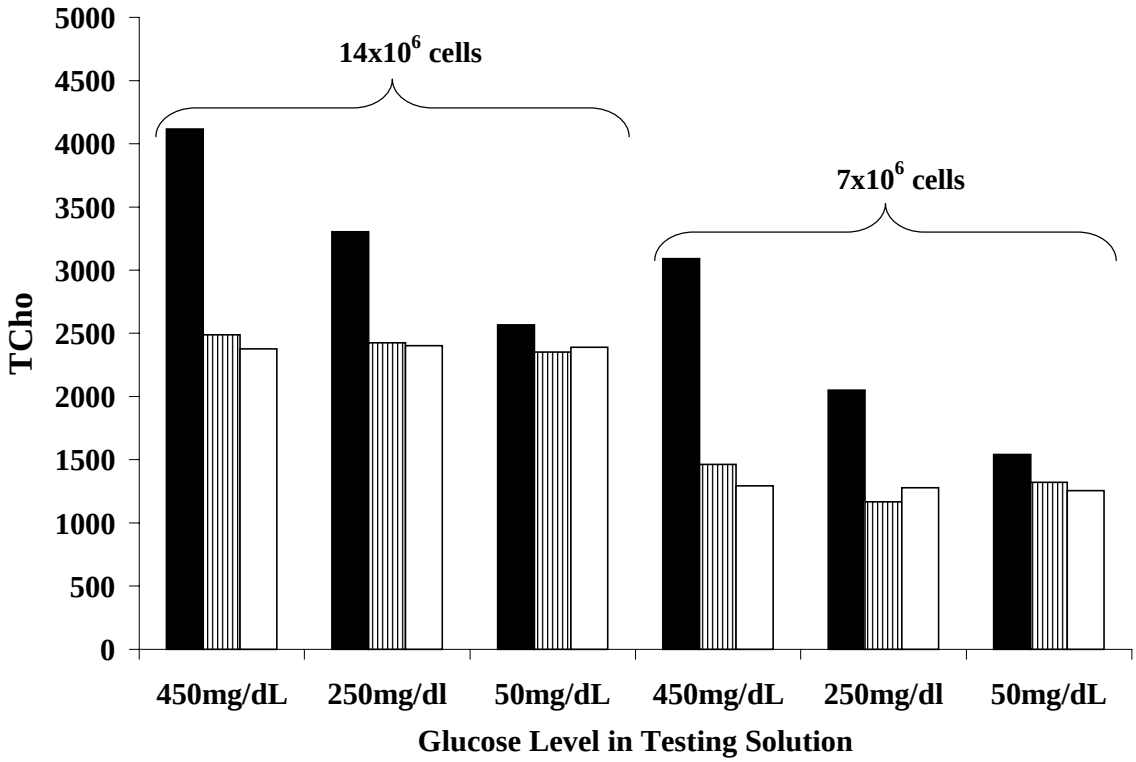

Figure 44. TCho measurement of buffered agarose constructs containing either $14x10^6$ or $7x10^6$ cells, collected in three different glucose concentrations: 450 mg/dL, 250 mg/dL, or 50 mg/dL. Black bars represent the raw TCho peak area under the specified glucose concentration. Striped bars represent the TCho peak area after the glucose contribution is subtracted using the technique presented in the text. White bars represent the control, i.e. the TCho peak area of the same construct in glucose- and sera-free DMEM.

cells. Periodic monitoring of TCho enabled the tracking of changes in viable cell number over time for constructs under dynamic conditions of cell growth or death. Assessment of viable cell number by measurement of TCho was found comparable with the traditional viability assay MTT, yet it did not impart detrimental effects to the cells. Thus, the TCho-based assay could be further expanded to monitor viable cell number over a prolonged time period through the development of an NMR-compatible bioreactor, such as the packed-bed bioreactor system used in earlier studies in our laboratory to

maintain βTC3 cells over a period exceeding 30 days [7]. *In vitro* studies where this noninvasive assay would be highly useful include long-term development of tissue substitutes, assessment of constructs before and after cyropreservation procedures, and quality control of constructs prior to implantation.

The correlation between TCho peak areas and their respective insulin secretion rates for the constructs studied suggest that this assay also provides a valuable indicator of construct function when cell viability is the dominating factor. In both construct types, dynamic changes were seen in the insulin secretion rates of the constructs over time; however, these variable insulin secretion rates correlated to results from the choline assay. Therefore, the observed trends for the insulin secretion rates in long-term cultures could mostly be attributed to changes in the number of viable cells in constructs. One major implication of the data presented in this study is the ability to monitor temporal changes in viable cell number for a relatively high cell turnover system under varying extents of cell growth. On Day 0, the majority of the entrapped cells were viable and in a proliferative state; however, over time, a heterogeneous cell population developed within the constructs with a large fraction of necrotic cells in the center and a band of highly proliferative cells on the periphery (CHAPTER 6). Monitoring the TCho of these constructs, as they remodel from the initial to the final state described above, raises the following questions: (i) does the presence of highly proliferative cells skew the data to higher levels of TCho; and (ii) does the presence of dead cells significantly contribute to the TCho signal within the VOI?

With regard to question (i), literature reports suggest that highly proliferative cells contain higher levels of water-soluble choline-containing compounds compared to their

quiescent counterparts. This is speculated to be due to the intensified membrane synthesis and enhanced production of PCho during the G_1-phase and S-phase of the cell cycle [176]. While *in vitro* ^{31}P NMR spectroscopy studies of numerous tumorigenic and non-tumorigenic cell types have found substantial increases in PCho levels during phases of rapid cell growth, a plateau of the PCho level was attained when the same culture entered a metabolic steady-state [3, 177]. A similar trend was also observed for ^{1}H NMR spectroscopy studies of TCho in βTC3 cells, which was expected given that PCho is the dominant component of the TCho resonance for this cell line [7]. In this study, the strong agreement between TCho measurements and the independent MTT assay, at all time points and for constructs with varying degrees of growth, also suggests that TCho measurement is not significantly skewed by the strong presence of highly proliferative cells.

Question (ii) addresses the concern that necrotic cells may contribute to erroneously high TCho signals, especially for constructs initially loaded with a cell number exceeding that supportable by the surrounding environment. Cell death typically activates phospholipases, which can degrade membrane bound phosphatidylcholine into its precursors GPC, PCho and Cho, resulting in a rapid increase in water-soluble choline-containing compounds within the cells [178]. However, in constructs initially loaded with a high cell number, where significant cell death occurred over the first 24 hours (Figure 6), the strong correlation between TCho and MTT indicate that the contribution of dead cells to TCho is minimal. On the other hand, when rapid and substantial cell death occurs, as illustrated in the results from the hyperthermia experiment, the TCho signal does not provide an accurate measurement of viable cell number in the first 5 to 10

hours following the initiation of cell death. Thus, the contribution from dead cells is negligible under slow cellular turnover conditions, whereas TCho measurements transiently are incorrectly high under conditions of massive and rapid cell death.

The inherent level of TCho varies between different cell types and degrees of differentiation or transformation [3]. Therefore, each cell line must be individually characterized to determine the appropriate calibration curve and range of cell numbers that result in a linear relationship between the TCho peak area and viable cell number. For this study, it was determined that the intercellular TCho level within βTC3 cells is approximately 0.1 mmol per 10^{10} cells. Published reports have documented the TCho for normal tissues, obtained from both human and animal sources. While commonly these values are presented as mmol/g of wet weight of tissue or as mmol/L, these values may be converted to mmol per cell by approximating the wet weight of the tissue and/or the cell density. The wet weight and cell density for tissue was assumed to be 1.05 gm/mL and 10^8 cells/mL, respectively. Both of these values are the average of data found for liver, brain, heart, and muscle tissue [179-182]. Using these approximations, the TCho ranges within varying tissues are: 0.07-0.20 mmol for brain [175, 183, 184], 0.05 mmol for heart[183], 0.27 mmol for liver[183], and 0.03 mmol for muscle[183], all normalized to 10^{10} cells. Therefore, the TCho level calculated for βTC3 cells is within the normal range found for tissues containing other cell types.

The effect of solute interference on the accuracy of the ^{1}H NMR detectable TCho resonance was also studied. The glucose artifact was expected to occur, given the range of cell numbers used in the agarose constructs. In natural tissues, where the cell number is typically 10-fold higher than what is used in this study, the effect of the glucose

resonance on the TCho peak area is minimal, given the dominant presence of choline compared to glucose within the VOI studied. *In vitro* choline studies of cell cultures have also avoided the glucose interference by either studying the ^{31}P nucleus or examining cellular extracts under high magnetic fields [185-187]. This ^{1}H NMR study, however, was able to develop a method for monitoring constructs under conditions where it is not desirable to remove glucose from the system or the glucose levels cannot be controlled, such as in closed-loop bioreactors or *in vivo*. By developing an indirect method for quantifying the glucose interference in the system, the contamination of the glucose signal on the TCho peak area can be precisely subtracted under a wide range of glucose concentrations and viable cell numbers. While the ratio between the 3.85 ppm and 3.22 ppm glucose resonances will stay fixed when collected under constant NMR parameters, this ratio is expected to vary under different NMR conditions, such as magnet strength and pulse sequences. Therefore, recalibration of the ratio between the glucose peaks may be necessary under different experimental conditions.

An implicit parameter in the design of this study was the ability to adapt the developed methods to monitoring tissue engineered constructs *in vivo*. To ease the transition to animal studies, RF coil designs were restricted to those where the signal from the implant can be collected from outside the animal, thereby eliminating the use of more sensitive coils that require close proximity to the construct. Higher magnetic fields and increases in collection times could vastly increase the sensitivity of the assay and the resolution of the construct images; however, NMR magnets of high field strength that accommodate *in vivo* sampling are scarce and the time frame for NMR acquisition is limited, given that the effective time period for standard anesthesia methods is on the

order of 45 min. Without these *in vivo* boundaries, the sensitivity of the TCho assay could be greatly increased, i.e. to measurements within a single 0.8 mm bead containing only 3x105 cells [188]. Furthermore, ^{1}H NMR choline measurements could be expanded from aggregate viable cell number measurements to the collection of spatial viability information using 1D-, 2D, or 3D-chemical shift imaging techniques, which could detect spatial heterogeneities within the construct itself [188].

Future work is focused on applying the methods developed in this study to the *in vivo* environment. Specifically, research is ongoing in monitoring TCho in buffered agarose disk constructs implanted within the peritoneal cavity of mice.

CHAPTER 9

9. *IN VIVO* NONINVASIVE MONITORING OF VIABLE CELL NUMBER IN TISSUE ENGINEERED CONSTRUCTS USING ^{1}H NMR SPECTROSCOPY[5]

9.1. ABSTRACT

Direct, noninvasive monitoring of tissue engineered constructs would provide valuable information on the dynamic changes that occur post-implantation. This study investigated ^{1}H NMR spectroscopy and imaging as a tool for noninvasively monitoring the viable cell number within a tissue engineered construct over time *in vivo*. The disk-shaped construct studied consisted of mouse βTC3 insulinoma cells in agarose, surrounded by a cell-free agarose layer. Utilization of the highly sensitive proton nucleus and intrinsic cellular signals eliminated the need to add extrinsic probes or markers to the system. Accurate *in vivo* measurements of the total-choline resonance within implanted constructs were collected by localized ^{1}H NMR spectroscopy, as verified by comparisons with *in vitro* total-choline measurements, and they correlated strongly to MTT cell viability results. Overall, total-choline measurements were able to accurately and noninvasively quantify viable βTC3 cell numbers *in vivo*, in the range of $1x10^{6}$ to more than $14x10^{6}$ cells.

[5] Modification of paper submitted for peer review, 2004.

9.2. INTRODUCTION

Tissue engineering is typically defined as the use of living cells and biocompatible materials for the development of biological substitutes to repair, replace, maintain, or enhance the function of a particular organ or tissue [189]. Upon implantation, the activity of the cells within the construct and its interaction with the host can result in significant changes in construct structure and function over time. Direct monitoring of such changes, however, is limited. *In vivo* monitoring of physiologic end-points, for instance the monitoring of blood glucose levels in a diabetic animal that has received a pancreatic implant, is useful but does not provide direct information on the implant itself. Therefore, there is a need to develop a reliable and direct methodology to noninvasively monitor a tissue engineered substitute *in vivo*, in regard to both its viable cell number and structure.

Although there are several reliable *in vitro* methods for assessing viable cell number [169-172], use of these destructive assays to monitor implants requires several animal experiments to be conducted in parallel, thereby imparting substantial inter-animal variability. Recently, promising studies monitoring tagged cells *in vivo* using optical and radionuclide imaging have recently been published [68, 73, 75, 79, 81]; however, the use of molecular probes for monitoring a tissue engineered implant is difficult, based on problems such as transient expression, toxicity, and poor resolution, sensitivity, and specificity issues [66].

Proton Nuclear Magnetic Resonance (NMR) spectroscopy and imaging is a promising modality for assessing tissue engineered substitutes *in vivo*, since it can provide accurate and detailed metabolic and spatial information of living systems by monitoring inherent

compounds. Although biologically-relevant, NMR-detectable nuclei such as ^{31}P and ^{13}C may be studied, the strong sensitivity of the proton nucleus allows for the efficient collection of ^{1}H NMR spectra and images with spatial and temporal resolution unmatched by other nuclei [190]. ^{1}H NMR spectroscopy and imaging has three particular advantages over other modalities: simultaneous collection of spatial and metabolic information; elimination of the need for external molecular probes or enriched media; and the ability to perform longitudinal studies on the same sample. Furthermore, through NMR gradient techniques, it is possible to isolate localized regions within the field studied to collect structural and metabolic information from that volume alone [2].

Of particular focus in this research is using ^{1}H NMR spectroscopy to measure viable cell number by monitoring the resonance at 3.2 ppm. This resonance commonly includes choline-containing compounds such as choline (Cho), phosphocholine (PCho), and glycerol 3-phosphocholine (GPC), with possible contributions from phosphoethanolamine (PEtn), inositol and taurine [3]. This peak is commonly referred to as "total-choline" (TCho), and this term is used henceforth in this study. Published reports have found strong correlations between TCho and cell number for a variety of cell types *in vitro* and *in vivo* [3-6]. More specifically, data presented in CHAPTER 8 found TCho to be an efficient, accurate, and noninvasive *in vitro* assay for measuring the number of viable βTC3 cells in agarose constructs.

This study tests the *in vivo* applicability of the NMR methods illustrated in CHAPTER 8 using a model tissue engineered construct. The disk-shaped implant consisted of mouse βTC3 insulinoma cells in agarose surrounded by an outer cell-free agarose layer. This construct design was identical to one of the constructs characterized

during the *in vitro* NMR experiments in CHAPTER 8. A critical parameter in this study was ensuring accurate and complete measurement of the TCho signal from the βTC3 cells within the implant. Therefore, the agarose construct was designed so that signal from the cell-containing region of the construct could be collected, without signal contamination from the surrounding host tissue. *In vivo* TCho measurements were acquired by ^{1}H NMR spectroscopy and correlated to respective *in vitro* results of TCho and the traditional MTT cell viability assay, performed on explanted constructs. ^{1}H NMR images of the implants were also collected. Methods for accounting for contaminating solutes and the minimal detection limit of the TCho assay are presented.

9.3. MATERIALS AND METHODS

9.3.1. Cell Culture

βTC3 cells were obtained from the laboratory of Shimon Efrat, Albert Einstein College of Medicine, Bronx, NY. Cells were cultured as monolayers in T-flasks and fed every 2-3 days with fresh medium consisting of Dulbecco's Modified Eagle's Medium (DMEM) (Sigma, St. Louis, MO) with 25 mM glucose and supplemented with 15% horse serum, 2.5% bovine serum, 1% penicillin-streptomycin, and L-glutamine to a final concentration of 6 mM (Sigma). Upon confluency, βTC3 cells were trypsinized using 0.25% Trypsin with EDTA (Mediatech, Herndon, VA) and either split for propagation or used in construct fabrication (passage numbers 33-48).

9.3.2. Construct Fabrication

The agarose disk-shaped construct used in this study is illustrated in Figure 45. It consisted of an inner cell-containing disk coated with a layer of pure 2% agarose to final dimensions of 3 mm height and 16 mm diameter. Experimental justification for the presence and thickness of the buffer layer are presented later in this article.

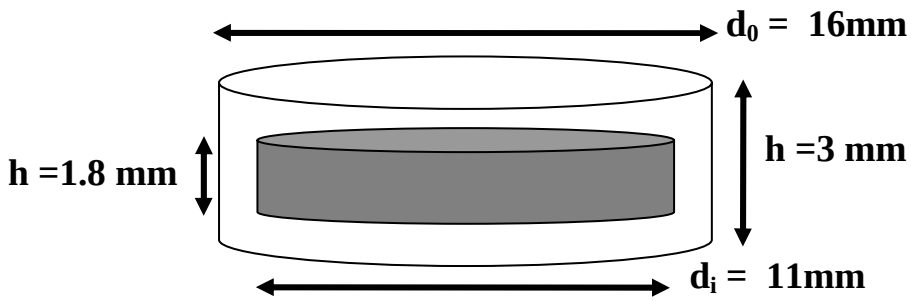

Figure 45. Schematic representation and dimensions of buffered agarose construct used for implantations. The shaded region represents the inner disk containing βTC3 cells entrapped in 2% agarose, while the white region indicates pure 2% agarose.

The agarose construct was fabricated by methods described in CHAPTER 6. Briefly, a suspension of βTC3 cells, at the density specified for each experiment, in 2%(w/v) SeaPlaque agarose (Cambrex, NJ) at 37ºC was poured into pre-fabricated sterile molds of 11 mm diameter and 1.8 mm height (0.2 mL in volume). After gelling, the disks were coated with an outer layer of pure 2%(w/v) agarose using larger Lexan molds (16 mm diameter, 3 mm height). Completed constructs were then placed in sera-free Hanks Buffered Saline Solution (HBSS) (Mediatech, Herndon, VA). Constructs were implanted within 4 hrs after manufacturing. During this period, constructs were maintained in a

humidified 37°C, 5% CO_2/95% air incubator in 125 mL spinner flasks (Wheaton, Millville, NJ), containing 35 mL of sera-free HBSS and agitated at 30 rpm.

In experiments aimed at determining the necessary thickness of buffer zones, cell-free constructs were fabricated from 2% (w/v) agarose using pre-sterilized Lexan molds, with systematic changes in diameter from 11 mm to 16 mm and in height from 1.8 mm to 3 mm.

9.3.3. Animal Studies

All animal experiments were approved by the Institutional Animal Care and Use Committee (IACUC) at Emory University. Male C57BL/6J mice of at least 20 grams were obtained from Jackson Laboratories (Bar Harbor, Maine) and used for surgical implantations. Mice were sedated using an IP injection of ketamine/xylazine (150/15 mg/kg body weight) prior to implantation, and a single buffered agarose construct was placed within the peritoneal cavity via a 2 cm midline celiotomy. For control studies, cell-free agarose constructs were implanted. For experimental studies, buffered agarose constructs containing three initial cell loadings of $14x10^6$, $8x10^6$, and $4x10^6$ cells were tested. NMR data were collected on Days 0, 1, 2, 3, 4, 5 and 14. All mice were scanned by NMR on Day 0, with subsequent NMR scans performed on other test days in groups of three or more. No single mouse was scanned more than three times. To relieve the transient hyperglycemia caused by the use of the chosen anesthetic (see APPENDIX A6), tested mice were fasted by removing food from their cages approximately 8 to 10 hrs before each NMR scan. Immediately prior to NMR scanning, the same mice were then sedated using an IP injection of ketamine/xylazine (150/15 mg/kg body weight).

Following confirmation of sedation, 1 mL of saline was injected into the peritoneal cavity, to further dilute the glucose concentration in the abdominal fluid. Upon completion of NMR scans, mice were either allowed to recover in a prewarmed cage and eat freely from the food provided, or euthanized using CO_2 asphyxiation. Constructs were removed from euthanized mice by cutting open the skin and muscle layers and removing the construct using forceps. Constructs were then washed three times in sera- and glucose-free DMEM to remove *in vivo* solutes prior to subsequent *in vitro* NMR scanning. *In vitro* NMR scanned constructs were then placed in complete DMEM for two hours prior to MTT viability analysis.

9.3.4. ^{1}H Magnetic Resonance Imaging and Spectroscopy

NMR imaging and spectroscopy examinations were performed using a Varian/Inova 4.7T horizontal bore magnet operating at 200.56 MHz (Varian, Inc., Palo Alto, CA). The magnet was equipped with an 11.7 cm inner diameter self-shielded gradient system with a maximum gradient strength of 25 gauss/cm. Constructs were investigated using a transmit/receive home-built surface coil measuring 35 mm in length and 24 mm in width, attached to a 32 mm diameter polycarbonate tube. The RF signal intensity decreased by 45% at 1 cm from the surface of the coil. For all experiments, the construct location was no more than 0.7 cm from the surface of the coil. The signal variability across the construct volume was found to be a maximum of ~17%. For *in vivo* experiments, the implanted construct was centered within the surface coil field of excitation, and the anesthetized mouse was secured. For *in vitro* experiments, constructs were loaded in a sterile centrifuge tube containing 50 mL of glucose- and sera-free DMEM and centered

within the surface coil field of excitation. The surface coil was subsequently positioned at the magnet's isocenter.

Standard ^{1}H NMR gradient-echo images (TR = 200 ms, TE = 3.5 ms, Acquisition time of 51 sec) were acquired to determine the exact positioning of the construct within the field of view. A single high resolution spin-echo image (TR = 2 sec, TE = 40 ms, Acquisition time of 17 min and 10 sec) was collected to provide a detailed image of the construct structure and the surrounding environment.

Localized ^{1}H NMR spectra were acquired from an 8x8x2 mm^{3} thick volume of interest (VOI), centered within the cell-containing region of the construct. Shimming of the water signal was performed on the selected VOI using a localized PRESS sequence [137]. Water-suppressed spectra on the same VOI were then acquired using three CHESS pulses prior to executing the PRESS localization sequence. The PRESS pulse parameters used in all experiments were TR equal to 3 sec and a total TE, defined as $2t_1 + 2t_2$ (t_1 = 12.5 ms, t_2 = 33 ms), of 91 ms. At the TR time selected, the magnetization was completely relaxed. The TE time, selected to reduce the glucose signal intensity, was found to result in minimal (~5%) changes in TCho, when compared to the shortest echo time allowable by the sequence. All localized, water-suppressed ^{1}H NMR spectra were the average of 256 acquisitions, collected at a constant receiver gain using real-time digital signal processing. The total time required to collect each water-suppressed spectrum was 12 min 56 sec. Spectral data were processed using the frequency domain analysis package supplied in VNMR from Varian. Time domain data were apodized with an exponential line broadening of 3 Hz, Fourier transformed, with the residual water signal removed by digital filtering, and the baseline corrected where necessary. A

Lorentzian function was fitted to the resulting TCho peak at 3.2 ppm using manufacturer-provided software to determine the area under the peak.

9.3.5. Analytical Techniques

Methods for assessing construct viable cell number using the CellTiter 96 MTT (3-(4,5-dimethylthiazol-2-yl)-2,5-diphenyl-tetrazolium bromide) assay (Promega, Madison, WI) have been described in CHAPTER 6. Briefly, three one-quarter segments of each construct were separately incubated in 3 mL of fully supplemented DMEM and 450 μL of MTT, for 4 hrs at 37°C, 5% CO_2/95% air. Solubilization of the resulting formazan crystals was achieved by 24 hr incubation in the solublization/stop solution within a humidified 37°C, 5% CO_2/95% air incubator. The resulting absorbance for each test was read at 595 nm and then numerically averaged.

The fourth and final construct segment was set aside for histological examination. Samples designated for histology were fixed in 3% glutaraldehyde for 48 hrs and then prepared for paraffin embedding and sectioning. After sectioning into 5μm samples, the slides were stained with hematoxylin/eosin (H/E).

9.3.6. Statistical Analysis

All measurements are presented as the mean ± SD. All statistical analyses were performed using a two-sample t-test. Results were considered significantly different when *p*-values were less than 0.05.

9.4. RESULTS

To assess the effectiveness of the PRESS localization sequence in acquiring NMR signal from the VOI without imparting contamination from the surrounding host tissue, a series of control experiments were performed *in vivo* utilizing cell-free constructs of varying dimensions. Figure 46 shows localized ^{1}H NMR spectra acquired from three different cell-free constructs implanted in the peritoneal cavity of C57BL/6J mice (one construct per mouse), where only the radial dimension was varied (the 8x8 mm^2 side of the VOI). Each ^{1}H NMR spectrum represents the average of 256 acquisitions with an exponential line broadening of 3 Hz and all spectra are displayed at the same vertical scale. All spectra were acquired within 1 hour after implantation and the VOI used to collect the signal was maintained constant at 8x8x2 mm^3. Since only freshly implanted, cell-free constructs were scanned, all resulting signals in the spectra were due to contamination from the surrounding host tissue. Spectrum A was collected from a construct 11 mm in diameter, while spectra B and C were obtained from constructs with diameters of 13 mm and 16 mm, respectively. The data show that abdominal fat dominated the spectrum when the construct diameter was 11 mm or 13 mm; however, spectra collected from the 16 mm diameter construct was free of host contamination. Therefore, when a 2.5 mm buffer layer is added to the 11 mm single agarose disk construct in the radial dimension, host contamination of the collected spectrum is eliminated. Similar experiments were also conducted to determine the minimum thickness of the buffer layer in the height dimension (the 8x2 mm^2 VOI side) and this thickness was determined to be 0.6 mm. The variation in buffer layer thickness required for the radial and height dimension is due to the difference in gradient strengths for each

axis of the VOI, where the larger the dimension, the smaller the gradient strength. Based on these experiments, a pure 2% agarose buffer layer was applied to the cell-containing disk at the dimensions illustrated in Figure 45. Constructs of these dimensions were used throughout the rest of this study.

Figure 47 shows typical spin-echo ^{1}H NMR images of a construct containing βTC3 cells implanted within the peritoneal cavity of a C57BL/6J mouse. Figure 47A shows a sagittal (parallel to the axis of the magnet bore) view of the implant, with a displayed pixel resolution of 78 μm by 40 μm. Note the construct position at the center of the excitation field of the surface coil. Figure 47B shows a spin-echo image of the coronal view through the planar center of the same agarose construct, with a displayed pixel resolution of 68 μm by 68 μm. The boundary between the inner cell-containing disk and the outer agarose layer is easily discernable, allowing for accurate central placement of the VOI in the cell-containing region, as indicated by the white square. ^{1}H NMR images collected from the constructs over time, showed no significant changes in the structure of the construct. For all time points used in this study, constructs were found to retain their initial structural integrity upon explantation. Histological sectioning of implants exhibited a moderate host response, typically no more than 2-3 cell layers thick, as illustrated in CHAPTER 7.

Figure 48 shows typical localized, water-suppressed ^{1}H NMR spectra, collected on Day 0 and Day 3, from implanted agarose disks containing either no (Panels A and B) or $14x10^{6}$ cells (Panels C and D). Day 0 spectra were collected within 1 hour after implantation. Day 0 spectra typically did not contain host solutes due to the short time frame between implantation and NMR acquisition, and the dilution of the peritoneal fluid

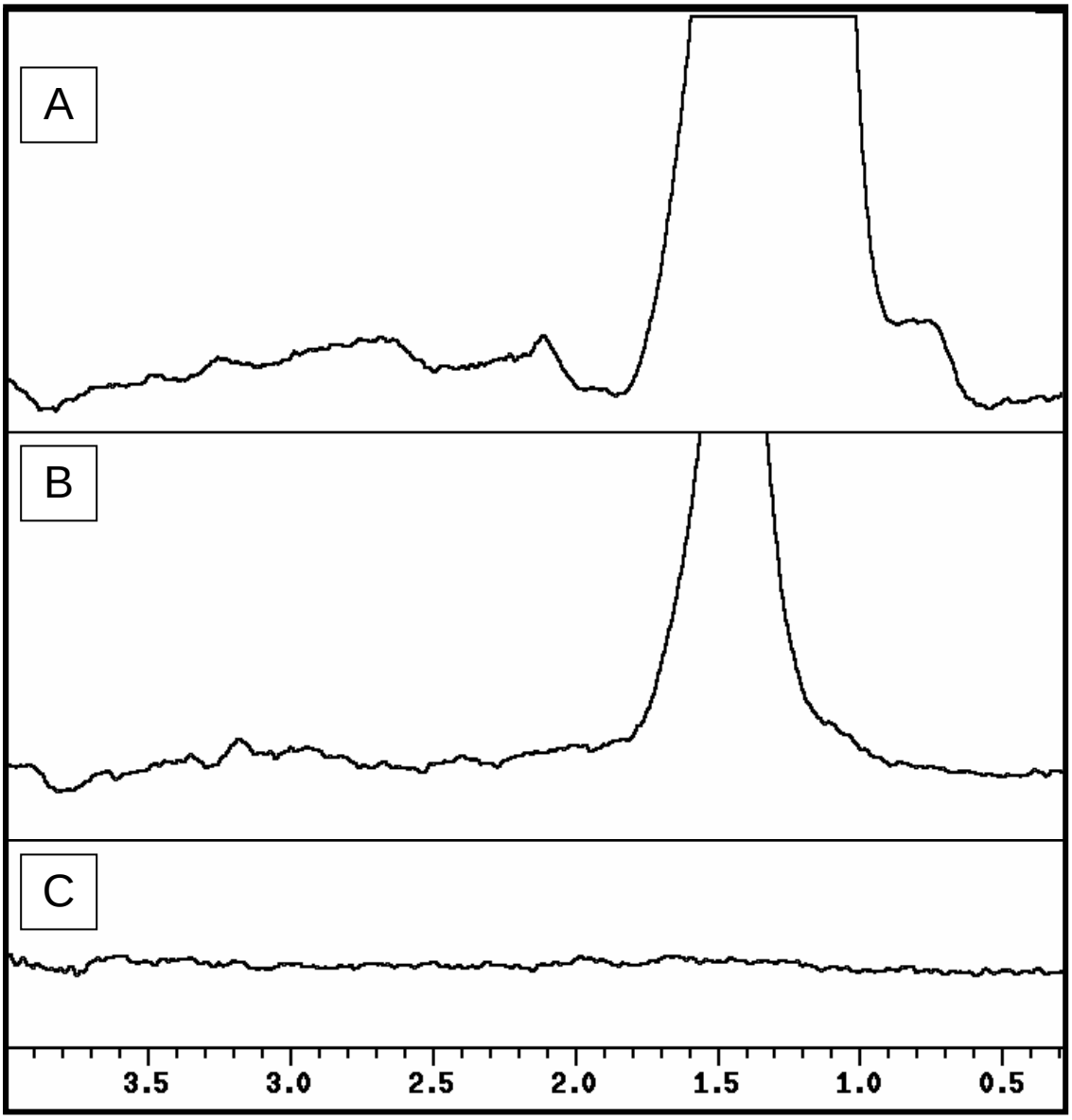

Figure 46. Water-suppressed, localized ^{1}H NMR spectra of implanted 3 mm thick cell-free buffered agarose constructs with radial buffer layers of 0 mm (A), 1 mm (B), and 2.5 mm (C) thickness.

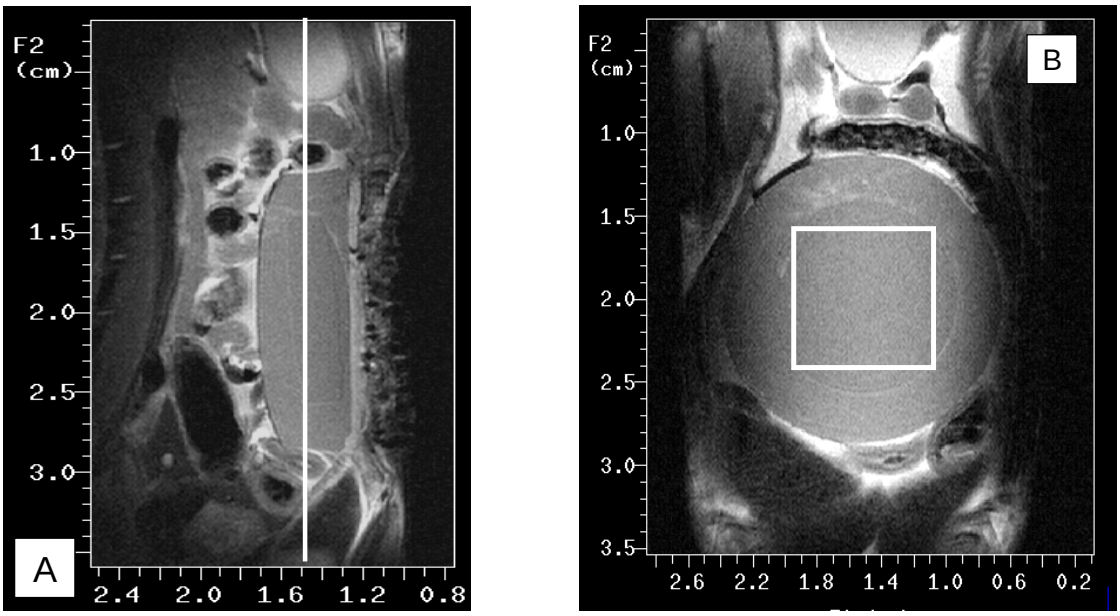

Figure 47. Sagittal (A) and coronal (B) spin-echo ^{1}H NMR images of a buffered agarose disk construct. The white square shown in the coronal image is the VOI used to collect the localized ^{1}H NMR spectrum from the inner cell-containing disk.

by saline during the surgical procedure. The spectrum of freshly implanted cell-freeconstructs (Figure 48A) showed no ^{1}H NMR detectable metabolites, while resonances attributed to glucose (resonance range from 3.85 ppm to 3.22 ppm) were discernable on the Day 3 spectrum (Figure 48B). In the Day 0 spectrum with cells, the resonance at 3.2 ppm is attributed to TCho (Figure 48C). The Day 3 ^{1}H NMR spectrum also displayed the TCho resonance, albeit at a reduced intensity in comparison to Day 0 (Figure 48D). Furthermore, glucose was also detected within the localized region of the construct. Previous ^{1}H NMR studies determined that glucose, specifically the βH2 resonance at 3.22 ppm, interferes with the accurate quantification of the TCho peak area, when examined under the cell ranges used in this study (see CHAPTER 8). Post-acquisition methods, however, can be employed to effectively remove the interfering glucose peak at 3.22 ppm, through the quantification of the glucose resonance at 3.85

ppm. Specifically, the measured intensity of glucose resonance at 3.85 ppm is multiplied by the calibration ratio found for the glucose peaks at 3.22 and 3.85 ppm, to evaluate the glucose peak area at3.22 ppm. This contribution is then subtracted from the calculated 3.2 ppm peak area to produce the area attributed only to TCho. Details on this procedure and *in vivo* calibration data, collected using cell-free implants, are given in APPENDIX A5.

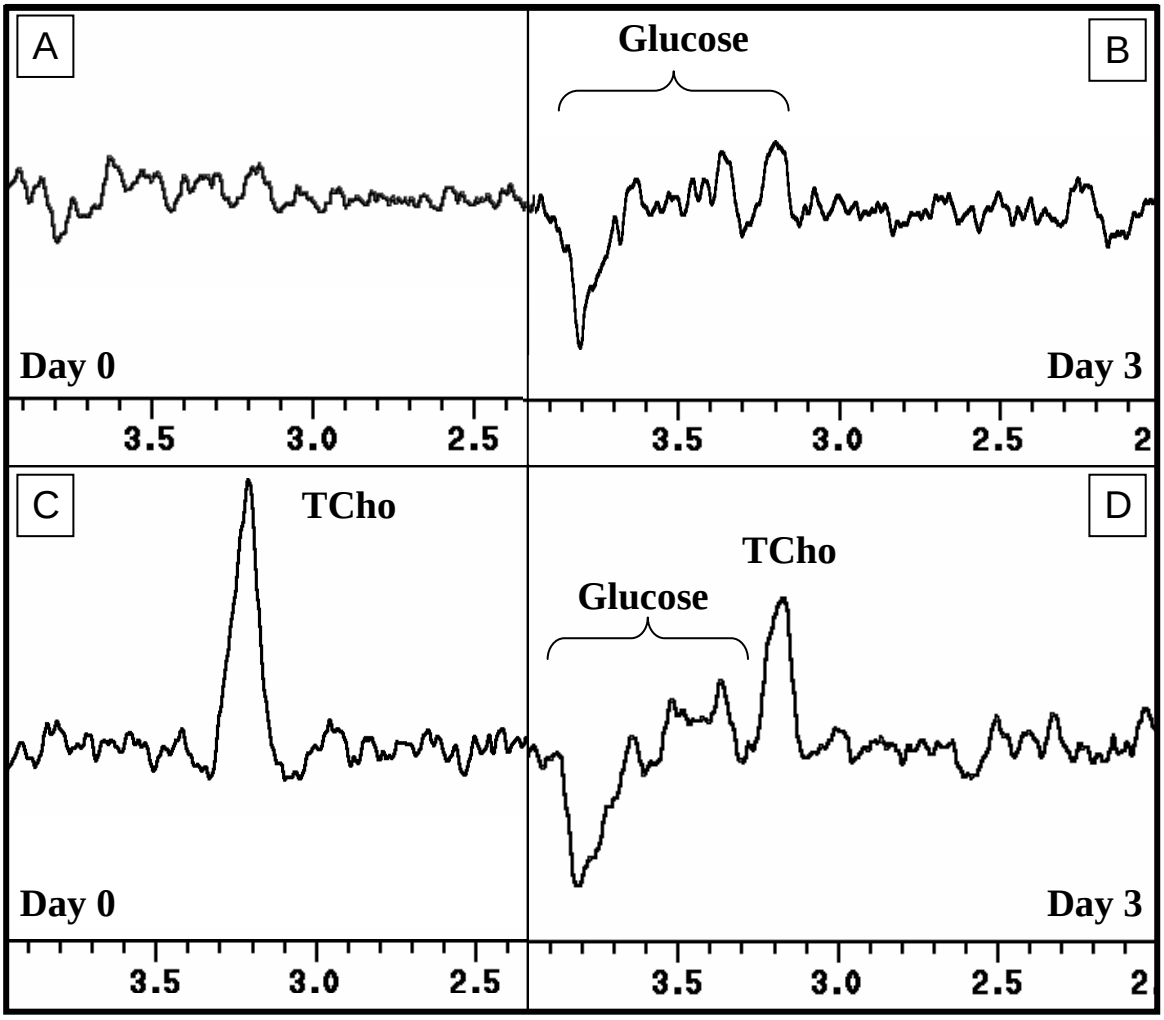

Figure 48. Localized, water-suppressed ^{1}H NMR spectra of an implanted buffered agarose construct containing either no (A, B) or $14x10^{6}$ (C, D) cells. For both constructs, spectra are shown for Day 0 (A, C) and Day 3 (B, D).

In vivo experiments monitored implanted constructs containing initial cell loadings of $14x10^6$, $8x10^6$, and $4x10^6$ cells, over a period of 14 days. These experiments monitored temporal changes in the *in vivo* collected TCho, which were then compared to respective *in vitro* measurements of TCho and MTT from explanted constructs. Figure 49 compares TCho measurements collected *in vivo* to their respective TCho measurements *in vitro*. Data shown were collected with constructs at various initial densities and time points, and all constructs are represented in the graph. Lines represent the best linear fit of data points. Figure 49A compares the TCho peak area *in vivo* and *in vitro*, when no corrections were made for measurements collected in the presence of glucose. Although a linear trend among the data points was found (R^2=0.54), this graph illustrates deviations between the TCho signal collected *in vivo* and *in vitro* for the same construct. Figure 49B plots the same measurements, except the post-acquisition method accounting for the interference of glucose on TCho quantification was employed. This data show a strong, linear relationship (R^2=0.96) between the two measurements with a slope close to 1. Day 0 data, which typically did not require glucose correction, were included in both plots. All subsequent results for *in vivo* collected TCho peak area are shown with glucose correction.

Figure 50 illustrates the strong linear correlation (R^2=0.87) between *in vivo* TCho and its respective *in vitro* MTT absorbance. Explanted constructs from all time points and cell loadings were included in the graph.

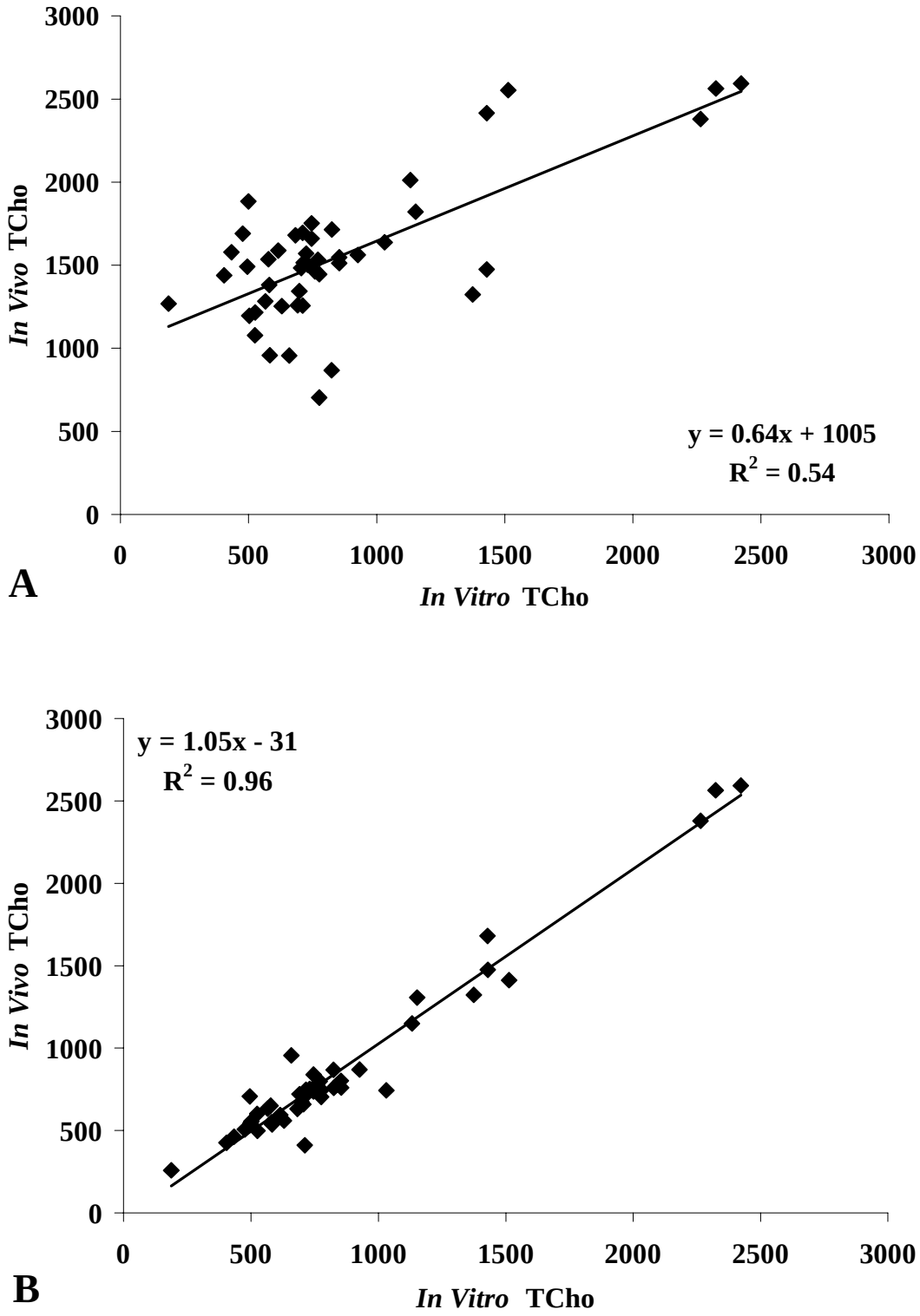

Figure 49. Correlation between raw (A) or glucose-corrected (B) *in vivo* TCho peak areas (y-axis) and respective *in vitro* post-explantation (x-axis) TCho peak areas for the same cell-containing construct.

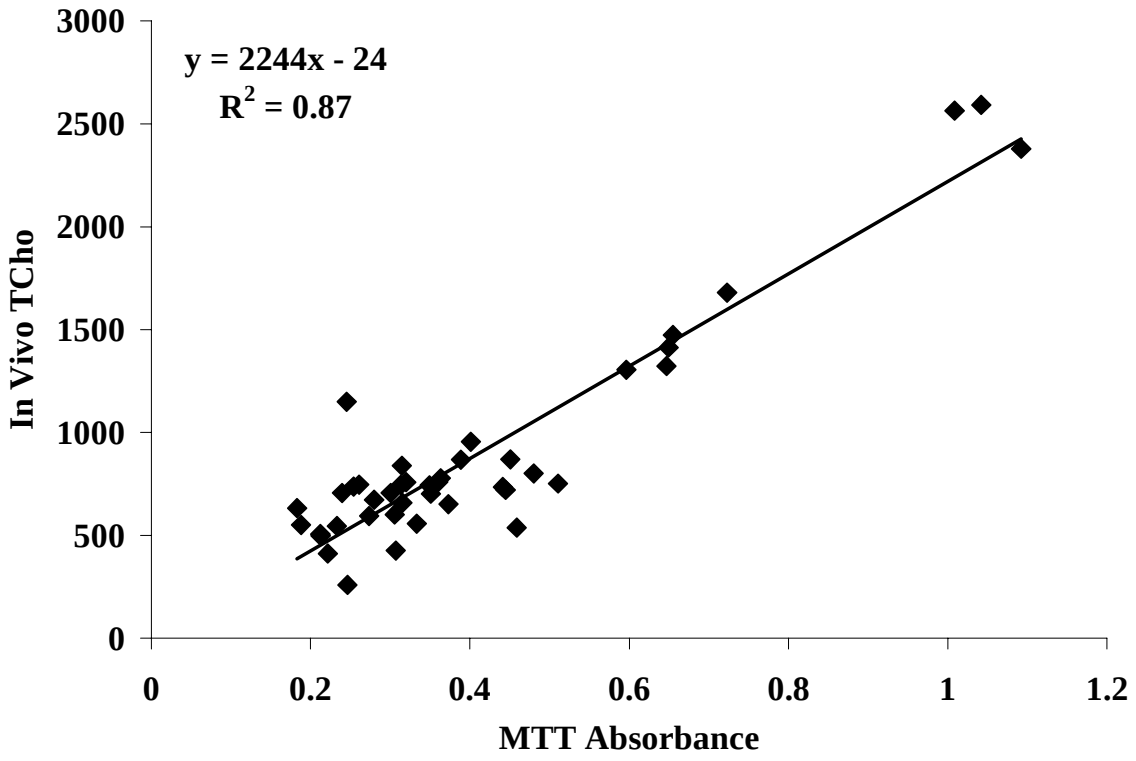

Figure 50. Correlation between *in vivo* glucose-corrected TCho peak area and respective *in vitro* MTT assay absorbance for βTC3 cells in agarose constructs.

In CHAPTER 8, a strong linear correlation was established between TCho and viable cell number *in vitro*. From these studies, a calibration curve was developed, where TCho data could be interpolated to viable cell number. Figure 51 illustrates the temporal changes of the *in vivo* TCho peak area, interpolated to viable cell number, for the three initial cell loadings tested. Within each cell density, statistically significant changes in viable cell number were found only within the first 2 days for constructs initially loaded with $14x10^6$ cells, and in the first day for constructs initially loaded with $8x10^6$ cells. Comparison among the three cell loadings at each time point found statistically significant differences on Day 0; however, by Day 1, statistical differences were found only between constructs initially loaded with $14x10^6$ and $8x10^6$ cells, and between

$14x10^6$ and $4x10^6$ cells. By Day 3, no statistically significant differences were found among any of the construct types for each time point.

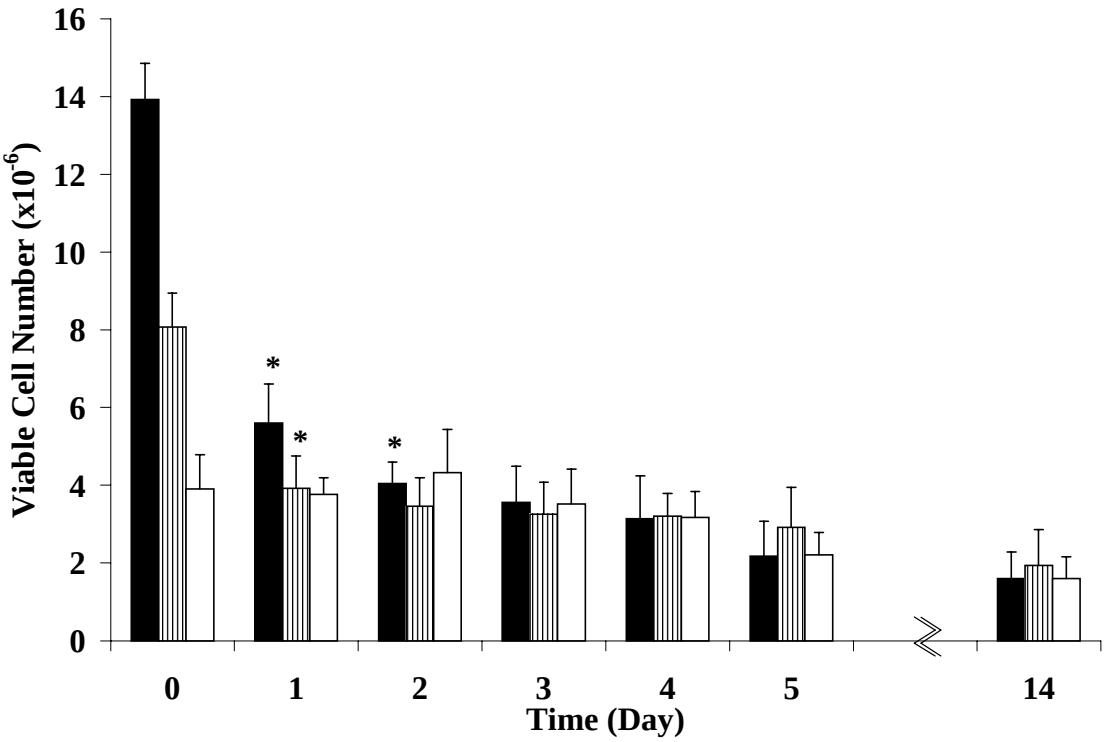

Figure 51. Time profile of *in vivo* TCho-assessed viable cell numbers for buffered agarose disk constructs with initial loadings of $14x10^6$ (solid bars), $8x10^6$ (striped bars), and $4x10^6$ (white bars) cells, over a period of 14 days. Each data point represents the mean ± SD, for a minimum of three independent implants. * indicates days when viable cell number results for a specific cell loading were significantly different ($p < 0.05$) from the previous day.

9.5. DISCUSSION

This is the first *in vivo* study to demonstrate the use of TCho, measured by ^{1}H NMR spectroscopy, for tracking changes in the viable cell number within a model tissue engineered construct. While CHAPTER 8 noninvasively correlated TCho to viable cell

number *in vitro*, this study was able to translate these methods to the *in vivo* environment. Minimizing contributions from the surrounding host tissue and correcting for glucose contamination effects allowed for the accurate collection of TCho measurements *in vivo*, as illustrated by the direct comparison to respective *in vitro* TCho data points. Noninvasive *in vivo* TCho results were comparable to results from the traditional cell viability assay MTT, obtained from explanted constructs.

The TCho assay provided a means to monitor the number of viable βTC3 cells in an implanted construct within a single animal over the entire implantation period, which provided valuable information of construct changes in the *in vivo* environment. Given the oxygen tension at the implantation site, estimated at ~40 mmHg, and the mass transfer characteristics of the construct, the stabilization in viable cell number of the three cell loadings to approximately $2x10^6$ cells was partially expected. Indeed, mathematical modeling predictions of the *in vivo* oxygen profile within these constructs estimated that approximately $1.3x10^6$ cells would retain oxygen tensions above 7 mm of Hg (see CHAPTER 6), which is slightly lower than the experimental plateau of viable cell number. While this deviation is not significant, experimental values could be higher due to (i) TCho contributions from residual dead cells, or (ii) use of conservative conditions for mathematical modeling, i.e. oxygen tensions could be higher than predicted or that cells could remain viable at oxygen concentrations lower than those supporting insulin secretion.

In vivo measurement of TCho using ^{1}H NMR spectroscopy has been experimentally studied for the characterization of tumors, primarily in brain and breast tissue [191-195]. Although these studies found strong correlations between TCho and markers of cell

proliferation in the early stages of growth, results from tumors at higher metastatic levels, such as III and IV, yielded ambiguous results [3, 196, 197]. This trend has mostly been attributed to the increasing presence of necrotic cells within the core of the tumor as it progresses over time [3, 196, 197]. Most of these *in vivo* studies used VOIs smaller than the actual size of the tumor, in order to reduce contamination from the surrounding tissue. Therefore, the resulting localized ^{1}H NMR signal was primarily skewed by the cells within inner region of the tumor, possibly resulting in unclear TCho results at the later stages of tumor growth. In this study, however, incorporation of the buffer regions permitted the use of a large VOI that resulted in the collection of TCho measurements reflecting the majority of the entrapped cells.

As the cells progressed from a population where the majority of the cells were viable and in a proliferative state to a heterogeneous mixture of cells in varying stages of cell growth, the collection of TCho signal from dead cells is a concern. Dissipation of TCho signal from dead cells out of the VOI has been established, in hyperthermic-induced cell death *in vitro* experiments using agarose constructs of identical dimensions and materials (see CHAPTER 7). While cell death may be continuously occurring in the implants used in this study, and thus a contribution to TCho from dead cells may always exist, this contribution is expected to be small. Furthermore, the cell densities used in this study, which are typically 10-fold lower than that found in tumors, may assist in the diffusion of TCho out of the agarose implants, whereas the TCho from dead cells within the inner tumor core may be retained for longer time periods.

In vivo, the TCho assay was found to accurately measure viable cell number from $1x10^{6}$ to over $14x10^{6}$ cells, which is similar to previous *in vitro* results obtained under

identical NMR parameters. *In vivo* quantification of TCho was complicated by the interference of glucose and the line broadening of the TCho peak due to movement of the animal. Therefore, under conditions of high glucose or significant movement, the minimum detection limits *in vivo* could be compromised. Furthermore, it has been well documented that the inherent level of TCho varies, depending on cell type and degree of differentiation or transformation [3]. Therefore, application of the methods illustrated in this study to other cell types would require the recalibration of TCho levels to viable cell number.

Although the NMR localization techniques and construct design employed in this study were found to accurately isolate the cell-containing region of the implant from the surrounding host tissue, the requirement of buffer zones results in additional mass transfer limitations, and thus a reduction in the number of viable cells supported in the construct. Therefore, future work is focused on two areas: (i) improvement of the localization sequence by employing other NMR techniques, such as volume preselection [198], spatially-selective lipid suppression [199], or inversion recovery [200], to dampen signal from surrounding host tissue; or (ii) modification of the RF coil design from an external coil to an implanted coil that would be wrapped around the cell-containing region of the construct. Either of these approaches could result in the reduction or elimination of the buffer zone layer, while possibly creating an overall increase in TCho signal sensitivity.

^{1}H NMR imaging is another facet that could provide useful information regarding the status of the implanted construct. Although significant structural changes were not seen for the implants used in this study, the pixel resolution of the images collected is capable

of detecting structural defects, such as cracks, in the agarose constructs. Furthermore, while the current ^{1}H NMR image resolution was unable to detect the moderate fibrotic response seen in these implants, earlier studies demonstrated the ability of the same system to detect the development of significant fibrosis over time *in vivo* (see APPENDIX A4). Improvements in coil design of the type outlined earlier could substantially increase the pixel resolution of the resulting images, thereby providing a more sensitive means to detect structural changes and host response effects on the implant.

CHAPTER 10

10. CONCLUSIONS AND FUTURE WORK

10.1. CONCLUSIONS

Noninvasive monitoring of tissue engineered constructs is of critical importance for accurate temporal characterization of constructs *in vitro* and *in vivo*. In this thesis, we have contributed to this field by developing a means to noninvasively monitor a model tissue engineered construct, which is applicable under different experimental conditions. The design of an appropriate model tissue engineered construct for our specific NMR application was the first challenge of this research. While earlier microbead results were promising, the need to confine the cells within a definable volume refocused the research to macroconstruct designs. The use of a disk-shaped construct allowed for ease in placement, identification, and retrieval of the construct *in vivo*, while confining the cell signal to a single definable region. The reduction of the surface to volume ratio, however, reduced the overall viable cell density, thereby decreasing the efficacy of the construct in restoring normoglycemia. In spite of these challenges, the final agarose-based, disk-shaped construct maintained the number of viable cells within the range necessary for quantification using current NMR methods, while also retaining its structural integrity over extended time periods *in vitro* and *in vivo*. Mathematical modeling and *in vitro* studies characterized the model construct and provided valuable information regarding the dynamic changes in cell number, growth patterns, and secretory function, under the studied environmental conditions.

The second phase of research quantified the direct relationship between total-choline and viable cell number within the constructs. *In vitro* studies established the strong linear correlation between total-choline and viable cell number not only for freshly made constructs, but as the cells remodeled over time periods extending several weeks. Using the accepted cell viability assays MTS and MTT as the standard, the total-choline assay was found to be highly comparable in accuracy and efficiency, without destruction of the construct or addition of external probes or markers to the system. Therefore, the use of this noninvasive total-choline assay could provide reliable, temporal assessment of viable βTC3 cell number within a single tissue engineered construct. The methods developed in this phase of study could provide a valuable tool for many *in vitro* tissue engineering applications, such as the testing of cyropreservation protocols, long-term construct development studies, and quality control of constructs prior to implantation.

The final phase of this thesis tested the applicability of the NMR total-choline assay *in vivo*. By designing a construct that minimizes contributions from the surrounding host tissue and accounting for glucose contamination effects, accurate total-choline measurements could be collected from implanted constructs and interpolated to determine viable cell number. Therefore, the NMR methods developed were able to demonstrate, for the first time, the ability of total-choline to provide direct and accurate temporal measurements of viable cell number in a tissue engineered construct *in vivo*. ^{1}H NMR imaging was also found to be a useful tool in providing detailed structural information of the implant. In cases where construct integrity is of critical importance, such as in blood vessel and cartilage substitutes, ^{1}H NMR imaging could provide a useful method for noninvasively assessing defects and degradation of structural elements. Temporal ^{1}H

NMR images of implanted constructs collected in this thesis also found these images to be helpful in characterizing the host response, by monitoring the development of a fibrotic cap. The ability to monitor constructs noninvasively *in vivo* can provide valuable information regarding the effects of implantation that cannot be precisely mimicked using mathematical modeling and *in vitro* testing. Therefore, the NMR methods presented in this thesis could be used to quantify integration of the implant and further understand the effects of specific *in vivo* parameters, such as immune-acceptance, on the overall viable cell number within an implant.

The data presented in this thesis outlined quantitative criteria for the capability and limitations of this NMR modality, such as cell number and construct architecture. ^{1}H NMR spectroscopy, under the specific NMR parameters used in this study, was found to accurately quantify viable βTC3 cell number *in vitro* and *in vivo*, at a minimum threshold of $2x10^{6}$ cells within a volume of 0.2 mL. While this cell density of $4x10^{6}$ cells/mL may be high for some applications, these NMR methods could be applicable in monitoring tissue engineered constructs that typically contain cell numbers of this magnitude, such as the bioartificial liver. Furthermore, advancements in RF coil sensitivity could increase this threshold to a cell level comparable to other tissue engineered systems, such as tissue engineered cartilage or myocardial patches. While the architectural constraints discussed in this thesis appear to limit the scope of the NMR monitoring system to constructs where buffer regions are implemented, it is feasible to assess substitutes where the viable cell number throughout the construct is assumed homogeneous, or in cases where measurements of the total viable cell number within the construct is not desired. In these cases, localized ^{1}H NMR spectra may be collected from implants where the volume of

interest is set to be smaller than the actual size of the construct, thereby creating a false "buffer" between the implant and the surrounding tissue. Furthermore, at the implantation site studied in this thesis, the strong presence of abdominal fat was the major factor of host contamination. For other implantation sites, such as the knee, fat may not be significant, thereby allowing for the reduction of the buffer zone requirement. Furthermore, in areas where surrounding host tissue is of a low cell density, a buffer region may be superfluous. Therefore, while the buffer regions implemented in this study assisted in accurate implementation of the NMR method, this requirement may not be necessary for other applications.

10.2. FUTURE WORK

The data presented in this thesis were primarily relegated to monitoring total-choline in βTC3 cells. In order to expand the applicability of the total-choline assay to other tissue engineered constructs, cells of varying lineages and degrees of transformation will need to be tested. APPENDIX A6 shows the comparison between βTC3 cells and βTC-tet, a continuous beta cell line transfected with a tetacycline-conditioned gene expression system to control proliferation. The strong agreement between the two cell lines suggests that total-choline levels for continuous beta cell lines are of similar magnitude. Furthermore, literature reports of total-choline levels within other tissue types found these values to be highly comparable to those calculated for the βTC3 cell line, see CHAPTER 8. These reports provide further evidence to suggest the broad applicability of the methods presented in this thesis for testing other tissue engineered prototypes.

Another aspect for future study would be the elimination or reduction of the buffer zones, which could relax the architectural constraints outlined in this thesis. Future work in this area is focused on two aspects: (1) improvement of the localization sequence by employing other NMR techniques, such as volume preselection [198], spatially-selective lipid suppression [199], or inversion recovery [200], to dampen signal from surrounding host tissue; or (2) modification of the RF coil design from an external coil to an implanted coil that would be wrapped around the cell-containing region of the construct, thereby reducing signals from outside of the coil. Either of these approaches could result in the reduction or elimination of the buffer zone layer, while possibly increasing the signal-to-noise ratio of the resulting spectrum.

The inference of glucose on the measurement of the total-choline signal is another aspect of this research that would benefit from future studies. Although the method developed in this thesis was able to effectively reduce glucose as a contaminating factor, these techniques could not be accurately implemented under conditions of high glucose and low total-choline concentrations. Separation of the two peaks would be the ideal solution to the contamination problem and could possibly be achieved through the use of higher magnetic fields and the manipulation of acquisition parameters and times. Since the glucose peaks are J-modulated, it is feasible to further reduce the intensity of the glucose peak at 3.22 ppm through the manipulation of pulse sequence parameters. Furthermore, employment of NMR methods described in the previous paragraph for reducing buffer zones could decrease glucose contamination by increasing the total-choline signal, while also reducing glucose contamination effects by decreasing the glucose contribution from non-cellular regions.

^{1}H NMR imaging is a promising aspect not extensively explored in this thesis. Future research could significantly expand imaging capabilities, to provide detailed spatial information concerning the implanted tissue engineered construct. Earlier published *in vitro* studies were able to demonstrate the ability of ^{1}H NMR imaging to collect spatial information regarding cellular growth patterns and the distribution of spheroids throughout the biomaterial [115]. While these *in vitro* studies are not currently translatable to *in vivo* systems due to the RF coil design, future research on the development of implantable RF coils could lead not only to the visualization of temporal changes in cellular growth patterns noninvasively *in vivo*, but also allow for the monitoring of host response and/or fibrotic development. Furthermore, through improvements in RF coil design and sequencing techniques, 1D-, 2D, or 3D-chemical shift imaging techniques could be employed to collect spatial total-choline information, which would expand from the current aggregate viable cell number measurements to the collection of spatial viability information to detect heterogeneities within the construct itself [188].

Other NMR techniques could also be applied to further advance this research. The use of superparamagnetic particles, such as MION and SPIRO (see INTRODUCTION for more details), have shown promising *in vivo* results for monitoring the immune response and tracking specific cell populations. Research in our laboratory have found MION to be highly compatible with beta cells including βTC3 and βTC-tet cells, see APPENDIX A7, while NMR studies have found MION to be retained within cell-filled APA beads for extended time periods (Oca-Cossio, J, *in preparation*). Incorporation of MION particles within cells would permit the monitoring of implanted constructs on the

microscale. Another NMR technique that could be applied to this research is the use of perfluorocarbons, which are monitored using ^{19}F NMR spectroscopy. Published reports have been able to assess oxygen levels *in vivo* using ^{19}F NMR monitoring and perfluorocarbon incorporation within APA beads [201]. While the effects of perfluorocarbon incorporation on cell viability have not yet been adequately explored, these results lay the foundation for the incorporation of perfluorocarbons within tissue engineered constructs to gain valuable information regarding the overall oxygenation of the construct *in vivo*.

APPENDIX

A.1. ^{1}H NMR SPECTROSCOPY OF APA BEADS

Earlier NMR experiments found a strong correlation between total-choline (TCho) and the overall oxygen consumption rate, for βTC3 cells in alginate/poly-L-lysine/alginate (APA) beads [7]. To explore the direct relationship between cell number and TCho for βTC3 cells, the initial cell density within APA beads was varied and TCho was measured on Day 0, using the same bioreactor system described in Long *et al* [7]. APA beads were generated using the same method described in CHAPTER 3, where the cell density was based on Trypan Blue viability measurements from the cell suspension prior to encapsulation. For each cell density, half of the beads were loaded in the NMR bioreactor and half were maintained in spinner flasks. Figure A1 plots the resulting correlation between cell density and TCho for Day 0. TCho levels were normalized to a reference compound from the media, as described in Long *et al* [7]. The plot shows a strong, linear correlation (R^2=0.97) between initial cell density and TCho. Since the volume of beads within the bioreactor remained constant, collected TCho measurements could be correlated to either total cell density or number. Furthermore, glucose consumption rates, collected from the spinner flasks and averaged over a 24 hr time period, show a strong, linear correlation (R^2=0.91) against their corresponding TCho measurements, as illustrated in Figure A2.

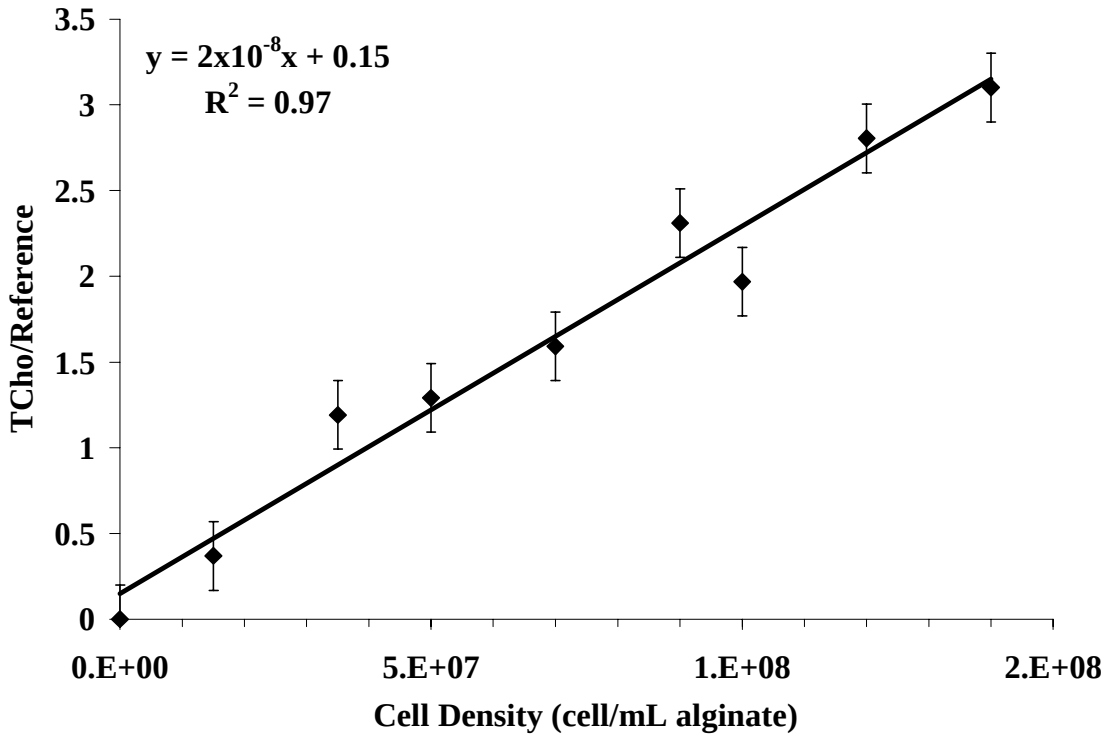

Figure A1. Correlation between TCho and cell density for Alginate/Poly-L-lysine/Alginate beads on Day 0.

While these APA experiments only examined initial time points, this study provides further evidence to support the hypothesis that TCho is a strong candidate for a noninvasive indicator of viable cell number.

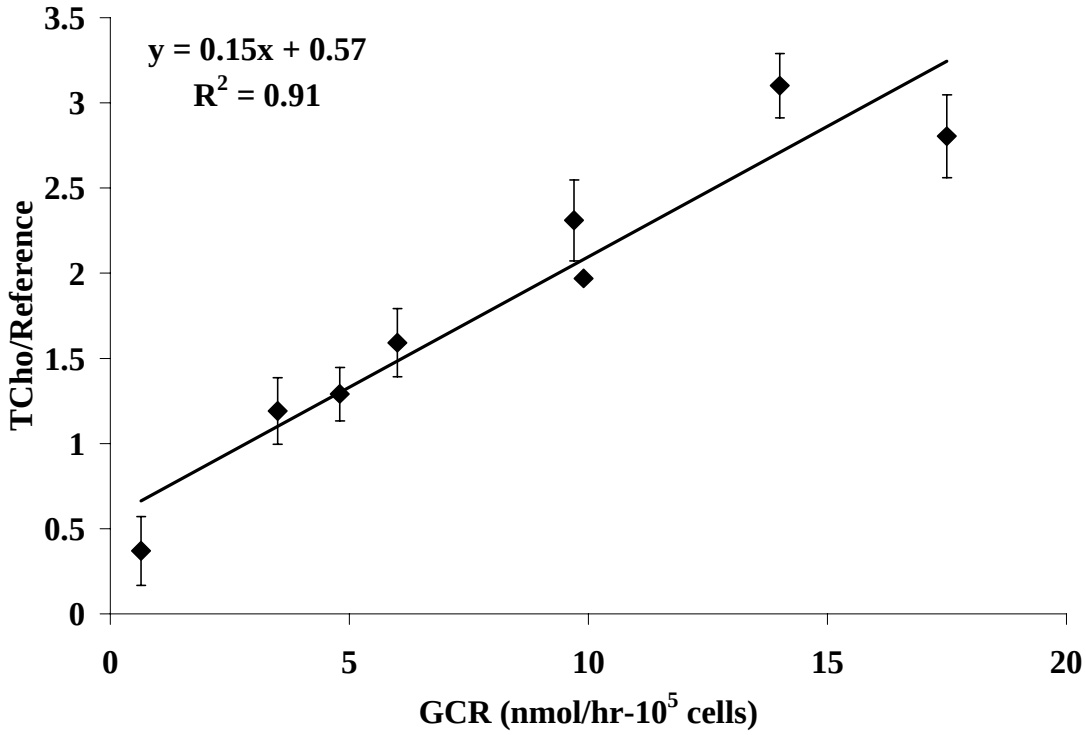

Figure A2. Correlation between TCho and glucose consumption rate (GCR) for Alginate/Poly-L-lysine/Alginate beads on Day 0.

A.2. IMPLANTATION OF APA BEADS

The efficacy of APA beads, containing βTC3 cells, in restoring normoglycemia in diabetic mice was tested using male C57BL/6J mice of at least 20 grams obtained from Jackson Laboratories (Bar Harbor, Maine). Mice were made diabetic through a single IP injection of streptozotocin (STZ; 200mg/kg body weight). Blood glucose levels were monitored daily via tail clipping and measured using an Elite Glucometer (Bayer, PA). Mice that maintained a blood glucose level above 350 mg/dL for three consecutive days were used for diabetic implantation studies. A volume of 0.2 mL of APA beads, with an initial cell density of $3.5x10^7$ βTC3 cells/mL alginate, were injected into the peritoneal cavity via midline celiotomy. Blood glucose levels were monitored over the course of 12 days. Figure A3 illustrates the resulting blood glucose levels. These experiments established the efficacy of a small volume of APA beads containing βTC3 cells in stabilizing blood glucose to normoglycemic levels.

Preliminary *in vivo* experiments were also conducted using APA beads to determine the feasibility of NMR imaging and spectroscopy for noninvasively monitoring a bioartificial pancreas. BALB/c mice were injected with 0.5 mL of 800 μm-diameter APA beads, containing $7x10^7$ cell/mL alginate, by midline celiotomy into the peritoneal cavity. ^{1}H NMR images were then collected on the anesthetized mouse three days after implantation. Images were obtained using a 3.8 cm diameter quadrature birdcage RF coil and the 4.7 T Varian/Inova magnet. Figure A4 illustrates the resulting T_2-weighted image of the peritoneal cavity of the BALB/c mouse. While the T_2-image was not able to accurately discern the APA beads, higher resolution diffusion-weighted images (Figure

A5) were able to identify the implanted beads. While these images lay the foundation for *in vivo* monitoring of implants, the poor resolution of the small microbeads and the significant distribution of the beads throughout the cavity of the mouse, relayed the need for a device that would confine the implant to a defined region.

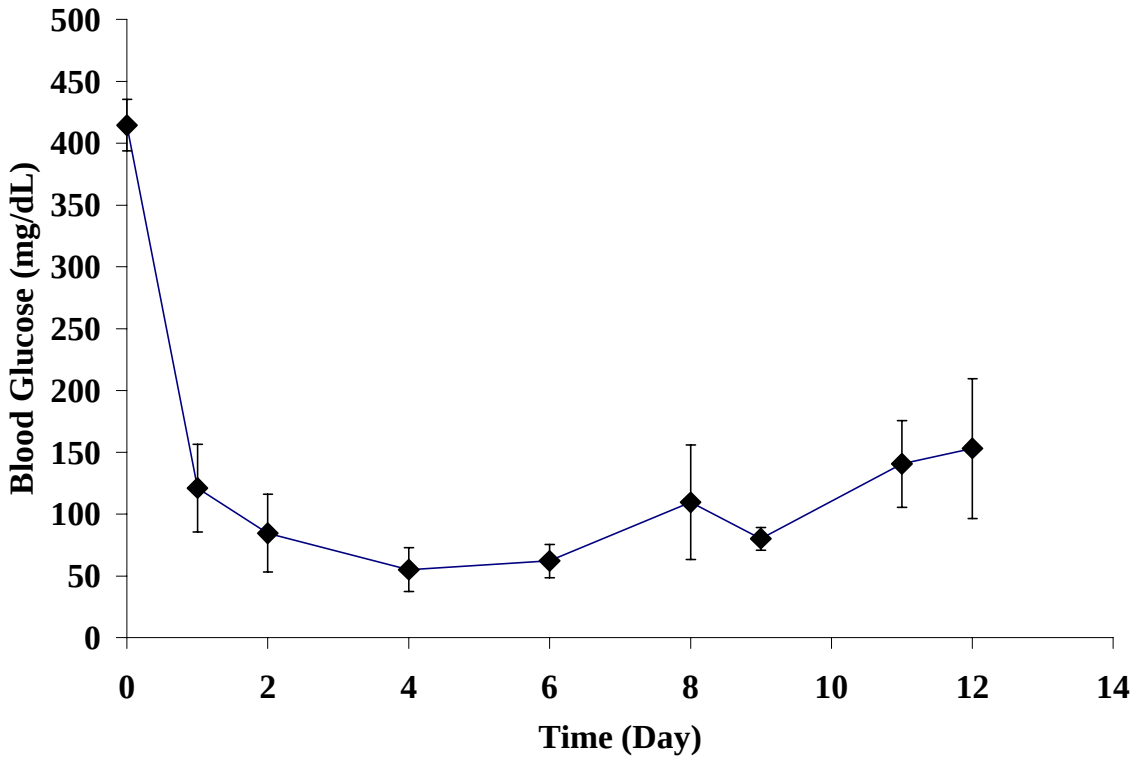

Figure A3. Temporal blood glucose levels of STZ-induced diabetic C57-BL/6J mice. A volume of 0.2 mL of APA beads, containing an initial cell density of 3.5×10^7 βTC3 cells/mL alginate, were implanted on Day 0. Day 0 data point was collected prior to implantation.

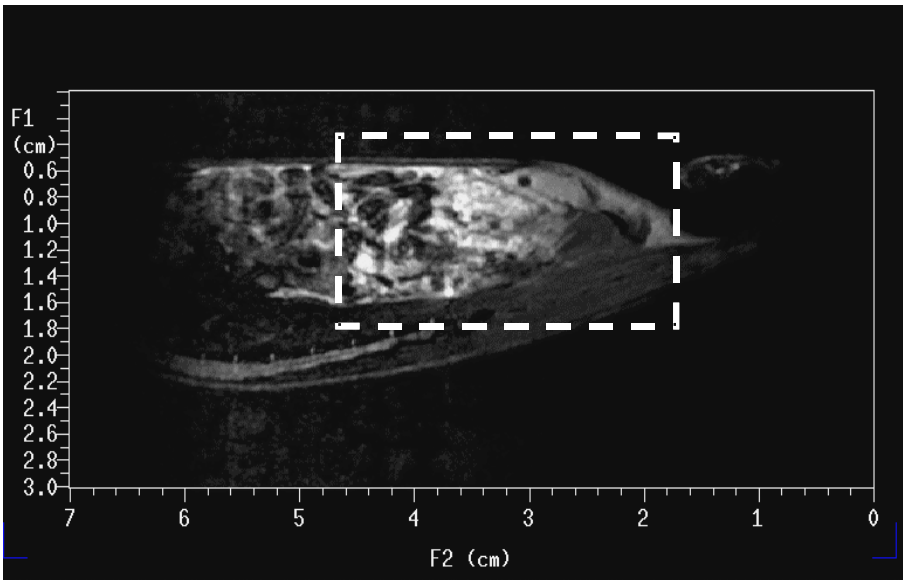

Figure A4. T_2-weighted ^1H NMR image of the peritoneal cavity of a live BALB/c mouse three days after the implantation of 0.5 mL of APA beads.

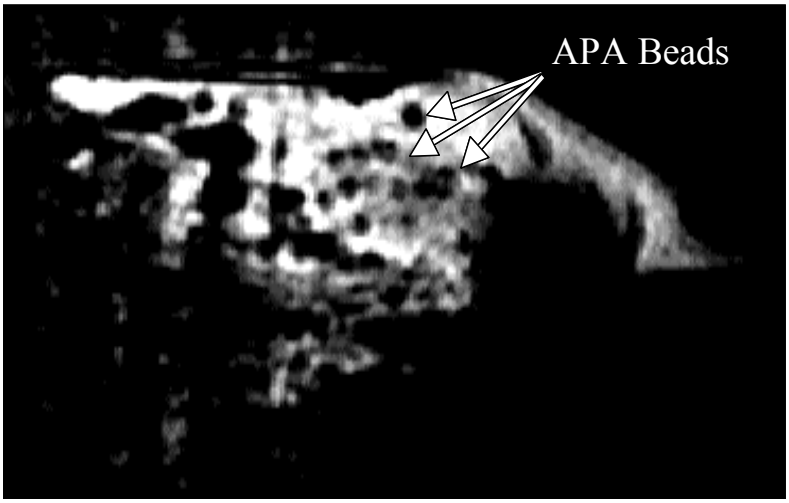

Figure A5. Diffusion weighted ^1H NMR image of the region shown in Figure A4 by the dashed box. A cluster of implanted APA beads, shown by dark circles in a bright background, is identified by arrows.

A.3. TESTING OF LOCALIZATION IMPERFECTIONS

Initial *in vitro* experiments to test imperfections in the NMR localization sequence were performed using the silicone/mesh constructs studied in CHAPTER 5. Localized, water-suppressed ^{1}H NMR spectra were collected from VOIs at varying locations at or near the cell-containing region of the construct. An example of this is shown in Figure A6, where the VOI selected is identified in the gradient-echo image by the white box. When the entire VOI was positioned approximately 2 mm outside of the cell-containing region of the construct, no choline signal was detected, as shown in Figure A6, Panel B. While these experiments helped to verify the accuracy in positioning of the VOI, the major contaminating factor *in vivo* was not choline or other low concentration metabolites, but contributions from abdominal fat.

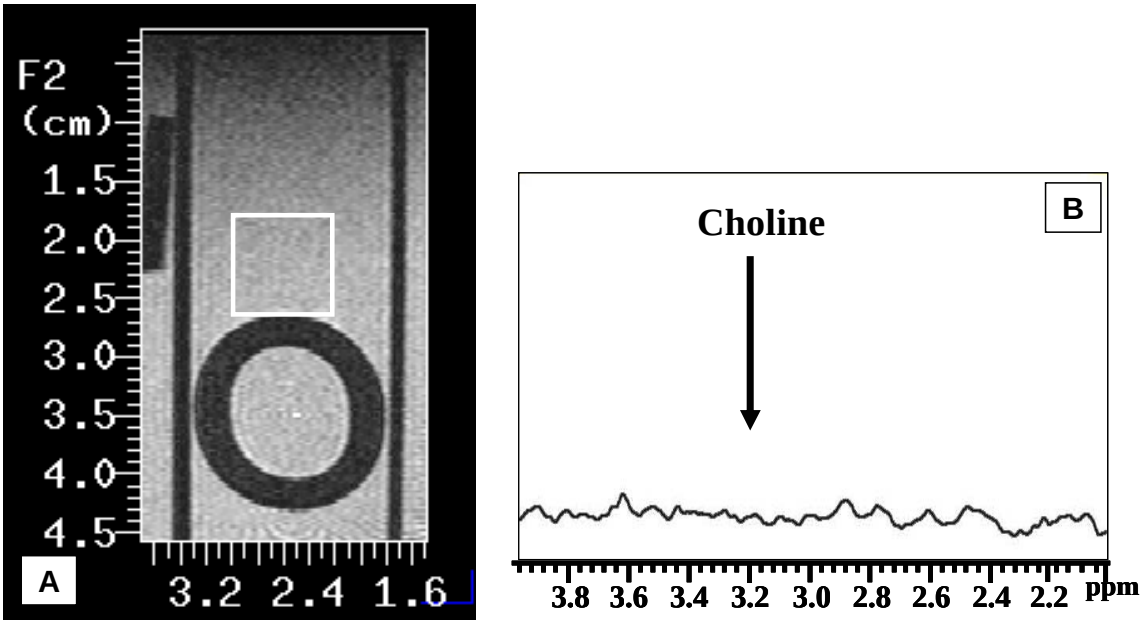

Figure A6. Gradient-echo ^{1}H NMR image of a silicone/mesh construct containing 0.4 mL of APA beads (Panel A). The white square is the volume of interest where the water-suppressed ^{1}H NMR spectrum was acquired (Panel B).

Therefore, the next phase of localization tests used two solutions confined to two separate layers: one containing choline buffered in saline, at a concentration similar to the cell-based experiments; and the other oil. The immiscibility of the two solutions permitted their separation into two identifiable volumes. Oil was selected because of its similarity in ^{1}H NMR resonances and concentration to *in vivo* abdominal fat. With this test solution, the disparity of concentrations between the choline and oil mimicked what was typically encountered *in vivo*. Using the RF surface coil and varying the location of the VOI within the choline solution, but keeping the dimensions constant, the ability to accurately quantify the choline resonance was examined. These studies found that a minimum distance of 1.5 mm in the planar dimension (the dimension of the sides of the box of the VOI) was required to eliminate the presence of oil signal in the resulting ^{1}H NMR spectrum, and allow for the accurate quantification of the choline resonance. In the height dimension, a minimum distance of 0.5 mm was required.

Preliminary *in vivo* experiments were also conducted, primarily to ensure the accurate positioning of the VOI within the field of view of the RF coil. The position of the implanted construct was determined through the collection of ^{1}H NMR scout images in the sagittal (Figure A7, Panel A), transverse (Figure A7, Panel C), and coronal planes. Once the position of the center of the construct, in all three-dimensions, was identified, the VOI was set to 8mmx8mmx2mm. Localized ^{1}H NMR images were collected of the specified VOI, as illustrated in Figure A7, Panels B and D. These experimented verified the accurate positioning of the VOI within the field of view of the RF coil. As can be illustrated in the VOI images, however, some signal was collected from outside the specified region, as seen by the appearance of bright areas outside of the localized VOI,

especially in the planar dimension (Panel B). Although not quantitative, these results provide evidence that localization accuracy may be aggravated *in vivo* possibly due to breathing of the animal.

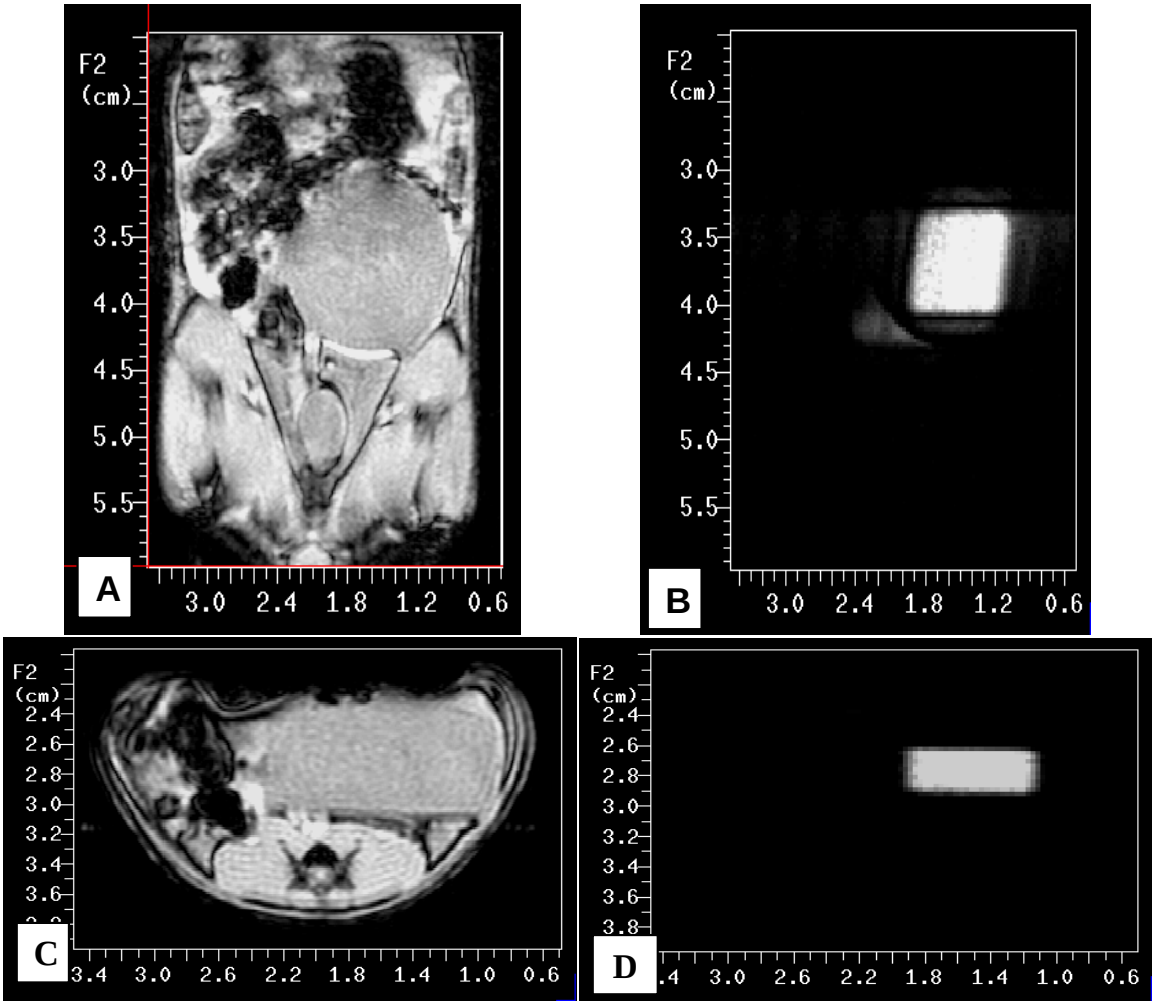

Figure A7. Spin-echo ^{1}H NMR images of a C57BL/6J mouse implanted with a single agarose disk construct (Panels A and C). Respective localized ^{1}H NMR images of the selected VOI (8x8x2mm^{3}), used to isolate the inner region of the implanted construct (Panels B and D).

A.4. TESTING OF AGAROSE/ALGINATE BEAD CONSTRUCTS

The next phase of experiments focused on the development of an alginate/agarose composite construct, which would confine the alginate beads to a defined space, restrict the infiltration of host tissue within the cell-containing region, provide a "buffer" zone between the implanted cells and the surrounding environment, and retain the viability of the cells. Figure A8 is a schematic representation of the agarose/alginate device. The thickness of the alginate bead region was set to be 1.8 mm, with a diameter of 11 mm. Detailed testing of the imperfections of the localization technique *in vivo* (see CHAPTER 9 for more detail) specified the resulting thickness of the outer buffer region at 0.6 mm along the thickness dimension and 2.5 mm in the radial dimension, as illustrated in Figure A8.

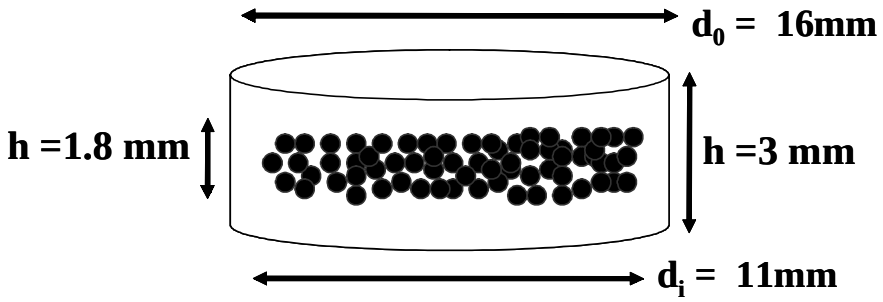

Figure A8. Schematic representation of construct prototype. Alginate beads contain entrapped βTC3 cells, while outer white region is agarose.

Upon implantation of the construct within the peritoneal cavity of C57BL/6J mice, ^{1}H NMR images and spectra were collected. Figure A9 (Panels A and B) illustrates typical spin-echo ^{1}H NMR images in both sagittal (parallel to the axis of the magnet) and coronal views. Note the striking contrast between the cell-filled alginate beads and the

surrounding agarose layer. Furthermore, the interface between the agarose and the surrounding host tissue is discernable. The contrast between the alginate beads and the surrounding agarose matrix allowed for ease in locating the center position of the cell-containing region of the implant, and thus accurate placement of the localized VOI. Figure A9, Panel C shows a typical localized, water-suppressed ^{1}H NMR spectrum collected *in vivo* on Day 0.

Spectra were collected over the course of 6 days from eight independent implants, each containing 0.2 mL of APA beads with βTC3 cells at a density of $7x10^{7}$ cells/mL of alginate. TCho resonance for each scan was analyzed and normalized to its respective Day 0 scan. These data points are shown in Figure A10 (solid bars). For each day, at least one construct was explanted, the alginate beads were released from the agarose matrix, and the viable cell number was assayed using MTS (for details on method see APPENDIX A.9.a). MTS results of the explanted constructs were also normalized to Day 0 measurements and plotted over time, Figure A10 (white bars). The number of implants used to collect the data for each time point is specified in the figure by n. Although statistical significance could not be attained due to the small sample size, TCho appeared to decline over the first 3 days *in vivo* in a manner comparable to the respective *in vitro* MTS results.

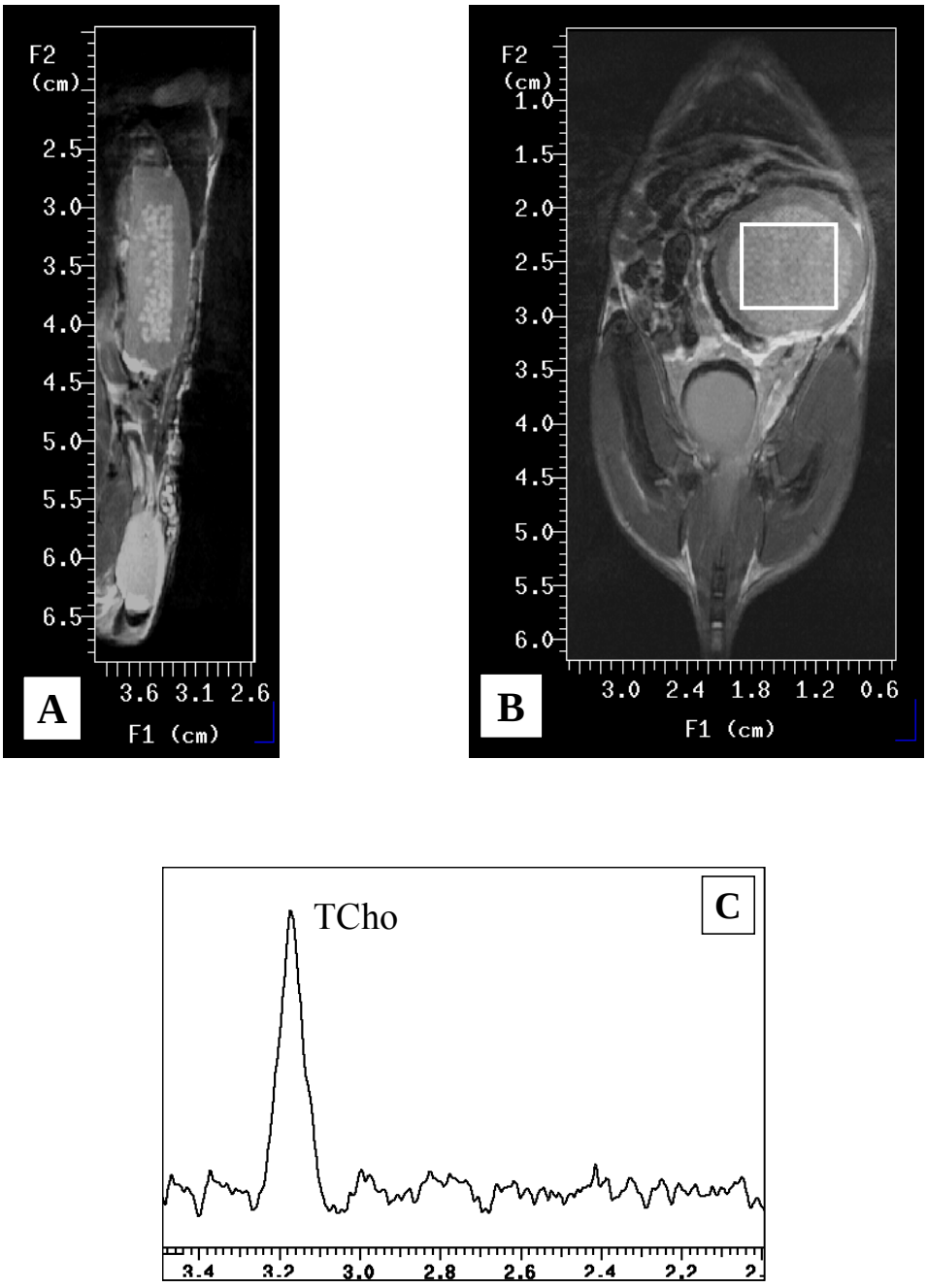

Figure A9. Sagittal (Panel A) and coronal (Panel B) spin-echo ^{1}H NMR images of an implanted agarose construct containing alginate beads loaded with 7x10^{7} βTC3 cells/mL alginate. The white box shown in Panel B is the VOI selected for the resulting localized, water-suppressed ^{1}H NMR spectra shown in Panel C.

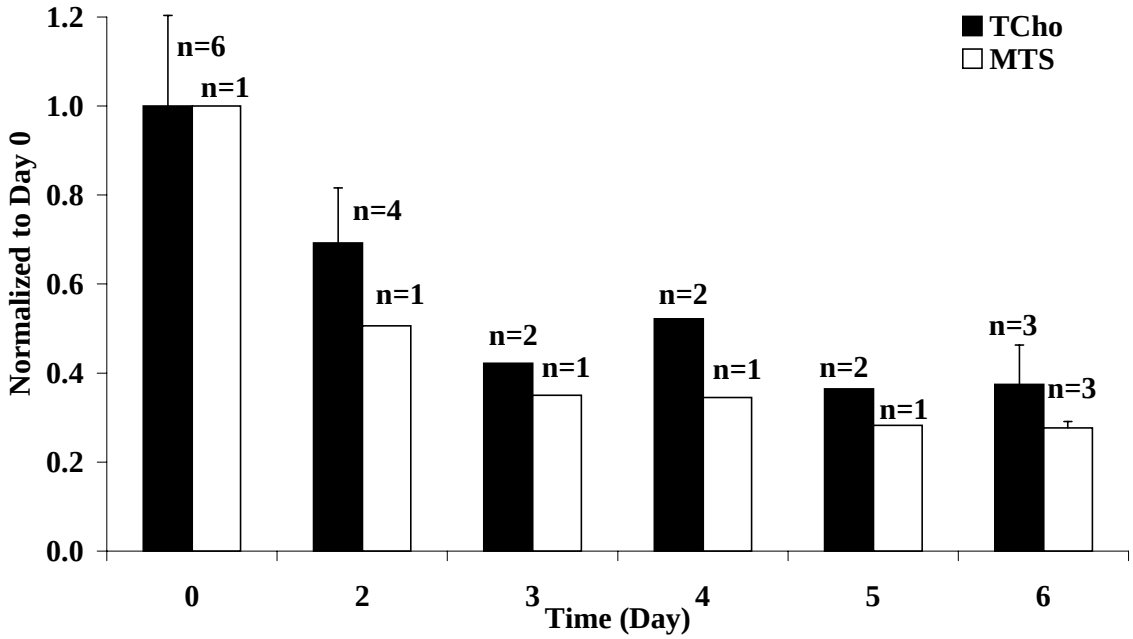

Figure A10. Temporal profile of *in vivo* TCho and *in vitro* MTS measurements within agarose constructs containing alginate beads loaded with $7x10^7$ βTC3 cells/mL alginate, over a period of six days.

Periodic ^{1}H NMR spin-echo images were collected from anesthetized mice during the duration of the experiments. For five animals, the implantation time was extended to two weeks to assess if structural changes in the implant could be visualized by ^{1}H NMR imaging. In four of the five animals, no changes were detectable in the implant over the two week period, and a moderate fibrotic response two to three cell layers thick was seen upon explantation; however, for one implant, the development of a white band was detected in the ^{1}H NMR spin-echo images, as shown in Figure A11. While a white band at the interface between the agarose and the host tissue was not seen on Day 1, the development of a thin white band at some portions of the interface was seen by Day 7, with the final Day 13 image showing a distinct bright band surrounding the entire construct.

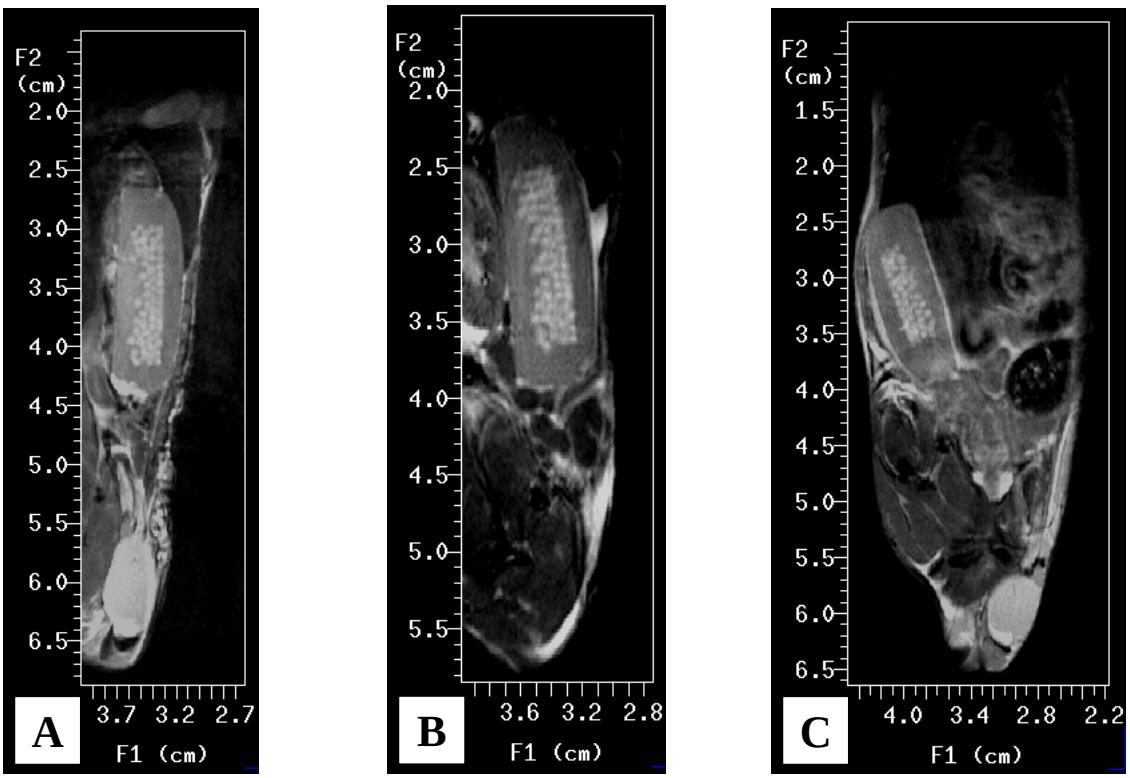

Figure A11. Sagittal spin-echo ^{1}H NMR images of a single implanted agarose construct containing alginate beads loaded with βTC3 cells on Day 1 (Panel A), Day 7 (Panel B), and Day 13 (Panel C).

Upon explantation, visual examination found a thick fibrotic cap coating the entire construct. H/E staining of a histological cross-section of the fibrotic cap illustrated a significant layer of host cells, as shown by Figure A12, Panel A (for details on histology method, see APPENDIX A.9.b). Compared to the typical host response, shown in Figure A12, Panel B, this fibrotic cap was significantly thicker and highly abnormal. While this response was not seen for any of the subsequent implants, these experiments provide evidence that the host response to the implant could be assessed noninvasively using ^{1}H NMR imaging.

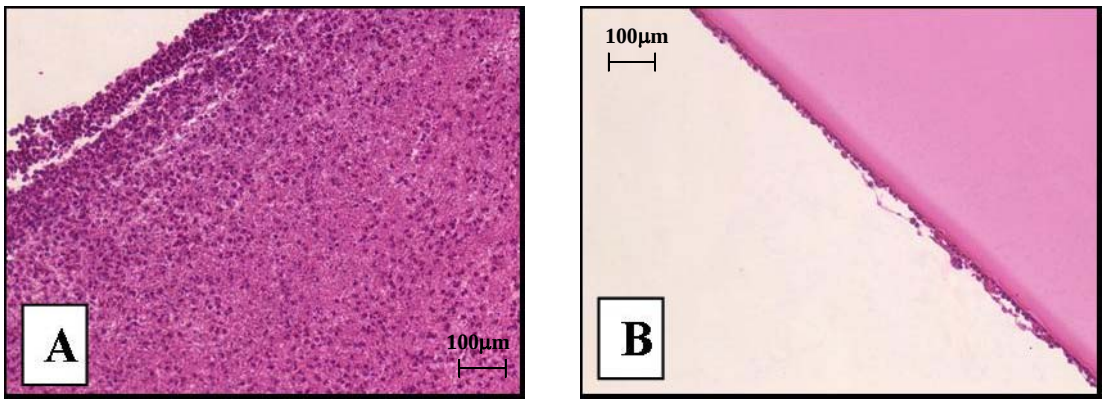

Figure A12. Paraffin embedded histological cross-sections of explanted agarose constructs containing alginate beads loaded with βTC3 cells stained with H/E. Panel A is the histological image of the fibrotic cap surrounding the construct explanted on Day 13 from Figure A11. Panel B represents the typical fibrotic response seen for explanted constructs on Day 13.

A.5. EFFECT OF GLUCOSE ON TOTAL-CHOLINE MEASUREMENT

As discussed in CHAPTER 8, glucose at the 3.22 ppm resonance interferes with the accurate quantification of the TCho peak area at 3.2 ppm. In order to account for this effect, a method was developed that would allow for the indirect, but accurate, quantification of the glucose peak at 3.22 ppm. Experimental data was collected using cell-free agarose constructs equilibrated in sera-free DMEM containing varying concentrations of glucose. Localized, water-suppressed ^{1}H NMR spectra were collected using the NMR acquisition parameters described in CHAPTERS 8 and 9. The resulting glucose peaks in the collected ^{1}H NMR spectra, such as the intensity of the glucose peak at 3.85 ppm, are strongly correlated to glucose concentration, as can be seen in Figure A13, where the intensity of the 3.85 ppm peak was calculated as the difference between the baseline of the spectra and the maximum value of the 3.95 ppm peak. The individual glucose peaks also share a strict, linear relationship to each other. To investigate the effects of glucose on accurately quantifying TCho peak area, the peak at 3.2 ppm was integrated for the varying glucose concentrations. Figure A14 correlates this area to the intensity of the glucose peak at 3.85 ppm. The intensity of the 3.85 ppm peak was used instead of peak area, given the fact that its peak shape is not easily fitted by Gaussian and/or Lorentzian functions (see spectra in CHAPTERS 8 & 9). Two conclusions were reached from these cell-free experiments: (1) glucose contributes significantly to TCho peak area quantification under high glucose concentrations; and (2) a strong, linear relationship (R^2=0.98) could be defined between the peak area at 3.2 ppm and the peak intensity at 3.85 ppm. Thus, while the glucose effects on TCho measurement can not be ignored, Figure A14 provides an indirect means to account for glucose effects on TCho,

by simply assessing the intensity of glucose peak at 3.85 ppm. The validity of this method for accurately measuring TCho in the presence of glucose is further explored in CHAPTER 8.

Once the construct is placed within the *in vivo* environment, solutes from the peritoneal cavity easily diffuse within the construct. Therefore, it was expected that glucose would infiltrate the VOI and result in the need to account for its effects. One concern, however, was using an *in vitro*-based relationship to account for *in vivo* solutes. While the strict relationship between the individual glucose peaks is inherent, the exact nature of this correlation is highly dependent upon NMR acquisition parameters and environmental conditions. Furthermore, *in vivo*, additional contaminating solutes or contributions from macromolecules that are not identifiable *in vitro* could be present. Therefore, several cell-free agarose implants were monitored over different time points, while the glucose level within the VOI was varied by fasting the mice for a time period extending from 0 to 12 hrs prior to NMR scanning. Interperitoneal saline injections were also performed to dilute the surrounding host fluid (see APPENDIX A6 for further details). Localized, water-suppressed ^{1}H NMR spectra were collected from the constructs, using the same acquisition parameters described in CHAPTERS 8 AND 9, and the resulting peaks at 3.85 ppm and 3.2 ppm were correlated. Figure A15 illustrates this relationship. While a strong, linear relationship (R^2=0.90) between the 3.2 ppm peak area and 3.85 ppm peak intensity was also established *in vivo*, the slope of the line is slightly different than that determined *in vitro*. Therefore, for all *in vivo* experiments, the linear relationship illustrated in Figure A15 was used to account for contaminating effects.

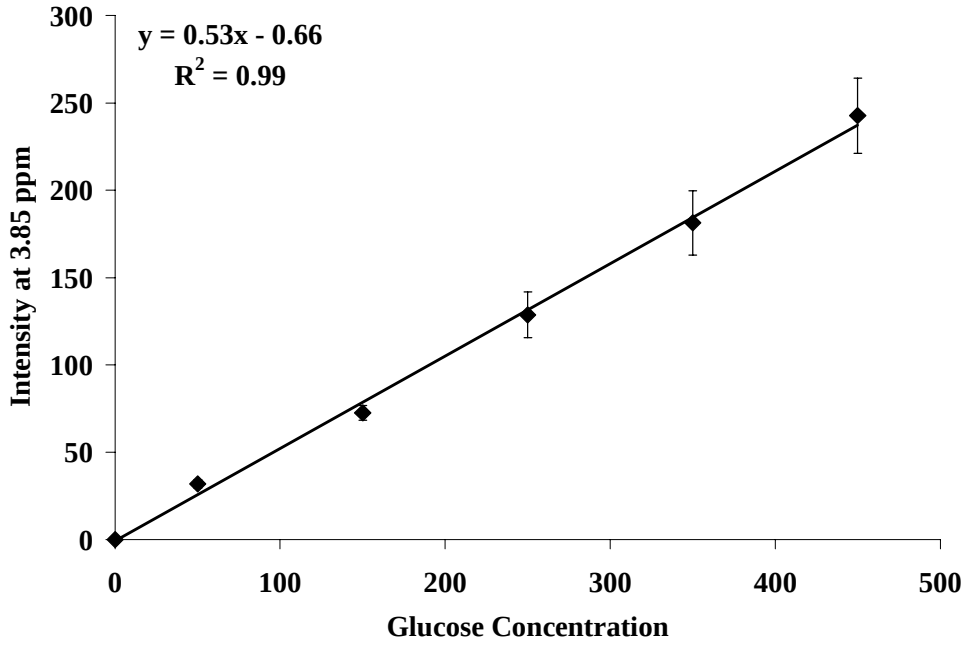

Figure A13. *In vitro* correlation between glucose concentration and the intensity of the resulting ^{1}H NMR spectroscopy peak at the 3.85 ppm resonance for cell-free agarose constructs bathed in varying concentrations of glucose.

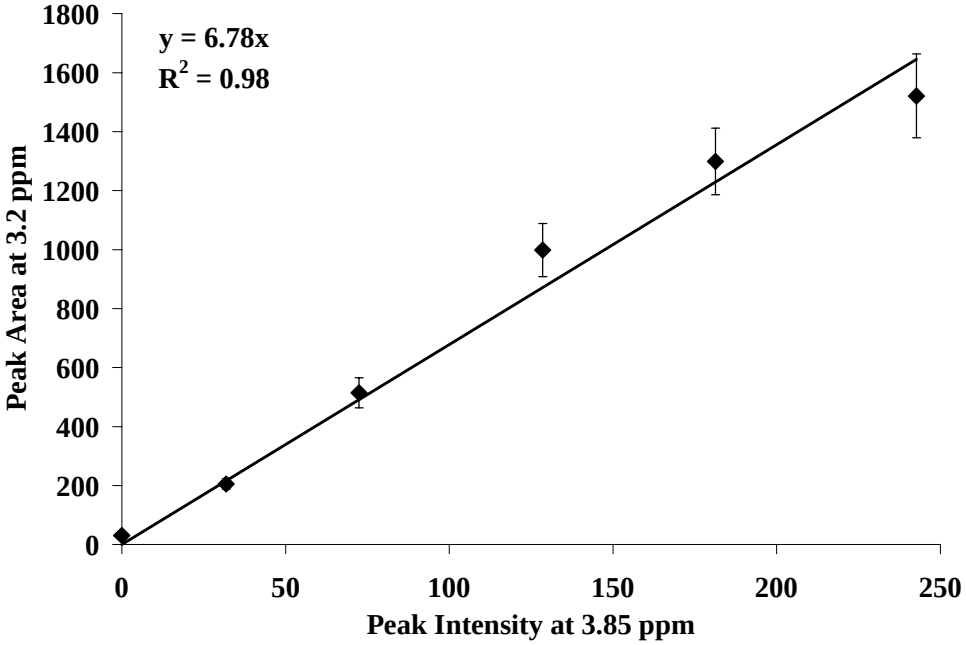

Figure A14. *In vitro* correlation between peak intensity at 3.85 ppm and peak area at 3.2 ppm for cell-free agarose constructs bathed in varying concentrations of glucose.

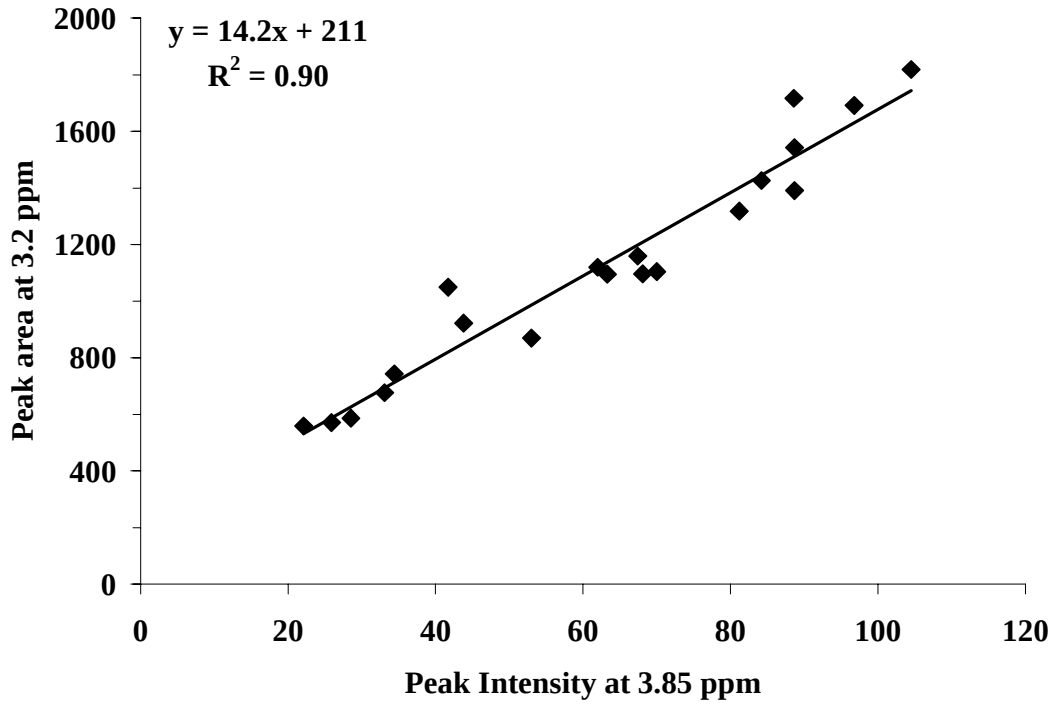

Figure A15. *In vivo* correlation between peak intensity at 3.85 ppm and peak area at 3.2 ppm for cell-free agarose constructs implanted in C57Bl/6J mice.

A.6. ANESTHESIA EFFECTS ON BLOOD GLUCOSE

As outlined in APPENDIX A5, when glucose concentrations are high, the contaminating effects of glucose on accurate TCho quantification are significant. For the accuracy of *in vivo* TCho measurements and to ensure the ability to monitor constructs at the lower limits of the TCho assay, the blood glucose levels of the studied mice must be maintained at a reasonable level. While it was expected that diabetic mice would exhibit high glucose levels, our initial NMR experiments found glucose levels within normal C57BL/6J mice to be comparable to their untreated diabetic counterparts. It was concluded that the high glucose levels found in normal C57BL/6J mice during NMR scanning were due to the anesthetic. Figure A16 illustrates the effect of the ketamine/xylazine anesthetic on the blood glucose levels for normal C57BL/6J mice over the course of 2.5 hrs. This figure shows the stark difference between the temporal blood glucose levels for anesthetized (filled diamonds) and non-anesthetized (open diamonds) mice, where blood glucose levels in the diabetic regime were transiently observed for anesthetized mice. The slight increase in blood glucose levels of the non-anesthetized mice was expected, given the documented relationship between blood glucose and stress levels [202]. Literature review supports this data, where researchers have found xylazine, an α_2-receptor mediated anesthetic, to transiently inhibit beta cell function [203]. Other anesthetics documented to inhibit insulin secretion include medetomidine, also an α_2-receptor agonist [204], isoflurane [205], and urethane [206] (see Table A1).

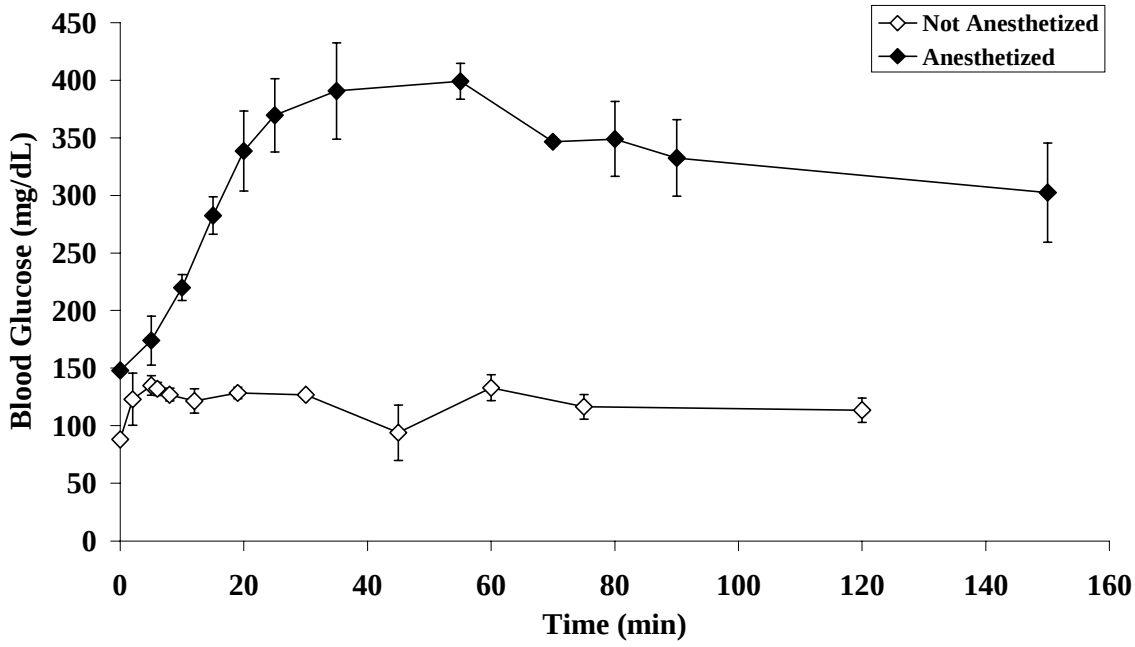

Figure A16. Temporal profile of blood glucose levels for normal C57BL/6J mice collected while either non-anesthetized (open diamonds) or anesthetized (solid diamonds).

Based on the NMR experimental protocols, four factors are critical in the anesthetization of the mice: (1) inducement of heavy anesthesia for over 1 hr; (2) stability of animal while confined in magnet; (3) ease in animal recovery; and (4) retention of effectiveness over multiple anesthetic doses. Therefore, selecting a comparable anesthetic to replace the ketamine/xylazine combination proved to be difficult, as outlined in Table A1. Traditional dosage and delivery method (Dsg/Dlv) for each anesthetic is listed (IP appreviation for interperitoneal). Dosage is in mg/kg unless otherwise noted. Known blood glucose effects are listed, along with common side effects. As can be see from the table, Avertin is not ideal, based on its sensitization and inflammatory properties after multiple doses [207-209]. Chloral hydrate is a harsh anesthetic not recommended for multiple applications [210], while pentobarbital induces

hypothermia and depresses respiration, making long-term stability of the mouse within the magnet difficult [209]. Therefore, the ability of the ketamine/xylazine combination to provide a safe, stable, and long-term anesthetic state makes this drug superior to the other commonly used anesthetics.

Table A1. Summary of common anesthetic agents for mice.

Agent	Dsg/Dlv	Blood Glucose Effects	Other Effects/Problems
Avertin (tribromoethanol)	240-375 IP	Unknown	Shown to have inflammatory properties/difficult to procure, sensitization to repetitive injections
Chloral hydrate	400 IP	Unknown	Not very stable, difficult for repetitive anesthesia
Medetomidine + ketamine	1 IP + 75 IP	**Medetomidin – inhibits beta cell function**	
Pentobarbital	50-80 IP	Minimal	Profound respiratory depressant, hypothermia a common problem
Pentobarbital + Ketamine	----	Minimal	Cannot be used in mice (Rats only)
Urethane	1000-1500 IP	**Inhibits beta cell function**	Chemical hazard, should only be used for non-survival procedures
Xylazine+ Ketamine	15 IP + 100 IP	**Zylazine inhibits beta cell function**	Effective anesthetic agent for over 1hour deep anesthesia
Isoflurane	Inhalant	**Isoflurane inhibits beta cell function**	
Methoxyflurane	Inhalant		Nephrogenic diabetes insipidus

If use of the ketamine/xylazine anesthetic was to continue, measures needed to be implemented to dampen the transient effects of the agent on glucose levels. Two procedures were employed to reduce the presence of glucose within the VOI during the

NMR experiments: (1) mice were fasted for 10 hrs prior to the start of the NMR experiment; and (2) 1 mL of saline was injected into the peritoneal cavity of the mice immediately following the administration of the anesthetic. The effectiveness of step (1) in reducing blood glucose levels is illustrated in Figure A17, where blood glucose levels under anesthesia were significantly dampened when mice were fasted (solid triangles), in comparison to non-fasted mice (solid diamonds). Fasting only occurred 10 hrs prior to the start of the NMR scan and was only implemented a maximum of three times per animal. Body weight measurements of normal C57BL/6J mice during experimental time periods found minimal effects of fasting (less than 1%), as shown in Figure A18. In this figure, fasted mice underwent three incidences of 10 hr fasting periods on Days, 2, 5, and 8. None of the mice shown in Figure A18 received surgical implants during the time frame shown in this graph. Saline injections in the peritoneal cavity prior to NMR scanning were also helpful in diluting glucose concentration in the VOI of the construct and assisted in the collection of NMR spectra, by increasing the shimming capacity of the sample.

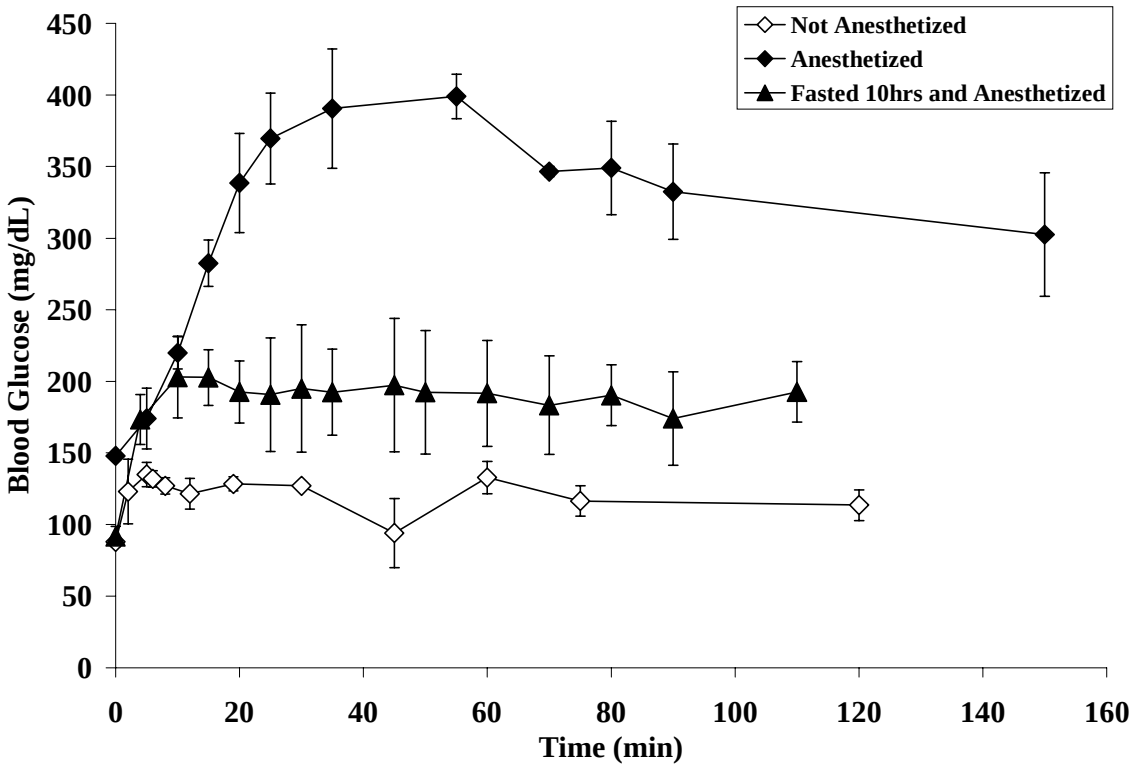

Figure A17. Temporal profile of blood glucose levels for normal C57BL/6J mice collected while either non-anesthetized (open diamonds), anesthetized (solid diamonds), or anesthetized after fasting for 10 hrs (solid triangles).

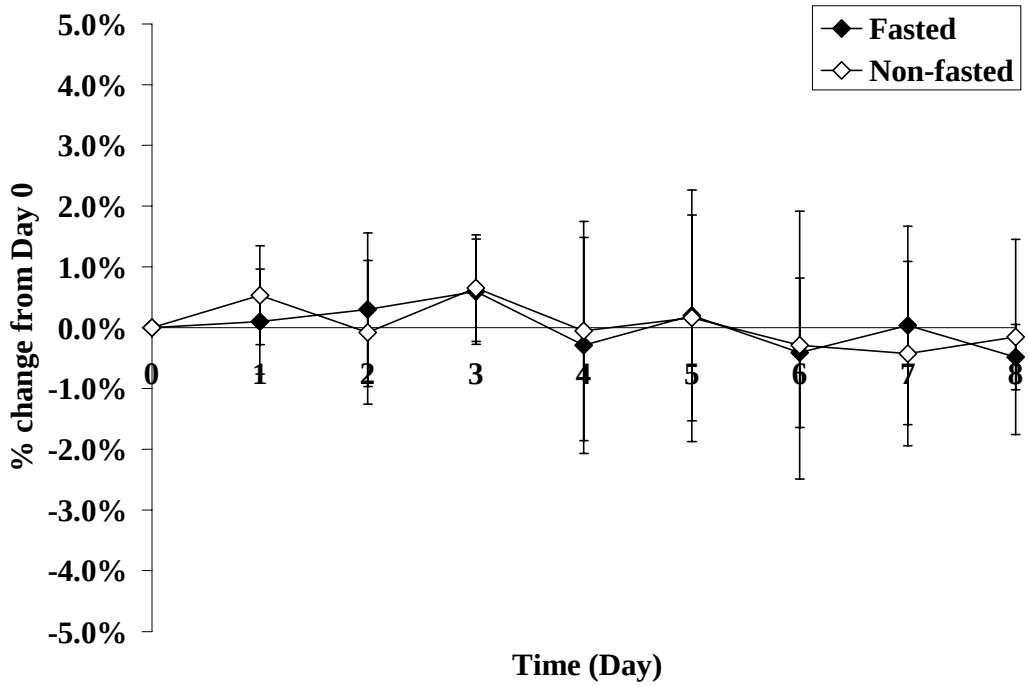

Figure A18. Body weight measurements of normal C57BL/6J mice under either non-fasted (open diamonds) or fasted (solid diamond) conditions.

A.7. TOTAL-CHOLINE CALIBRATION CURVE FOR OTHER BETA CELL LINE

The primary cell line explored in this thesis was the βTC3 cell line. In order to explore the applicability of the techniques developed in this thesis to monitoring other beta cells lines, preliminary experiments were conducted using the βTC-tet cell line, a continuous beta cell line transfected with a tetacycline-conditioned gene expression system to control proliferation. For these experiments, a calibration curve correlating TCho and viable cell number on Day 0, similar to that described in Chapter 8 for βTC3 cells, were generated. Figure A19 compares the βTC-tet calibration curve to that for βTC3 cells. These two cell lines exhibit very similar TCho values.

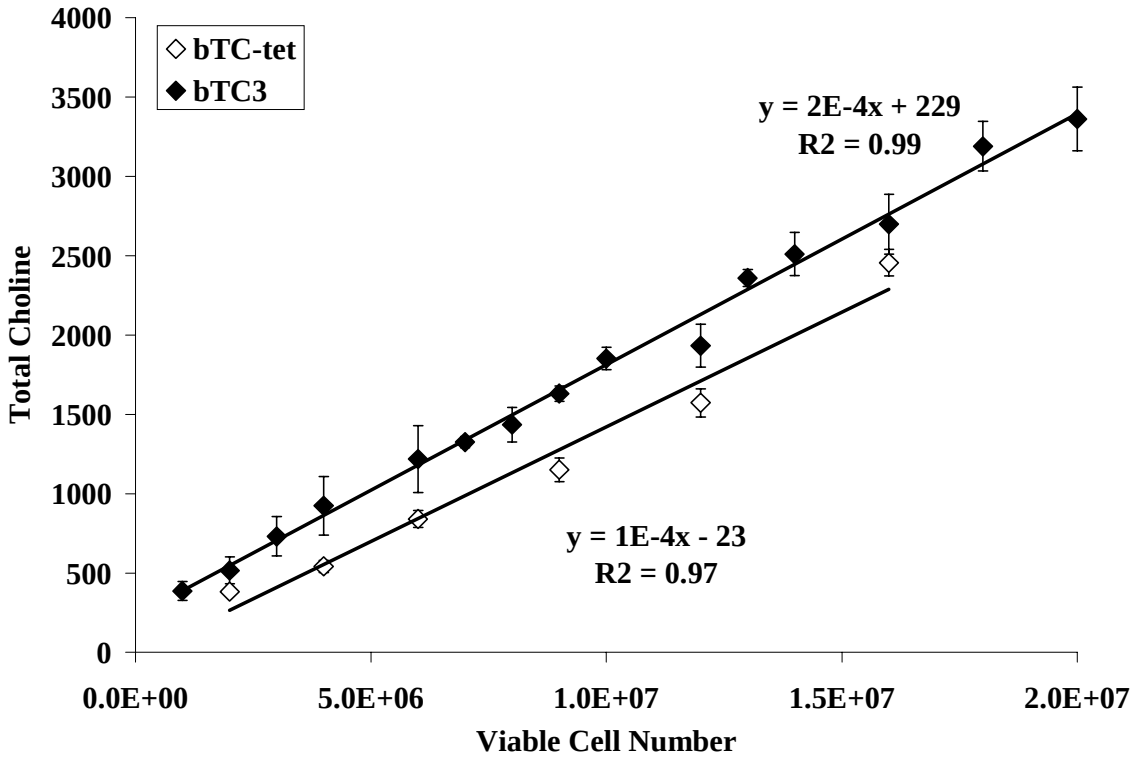

Figure A19. Comparison between TCho and viable cell number for βTC3 cells (solid diamonds) and βTC-tet cells (open diamonds).

A.8. EFFECTS OF MION ON METABOLIC AND SECRETORY ACTIVITY OF βTC3 AND βTC-TET CELLS

Monocrystalline iron oxide nanoparticles (MION) have shown significant promise for noninvasive imaging of cells *in vivo*, such as T cells. We explored the applicability of superparamagnetic labeling for beta cells. Preliminary studies were conducted to test the effects of MION particles on the metabolic and secretory activity for βTC3 and βTC-tet cells in monolayer cultures when exposed to varying dilutions of 30 mM MION over time periods from 4 to 24 hrs. For both cell types and incubation periods, the majority of the dilutions, from 1 to 5 up to 1 to 50, showed were comparable to the control monolayers, which contained no MION. In some cultures, the presence of MION appeared to cause slight declines in the metabolic or secretory activity of the cells, see Figures A 20-22, but primarily at the lower dilutions. Each data point represents the average ± std from three independent cultures. * indicates statistically different values ($p < 0.05$) compared to the control (no MION). These experiments establish the feasibility of using MION superparamagnetic particles for use in beta cell lines.

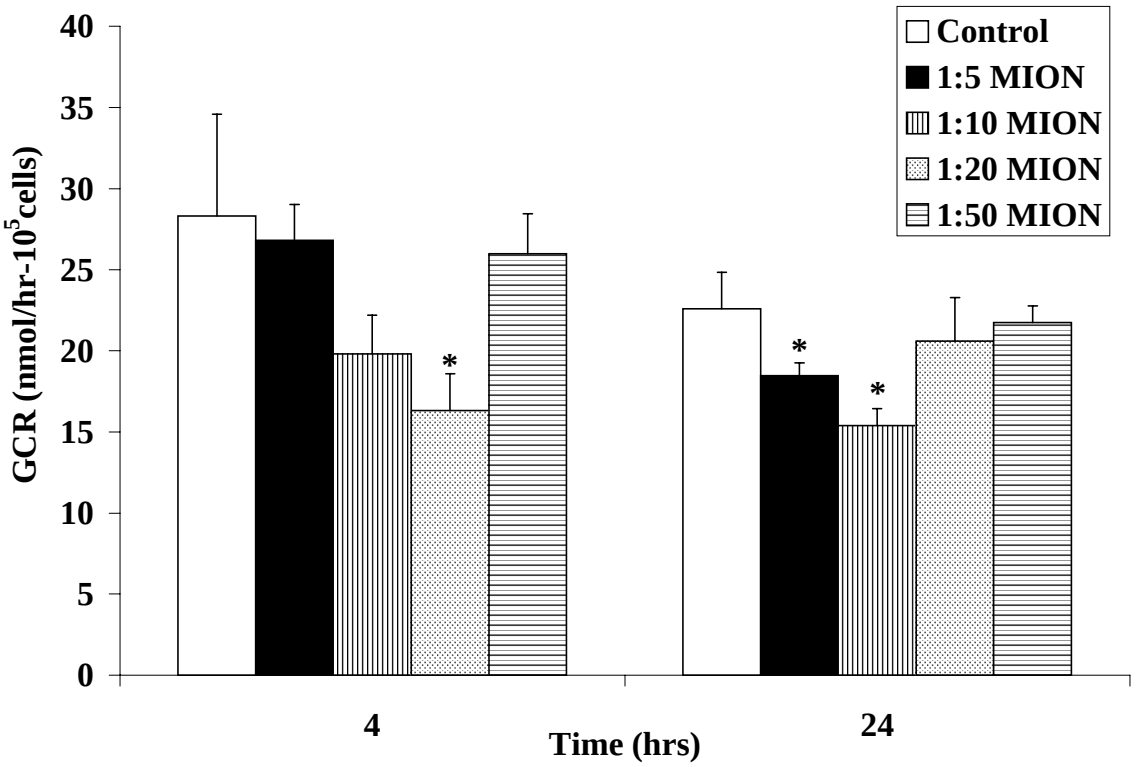

Figure A20. Comparison of glucose consumption rates for βTC3 cells in monolayers. Cells were exposed to varying dilutions (specified by 1:5, etc) of 30mM MION solution and glucose consumption rates were calculated for 4 and 24 hr time periods.

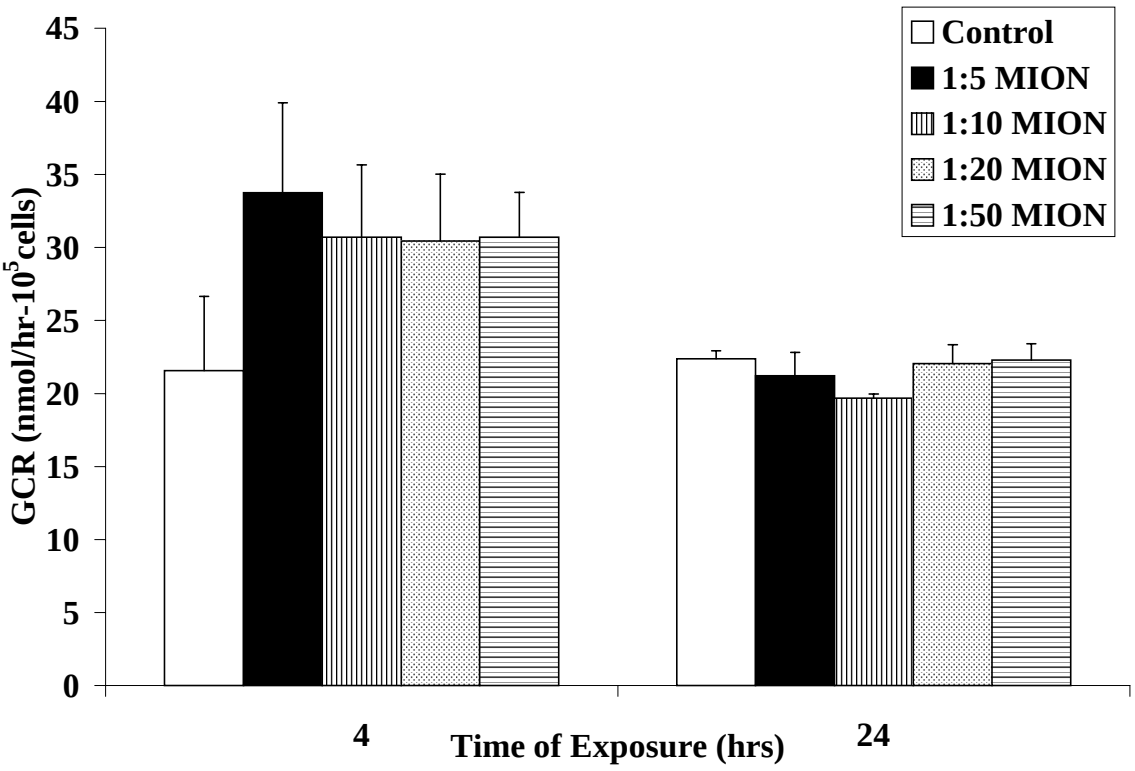

Figure A21. Comparison of glucose consumption rates for βTC-tet cells in monolayers. Cells were exposed to varying dilutions (specified by 1:5, etc) of 30mM MION solution and glucose consumption rates were calculated for 4 and 24 hr time periods.

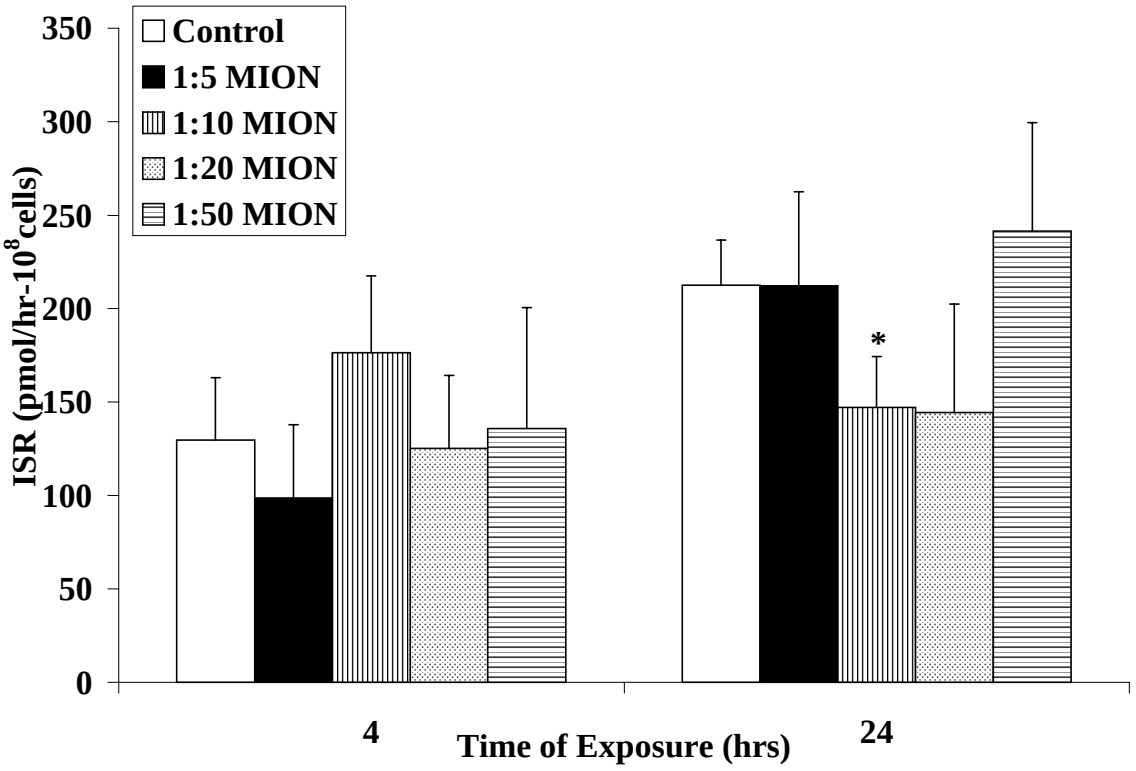

Figure A22. Comparison of insulin secretion rates for βTC-tet cells in monolayers. Cells were exposed to varying dilutions (specified by 1:5, etc) of 30mM MION solution and insulin secretion rates were calculated for 4 and 24 hr time periods.

A.9. REFERENCED METHODS

A.9.a MTS measurement of viable cell number of alginate beads in agarose

To measure the viable cell number for the agarose/alginate constructs using the CellTiter 96 MTS assay (Promega, Madison, WI), the alginate beads were first released from the agarose matrix using a scalpel. Beads were taken from varying regions of the construct to ensure a heterogeneous distribution. Single beads were incubated in separate wells of a 96-well plate (Corning, Acton, MA), each containing 100 μL of fully supplemented DMEM and 20 μL of MTS, for 3 hrs at 37°C, 5% CO_2 / 95% air. For background absorbance, cell-free alginate beads were used. Following incubation, the absorbance was read at 490 nm, while ensuring protection from light in the interim stages. Absorbance values were then corrected by subtracting the controls, converted to cell number using a previously generated calibration curve, and numerically averaged.

A.9.b Histological processing of Alginate/Poly-L-lysine/Alginate beads

Alginate/poly-L-lysine/alginate beads are quite sensitive to normal fixation methods involving formalin or formaldehyde. APA beads have a tendency to rapidly break open upon exposure to these compounds due to disruption of the ionic bonds holding the beads together. Therefore, to prepare beads properly for paraffin embedding, a fixation by 3% glutaraldehyde for a minimum of 48 hrs was necessary. For high mannuronic alginates, quick exposure to glutaraldehyde can cause bead rupture, therefore these beads were exposed to a quick rinse of calcium chloride prior to glutaraldehyde exposure. After 48 hrs, the glutaraldehyde was removed, beads were washed with Millonig's Buffer four times, fixed with 70% ethanol, and incubated for a minimum of 24 hrs. The beads were

then placed in labeled cassettes and processed using the following sequence of steps: 70% alcohol rinse (3 times); incubation in 80% alcohol for 15 minutes, in 95% alcohol for 15 minutes, and 100% alcohol for 20 minutes; 100% alcohol incubation repeated five times; xylene incubation six times at 10 min per wash; paraffin incubation three times at 20 min per wash; and a final wash with paraffin for 30 mins. Following processing, cassettes were then embedded and cut to 10 mm thick slices using standard histological methods.

REFERENCES

1. Centers for Disease Control and Prevention. National diabetes fact sheet: general information and national estimates on diabetes in the United States, 2003. Atlanta, GA, U.S. Department of Health and Human Services, Centers for Disease Control and Prevention, 2003.

2. Gadian, D. NMR and its applications to living systems. Oxford: Oxford University Press. 1995.

3. Podo, F. Tumour phospholipid metabolism. NMR Biomed 12:413-439. 1999.

4. Negendank, W.G., Sauter, R., Brown, T.R., Evelhoch, J.L., Falini, A., Gotsis, E.D., Heerschap, A., Kamada, K., Lee, B.C., Mengeot, M.M. *et al*. Proton magnetic resonance spectroscopy in patients with glial tumors: a multicenter study. J Neurosurg 84(3):449-58. 1996.

5. Certaines, J.d., Bovee, W., Podo, F. Magnetic resonance spectroscopy in biology and medicine: functional and pathological tissue characterization. Oxford: Pergamon Press. 1992.

6. Miller, B., Change, L., Booth, R., Ernst, T., Cornford, M., Nikas, D., McBride, D., Jenden, D. In vivo 1H MRS choline: correlation with in vitro chemistry/histology. Life Sciences 58(22):1929-1935. 1996.

7. Long, R.C., Papas, K.K., Sambanis, A., Constantinidis, I. In vitro monitoring of total choline levels in a bioartificial pancreas: (1)H NMR spectroscopic studies of the effects of oxygen level. J Magn Reson 146(1):49-57. 2000.

8. Papas, K.K., Long, R.C., Sambanis, A., Constantinidis, I. Development of a bioartificial pancreas: I. long-term propagation and basal and induced secretion from entrapped betaTC3 cell cultures. Biotechnol Bioeng 66(4):219-30. 1999.

9. Papas, K.K., Long, R.C., Sambanis, A., Constantinidis, I. Development of a bioartificial pancreas: II. Effects of oxygen on long-term entrapped betaTC3 cell cultures. Biotechnol Bioeng 66(4):231-7. 1999.

10. Tziampazis, E. Engineering functional, insulin-secreting cell systems: effect of entrapment on cellular environment and secretory response [Masters Thesis]. Atlanta: Georgia Institute of Technology. 115 pgs. 1993.

11. Report of the expert committee on the diagnosis and classification of diabetes mellitus. Diabetes Care 26 Suppl 1:S5-20. 2003.

12. The effect of intensive treatment of diabetes on the development and progression of long-term complications in insulin-dependent diabetes mellitus. The Diabetes Control and Complications Trial Research Group. N Engl J Med 329(14):977-86. 1993.

13. Ryan, E.A., Lakey, J.R., Paty, B.W., Imes, S., Korbutt, G.S., Kneteman, N.M., Bigam, D., Rajotte, R.V., Shapiro, A.M. Successful islet transplantation: continued insulin reserve provides long-term glycemic control. Diabetes 51(7):2148-57. 2002.

14. Ryan, E.A., Lakey, J.R., Rajotte, R.V., Korbutt, G.S., Kin, T., Imes, S., Rabinovitch, A., Elliott, J.F., Bigam, D., Kneteman, N.M. *et al*. Clinical outcomes and insulin secretion after islet transplantation with the Edmonton protocol. Diabetes 50(4):710-9. 2001.

15. Lim, F., Sun, A. Microencapsulated islets as bioartificial endocrine pancreas. Science 210:908-10. 1980.

16. Sun, A.M., Parisius, W., Healy, G.M., Vacek, I., Macmorine, H.G. The use, in diabetic rats and monkeys, of artificial capillary units containing cultured islets of Langerhans (artificial endocrine pancreas). Diabetes 26(12):1136-9. 1977.

17. Reach, G. Bioartificial pancreas. Transplant Proc 26(2):397-8. 1994.

18. Soon-Shiong, P., Heintz, R.E., Merideth, N., Yao, Q.X., Yao, Z., Zheng, T., Murphy, M., Moloney, M.K., Schmehl, M., Harris, M. *et al*. Insulin independence in a type 1 diabetic patient after encapsulated islet transplantation. Lancet 343(8903):950-1. 1994.

19. Lanza, R.P., Chick, W.L. Transplantation of encapsulated cells and tissues. Surgery 121(1):1-9. 1997.

20. Efrat, S. Cell replacement therapy for type 1 diabetes. Trends Molec Med 8(7):334-339. 2002.

21. Soria, B., Andreu, E., Berna, G., Fuentes, E., Gil, A., Leon-Quinto, T., Martin, F., Montanya, E., Nadal, A., Reig, J.A. *et al*. Engineering pancreatic islets. Pflugers Arch 440(1):1-18. 2000.

22. Efrat, S., Linde, S., Kofod, H., Spector, D., Delannoy, M., Grant, S., Hanahan, D., Baekeskov, S. Insulin synthesis in a clonal cell line of simian virus 40-transformed hamster pancreatic beta cells. Proc Natl Acad Sci USA 85:9037-9041. 1988.

23. Efrat, S., Linde, S., Kofod, H., Spector, D., Delannoy, M., Grant, S., Hanahan, D., Baekkeskov, S. Beta-cell lines derived from transgenic mice expressing a hybrid insulin gene-oncogene. Proc Natl Acad Sci U S A 85(23):9037-41. 1988.

24. Efrat, S., Fusco-DeMane, D., Lemberg, H., al Emran, O., Wang, X. Conditional transformation of a pancreatic beta-cell line derived from transgenic mice expressing a tetracycline-regulated oncogene. Proc Natl Acad Sci U S A 92(8):3576-80. 1995.

25. Papas, K.K., Long, R.C., Constantinidis, I., Sambanis, A. Effects of oxygen on metabolic and secretory activities of beta TC3 cells. Biochim Biophys Acta 1291(2):163-6. 1996.

26. Dionne, K.E., Colton, C.K., Yarmush, M.L. Effect of hypoxia on insulin secretion by isolated rat and canine islets of Langerhans. Diabetes 42(1):12-21. 1993.

27. De Vos, P., Hamel, A.F., Tatarkiewicz, K. Considerations for successful transplantation of encapsulated pancreatic islets. Diabetologia 45(2):159-73. 2002.

28. Stock, U.A., Vacanti, J.P. Tissue engineering: current state and prospects. Annu Rev Med 52:443-51. 2001.

29. Grant, G.T., Morris, E.R., Rees, D.A., Smith, P.J.C., Thom, D. Biological interactions between polysaccharides and divalent cations: the egg-box model. FEBS Letters 32(1):195-198. 1973.

30. Martinsen, A., Skjak-Braek, G., Smidsred, O. Alginate as immobilization material: I. Correlation between chemical and physical properties of alginate gel beads. Biotechnology and Bioengineering 33:79-89. 1989.

31. Colton, C.K. Engineering challenges in cell-encapsulation technology. Trends Biotechnol 14(5):158-62. 1996.

32. Araki, C., Arai, K. Studies on the chemical constitution of agar-agar. XXIV. Isolation of a new disaccharide as a reversion product from acidic hydrolysate. Bull Chem Soc Jpn 40(6):1452-6. 1967.

33. Ng-Ying-Kin, N.M., Yaphe, W. Properties of agar: parameters affecting gel-formation and the agarose-iodine reaction. Carbohydr Res 25(2):379-85. 1972.

34. Liang, J., Stevens, E., Morris, E., Rees, D. Spectroscopic Origin of Conformation-Sensitive Contributions to Polysaccharide Optical Activity: Vacuum-Ultraviolet Circular Dichroism of Agarose. Biopolymers 18:327-333. 1979.

35. Normand, V., Lootens, D.L., Amici, E., Plucknett, K.P., Aymard, P. New insight into agarose gel mechanical properties. Biomacromolecules 1(4):730-8. 2000.

36. Xu, B., Iwata, H., Miyamoto, M., Balamurugan, A.N., Murakami, Y., Cui, W., Imamura, M., Inoue, K. Functional comparison of the single-layer agarose microbeads and the developed three-layer agarose microbeads as the bioartificial pancreas: an in vitro study. Cell Transplant 10(4-5):403-8. 2001.

37. Hayashi, H., Inoue, K., Aung, T., Tun, T., Yanjun, G., Wenjing, W., Shinohara, S., Kajl, H., Doi, R., Setoyama, H. *et al*. Application of a novel B cell line MIN6 to a mesh-reinforced polyvinyl alcohol hydrogel tub and three layer agarose microcapsules: an in vitro study. Cell Transplant 5(5S-1):S65-S69. 1996.

38. Hung, C.T., Lima, E.G., Mauck, R.L., Taki, E., LeRoux, M.A., Lu, H.H., Stark, R.G., Guo, X.E., Ateshian, G.A. Anatomically shaped osteochondral constructs for articular cartilage repair. J Biomech 36(12):1853-64. 2003.

39. Maki, T., Lodge, J., Carretta, M., Ohzato, H., Borland, K., Sullivan, S., Staruk, J., Muller, T., Solomon, B., Chick, W.L. *et al*. Treatment of severe diabetes mellitus for more than 1 year using a vascularized hybrid artificial pancreas. Transplantation 55:713-718. 1993.

40. Sun, A.M. Microencapsulation of pancreatic islet cells: a bioartificial endocrine pancreas. Methods Enzymol 137:575-80. 1988.

41. Archer, J., Kaye, R., Mutter, G. Control of streptozotocin diabetes in Chinese hamsters by cultured mouse islet cells without immunosuppression: a preliminary report. J Surg Res 28(1):77-85. 1980.

42. Altman, J.J., McMillan, P., Callard, P., Galletti, P.M. A bioartificial pancreas prevents chronic complications of diabetes in rats. ASAIO Trans 32(1):145-7. 1986.

43. Hirotani, S., Eda, R., Kawabata, T., Fuchinoue, S., Teraoka, S., Agishi, T., Ohgawara, H. Bioartificial endocrine pancreas (bio-AEP) for treatment of diabetes: effect of implantation of bio-AEP on the pancreas. Cell Tranplant 8:399-404. 1999.

44. Prevost, P., Flori, S., Collier, C., Muscat, E., Rolland, E. Application of AN69 hydrogel to islet encapsulation. Ann NY Acad Sci 831:344-349. 1997.

45. Rafeal, E., Wernerson, A., Arner, P., Wu, G., Tibell, A. In vivo evaluation of glucose permeability of an immunoisolation device intended for islet transplantation: a novel application of the microdialysis technique. Cell Transplant 8:317-326. 1999.

46. Zmora, S., Glicklis, R., Cohen, S. Tailoring the pore architecture in 3-D alginate scaffolds by controlling the freezing regime during fabrication. Biomaterials 23(20):4087-94. 2002.

47. Yang, H., Iwata, J., Shimizu, H., Takagi, T., Tsuji, T., Ito, F. Comparative studies of in vitro and in vivo function of three different shaped bioartificial pancreases made of agarose hydrogel. Biomaterials 15(2):113-120. 1994.

48. Maki, T., Otsu, I., O'Neil, J., Dunleavy, K., Mullon, C., Solomon, B., Monaco, A. Treatment of diabetes by xenogeneic islets without immunosuppression. Diabetes 45:342-347. 1996.

49. Wolters, G., Fritschy, W., Gerrits, D., Schilfgaarde, R.C. A versatile alginate droplet generator applicable for microencapsulate of pancreatic islets. J Appl Biomat 3:281-286. 1992.

50. Halle, J., Leblond, F., Pariseau, J., Jutras, P., Brabant, M., Lepage, Y. Studies on small (<300 microns) microcapsules: II. Parameters governing the production of alginate beads by high voltage electrostatic pulses. Cell Tranplant 3:365-372. 1994.

51. O'Shea, G., Goosen, M., Sun, A. Prolonged survival of transplanted islets of Langerhans encapsulated in a biocompatible membrane. Biochim Biophys Acta 804:133-136. 1984.

52. O'Shea, G., Sun, A. Encapsulation of rat islets prolongs xenograft survival in diabetic mice. 1986 Diabetes(35):943-946. 1986.

53. Fan, M., Lum, Z., Fu, X., Levesque, L., Tai, I., Sun, A. Reversal of diabetes in BB rats by transplantation of encapsulated pancreatic islets. Diabetes 39:519-522. 1990.

54. Lum, Z.P., Tai, I.T., Krestow, M., Norton, J., Vacek, I., Sun, A.M. Prolonged reversal of diabetic state in NOD mice by xenografts of microencapsulated rat islets. Diabetes 40(11):1511-6. 1991.

55. Lysaght, M.J., Aebischer, P. Encapsulated cells as therapy. Sci Am 280(4):76-82. 1999.

56. Soon-Shiong, P., Feldman, E., Nelson, R., Heintz, R., Merideth, N., Sandford, P., Zheng, T., Komtebedde, J. Long-term reversal of diabetes in the large animal model by encapsulated islet transplantation. Transplant Proc 24(6):2946-7. 1992.

57. Iwata, H., Takagi, T., Amemiya, H., Shimizu, H., Yamashita, K., Kobayashi, K., Akutsu, T. Agarose for a bioartificial pancreas. J Biomed Mater Res 26(7):967-77. 1992.

58. Tashiro, H., Iwata, H., Warnock, G.L., Takagi, T., Machida, H., Ikada, Y., Tsuji, T. Characterization and transplantation of agarose microencapsulated canine islets of Langerhands. Ann Transplant 2:33-39. 1997.

59. Tun, T., Inoue, K., Hayashi, H., Aung, T., Gu, Y.J., Doi, R., Kaji, H., Echigo, Y., Wang, W.J., Setoyama, H. *et al*. A newly developed three-layer agarose microcapsule for a promising biohybrid artificial pancreas: rat to mouse xenotransplantation. Cell Transplant 5(5 Suppl 1):S59-63. 1996.

60. Aomatsu, Y., Nakajima, Y., Ohyama, T., Kin, T., Kanehiro, H., Hisanaga, M., Ko, S., Nagao, M., Tatekawa, Y., Sho, M. *et al*. Efficacy of agarose/polystyrene sulfonic acid microencapsulation for islet xenotransplantation. Transplant Proc 32:1071-72. 2000.

61. Ohgawara, H., Hirotani, S., Miyazaki, J., Teraoka, S. Membrane immunoisolation of a diffusion chamber for bioartificial pancreas. Artif Organs 22(9):788-94. 1998.

62. Ohgawara, H., Miyazaki, J., Karibe, S., Katagiri, N., Tashiro, F., Akaike, T. Assessment of pore size of semipermeable membrane for immunoislation on xenoimplantation of pancreatic B cells using a diffusion chamber. Transplant Proceed 27(6):3319-3320. 1995.

63. Hirotani, S., Ohgawara, H., Agishi, T., Akaike, T., Miyazaki, S. A bio-aritificial endocrine pancreas for the treatment of diabetes. Transplant Proceed 30:485-489. 1998.

64. Kuo, C.K., Ma, P.X. Ionically crosslinked alginate hydrogels as scaffolds for tissue engineering: part 1. Structure, gelation rate and mechanical properties. Biomaterials 22(6):511-21. 2001.

65. Lahooti, S., Sefton, M.V. Agarose enhances the viability of intraperitoneally implanted microencapsulated L929 fibroblasts. Cell Transplant 9(6):785-96. 2000.

66. Massoud, T., Gambhir, S. Molecular imaging in living subjects: seeing fundamental biological processes in a new light. Genes Dev 17(5):545-580. 2003.

67. Cherry, S.R., Gambhir, S. use of positron emission tomography in animal research. Ilar J 42:219-232. 2001.

68. Gambhir, S.S., Herschman, H.R., Cherry, S.R., Barrio, J.R., Satyamurthy, N., Toyokuni, T., Phelps, M.E., Larson, S.M., Balatoni, J., Finn, R. *et al*. Imaging transgene expression with radionuclide imaging technologies. Neoplasia 2(1-2):118-38. 2000.

69. Koehne, G., Doubrovin, M., Doubrovina, E., Zanzonico, P., Gallardo, H.F., Ivanova, A., Balatoni, J., Teruya-Feldstein, J., Heller, G., May, C. *et al*. Serial in vivo imaging of the targeted migration of human HSV-TK-transduced antigen-specific lymphocytes. Nat Biotechnol 21(4):405-13. 2003.

70. Nakamoto, Y., Higashi, T., Sakahara, H., Tamaki, N., Itoh, K., Imamura, M., Konishi, J. Evaluation of pancreatic islet cell tumors by fluorine-18 fluorodeoxyglucose positron emission tomography: comparison with other modalities. Clin Nucl Med 25(2):115-9. 2000.

71. Sweet, I.R., Cook, D.L., Lernmark, A., Greenbaum, C.J., Wallen, A.R., Marcum, E.S., Stekhova, S.A., Krohn, K.A. Systematic screening of potential beta-cell imaging agents. Biochem Biophys Res Commun 314(4):976-83. 2004.

72. Moore, A., Bonner-Weir, S., Weissleder, R. Noninvasive in vivo measurement of beta-cell mass in mouse model of diabetes. Diabetes 50(10):2231-6. 2001.

73. Wu, J., Chen, I., Sundaresan, G., Min, J.-J., De, A., Qiao, J.-H., Fishbein, M., Gambhir, S. Molecular imaging of cardiac cell transplantation in living animals using optical bioluminescence and positron emission tomography. Circulation 108:1302-1305. 2003.

74. Smith, S.J., Purchio, T., West, D.B. In vivo monitoring of pancreatic islet mass and function in a transgenic mouse model. Obes Res 12(1):170. 2004.

75. Kaneko, K., Yano, M., Yamano, T., Tsujinaka, T., Miki, H., Akiyama, Y., Taniguchi, M., Fujiwara, Y., Doki, Y., Inoue, M. *et al*. Detection of peritoneal micrometastases of gastric carcinoma with green fluorescent protein and carcinoembryonic antigen promoter. Cancer Res 61(14):5570-4. 2001.

76. Chan, W.C., Maxwell, D.J., Gao, X., Bailey, R.E., Han, M., Nie, S. Luminescent quantum dots for multiplexed biological detection and imaging. Curr Opin Biotechnol 13(1):40-6. 2002.

77. Mitchell, P. Turning the spotlight on cellular imaging. Nat Biotechnol 19(11):1013-7. 2001.

78. Dubertret, B., Skourides, P., Norris, D.J., Noireaux, V., Brivanlou, A.H., Libchaber, A. In vivo imaging of quantum dots encapsulated in phospholipid micelles. Science 298(5599):1759-62. 2002.

79. Larson, D.R., Zipfel, W.R., Williams, R.M., Clark, S.W., Bruchez, M.P., Wise, F.W., Webb, W.W. Water-soluble quantum dots for multiphoton fluorescence imaging in vivo. Science 300(5624):1434-6. 2003.

80. Akerman, M.E., Chan, W.C., Laakkonen, P., Bhatia, S.N., Ruoslahti, E. Nanocrystal targeting in vivo. Proc Natl Acad Sci U S A 99(20):12617-21. 2002.

81. Arbab, A.S., Bashaw, L.A., Miller, B.R., Jordan, E.K., Bulte, J.W., Frank, J.A. Intracytoplasmic tagging of cells with ferumoxides and transfection agent for cellular magnetic resonance imaging after cell transplantation: methods and techniques. Transplantation 76(7):1123-30. 2003.

82. Kang, H.W., Josephson, L., Petrovsky, A., Weissleder, R., Bogdanov, A., Jr. Magnetic resonance imaging of inducible E-selectin expression in human endothelial cell culture. Bioconjug Chem 13(1):122-7. 2002.

83. Weissleder, R., Cheng, H.C., Bogdanova, A., Bogdanov, A., Jr. Magnetically labeled cells can be detected by MR imaging. J Magn Reson Imaging 7(1):258-63. 1997.

84. Sundstrom, J.B., Mao, H., Santoianni, R., Villinger, F., Little, D.M., Huynh, T.T., Mayne, A.E., Hao, E., Ansari, A.A. Magnetic resonance imaging of activated proliferating rhesus macaque T cells labeled with superparamagnetic monocrystalline iron oxide nanoparticles. J Acquir Immune Defic Syndr 35(1):9-21. 2004.

85. Zhao, M., Beauregard, D.A., Loizou, L., Davletov, B., Brindle, K.M. Non-invasive detection of apoptosis using magnetic resonance imaging and a targeted contrast agent. Nat Med 7(11):1241-4. 2001.

86. Remsen, L.G., McCormick, C.I., Roman-Goldstein, S., Nilaver, G., Weissleder, R., Bogdanov, A., Hellstrom, I., Kroll, R.A., Neuwelt, E.A. MR of carcinoma-specific monoclonal antibody conjugated to monocrystalline iron oxide nanoparticles: the potential for noninvasive diagnosis. AJNR Am J Neuroradiol 17(3):411-8. 1996.

87. Weissleder, R., Moore, A., Mahmood, U., Bhorade, R., Benveniste, H., Chiocca, E.A., Basilion, J.P. In vivo magnetic resonance imaging of transgene expression. Nat Med 6(3):351-5. 2000.

88. Moore, A., Sun, P.Z., Cory, D., Hogemann, D., Weissleder, R., Lipes, M.A. MRI of insulitis in autoimmune diabetes. Magn Reson Med 47(4):751-8. 2002.

89. Minichiello, M., Albert, D., Kolodny, N., Lee, M., Craft, J. A perfusion system developed for 31P NMR study of melanoma cells at tissue-like density. Magn Res Med 10:96-107. 1989.

90. Fernandez, E., Mancuso, A., Murphy, M., Blanch, H., Clark, D. Nuclear magnetic resonance methods for observing the intracellular environment of mammalian cells. Ann NY Acad Sci 589:458-475. 1990.

91. Gillies, R., Galons, J., McGovern, K., Scherer, P., Lien, Y., Job, C., Ratcliff, R., Chapa, F., Cerdan, S., Dale, B. Design and application of NMR-compatible bioreactor circuits for entended perfusion of high density mammalian cell cultures. NMR Biomedicine 6:95-104. 1993.

92. Papas, K.K., Long, R.C., Constantinidis, I., Sambanis, A. Effects of short-term hypoxia on a transformed cell-based bioartificial pancreatic construct. Cell Transplant 9(3):415-22. 2000.

93. Constantinidis, I., Sambanis, A. Towards the development of artificial endocrine tissues: 31P NMR spectroscopic studies of immunoisolated, insulin-secreting AtT-20 cells. Biotechnol Bioeng 47:431-443. 1995.

94. Papas, K.K., Long, R.C., Jr., Constantinidis, I., Sambanis, A. Role of ATP and Pi in the mechanism of insulin secretion in the mouse insulinoma betaTC3 cell line. Biochem J 326(Pt 3):807-14. 1997.

95. Stegman, L.D., Rehemtulla, A., Beattie, B., Kievit, E., Lawrence, T.S., Blasberg, R.G., Tjuvajev, J.G., Ross, B.D. Noninvasive quantitation of cytosine deaminase transgene expression in human tumor xenografts with in vivo magnetic resonance spectroscopy. Proc Natl Acad Sci U S A 96(17):9821-6. 1999.

96. Pykett, I.L. NMR imaging in medicine. Sci Am 246(5):78-88. 1982.

97. Hornung, P.A., Schuff, N. Noninvasive imaging and spectroscopy--broad applications of magnetic resonance. Clin Chem 38(9):1608-12. 1992.

98. Porter, D.A., Smith, M.A. Magnetic resonance spectroscopy in vivo. J Biomed Eng 10(6):562-8. 1988.

99. Bhujwalla, Z.M., Shungu, D.C., Glickson, J.D. Effects of blood flow modifiers on tumor metabolism observed in vivo by proton magnetic resonance spectroscopic imaging. Magn Reson Med 36(2):204-11. 1996.

100. Kaplan, O., Kushnir, T., Askenazy, N., Knubovets, T., Navon, G. Role of nuclear magnetic resonance spectroscopy (MRS) in cancer diagnosis and treatment: 31P, 23Na, and 1H MRS studies of three models of pancreatic cancer. Cancer Res 57(8):1452-9. 1997.

101. Koutcher, J.A., Motwani, M., Zakian, K.L., Li, X.K., Matei, C., Dyke, J.P., Ballon, D., Yoo, H.H., Schwartz, G.K. The in vivo effect of bryostatin-1 on paclitaxel-induced tumor growth, mitotic entry, and blood flow. Clin Cancer Res 6(4):1498-507. 2000.

102. Savic, I., Thomas, A.M., Ke, Y., Curran, J., Fried, I., Engel, J., Jr. In vivo measurements of glutamine + glutamate (Glx) and N-acetyl aspartate (NAA) levels in human partial epilepsy. Acta Neurol Scand 102(3):179-88. 2000.

103. Stoppe, G., Bruhn, H., Pouwels, P.J., Hanicke, W., Frahm, J. Alzheimer disease: absolute quantification of cerebral metabolites in vivo using localized proton magnetic resonance spectroscopy. Alzheimer Dis Assoc Disord 14(2):112-9. 2000.

104. Bowen, B.C., Pattany, P.M., Bradley, W.G., Murdoch, J.B., Rotta, F., Younis, A.A., Duncan, R.C., Quencer, R.M. MR imaging and localized proton spectroscopy of the precentral gyrus in amyotrophic lateral sclerosis. AJNR Am J Neuroradiol 21(4):647-58. 2000.

105. Constantinidis, I., Malko, J.A., Peterman, S.B., Long, R.C., Jr., Epstein, C.M., Boor, D., Hoffman, J.C., Jr., Shutter, L., Weissman, J.D. Evaluation of 1H magnetic

resonance spectroscopic imaging as a diagnostic tool for the lateralization of epileptogenic seizure foci. Br J Radiol 69(817):15-24. 1996.

106. Barth, J.D. Which tools are in your cardiac workshop? Carotid ultrasound, endothelial function, and magnetic resonance imaging. Am J Cardiol . 87(4A):8A-14A. 2001.

107. Baur, A., Reiser, M.F. Diffusion-weighted imaging of the musculoskeletal system in humans. Skeletal Radiol 29(10):555-562. 2000.

108. Chung, C.B., Lektrakul, N., Gigena, L., Resnick, D. Magnetic resonance imaging of the upper extremity: advances in technique and application. Clin Orthop 383:162-74. 2001.

109. May, D.A., Disler, D.G., Jones, E.A., Balkissoon, A.A., Manaster, B.J. Abnormal signal intensity in skeletal muscle at MR imaging: patterns, pearls, and pitfalls. Radiographics 20:S295-315. 2000.

110. Bencardino, J.T., Rosenberg, Z.S., Brown, R.R., Hassankhani, A., Lustrin, E.S., Beltran, J. Traumatic musculotendinous injuries of the knee: diagnosis with MR imaging. Radiographics 20:S103-20. 2000.

111. Burstein, D., Bashir, A., Gray, M.L. MRI techniques in early stages of cartilage disease. Invest Radiol 35(10):622-38. 2000.

112. Eskey, C.J., Robson, C.D., Weber, A.L. Imaging of benign and malignant soft tissue tumors of the neck. Radiol Clin North Am 38(5):1091-104. 2000.

113. Frank, H. Characterization of atherosclerotic plaque by magnetic resonance imaging. Am Heart J 141(2 Suppl):S45-8. 2001.

114. Beckmann, N., Hof, R.P., Rudin, M. The role of magnetic resonance imaging and spectroscopy in transplantation: from animal models to man. NMR Biomed 13(6):329-48. 2000.

115. Constantinidis, I., Long, R., Jr., Weber, C., Safley, S., Sambanis, A. Non-Invasive monitoring of a bioartificial pancreas in vitro and in vivo. Ann N Y Acad Sci 944:83-95. 2001.

116. Bilgen, M., Elshafiey, I., Narayana, P.A. In vivo magnetic resonance microscopy of rat spinal cord at 7 T using implantable RF coils. Magn Reson Med 46(6):1250-3. 2001.

117. Silver, X., Ni, W.X., Mercer, E.V., Beck, B.L., Bossart, E.L., Inglis, B., Mareci, T.H. In vivo 1H magnetic resonance imaging and spectroscopy of the rat spinal cord using an inductively-coupled chronically implanted RF coil. Magn Reson Med 46(6):1216-22. 2001.

118. Hicks, B.A., Stein, R., Efrat, S., Grant, S., Hanahan, D., Demetriou, A.A. Transplantation of beta cells from transgenic mice into nude athymic diabetic rats restores glucose regulation. Diabetes Res Clin Pract 14(3):157-64. 1991.

119. Benson, J.P., Papas, K.K., Constantinidis, I., Sambanis, A. Towards the development of a bioartificial pancreas: effects of poly-L-lysine on alginate beads with BTC3 cells. Cell Transplant 6(4):395-402. 1997.

120. Sun, A., O'Shea, G. Microencapsulation of living cells: a long-term delivery system. J Control Release 2:137-141. 1985.

121. Smidsrod, O. Molecular basis for some physical properties of alginates in gel state. J Chem Soc Faraday Trans 57:263-274. 1974.

122. Skjak-Braek, G., Grasdalen, H., Smidsred, O. Inhomogeneous Polysaccharide Ionic Gels. Carbohydrate Polymers 10:31-54. 1989.

123. Smidsrod, O., Skayak-Braek, G. Alginate as immobilization matrix for cells. Trends Biotechno 8:71-78. 1990.

124. Martinsen, A., Storro, I., Skjak-Braek, G. Alginate as immobilization material: III. Diffusional properties. Biotechnol Bioeng 29:186-194. 1992.

125. Thu, B., Bruheim, P., Espevik, T., Smidsrod, O., Soon-Shiong, P., Skjak-Braek, G. Alginate polycation microcapsules. II. Some functional properties. Biomaterials 17(11):1069-79. 1996.

126. Thu, B., Bruheim, P., Espevik, T., Smidsrod, O., Soon-Shiong, P., Skjak-Braek, G. Alginate polycation microcapsules. I. Interaction between alginate and polycation. Biomaterials 17(10):1031-40. 1996.

127. De Vos, P., De Haan, B., Wolters, G.H., Van Schilfgaarde, R. Factors influencing the adequacy of microencapsulation of rat pancreatic islets. Transplantation 62(7):888-93. 1996.

128. Soon-Shiong, P., Feldman, E., Nelson, R., Heintz, T., Yao, Q., Yao, Z. Long-term reversal of diabetes by the injection of immunoprotected islets. Proc Natl Acad Sci 90:5843-5847. 1993.

129. Klock, G., Frank, H., Houben, R., Zekorn, T., Horcher, A., Siebers, U., Wohrle, M., Federlin, K., Zimmermann, U. Production of purified alginates suitable for use in immunoisolated transplantation. Appl Microbiol Biotechnol 40(5):638-43. 1994.

130. Constantinidis, I., Rask, I., Long, R.C., Jr., Sambanis, A. Effects of alginate composition on the metabolic, secretory, and growth characteristics of entrapped beta TC3 mouse insulinoma cells. Biomaterials 20(21):2019-27. 1999.

131. Sun, A., Parisius, W., Macmorine, H., Sefton, M., Stone, R. An artificial pancreas containing cultured islets of Langerhans. Art Organs 4:275-278. 1980.

132. Leblond, F.A., Tessier, J., Halle, J.-P. Quantitative method for the evaluation of biomicrocapsule resistance to mechanical stress. Biomaterials 17(21):2097-2102. 1996.

133. Coger, R., Toner, M., Moghe, P., Ezzell, R., Yarmush, M.L. Hepatocyte aggregation and reorganization of EHS matrix gel. Tissue Eng 3(4):375-390. 1997.

134. Stokke, B.T., Drager, K.I., Yuguchi, Y., Urakawa, H., Kajiwara, K. Small-angle X-ray scattering and rheological characterization of alginate gels. Macromol Symp 120:91-101. 1997.

135. Helmlinger, G., Netti, P.A., Lichtenbeld, H.C., Melder, R.J., Jain, R.K. Solid stress inhibits the growth of multicellular tumor spheroids. Nat Biotechnol 15(8):778-83. 1997.

136. Lanza, R., Ecker, D., Kuhtreiber, W., Marsh, J., Ringeling, J., Chick, W. Transplantation of islets using microencapsulation: studies in diabetic rodents and dogs. J Mol Med 77(1):206-210. 1999.

137. Bottomley, P.; General Electric Company, assignee. 1984 October 30th. Selective volume method for performing localized NMR spectroscopy. USA patent 4,480,228.

138. Efrat, S. Prospects for treatment of type 2 diabetes by expansion of the beta-cell mass. Diabetes 50(Suppl 1):S189-90. 2001.

139. Jain, K., Asina, S., Yang, H., Blount, E.D., Smith, B.H., Diehl, C.H., Rubin, A.L. Glucose control and long-term survival in biobreeding/Worcester rats after intraperitoneal implantation of hydrophilic macrobeads containing porcine islets without immunosuppression. Transplantation 68(11):1693-700. 1999.

140. van Schilfgaarde, R., de Vos, P. Factors influencing the properties and performance of microcapsules for immunoprotection of pancreatic islets. J Mol Med 77(1):199-205. 1999.

141. Carslaw, H., Jaeger, J. Conduction of Heat in Solids: Clarendon. 1959.

142. Crank, J. The mathematics of diffusion: JW Arrowsmith Ltd. 1975.

143. Longsworth, L. Diffusion Measurements at 25C of Aqueous Solutions of Amino Acids, Peptides and Sugars. J Am Chem Soc 75:5705. 1953.

144. Ashcroft, F., Ashcroft, S. Insulin : molecular biology to pathology. Oxford: IRL Press. 1992.

145. Ochoa, E., Vacanti, J.P. An overview of the pathology and approaches to tissue engineering. Ann N Y Acad Sci 979:10-26. 2002.

146. Kaihara, S., Vacanti, J.P. Tissue engineering: toward new solutions for transplantation and reconstructive surgery. Arch Surg 134(11):1184-8. 1999.

147. Wu, H., Avgoustiniatos, E.S., Swette, L., Bonner-Weir, S., Weir, G.C., Colton, C.K. In situ electrochemical oxygen generation with an immunoisolation device. Ann N Y Acad Sci 875:105-25. 1999.

148. Dulong, J.L., Legallais, C., Darquy, S., Reach, G. A novel model of solute transport in a hollow-fiber bioartificial pancreas based on a finite element method. Biotechnol Bioeng 78(5):576-82. 2002.

149. Tziampazis, E., Sambanis, A. Tissue engineering of a bioartificial pancreas: modeling the cell environment and device function. Biotechnol Prog 11(2):115-26. 1995.

150. Wohlpart, D., Kirwan, D., Gainer, J. Effects of cell density and glucose and glutamine levels on the respiration rates of hybridoma cells. Biotechnol Bioeng 36:630-635. 1990.

151. Westrin, B., Alxelsson, A. Diffusion in gels containing immobilized cells: a critical review. Biotechnol Bioeng 39:439-445. 1991.

152. Chresand, T., Dale, B., Hanson, S. A Stirred Bath Technique for Diffusivity Measurements in Cell Matrices. Biotechnol Bioeng 32:1029-1036. 1988.

153. Lundberg, P., Kuchel, P.W. Diffusion of solutes in agarose and alginate gels: 1H and 23Na PFGSE and 23Na TQF NMR studies. Magn Reson Med 37(1):44-52. 1997.

154. Schantz, E., Lauffer, M. Diffusion Measurements in Agar Gel. Biochemistry 1(4):658-663. 1962.

155. Hildebrandt, P., Sejrsen, P., Nielsen, S., Birch, K., Sestoft, L. Diffusion and polymerization detemrines the insulin absorption from subcutaneous tissue in diabetic patients. Scand J Clin Lab Invest 45:685-690. 1985.

156. Sakai, S., Ono, T., Ijima, H., Kawakami, K. In vitro and in vivo evaluation of alginate/sol-gel synthesized aminopropyl-silicate/alginate membrane for bioartificial pancreas. Biomaterials 23(21):4177-83. 2002.

157. Hannoun, B., Stephanopoulos, G. Diffusion coefficients of glucose and ethanol in cell-free and cell-occupired calcium alginate membranes. Biotechnol Bioeng 28:829-835. 1986.

158. Pu, H., Yang, R. Diffusion of sucrose and yonimbine in calcium alginate ge beads with or without entrapped plant cells. Biotechnol Bioeng 32:891-896. 1988.

159. Dulong, J.L., Legallais, C. Contributions of a finite element model for the geometric optimization of an implantable bioartificial pancreas. Artif Organs 26(7):583-9. 2002.

160. Constantinidis, I., Stabler, C., Long, R.C., Jr., Sambanis, A. Non-invasive monitoring of a retrievable bioartificial pancreas in vivo. Ann N Y Acad Sci 961:298-301. 2002.

161. Alberts, B., Bray, D., Lewis, J., Raff, M., Roberts, K., Watson, J. Molecular biology of the cells. New York: Garland Publishing. 1998.

162. De Vos, P., De Haan, B., Wolters, G.H., Van Schilfgaarde, R. Factors influencing the adequacy of microencapsulation of rat pancreatic islets. Transplantation 62(7):888-93. 1996.

163. Iwata, H., Amemiya, H., Matsuda, T., Takano, H., Hayashi, R., Akutsu, T. Evaluation of microencapsulated islets in agarose gel as bioartificial pancreas by studies of hormone secretion in culture and by xenotransplantation. Diabetes 38(Suppl 1):224-5. 1989.

164. Lanza, R.P., Ecker, D., Kuhtreiber, W.M., Staruk, J.E., Marsh, J., Chick, W.L. A simple method for transplanting discordant islets into rats using alginate gel spheres. Transplantation 59(10):1485-7. 1995.

165. Jain, K., Yang, H., Cai, B.R., Haque, B., Hurvitz, A.I., Diehl, C., Miyata, T., Smith, B.H., Stenzel, K., Suthanthiran, M. *et al*. Retrievable, replaceable, macroencapsulated pancreatic islet xenografts. Long-term engraftment without immunosuppression. Transplantation 59(3):319-24. 1995.

166. Aomatsu, Y., Nakajima, Y., Iwata, H., Amemiya, H., Kanehiro, H., Hisanaga, M., Yoshimura, A., Kido, K., Taki, J., Horikawa, M. *et al*. Significance of low doses of 15-deoxyspergualin in agarose-microencapsulated discordant islet xenotransplantation. Transplant Proc 27(1):292-3. 1995.

167. Aomatsu, Y., Nakajima, Y., Iwata, H., Takagi, T., Amemiya, H., Kanehiro, H., Hisanaga, M., Fukuoka, T., Yoshimura, A., Kido, K. *et al*. Indefinite graft survival

of discordant islet xenografts in the NOD mouse with agarose microencapsulation and 15-deoxyspergualin. Transplant Proc 26(2):805-6. 1994.

168. Iwata, H., Takagi, T., Amemiya, H. Marked prolongation of islet xenograft survival (hamster to mouse) by microencapsulation and administration of 15-deoxyspergualin. Transplant Proc 24(4):1517-8. 1992.

169. Mosmann, T. Rapid colorimetric assay for cellular growth and survival: application to proliferation and cytotoxicity assays. J Immunol Methods 65(1-2):55-63. 1983.

170. Goodwin, C.J., Holt, S.J., Downes, S., Marshall, N.J. Microculture tetrazolium assays: a comparison between two new tetrazolium salts, XTT and MTS. J Immunol Methods 179(1):95-103. 1995.

171. Fields, R.D., Lancaster, M.V. Dual-attribute continuous monitoring of cell proliferation/cytotoxicity. Am Biotechnol Lab 11(4):48-50. 1993.

172. Crouch, S.P., Kozlowski, R., Slater, K.J., Fletcher, J. The use of ATP bioluminescence as a measure of cell proliferation and cytotoxicity. J Immunol Methods 160(1):81-8. 1993.

173. Porstmann, T., Ternynck, T., Avrameas, S. Quantitation of 5-bromo-2-deoxyuridine incorporation into DNA: an enzyme immunoassay for the assessment of the lymphoid cell proliferative response. J Immunol Methods 82(1):169-79. 1985.

174. Yang, H., Acker, J., Chen, A., McGann, L. In situ assessment of cell viability. Cell Tranplant 7(5):443-451. 1998.

175. Keevil, S.F., Barbiroli, B., Brooks, J.C., Cady, E.B., Canese, R., Carlier, P., Collins, D.J., Gilligan, P., Gobbi, G., Hennig, J. *et al*. Absolute metabolite quantification by in vivo NMR spectroscopy: II. A multicenter trial of protocols for in vivo localized proton studies of human brain. Magn Reson Imaging 16(9):1093-106. 1998.

176. Jackowski, S. Cell cycle regulation of membrane phospholipid metabolism. J Biol Chem 271(34):20219-22. 1996.

177. Constantinidis, I., Mukundan, N.E., Gamcsik, M.P., Sambanis, A. Towards the development of a bioartificial pancreas: a 13C NMR study on the effects of alginate/poly-L-lysine/alginate entrapment on glucose metabolism by beta TC3 mouse insulinoma cells. Cell Mol Biol (Noisy-le-grand) 43:721-9. 1997.

178. Walker, N.I., Harmon, B.V., Gobe, G.C., Kerr, J.F. Patterns of cell death. Methods Achiev Exp Pathol 13:18-54. 1988.

179. Damjanov, I., Linder, J. Anderson's Pathology. St Louis: Mosby. 1996.

180. Forbes, G. Human body composition: growth, aging, nutrition, and activity. New York: Springer-Verlag. 1987.

181. Williams, P., Warwick, R., Dyson, M., Bannister, L. Gray's Anatomy. New York: Churchill Livingstone. 1989.

182. Millard, N., King, B., M, S. Human Anatomy and Physiology. Philadephia: Saunders Company. 1956.

183. Pomfret, E., da Costa, K., Schurman, L., Zeisel, S. Measurement of choline and choline metabolite concentrations using high-pressure liquid chromatography and gas chromatography-mass spectrometry. Anal Biochem 180:85-90. 1989.

184. Kinoshita, K., Yokota, A. Absolute concentrations of metabolites in human brain tumors using in vitro proton magnetic resonance spectroscopy. NMR Biomed 10:2-12. 1997.

185. Ting, Y.L., Sherr, D., Degani, H. Variations in energy and phospholipid metabolism in normal and cancer human mammary epithelial cells. Anticancer Res 16(3B):1381-8. 1996.

186. Freyer, J.P., Schor, P.L., Jarrett, K.A., Neeman, M., Sillerud, L.O. Cellular energetics measured by phosphorous nuclear magnetic resonance spectroscopy are not correlated with chronic nutrient deficiency in multicellular tumor spheroids. Cancer Res 51(15):3831-7. 1991.

187. Bhakoo, K., Williams, S., Florian, C., Land, H., Noble, M. Immortilization and transformation are associated with specific alterations in choline metabolism. Cancer Res 56:4630-4635. 1996.

188. Grant, S.C., Simpson, N.E., Blackband, S.J., Constantinidis, I. MR microscopy and spectroscopy of in vitro alginate constructs: the engineering of a bioartificial pancreas; Snow Bird, Utah. 2003

189. Nerem, R., Sambanis, A. Tissue engineering: from biology to biological substitutes. Tissue Engineering 1(1):3-13. 1995.

190. Kaplan, O., Sijl, P.v., Cohen, J. NMR studies of metabolism of cells and perfused organs. In: Seelig, J., Rudin, M., editors. In vivo magnetic resonance spectroscopy III: In vivo MR spectroscopy: Poltential, and Limitations. Heidelberg: Springer-Verlag. p 4-52. 1992.

191. Burtscher, I.M., Holtas, S. Proton MR spectroscopy in clinical routine. J Magn Reson Imaging 13(4):560-7. 2001.

192. Sijens, P.E., Knopp, M.V., Brunetti, A., Wicklow, K., Alfano, B., Bachert, P., Sanders, J.A., Stillman, A.E., Kett, H., Sauter, R. *et al*. 1H MR spectroscopy in

patients with metastatic brain tumors: a multicenter study. Magn Reson Med 33(6):818-26. 1995.

193. Preul, M., Caramanos, Z., Collins, D., Villemure, J., Leblanc, R., Olivier, A., Pokrupa, R., Arnold, D. Accurate, non-invasive diagnosis of human brain tumors by using proton magnetic resonance spectroscopy. Nature Med 2:317-325. 1996.

194. Thomas, M.A., Binesh, N., Yue, K., DeBruhl, N. Volume-localized two-dimensional correlated magnetic resonance spectroscopy of human breast cancer. J Magn Reson Imaging 14(2):181-6. 2001.

195. Mackinnon, W., Barry, P., Malycha, P., Gillet, D., Russell, P., Lean, C., Doran, S., Barrachough, B., Bilous, M., Mountford, C. Fine-needle biopsy specimens of benign breast lesions distinguished from invasive cancer ex vivo with proton MR spectroscopy. Radiology 204:661-666. 1997.

196. Herminghaus, S., Pilatus, U., Moller-Hartmann, W., Raab, P., Lanfermann, H., Schlote, W., Zanella, F. Increased choline levels coincide with enhanced proliferative activity of human neuroepithelial brian tumors. NMR Biomed 15:385-392. 2002.

197. Lindskog, M., Kogner, P., Ponthan, F., Schweinhardt, P., Sandstedt, B., Heiden, T., Helms, G., Spenger, C. Noninvasive estimation of tumour viability in a xenograft model of human neuroblastoma with proton magnetic resonance spectroscopy (1H MRS). Br J Cancer 88:478-485. 2003.

198. Duijn, J., Matson, G., Maudsley, A., Weiner, M. 3D phase encoding 1H spectroscopic imaging of human brain. Magn Reson Imaging 10:315-319. 1992.

199. Duyn, J., Gillen, J., Sobering, G., van Zijl, P.C., Moonen, C. Multisection proton MR spectroscopic imaging of the brain. Radiology 188:277-282. 1993.

200. Ebel, A., Govindaraju, V., Maudsley, A. Comparison of inversion recovery preparation schemes for lipid suppression in 1H MRSI of human brain. Magn Red Med 49:903-908. 2003.

201. Noth, U., Grohn, P., Jork, A., Zimmermann, U., Haase, A., Lutz, J. 19F-MRI in vivo determination of the partial oxygen pressure in perfluorocarbon-loaded alginate capsules implanted into the peritoneal cavity and different tissues. Magn Reson Med 42(6):1039-47. 1999.

202. Arola, L., Palou, A., Remesar, X., Herrera, E., Alemany, M. Effect of stress and sampling site on metabolite concentration in rat plasma. Arch Int Physiol Biochim 88(2):99-105. 1980.

203. Abdel el Motal, S.M., Sharp, G.W. Inhibition of glucose-induced insulin release by xylazine. Endocrinology 116(6):2337-40. 1985.

204. Ambrisko, T.D., Hikasa, Y. Neurohormonal and metabolic effects of medetomidine compared with xylazine in beagle dogs. Can J Vet Res 66(1):42-9. 2002.

205. Desborough, J.P., Jones, P.M., Persaud, S.J., Landon, M.J., Howell, S.L. Isoflurane inhibits insulin secretion from isolated rat pancreatic islets of Langerhans. Br J Anaesth 71(6):873-6. 1993.

206. Kansal, P.C., Buse, M.G. The effect of adrenergic blocking agents on plasma insulin and blood glucose during urethan or epinephrine induced hyperglycemia. Metabolism 16(6):548-56. 1967.

207. Weiss, J., Zimmermann, F. Tribromoethanol (Avertin) as an anaesthetic in mice. Lab Anim 33(2):192-3. 1999.

208. Reid, W.C., Carmichael, K.P., Srinivas, S., Bryant, J.L. Pathologic changes associated with use of tribromoethanol (avertin) in the Sprague Dawley rat. Lab Anim Sci 49(6):665-7. 1999.

209. Gardner, D.J., Davis, J.A., Weina, P.J., Theune, B. Comparison of tribromoethanol, ketamine/acetylpromazine, Telazol/xylazine, pentobarbital, and methoxyflurane anesthesia in HSD:ICR mice. Lab Anim Sci 45(2):199-204. 1995.

210. Field, K.J., White, W.J., Lang, C.M. Anaesthetic effects of chloral hydrate, pentobarbitone and urethane in adult male rats. Lab Anim 27(3):258-69. 1993.